A Quest for Precision:

Theory and Phenomenology of Strong Interactions at Hadron Colliders

Wojciech Józef Bizoń

Wadham College

University of Oxford

A thesis submitted for the degree of

Doctor of Philosophy

Trinity Term 2018

Abstract

This thesis considers recent advances in applications of perturbative Quantum Chromodynamics (pQCD) to hadron collider physics, especially the LHC. In the main part it focuses on combining fixed-order predictions with all-order methods such as resummation and parton showers.

After a general introduction to the realm of pQCD we consider a take on the resummation technique in momentum space to provide results for colour singlet production processes for distributions of transverse inclusive observables that vanish away from the Sudakov region. We work at (next-to-)^3-leading-logarithmic (N^{3}LL) accuracy and match our results to the (next-to-)^2-leading order (NNLO) calculations. We present results for distributions of the transverse momentum of the Higgs boson (p_t^{H}) as well as the transverse momentum of the Z boson (p_t^{Z}) and ϕ^*_η in the Drell-Yan production process.

In the second part we discuss matching of the NNLO accurate calculations to parton showers using the `MiNLO` technique. The results are obtained by reweighting a sample of hard events at the partonic level with a K-factor that is fully differential in the Born phase space of the considered process. We treat the case of associated Higgs production (VH). We provide validation of our results and a short phenomenological study. In case of the HZ production we have considered the Higgs boson decay into a pair of b-quarks at the next-to-leading (NLO) order in QCD. Similarly we provide a phenomenological overview.

In the last part we examine a constraint on the Higgs boson self-coupling that may be obtained in the HL-LHC programme. We work in the framework of Standard Model Effective Field Theory (SM EFT) and consider loop-induced effects of one additional dimension-six operator that modifies the SM Higgs sector.

Acknowledgements

This thesis is a result of a four-year DPhil programme at the University of Oxford but it would have never been completed without an enormous help and support of many people around!

First and foremost I wish to express my gratitude to my supervisor Giulia Zanderighi for giving me an opportunity to pursue and develop my interest in theoretical physics. She has guided me through various regions of precision QCD and academic world. I want to thank for her guidance and encouragement to undertake a range of research projects.

Among my collaborators, I am especially indebted to Ulrich Haisch, Pier Monni and Emanuele Re, with whom I have spent a substantial amount of time in Oxford. Everything I know about physics beyond the Standard Model that might exist, but not necessarily does, I have learned from Uli. I was very fortunate to work with Pier and learn many aspects of resummation from him as he was always keen on explaining intricate concepts and sharing his knowledge. I would like to thank Emanuele for his patience in explaining meanders of parton showers, Monte Carlo's, `FORTRAN` and many other concepts. Equally or even more importantly, I have always appreciated his good advice on a variety of issues. It was also a pleasure to work with Martin Gorbahn and Paolo Torrielli with whom I shared prolonged calls.

I wish to thank William Astill and Luca Rottoli for sharing countless hours in our office as well as the ones outside. It was wonderful to have each other around, share many interesting and inspiring discussions and solve many problems together. I am very happy about meeting a number of people in Oxford; it was delightful to have an unexpected chat over lunch or coffee with Shaun Bailey, Valerio Bertone, Fady Bishara, Marco Bonvini, Alessandro Geraldini, Francesco Giuli, Nathan Hartland, Nick Jennings, George Johnson, Alexander Karlberg, Emanuele Nocera, Fabian Ruehle, Emma Slade, Jim Talbert, and many other fellow students and staff members. I am also grateful to Mike Teper who has been my co-supervisor and to my college adviser Candadi Sukumar for making sure that this thesis is on its way. I thank Michelle and Natalie for their help with everything at the department.

I cannot forget about people who have paved the way to my scientific adventure. I would like to thank Maciej Skrzypek for unveiling some secrets of the loop-calculations over one lazy summer in Kraków that kept me hooked on QCD. Teresa Młocek, Małgorzata Pasternak and Piotr Toma deserve a particularly special credit for their inspiration and dedication during my education.

Last but not least, I need to thank my family. I am obliged to my parents for everything they did for me, especially for their support in all my passions and decisions. I wish to thank my younger brother and sister for their company, even if separated by a long distance from home. I am exceptionally grateful to my wife Edyta for her unconditional love, support and her understanding. Lastly I thank my tiny daughter Hanna who did her best to interrupt progression of this thesis but fortunately did not succeed.

My research has been supported by the ERC Consolidator Grant HICCUP.

Contents

Preface

The history of subatomic physics now spans over a century. An advancement of our knowledge about the fundamental interactions has always been fuelled by two aspects of the scientific method - building theoretical models and their experimental verification. The discoveries of the electron, the atomic nucleus and further subatomic particles have always been intertwined with theoretical developments of some sort. Most importantly, the beginning of the 20$^{\text{th}}$ century has been marked by the formulation of two groundbreaking theories – Quantum Mechanics and Special Relativity. Their amalgamation has guided the invention of Quantum Field Theory (QFT) that provides a basis for all currently known theories at the smallest scales.

Our current understanding of physics of elementary particles can be summarised in the *Standard Model* (SM) of particle physics which incorporates three of the four fundamental interactions: electromagnetism and the weak and strong interactions. SM is a renormalisable QFT that has been constructed on the grounds of principle of local gauge invariance with

$$SU(3) \otimes SU(2) \otimes U(1)_Y$$

as the symmetry group. The corresponding three gauge couplings are free parameters. Further SM parameters include Yukawa couplings of six quarks and three leptons, three mixing angles and a CP violating phase, two parameters describing the Higgs sector and a parameter responsible for a potential CP violation in the strong interaction sector. Moreover, we now know that a deeper description of neutrino masses and their mixing angles is required. The full SM Lagrangian has been gradually uncovered over the years by studying Quantum Electrodynamics (QED) and the Fermi theory of weak interactions which are its low energy limits. The electroweak sector undergoes a spontaneous symmetry breaking (SSB) according to the Higgs mechanism that gives rise to masses of some of the gauge bosons, quarks and leptons. The Higgs boson, remnant of the SSB, was finally discovered in 2012 by the ATLAS and CMS experiments at CERN's Large Hadron Collider (LHC) and is the last of the SM building blocks.

This thesis will be predominantly focused on the strong interactions sector of the SM known as Quantum Chromodynamics (QCD). It governs relations between particles that carry colour charge, i.e. quarks and gluons. QCD is an ultimate product of the experimental and theoretical advancements achieved in 1960's and 1970's. Fractionally charged quarks seemed a bizarre attempt at a systematic description of multiplets of strongly interacting particles; nevertheless, further evidence provided by Deep Inelastic Scattering (DIS) experiment conducted at SLAC and the discovery of Bjorken scaling has attracted more attention to the idea and prompted the appearance of the parton model, which considered hadrons as composite objects. Together with the theoretical discoveries of asymptotic freedom and renormalisability of gauge theories, QCD has been formulated. Throughout the past decades, many experiments have only strengthened the body of evidence in favour of QCD.

Although it might seem like a closed chapter in particle physics, the theory of strong interactions still poses many challenges that need to be addressed. Progress in understanding the fundamental interactions has been usually driven by two aspects – high-energy experiments that provide access to new regions of phase space, and high-precision experiments that give an insight into subtle effects and verify our understanding of the theory. The dynamics of strong interactions is deeply ingrained into the physics at the LHC due to the nature of particles participating in the collisions. Combining the precision and energy frontiers at the LHC is possible to some extent, but the availability of the right tools is crucial for such achievement. In the following sections, we will present different techniques that are suited for obtaining reliable and precise predictions for processes studied at hadron colliders. In recent years we have witnessed a true revolution in the availability and automation of such perturbative QCD calculations. Once again, the story is not yet at the end with many relevant problems still to tackle.

This thesis is an outcome of a four-year postgraduate programme in Theoretical Particle Physics undertaken at the University of Oxford. The results presented throughout this work have been a product of research undertaken in various collaborations.

The 1-st chapter is aimed at introducing *Quantum Chromodynamics* (QCD) – the theory of strong interactions – and is an account of a long journey throughout many quantum field theory textbooks [1, 2, 3], lecture notes and reviews [4, 5, 6, 7] as well as some works focused particularly at the collider physics [8, 9, 10]. We extend this introduction into the 2-nd chapter where we describe in slightly more detail the main calculational techniques that have been employed to obtain the results presented in the remaining parts. We briefly describe the fixed-order perturbation theory that allows to tackle problems in terms of a power series, with the strong coupling as an expansion parameter. We further recount a few facts about resummed calculations and parton showers both of which attempt to treat enhanced logarithmic terms up to all orders in perturbation theory capturing some effects which are beyond the scope of a fixed-order analysis. We provide merely a glimpse on those areas taking an inspiration from much broader reviews [11, 12, 13, 14, 15].

In the 3-rd chapter we describe a resummation technique that operates in the momentum space and can be implemented in a numerical program as a transverse-momentum ordered Monte Carlo shower. We follow this discussion by phenomenological study of some distributions related to the Higgs boson production in gluon-gluon fusion as well as the Drell-Yan process. This work has been already presented in Refs. [16, 17] and is a product of a collaboration with Pier Monni, Emanuele Re, Luca Rottoli and Paolo Torrielli.

The 4-th chapter considers merging of event generators for various jet multiplicities using the `MiNLO` method and is further utilised to match parton shower to higher fixed-order QCD calculations. We focus explicitly on the associated Higgs (HW and HZ) production processes: we provide validation of our results and offer a short phenomenological study. This work has been already reported in Refs. [18, 19] and has been developed in a collaboration with William Astill, Emanuele Re and Giulia Zanderighi.

The 5-th chapter delivers an example of the impact of loop-induced anomalous effects on the physical observables in the context of the Higgs boson self-coupling. We parametrise the anomalous coupling in terms of dimension-six operator in the framework of Effective Field Theory and provide constraints on the corresponding Wilson coefficient. This work has been already shown in Ref. [20] and is a result of a collaboration with Martin Gorbahn, Ulrich Haisch and Giulia Zanderighi.

Finally, we summarise the thesis in chapter 6. We recollect all results that have been derived throughout this work and provide concluding remarks.

Wojciech Bizoń
Oxford, 2018

1
Introduction

Quantum Chromodynamics (QCD) is a self-consistent relativistic quantum field theory (QFT) built on the basis of a non-abelian local gauge symmetry. It governs the behaviour of quark fields (spin-$\frac{1}{2}$ fermions) and gluon fields (spin-1 bosons). Quarks correspond to matter fields and as such they provide building blocks for hadrons, bound states of strong interactions, while gluons serve as force carriers binding quarks together. Isolated quark or gluon states have not been observed so far and it is anticipated that they are always confined inside hadrons [21] due to strongly-coupled dynamics at low energies. Nevertheless, thanks to *asymptotic freedom*, a key property of QCD [22, 23], many short-distance phenomena fall under the scrutiny of highly developed methods of perturbation theory.

1.1 QCD: theory declaration

To uniquely define QCD we need to specify its field content as well as the Lagrangian density.

Quark fields are spin-$\frac{1}{2}$ Dirac fields, $\psi_{\sigma a f}$ with σ, a and f being respectively a Dirac spinor index, a *colour* index in the fundamental representation of the gauge group and a flavour index responsible for different quark types present in the theory. We currently distinguish six different quark flavours which are listed in Table 1.1. The group transformation acts on the colour index.

Quark	**Symbol**	**Mass**	**Electric charge**	**Weak isospin**
up	u	~ 2.2 MeV	$+2/3$	$+1/2$
down	d	~ 4.7 MeV	$-1/3$	$-1/2$
strange	s	~ 95 MeV	$-1/3$	$-1/2$
charm	c	~ 1.275 GeV	$+2/3$	$+1/2$
bottom	b	~ 4.18 GeV	$-1/3$	$-1/2$
top	t	~ 173 GeV	$+2/3$	$+1/2$

Table 1.1: List of the six known quarks ordered according to their masses, for the details of the mass definition see [24].

Gluon fields, A^{A}_{μ}, are spin-1 bosonic fields, where index μ corresponds to a Lorentz vector index while A is a colour index in the adjoint representation of the gauge group. We note that, contrary to Quantum Electrodynamics (QED), the force mediators carry a charge. This is a consequence of non-abelian feature of the gauge group and will play a crucial role in characteristics of the theory.

So far, we have been only referring to a gauge symmetry, that underpins the QCD theory, without specifying any further details. We now recognise a fact that the Lagrangian of strong interactions is controlled by an $SU(N_c)$ gauge group with $N_c = 3$ [25, 26].

The $SU(3)$ is a non-abelian Lie group consisting of 3×3 complex unitary matrices U with unit determinant ($U^{\dagger}U = \mathbb{1}$ and $\det U = +1$). An infinitesimal group element $U(\omega)$ (transformation) can be expressed as

$$U(\omega) = \mathbb{1} + i\omega^{\mathrm{A}}T^{\mathrm{A}} + \mathcal{O}(\omega^2), \tag{1.1}$$

where ω^{A} are the parameters of the transformation and T^{A} form a set of generators that span the Lie algebra, $\mathfrak{su}(3)$, corresponding to the symmetry group $SU(3)$. A finite transformation U can be reconstructed with the help of the *exponential* map that provides a link from Lie algebra to the Lie group.

For a finite-dimensional representation, the generators are a set of traceless Hermitian matrices. In our case, we consider matrices $(t^{\mathrm{A}})_{bc}$ and $(T^{\mathrm{A}})_{\mathrm{BC}}$ to be generators in the fundamental and adjoint representations of $SU(3)$, respectively. They satisfy:

$$[t^{\mathrm{A}}, t^{\mathrm{B}}] = if^{\mathrm{ABC}}t^{\mathrm{C}}, \qquad [T^{\mathrm{A}}, T^{\mathrm{B}}] = if^{\mathrm{ABC}}T^{\mathrm{C}}, \tag{1.2}$$

where $f^{\rm ABC}$ are the Lie group *structure constants*; $a, b, c = \{1, 2, 3\}$, while A, B, C $= \{1, \ldots, 8\}$. The commutation relations of Eq. (1.2) imply the *Jacobi identity*,

$$f^{\rm ADE} f^{\rm BCD} + f^{\rm BDE} f^{\rm CAD} + f^{\rm CDE} f^{\rm ABD} = 0. \tag{1.3}$$

Generators of the adjoint representation can be constructed from the structure constants, $(T^{\rm A})_{\rm BC} = -i f^{\rm ABC}$, while the ones of the fundamental representation are often assembled with the help of the eight Gell-Mann matrices, $t^{\rm A} = \frac{1}{2}\lambda^{\rm A}$. It is conventional to set the normalisation of the generators $t^{\rm A}$ such that

$$\mathrm{Tr}\left(t^{\rm A} t^{\rm B}\right) = T_R\, \delta^{\rm AB}, \qquad \text{with} \qquad T_R = \tfrac{1}{2}. \tag{1.4}$$

Furthermore, since the operator $T^2_{(r)} \equiv \sum_{\rm A} T^{\rm A}_{(r)} T^{\rm A}_{(r)}$ commutes with all symmetry group generators, it is therefore proportional to the identity operator, $T^2_{(r)} = C_r\, \mathbb{1}$, where C_r is known as *quadratic Casimir invariant.* For fundamental and adjoint representations we have:

$$\textstyle\sum_{\rm A} \left(t^{\rm A}\right)_{ab} \left(t^{\rm A}\right)_{bc} = C_F\, \delta_{ac}, \qquad \text{with} \qquad C_F = \dfrac{N_c^2 - 1}{2N_c} = \dfrac{4}{3}, \tag{1.5}$$

$$\textstyle\sum_{\rm A} \left(T^{\rm A}\right)_{\rm AB} \left(T^{\rm A}\right)_{\rm BC} = C_A\, \delta_{\rm AC}, \qquad \text{with} \qquad C_A = N_c = 3. \tag{1.6}$$

Much more detailed discussions of Lie groups and algebras, with their applications to the Elementary Particle Physics, can be found in standard textbooks [1, 2, 8].

Having specified the field content and after a brief discussion of the $SU(3)$ symmetry group, we can finally attempt to construct a Lagrangian for the theory of strong interactions, $\mathcal{L}_{\rm QCD}$. We start by writing a standard Lagrangian for a generic Yang-Mills theory with minimally coupled matter fields [27]:

$$\mathcal{L}_{\rm QCD} = -\frac{1}{4} F^{\rm A}_{\mu\nu} F^{{\rm A},\mu\nu} + \sum_{\text{flavours}} \bar{\Psi}_a \left(i\not{D} - m_f\right)_{ab} \Psi_b, \tag{1.7}$$

where $F^{\rm A}_{\mu\nu}$ represents the field strength tensor, defined as

$$F^{\rm A}_{\mu\nu} = \partial_\mu A^{\rm A}_\nu - \partial_\nu A^{\rm A}_\mu - g_s f^{\rm ABC} A^{\rm A}_\mu A^{\rm B}_\nu, \tag{1.8}$$

with g_s being the strong coupling; we have used a shorthand slash notation $\not{D} \equiv \gamma^\mu D_\mu$ for the covariant derivative,

$$\left(D_\mu\right)_{ab} = \partial_\mu \delta_{ab} + i g_s \left(t^{\rm A} A^{\rm A}_\mu\right)_{ab}. \tag{1.9}$$

Additionally, Ψ is a four-component Dirac spinor. We have also omitted a flavour index f, since a diagonalisation of the mass matrix in flavour space is always possible [28, 29]. This means that sum over flavours can be considered as a sum of six separate quark fields.

The QCD Lagrangian in Eq. (1.7) is invariant under a local gauge transformation:

$$\begin{aligned} \Psi(x) &\longrightarrow \Psi'(x) = \mathbf{U}(x)\Psi(x) \\ \mathbf{A}_\mu(x) &\longrightarrow \mathbf{U}(x)\mathbf{A}_\mu(x)\mathbf{U}^{-1}(x) + \frac{i}{g_s}(\partial_\mu \mathbf{U}(x))\mathbf{U}^{-1}(x), \end{aligned} \tag{1.10}$$

where bold symbols indicate a matrix in fundamental representation in colour space, and we have used an abbreviation $\mathbf{A}_\mu = \sum_{\mathrm{A}} t^{\mathrm{A}} A^{\mathrm{A}}_\mu$. We note that the field strength tensor $F^{\mathrm{A}}_{\mu\nu}$, defined in Eq. (1.8), is not invariant under the gauge transformation of Eq. (1.10) and therefore cannot be associated with a simple physical interpretation. We recall that in the case of QED the field strength tensor is gauge invariant and can be associated with electric and magnetic fields which are physical objects.

The Lagrangian (1.7) allows us to specify a generating functional for the theory in terms of a path integral. We can then calculate Green's functions, i.e. vacuum expectation values of time-ordered products of fields:

$$\langle 0|\mathrm{T}F[\Psi,\bar{\Psi},\mathbf{A}_\mu]|0\rangle = \mathcal{N}\int \mathcal{D}\mathbf{A}_\mu \mathcal{D}\Psi\mathcal{D}\bar{\Psi}\; F[\Psi,\bar{\Psi},\mathbf{A}_\mu]\; e^{iS_{\mathrm{QCD}}[\Psi,\bar{\Psi},\mathbf{A}_\mu]}, \tag{1.11}$$

with

$$S_{\mathrm{QCD}}[\Psi,\bar{\Psi},\mathbf{A}_\mu] \equiv \int d^4x\; \mathcal{L}_{\mathrm{QCD}}[\Psi,\bar{\Psi},\mathbf{A}_\mu], \tag{1.12}$$

where $F[\Psi,\bar{\Psi},\mathbf{A}_\mu]$ is a functional of the fields, T stands for the time-ordering as on the left-hand side we deal with quantum fields, $|0\rangle$ is the true vacuum state of the theory and the the normalisation factor $\mathcal{N}$ has been fixed using a usual condition $\langle 0|0\rangle = 1$. The S-matrix elements, and further measurable quantities like cross sections and decay rates, can be computed from Green's functions using the Lehmann-Symanzik-Zimmermann (LSZ) reduction formula [30, 31].

Unfortunately, since the action (1.12) is invariant under the symmetry transformation (1.10), the path integral (1.11) is proportional to the volume of the gauge orbit, i.e. field configurations connected by some gauge transformation. This poses a serious problem for the formulation of perturbation theory. The unwanted redundancy can be removed by restricting the functional measure with a suitable gauge fixing condition [32]. For a family of *covariant gauges*, one can supplement the Lagrangian, $\mathcal{L}_{\rm QCD}$, with a gauge-fixing part,

$$\mathcal{L}_{\rm gf} = -\frac{1}{2\xi}\left(\partial^\mu A^{\rm A}_\mu\right)^2, \tag{1.13}$$

that is naturally accompanied by a ghost Lagrangian,

$$\mathcal{L}_{\rm ghost} = \left(\partial_\mu \eta^{\rm A}\right)^\dagger \left(D^\mu_{\rm AB}\eta^{\rm B}\right), \tag{1.14}$$

where $\eta^{\rm A}$ is a ghost field – a complex scalar field respecting Fermi statistics and ξ is a free gauge parameter (special choices include $\xi = 1$ for Feynman gauge, $\xi = 0$ for Landau gauge). Other choices of gauge conditions are possible [33].

This resolves the issue of treating the gauge symmetry under the sign of a path integral, and finally we can define the Feynman rules that will provide building blocks for the perturbation theory.

1.2 Renormalisation and running of the strong coupling

Evaluation of the higher-order corrections to Green's functions and S-matrix elements generates Feynman diagrams containing loop integrals, many of which turn out to be divergent. We often refer to these singularities, resulting from highly energetic momenta running in the loop, as *ultraviolet* (UV) divergences. These quantum effects modify relations between parameters of the original Lagrangian, the *bare parameters*, which are no longer directly related to physical quantities. As a consequence, one needs to specify a *regularisation* procedure that will allow for a consistent treatment of the divergences. A procedure of redefining the original parameters leading to a theory with measurable finite predictions is known as *renormalisation.*

A widely used method of regulating the divergent integrals in QFT is the dimensional regularisation scheme [34], where the loop integrals are evaluated in $d = 4 - 2\epsilon$ space-time dimensions and the divergences manifest themselves as poles in the ϵ parameter. Such singularities can be easily subtracted by means of the *counterterms* included in the counterterm Lagrangian, $\mathcal{L}_{\rm ct}$, which features terms of exactly the same form as the ones appearing in the original Lagrangian,

$$\mathcal{L} = \mathcal{L}_{\rm QCD} + \mathcal{L}_{\rm gf} + \mathcal{L}_{\rm ghost}, \tag{1.15}$$

but with appropriately chosen prefactors. The renormalised Lagrangian,

$$\mathcal{L}_{\rm ren} = \mathcal{L} + \mathcal{L}_{\rm ct}, \tag{1.16}$$

yields finite Green's functions and S-matrix elements. The regularisation procedure introduces an additional mass scale μ, at which the subtractions are performed. It is an arbitrary parameter and is often referred to as the *renormalisation scale.*

Furthermore, the subtraction procedure is not uniquely defined, with elimination of the divergences being the only requirement. Various schemes can differ by parts which are analytic as $\epsilon \to 0$. A simple choice with only the divergent parts subtracted is called the *minimal subtraction* (MS) scheme, while more often one also cancels the remnants of the regularisation procedure which amounts to the *modified minimal-subtraction* ($\overline{\rm MS}$) scheme.

In the case of QCD, and gauge theories in general, it is crucial to perform the renormalisation procedure without violating the gauge invariance. It is relatively easy to show that for theories invariant under a global symmetry the counterterm Lagrangian also respects the initial symmetry and therefore the renormalisation procedure can be carried out. However, in our case we consider a local gauge symmetry instead of global one. The manifest gauge invariance of the original Lagrangian has been already broken by the introduction of the gauge-fixing term. Nevertheless, a particularly elegant solution has been gradually constructed. It has been shown that the original Lagrangian $\mathcal{L}$ is invariant under the Becchi-Rouet-Stora-Tyutin (BRST) symmetry [35, 36, 37] that provides a set of Ward identities. The identities imply relations between various Green's functions and further can be translated into constraints on various counterterms. Consequently, one can demonstrate renormalisability of a gauge theory at any number of loops. A first formal proof has been obtained in Ref. [34] that paved a road to a QFT of strong interactions, as well as the Standard Model.

As it was already indicated before, we have freedom in not only choosing a subtraction scheme but also a scale μ at which the subtraction is performed. However, physical quantities should be independent of these arbitrary choices. By exploring the invariance of physical quantities upon scale μ, we can obtain a differential equation that relates renormalised parameters, such as the strong coupling α_s, defined at one scale to those acquired for a different scale choice. This powerful tool is known as the Renormalisation Group (RG) [38, 39, 40] and is extensively used when studying various aspects of QFTs.

One of the important examples of an RG flow is the running of the strong coupling,

$$\alpha_s = \left(\frac{g_s^2}{4\pi}\right), \tag{1.17}$$

which is a dimensionless parameter responsible for strength of QCD interactions; it is expressed in terms of a renormalised gauge coupling g_s. The running is determined by a differential equation,

$$\mu^2 \frac{\partial \alpha_s(\mu^2)}{\partial \mu^2} = \beta\left(\alpha_s\left(\mu^2\right)\right), \tag{1.18}$$

where the function on the right hand side is known as β-function of the theory and it can be perturbatively expanded in powers of the strong coupling. Currently the β-function is known up to five-loops [41, 42]. We report our convention and the first four coefficients in Appendix A.2.

Computation of the leading coefficient β_0 in Refs. [22, 23] has been an important milestone in establishing the theory of strong interactions, as it verified that a non-abelian quantum field theory coupled to a sufficiently small number of fermions is *asymptotically free*, which means that the gauge coupling vanishes in the limit $\mu \to \infty$, i.e. for processes involving large momentum transfers. In the limit $\mu \to 0$, on the other hand, QCD becomes a strongly coupled theory that binds quarks and gluons into colourless states, i.e. states which behave as singlets under $SU(3)$ gauge transformations. Such a property is known as *confinement* and is the reason why free quarks and gluons are not directly observed as asymptotic states. The low energy behaviour of the strong interactions can be studied by means of the lattice QCD in a discretised space-time with finite volume [43].

A leading order solution to Eq. (1.18) can be written as

$$\alpha_s(\mu) = \frac{1}{\beta_0 \log\left(\frac{\mu}{\Lambda_{\rm QCD}}\right)}, \tag{1.19}$$

where $\Lambda_{\rm QCD}$ is a scale parameter that characterises QCD. As already anticipated, the Eq. (1.19) features the two properties that are typical for QCD, i.e. the strong coupling vanishes for $\mu \to \infty$ but on the other hand the perturbation theory breaks down at small scales at around $\mu \sim \Lambda_{\rm QCD}$ where the effects of strongly coupled dynamics take over.

1.3 Symmetries of the QCD Lagrangian

When discussing symmetries of the QCD Lagrangian we should naturally start with a local $SU(3)$ gauge invariance whose mathematical formalism has been already described in detail in Section 1.1. It is an exact symmetry in colour space and all terms in Eq. (1.7) respect it.

Additionally, we can distinguish a number of approximate symmetries that appear when exploring the strong interactions sector which we should identify on the basis of the presented QCD Lagrangian in Eq. (1.7).

First of all, we take a look at multiplets of particles with nearly the same mass, i.e. the proton and neutron doublet or the triplet of charged and neutral pions. This symmetry has been established long before the birth of QCD as the theory of strong interactions and is known as *isospin* symmetry. Assuming that the aforementioned particles are constructed from only two types (flavours) of quarks we can consider a symmetry in flavour space,

$$\Psi_q \longrightarrow \mathbf{M}_{qq'}\Psi_{q'}, \tag{1.20}$$

where q and q' are restricted to the lightest two flavours (up and down) and $\mathbf{M}_{qq'}$ is a two-dimensional $SU(2)$ matrix. Such a symmetry can be realised in the QCD Lagrangian in two cases, either $m_u = m_d$ or both $m_u, m_d \to 0$. In other words, if m_u and m_d are of the order of the Λ_{QCD} then we need $m_u \simeq m_d$; the other possibility being $m_u, m_d \ll \Lambda_{\mathrm{QCD}}$. The first alternative would require a justification for the similarity between quark masses while the second one is not only more theoretically appealing but is also favoured by the experimental evidence. We could actually split the fermionic fields into left- and right-handed components using projection operators:

$$\Psi_L = \tfrac{1}{2}\left(\mathbb{1} - \gamma_5\right)\Psi \qquad \text{and} \qquad \Psi_R = \tfrac{1}{2}\left(\mathbb{1} + \gamma_5\right)\Psi, \tag{1.21}$$

where γ_5 is the fifth gamma matrix, $\gamma_5 = i\gamma^0\gamma^1\gamma^2\gamma^3$. If the quark mass terms are absent, the fields with opposite chiralities (left/right-handedness) do not mix with each other and the full Lagrangian acquires a large symmetry,

$$SU(n_f)_L \otimes SU(n_f)_R \otimes U(1)_L \otimes U(1)_R, \tag{1.22}$$

where n_f indicates the number of massless flavours. The $SU(n_f)_L \otimes SU(n_f)_R$ contains a vector $SU(n_f)_V$ subgroup which is realised in the already mentioned part of the QCD spectrum. Considering the three lightest quarks (u, d and s) as nearly massless explains larger hadron multiplets that played a major role in establishing the theory of strong interactions [25, 26].

The remaining axial transformations are broken symmetries and result in eight Goldstone bosons – the pion fields. The two $U(1)$ groups are related to phase shifts of the quark fields. The vector subgroup $U(1)_V$ of the $U(1)_L \otimes U(1)_R$ symmetry corresponds to the isospin symmetry and the associated Noether current leads to baryon number conservation. The remaining axial symmetry $U(1)_A$ does not survive quantisation as certain loop-diagrams involving fermions introduce anomalous terms which break the relations between Ward identities associated with $U(1)_A$ [44, 45].

1.4 Infrared structure of QCD

In previous sections we have shown that, following a renormalisation procedure, QCD is a consistent theory that could be valid up to an arbitrary large energy scale – thanks to asymptotic freedom there is no UV Landau pole, unlike in the case of QED.

However, in addition to UV divergences that come from infinite loop momenta, we encounter singularities that occur when considering finite or infinitely small momenta in some special configurations [46]. We usually refer to them as *infrared* (IR) singularities. They can result not only from loop integrals when computing virtual corrections, in which case they are associated with a massless particle being exchanged in between two external legs, but also when additional real emissions of massless particles are integrated over the available phase space.

In order to illustrate the mechanism leading to IR singularities it is instructive to consider a simple example of a scalar decaying into a quark-antiquark pair [6]. The amplitude associated to a tree-level diagram, shown in Fig. 1.1 (left), reads

$$\mathcal{M}_{q\bar{q}} = \bar{u}_a(p_1) \left[i\, y_q\, \delta_{ab}/\sqrt{2} \right] v_b(p_2), \tag{1.23}$$

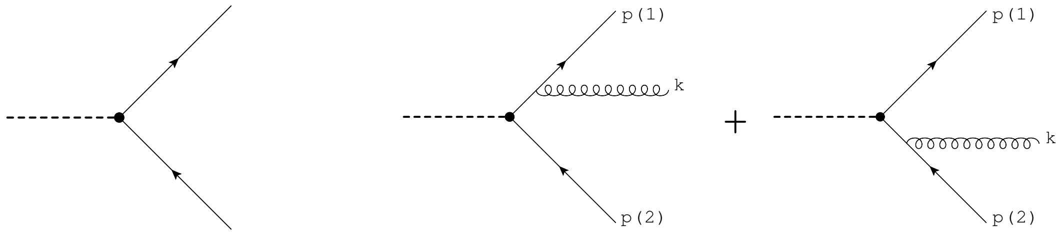

Figure 1.1: The Feynman diagrams that contribute to a scalar decaying into a quark-antiquark pair process. The first diagram on the left provides a tree-level leading amplitude while the two diagrams on the right contribute to a first order real correction to the process.

where $\bar{u}_a(p_1)$ and $v_b(p_2)$ are spinors for the external quarks, y_q is the quark Yukawa coupling and δ_{ab} indicates colour conservation in the vertex. A first correction to this process involves a real gluon emitted from a quark line, the two relevant diagrams are shown in Fig. 1.1 (right). Using on-shellness of quarks and the gluon, as well as the soft approximation, i.e. $k_\mu \ll p_{i,\mu}$, we get

$$\mathcal{M}_{q\bar{q}g} \simeq \bar{u}_a(p_1) \left[i\, y_q \left(t^{\mathrm{A}} \right)_{ab} / \sqrt{2} \right] v_b(p_2) \cdot g_s \left(\frac{p_1 \cdot \varepsilon_{\mathrm{A}}}{p_1 \cdot k} - \frac{p_2 \cdot \varepsilon_{\mathrm{A}}}{p_2 \cdot k} \right), \tag{1.24}$$

with ε_{A} being the polarisation vector of the gluon. Squaring the amplitude we obtain

$$|\mathcal{M}_{q\bar{q}g}|^2 \simeq |\mathcal{M}_{q\bar{q}}|^2 \cdot C_F \, (4\pi\alpha_s) \, \frac{2(p_1 \cdot p_2)}{(p_1 \cdot k)(p_2 \cdot k)}, \tag{1.25}$$

where the proportionality of $q\bar{q}g$ amplitude to the $q\bar{q}$ one is apparent. Using a fact that phase space can also be factorized in the soft limit, i.e.

$$d\Phi_{q\bar{q}g} \simeq d\Phi_{q\bar{q}} \times \frac{d^3\vec{k}}{2k_0(2\pi)^3}, \tag{1.26}$$

we can write

$$|\mathcal{M}_{q\bar{q}g}|^2 \, d\Phi_{q\bar{q}g} \simeq |\mathcal{M}_{q\bar{q}}|^2 \, d\Phi_{q\bar{q}} \times 4C_F \left(\frac{\alpha_s}{2\pi} \right) \frac{d\phi}{2\pi} \frac{dE}{E} \frac{d(\cos\theta)}{(1-\cos\theta)(1+\cos\theta)}, \tag{1.27}$$

where E is the energy of a soft gluon, θ is the angle between the soft emission and the quark, and we recall that in the soft kinematics quark and antiquark are back-to-back. We can immediately see that the expression (1.27) features two singular regions: *soft* when $E \to 0$ and *collinear/anticollinear* when $\theta \to 0/\pi$. Integration over the phase space can produce double-logarithmic corrections known as the Sudakov enhancement [47].

Factorization in the soft and collinear limits can be generalised to cases involving more coloured partons, see for example Ref. [48]. The structure of singularities is well-known, see for example Ref. [49], and it has been verified that the IR singularities between the real and virtual corrections cancel each other yielding finite predictions for measurable cross sections [50, 51].

Moreover, it has been realised that it is possible to design more exclusive observables than the total cross section which are calculable in perturbation theory, prime example being the Sterman-Weinberg jet definition [52]. The key property of the observable, to be accessible via perturbation theory, is the *infrared and collinear safety* (IRC safety). It requires the observable to be insensitive to low-energy (soft) and small-angle (collinear) real emissions,

$$
\begin{aligned}
&\mathcal{O}(p_1,\ldots,p_n,p_{n+1}) \xrightarrow[E_{n+1}\to 0]{} \mathcal{O}(p_1,\ldots,p_n),\\
&\mathcal{O}(p_1,\ldots,p_n,p_{n+1}) \xrightarrow[p_n||p_{n+1}]{} \mathcal{O}(p_1,\ldots,p_n+p_{n+1}),
\end{aligned} \tag{1.28}
$$

where in the above equations we have assumed, without loss of generality, that the soft and/or collinear parton is the last one. Note that conditions expressed in Eq. (1.28) should be satisfied $\forall n$, i.e. for arbitrary number of soft and/or collinear emissions.

Having defined the underlying concepts and properties of gauge theories and their relevance to the theory of strong interactions, we can now attempt a more detailed analysis. In the next chapter we will review different approaches to calculations in perturbative QCD. The remaining parts of the thesis will be devoted to discussion of results obtained in Refs. [16, 17], [18, 19] and [20].

2 Predictions for Hadron Collider Experiments

In a typical high-energy hadronic collision hundreds or even thousands of particles are produced and their enegries/momenta span many orders of magnitude. We soon realise that a customary perturbation theory approach, based on a simple expansion in powers of the strong coupling, fails as the quantum amplitudes are becoming incredibly complicated and the dimensionality of the phase space grows quickly ($\dim(\Phi) = 3N - 4 + 2$, where N is the number of particles in final state and the additional two degrees of freedom correspond to momentum fractions of the colliding hadrons inherited by the partons, according to collinear factorization). Moreover, we encounter regions of the phase space where scales appearing in the process are widely separated and lead to an enhancement of particular logarithmic terms that spoil the convergence of the perturbative series.

In order to deal with these problems various techniques have been established. A conventional perturbation theory, discussed in Section 2.2, can be aided with other approximations. In this chapter we will briefly discuss basic ideas behind resummation, which will be introduced in Section 2.3, that allows for a consistent treatment of terms enhanced by soft and/or collinear radiation. Further, in Section 2.4 we will focus on parton showers – an algorithmic approach that allows for an exclusive simulation of particle collisions.

2.1 Factorization formula for the cross section

A principal property behind the perturbative approach to strong interactions, that allows us to provide predictions for various processes occurring inside a hadron collider, is the *hard-process factorization.* It establishes a separation of the short-distance effects, usually referred to as a *hard process*, from the the non-perturbative long-distance physics that is responsible for holding the partons (constituents of the hadron, i.e. quarks and gluons) together.

One can introduce objects $f_a^h(\xi, \mu_F)$ known as *parton distribution functions* (PDFs) that can be treated as number density of partons of type a in the hadron h. Partonic momenta are approximately aligned with momentum of their parent hadron and ξ denotes the fraction of the hadron momentum inherited by the parton. The factorization scale μ_F indicates the division between the non-perturbative physics, described by PDFs, and the perturbative short-distance effects, delineated by hard partonic cross section which can be successively approximated in perturbation theory. An RG evolution equation that describes a relation between PDFs evaluated at different factorization scales can be derived. It has been independently formulated in Refs. [53, 54, 55] and is widely-known as the *Dokshitzer-Gribov-Lipatov-Altarelli-Parisi* (DGLAP) equation. It is extensively used in the fits of parton distribution functions [56] in order to incorporate data sets from various experiments. The ideas behind parton model predate the exact formulation of QCD itself [57, 58], nevertheless *the factorization theorems* can be rigorously formulated using the modern QCD language and, in some cases, proved with the help of operator product expansion (OPE), see Ref. [59] for a comprehensive review.

The factorized cross section for hadronic collisions can be summarised with a process independent formula:

$$\sigma = \sum_{a,b} \int_0^1 dx_a dx_b \int f_a^{h_1}(x_a, \mu_F) f_b^{h_2}(x_b, \mu_F) d\hat{\sigma}_{ab\to\psi}(\mu_F, \mu_R), \tag{2.1}$$

where the sums over a and b are meant to take into account contributions from all types of partons that constitute for hadrons h_1 and h_2 respectively. PDFs are evaluated at momentum fractions $x_{a,b}$ and at the factorization scale μ_F. Furthermore, $d\hat{\sigma}$ denotes the differential partonic cross section for $a + b$ scattering into state ψ consisting of n final state particles,

$$d\hat{\sigma}_{ab\to\psi}(\mu_F, \mu_R) = \frac{1}{2\hat{s}}\Big|\mathcal{M}_{ab\to\psi}(\Phi_n, \mu_F, \mu_R)\Big|^2 \, d\Phi_n, \tag{2.2}$$

where we have explicitly denoted the flux factor with $\hat{s}$ being the squared partonic centre-of-mass energy, and the phase space measure reads

$$d\Phi_n = \prod_{i=1}^{n} \frac{d^3 p_i}{(2\pi)^3 \, 2E_i} \cdot (2\pi)^4 \delta^{(4)} \left(p_1 + \ldots + p_n - p_a - p_b\right). \tag{2.3}$$

The squared amplitude $|\mathcal{M}_{ab\to\psi}|^2$ depends on the phase space point as well as the renormalisation scale μ_R.

As such, Eq. (2.1) can be evaluated provided the input parameters, i.e. the parton distribution functions $f_a^h(x_a, \mu_F)$ and the squared matrix elements $|\mathcal{M}_{ab\to\psi}|^2$. The dimensionality of the integral grows quickly with the number of particles in the final state, as evident from Eq. (2.3), and hence Monte Carlo (MC) techniques provide an optimal method for efficient calculation of the cross sections in scattering processes.

The calculation of the total cross section can be generalised to other observables $\mathcal{O}$ which, in general, are functions of momenta of particles involved in the scattering process:

$$\mathcal{O} = \mathcal{O}\left(p_1, \ldots, p_n\right). \tag{2.4}$$

An expectation value $\langle\mathcal{O}\rangle$ can be evaluated simply by inserting a measurement function $\mathcal{O}$ under the integral sign in Eq. (2.1). We should keep in mind the restrictions posed by IRC safety described in Section 1.4.

2.2 Fixed-order perturbation theory

One of the simplest methods of tackling physical problems is by means of the perturbation theory. We need to find a small parameter that is suitable for expansion and then systematically include higher-order corrections to the basic solution. A natural expansion parameter in QCD is the strong coupling α_s. We can then write a partonic cross section for the hard process as a Taylor series:

$$d\hat{\sigma}_{ab\to\psi} = \sum_{k=0}^{\infty} \left(\frac{\alpha_s}{2\pi}\right)^{k+k_0} d\hat{\sigma}^{(k)}_{ab\to\psi}, \tag{2.5}$$

where k_0 is the power of strong coupling present in the zeroth term of the expansion.

We can compute corrections at a given order of perturbation theory by performing relevant integrals as specified in Eqs. (2.1), (2.2), (2.3). A fully differential calculation allows for completely exclusive treatment of the final-state, i.e. we can consider fiducial cross sections which are obtained by phase-space integration constrained to a specific region that takes into account detector's geometry or aims at optimisation of a signal extraction from the background processes. We can also prepare differential cross sections that provide predictions as functions of kinematical configurations of produced particles.

Let us now assume that the leading term is well-defined and finite.[1] We immediately realise that often already the first correction is divergent. This is a well-known fact stemming from the infrared structure of QCD amplitudes in the presence of massless partons, as already discussed in Section 1.4. In order to address this issue we need to take a quick look at the process that involves production of state ψ in association with an additional QCD parton $x \in \{q, \bar{q}, g\}$:

$$d\hat{\sigma}_{ab\to\psi+x} = \sum_{k=0}^{\infty} \left(\frac{\alpha_s}{2\pi}\right)^{k+k_0+1} d\hat{\sigma}^{(k)}_{ab\to\psi+x}. \tag{2.6}$$

We notice that the leading term of Eq. (2.6) has the same power of the strong coupling as the first-order correction in Eq. (2.5). Moreover, the structure of divergences of process in Eq. (2.6) resembles the one of virtual corrections to Eq. (2.5). Thanks to IRC safety and arguments of *Kinoshita-Lee-Nauenberg* (KLN) theorem [50, 51] the resulting sum of the two is finite,

$$\int \left(d\hat{\sigma}^{(0)}_{ab\to\psi+x} + d\hat{\sigma}^{(1)}_{ab\to\psi}\right) \longrightarrow \text{finite}. \tag{2.7}$$

In summary, we can state a master formula for the $ab \to \psi$ cross section. We assume, at this point, that all UV divergences have been removed by the renormalisation procedure and the initial-state collinear singularities have been absorbed into the renormalised PDFs. We can organise the final formula in a way where we explicitly collect terms featuring

[1] Sometimes we need a suitable fiducial (generation) cut to avoid the divergence due to singular regions in squared amplitudes.

the IRC divergences that cancel each other into square brackets:

$$
\begin{aligned}
d\hat{\sigma}_{ab\to\psi} &= \mathrm{B}(\Phi_n)d\Phi_n \\
&+ \left(\frac{\alpha_s}{2\pi}\right)\left[\mathrm{V}(\Phi_n) + \int d\Phi_r\,\mathrm{R}(\Phi_{n+1})\right]d\Phi_n \\
&+ \left(\frac{\alpha_s}{2\pi}\right)^2\left[\mathrm{VV}(\Phi_n) + \int d\Phi_r\,\mathrm{RV}(\Phi_{n+1}) + \int d\Phi_{r_1}d\Phi_{r_2}\,\mathrm{RR}(\Phi_{n+2})\right]d\Phi_n \\
&+ \mathcal{O}(\alpha_s^3),
\end{aligned}
\tag{2.8}
$$

where the first line contains the Born or *leading-order* (LO) cross section, the second line presents the *next-to-leading-order* (NLO) term and the third one corresponds to the *next-to-next-to-leading-order* (NNLO) correction. Born term is a function of the leading order kinematics with n particles in the final-state. The second line contains two types of corrections – virtual (V) and real (R). The virtual correction is a function of Born kinematics and contains one additional loop-integral in the squared amplitude. The real correction has no additional loop-integrals but it contains an integral over the phase space of the real emission r. The combination of virtual and real corrections is finite as a consequence of the KLN theorem. Similar classification appears at NNLO, where we have double-virtual (VV) corrections containing extra two-loop integrals with respect to the Born configuration, real-virtual (RV) term with a one-loop integral and one additional real emission, and finally double-real (RR) correction with two real emissions.

Although the KLN theorem and the IRC safety ensures that the corrections will be finite it is not evident from Eq. (2.8), as each of the corrections is individually divergent and their combination may not be a straightforward task due to different origin of the infrared singularities. The main strategy for cancelling the infrared and collinear poles of the real and virtual origin is by designing a *subtraction formalism* which entails counterterms that can be used for removing divergences from the real-emission correction rendering them finite. Such counterterms need to encode the same singularity structure as the one of the real-radiation contributions. At the same time they should be simple enough allowing for their integration and subsequent combination with the virtual corrections that will lead to cancellation of the remaining IRC singularities. In practice, the simplified counterterm in the limiting case can be obtained using a matrix element of lower multiplicity, i.e. without the additional parton, combined with the relevant splitting function in the collinear case, or using a color correlated Born amplitude with an eikonal factor in the soft limit. Construction of a fully general subtraction formalism for NLO calculations has been successfully completed a long time ago [60, 48]. Although the structure of singularities at NNLO has been studied for a long time [49, 61, 62], a completely generic subtraction method is still missing. Nevertheless, there has been a significant progress achieved in the last decade and numerous approaches have been developed [63, 64, 65, 66, 67, 68, 69, 70]. While each of these techniques holds its own set of advantages and pitfalls, they all rely on the concept of factorization of soft and collinear singularities.

Another obstacle that stands in the way of computing higher-order corrections in Eq. (2.8) is the actual evaluation of loop integrals. This incorporates evaluation of integrals over the momenta of the extra virtual particles. In return the result often contains special functions. Moreover, these functions need to respect an intricate branch structure and have imaginary parts that will meet the thresholds when virtual particles become on-shell. All one-loop amplitudes in four dimensions can be expressed as combinations of logarithms and polylogarithms with coefficients that are rational functions. The structures that appear in virtual corrections at one-loop are well-known and many techniques [71, 72] allowing for automatic evaluation of virtual corrections in terms of master integrals [73, 74] were established [75, 76, 77]. Unfortunately, starting from two loops we encounter special functions which are generalisations of polylogarithms, i.e. *multiple polylogarithms* [78, 79], which have been a subject of active research with many unexpected properties identified. A parallel path attempting a numerical evaluation of the two-loop integrals has been followed [80, 81, 82]. A significant progress has been achieved in recent years allowing for many sophisticated NNLO calculations. Nevertheless, an automation of two-loop integrals at a level comparable to the one available for one-loop integrals is still ahead of us.

The era of NNLO QCD computations has taken off at the beginning of this century. After the first decade solutions for only a few important processes had been available. More importantly, in the past few years we have witnessed an intensified effort into designing new NNLO calculational techniques which led to numerous interesting results, including many challenging processes that involve additional coloured partons in final state. Instead of reporting a long list of processes that have already been tackled at

NNLO we refer the reader to reviews of the subject, such as Refs. [11, 12]. The case of NNLO calculations is definitely not a closed subject with a high research activity involved and many interesting problems, examples including integrals with multiple scales involved or corrections due to quark masses, still to be tackled. Furthermore, the first $\mathrm{N^3LO}$ results have been already reported [83, 84, 85].

2.3 Resummation – all-order approach

A fixed-order perturbation theory, as discussed in previous section, allows us to calculate predictions for IRC safe observables with ever greater accuracy. At k-th order of perturbation theory the difference between the exact result and prediction of a truncated series is

$$\frac{\sigma_{\mathrm{N}^k\mathrm{LO}}}{\sigma_{\mathrm{exact}}} \sim 1 + \mathcal{O}(\alpha_s^{k+1}). \tag{2.9}$$

However, it is important to note that expansion coefficients contain logarithmic (L) terms which include ratios of various scales present in the problem. In a typical high-energy collision many disparate energy scales may appear, ranging from the large energy of the collision, through the ones corresponding to electroweak sector, down to Λ_{QCD} and hadron masses. Often, presence of such widely separated scales enhances logarithmic terms and, in consequence, spoils the convergence of α_s expansion, as it is not exceptional to reach phase-space regions with $L \sim 1/\sqrt{\alpha_s}$ or even $L \sim 1/\alpha_s$.

As we have already discussed in Section 1.4, after UV renormalisation QCD amplitudes feature two types of singularities related to soft and collinear divergences, as evident from Eq. (1.27). The phase-space integration of the real radiation may therefore generate up to two powers of large logarithms L at each order of perturbation theory.

For this reason it is useful to consider an approach that is entirely different than the one of fixed-order perturbation theory. We can identify parts containing the most logarithmically divergent terms, that is to keep the most singular parts of the amplitudes and the phase space measure, and then to perform sum up to all orders in powers of the strong coupling. Such method provides a reasonable expansion as long as the logarithmic terms, that appear in these expressions, are large ($L \gg 1$). We can further define the *logarithmic* accuracy of the perturbative series as

$$\ln\left[\frac{\sigma_{\mathrm{N}^k\mathrm{LL}}}{\sigma_{\mathrm{exact}}}\right] \sim \mathcal{O}(\alpha_s^m L^{m-k}), \quad \text{for all } m \geq k, \tag{2.10}$$

where m runs up to infinity as we treat the logarithmic terms up to all orders in the powers of strong coupling.

Considering a generic observable $\mathrm{V}(\Phi_n)$ that is a function of the kinematical configuration of all particles particles involved in the scattering (Φ_n) and vanishes in the Born kinematics, i.e.

$$\mathrm{V}(\Phi_n) \xrightarrow[\Phi_n \to \Phi_{\mathrm{B}}]{} 0, \tag{2.11}$$

we can construct a cumulative cross section as a function of a value of the observable v:

$$\Sigma(v) = \sum_n \int \Phi_n \left(\frac{d\sigma}{d\Phi_n}\right) \Theta\left[v - \mathrm{V}(\Phi_n)\right]. \tag{2.12}$$

The resummed cumulative cross section can be expressed in terms of a power series and exponentiated logarithmic terms as follows:

$$\Sigma(v) = \sigma_{\mathrm{B}}\left[1 + \alpha_s c_1 + \alpha_s^2 c_2 + \dots\right] \times \exp\left\{L g_1(\alpha_s L) + g_2(\alpha_s L) + \dots\right\}, \tag{2.13}$$

where σ_{B} stands for the Born cross section and now we can explicitly define the logarithmic terms that we are interested in as $L \equiv \log(1/v)$. Coefficients c_i and functions $g_j(\alpha_s L)$ parametrise the cumulant $\Sigma(v)$. An N^kLL accurate resummation requires the knowledge of functions g_j with $j \leqslant k+1$ and coefficients c_i with $i \leqslant k-1$.

The research in pursuit of resummed expressions has been undertaken a long time ago and now we can distinguish two main perspectives on delivering results. The first one relies on considering a factorization theorem for a specific cross section and then using evolution equations for the resummation of large logarithms. This technique has been first proposed and used for studying the transverse momentum spectrum of the W and Z bosons in the Drell-Yan production process in Ref. [86]. More recently, it has been reformulated in the framework of soft-collinear effective theory (SCET) [87, 88, 89, 90], where the interactions between soft and collinear modes are parametrised in terms of effective operators at the level of the SCET Lagrangian. Subsequently, the renormalisation group (RG) evolution is used to obtain identify logarithmic terms.

Another technique of performing resummation is based on the branching formalism that relies on the structure of infrared and collinear singularities of the QCD squared amplitudes. It has been pioneered in Refs. [91, 92] and has been widely used since. The branching formalism can be realised in terms of a computer algorithm and a resummed expression might be obtained using an MC simulation. A particular automated implementation has been developed on the grounds of a semi-numerical resummation first proposed in Ref. [93]. The NLL accurate resummation for continuously global and recursively infrared and collinear (rIRC) safe[2] observables has been solved in Refs. [94, 95] and can be performed with a help of the computer program `CAESAR`. Subsequently, the `ARES` program has been created and it provides an NNLL extension of the formalism to cases involving event shapes and jet rates in the e^+e^- annihilation process. It has been studied in Refs. [96, 97] and recently completed in Ref. [98]. The treatment of resummation in hadronic-collisions has been proposed in Ref. [99]. Moreover, the ideas behind `CAESAR/ARES` implementations can be also utilised in the SCET-based approach to resummation, as has been studied in Ref. [100].

2.4 Parton shower

The techniques discussed in the previous section allow for an all-order treatment of QCD processes resulting in resummed distributions of a particular observable. However, in real life the collisions occurring inside a detector are recorded and stored in a much more detailed manner. We often have an access to momenta of individual particles appearing in an event and hence the studies might involve much more refined analyses than a treatment of a single observable. To match the level of sophistication on the theoretical side many *event generators* have been developed with the purpose of fully exclusive simulation of the kinematics of the collision.

An event generator provides a comprehensive account of a hadronic collision, starting from the two hadrons on the collision course up to the resulting final-state hadrons (and other particles) observed in the detector. A complete simulation can be decomposed into a few stages. The first part constructs a *hard process* that involves a $2 \to n$ scattering

[2] We postpone the precise definition until Section 3.1.2.

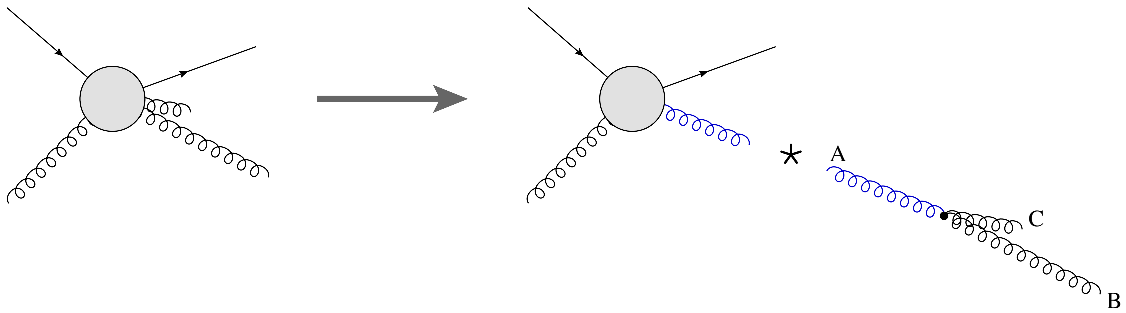

Figure 2.1: An illustration of the soft and collinear factorization of the QCD amplitudes that provides a basis for the branching formalism. A five-point amplitude factorises into a four-point amplitude and the A→B+C splitting.

generated according to a squared quantum amplitude prepared with the help of a list with Feynman rules. Nowadays there are many available systems allowing for a generation of numerous processes both within the Standard Model as well as ones belonging to its possible extensions, *e.g.* `MadGraph` [101, 102]. The restriction on the number of particles n in the hard process is posed only by the available computational power and usually is not larger than a few particles, as the complexity of the matrix elements quickly grows with the number of participants of the scattering.

General-purpose programs, such as `Pythia` [103, 104], `Herwig` [105, 106], and `Sherpa` [107], are then used to complete the picture of hadronic collisions; they work starting from the core hard process, generated as described above, and dress it with subsequent real emissions resulting from parton shower (PS), including additional interactions in the same collision, i.e. *multi-parton interactions* (MPI), simulating the beam remnants, i.e. *underlying event*, all the way down to hadronization and decays of unstable hadrons. While simulation of many of these effects relies on phenomenologically driven models, a PS itself can be derived from first principles as the leading solution to the branching formalism already mentioned in the previous section.

To illustrate the principles that are driving a PS evolution we look back at the Eq. (1.27) yet again. This time we consider a general amplitude involving $n+1$ partons and approximate it using a one involving n partons with an additional splitting A→B+C, as illustrated in Fig. 2.1. We assume that partons B and C are much closer to being on-shell than parton A, that is

$$p_{\mathrm{B}}^2,\, p_{\mathrm{C}}^2 \;\ll\; p_{\mathrm{A}}^2 \equiv t, \tag{2.14}$$

where by t we denote the virtuality of parton A. Furthermore, we can write

$$t = 2z(1-z)E_{\mathrm{A}}^2(1-\cos\theta), \tag{2.15}$$

with $z = (E_{\mathrm{B}}/E_{\mathrm{A}})$ being the fraction of energy taken by parton B and θ being the opening angle between partons B and C. The amplitude together with the phase-space element for $n+1$ partons can be expressed as

$$|\mathcal{M}_{n+1}|^2\, d\Phi_{n+1} \;\simeq\; |\mathcal{M}_n|^2\, d\Phi_n \times \left(\frac{\alpha_s}{2\pi}\right) \frac{dt}{t}\, P_{\mathrm{BA}}(z)dz, \tag{2.16}$$

where $P_{\mathrm{BA}}(z)$ is the *unregularised* Altarelli-Parisi splitting function [53, 54, 55] governing the A→BC branching, and A and B subscripts should be regarded as types of the partons (quark/gluon). The relevant leading-order splitting functions are[3]:

$$\begin{aligned}
P_{gg}^{(0)}(z) &= C_A\left[\frac{1-z}{z} + \frac{z}{1-z} + z(1-z)\right], \\
P_{qg}^{(0)}(z) &= T_R\left[z^2 + (1-z)^2\right], \\
P_{qq}^{(0)}(z) &= C_F\left[\frac{1+z^2}{1-z}\right].
\end{aligned} \tag{2.17}$$

Following the Eq. (2.16) we can define the probability of a splitting at a scale t as

$$d\mathcal{P}(z,t) = \left(\frac{\alpha_s}{2\pi}\right)\frac{dt}{t}\, P_{\mathrm{BA}}(z)dz \equiv F(z,t)dzdt, \tag{2.18}$$

where we have used a shorthand notation $F(z,t)$ for the probability distribution. It is easy to notice that the probability in Eq. (2.18) blows up as $t \to 0$ or as $z \to 0/1$ (depending on a type of the splitting). However, we need to remember that Eq. (2.16) takes care only of the real emission, while for consistency we should also consider virtual correction which will regulate the divergences. We can now define the *Sudakov form factor* $\Delta(t_2,t_1)$ which describes a no-emission probability during evolution between scales

[3]Note that we use the P notation for unregularised splitting functions, while leaving $\hat{P}$ for the regularised ones, introduced later in Chapter 3 and Appendix A. This differs from the convention used in Ref. [8].

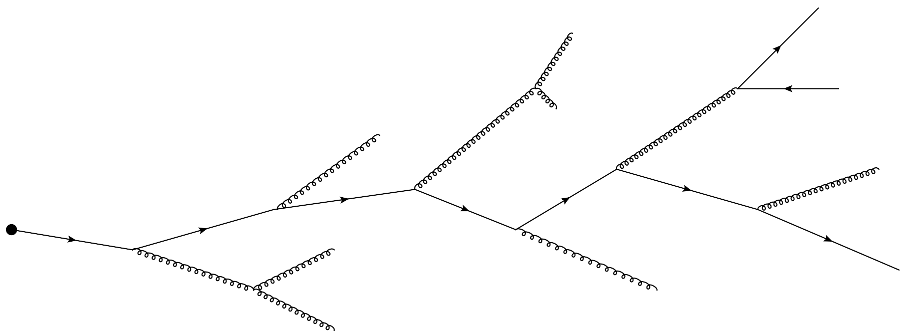

Figure 2.2: An illustration of a cascade of splittings generated by a parton shower algorithm according to probabilities encoded in the Sudakov radiator.

t_1 and t_2 ($t_1 > t_2$). Given that during an evolution from some initial scale t_I until the cut-off scale t_F the unitarity has to be preserved, i.e.

$$1 = \Delta(t_F, t_I) + \int_{t_F}^{t_I} \Delta(t, t_I)\, F(z, t) dz dt, \tag{2.19}$$

and that the real emissions should be mutually independent, i.e.

$$\Delta(t_F, t_I) = \Delta(t, t_I) \times \Delta(t_F, t) \qquad \forall t : t_F < t < t_I, \tag{2.20}$$

leads to the solution

$$\Delta(t_2, t_1) = \exp\left\{ - \int_{t_2}^{t_1} F(z, t) dz dt \right\}, \tag{2.21}$$

which describes a probability of no branching between scales t_1 and t_2. Such a setup is suitable for implementation in a Markov Chain Monte Carlo (MCMC) program, where one generates a random number r between 0 and 1, and subsequently solves the equation

$$\Delta(t_{i+1}, t_i) = r, \tag{2.22}$$

where t_i is a scale of a most recent splitting and the solution t_{i+1} gives the scale of the new splitting, we consider $t_0 = t_I$. We can iterate the procedure until reaching the cut-off scale, i.e. $t_{i+1} < t_F$ for some i. This generates a cascade of splittings, as depicted in Fig. 2.2. Note that we have discussed a case of final-state radiation (FSR) where we deal with *timelike* branchings, $t > 0$. A similar construction can be prepared for initial-state radiation (ISR). However, the kinematics of initial-state branchings is *spacelike*, $t < 0$.

We also remark that even though we have described an evolution according to virtuality of the parton t such a choice is by no means unique. Other evolution variables might include transverse momentum or angle of the splitting.

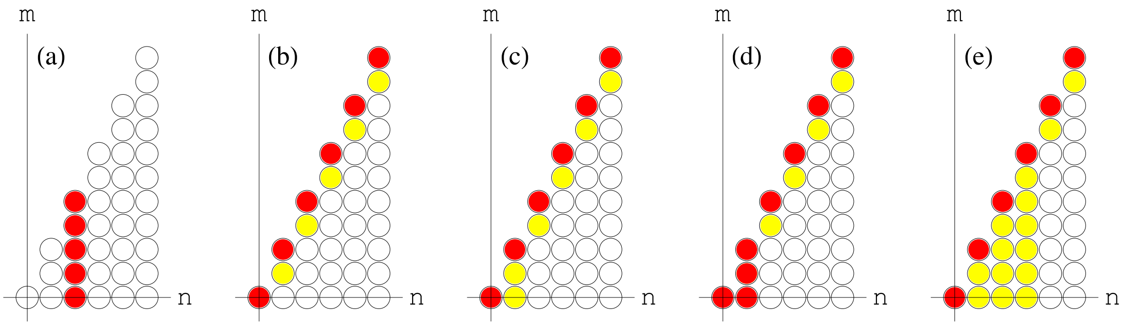

Figure 2.3: Pictorial view of the $\alpha_s^n L^m$ terms that enter various types of calculations: (a) tree-level matrix element treatment, (b) PS algorithm alone, (c) PS with matrix element corrections (ME+PS), (d) NLO+PS matched calculation, (e) PS with CKKW merging. Red circles represent terms fully included in the calculation, yellow circles denote terms which are partially taken into account. Figure inspired by Ref. [15].

2.4.1 MEC and NLO matching with parton shower

As we have already mentioned a PS is an algorithmic implementation of the leading approximation of the branching formalism. It correctly encodes the singular structure of matrix elements, however it disregards the finite non-universal parts of the virtual and real matrix elements. A lot of theoretical effort has been put into combining a PS approximation with more accurate treatment of real emissions or even matching with existing fixed-order calculations.

In Fig. 2.3 we illustrate towers of $\alpha_s^n L^m$ terms that enter various kinds of perturbative QCD calculations. When treating a particular process with a tree-level matrix element, Fig. 2.3(a), we include only terms proportional to a particular power of the strong coupling but all logarithmic and finite terms present in the squared amplitude are included. A PS approximation, Fig. 2.3(b), allows for an all order treatment inside an MCMC algorithm, but only the $\alpha_s^n L^{2n}$ terms are properly accounted for, and for some simple observables in a colour singlet production also the terms $\alpha_s^n L^{2n-1}$.

A first implementation of a shower with matrix-element corrections, i.e. the first emission is generated with a true real-emission matrix element instead of the factorized form of Eq. (2.16), has been proposed in Ref. [108]. This provided a control over the shape of distributions related to the first real emission. The virtual corrections were not included yet, hence the extra circle in Fig. 2.3(c) is marked with yellow colour which indicates only a partial treatment of the terms. A full inclusion of virtual and real corrections to the underlying process, as illustrated in Fig. 2.3(d), is known as *matching* an NLO fixed-order calculation with a parton shower (NLO+PS) and came slightly later. The two widely-used implementations are the MC@NLO [109, 110] generator and the `POWHEG` [111] implementation, which we will discuss in a more detailed fashion in the next subsection. Finally we mention an area of *multi-jet merging*, Fig. 2.3(e), where not only the first one but also further emissions are treated more carefully. In such programs the real emissions are corrected with a genuine tree-level matrix element as long as the emission is above a *merging scale*, otherwise one follows a basic PS algorithm. The first implementation of multi-jet merging, the CKKW merging procedure, has been proposed in Ref. [112].

Improving the accuracy of parton showers has been an active field of research in recent years. One can consider multi-jet merging with inclusion of one-loop corrections such as presented in Refs. [113, 114], the extension of matching to fixed-order calculations at NNLO [115, 116] which will be a subject of Chapter 4, or recent studies of logarithmic accuracy of parton showers [117].

2.4.2 NLO+PS matching in POWHEG

The `POWHEG` stands for framework for combining NLO QCD corrections with a parton shower. Currently it incorporates a large number of Standard Model processes as well as some possible extensions ready to employ to work by its users.[4] It has been proposed in Ref. [111] and the details were thoroughly discussed in Ref. [118]. A practical implementation, known as the `POWHEG-BOX`, has been described in Ref. [119]. In this section we will provide a short summary of the key ideas behind the program.

The `POWHEG` program allows for a generation of a Les Houches event (LHE) sample [120] that can be interfaced with various implementations of parton shower to obtain an NLO+PS accurate description. We stress that a straightforward matching requires a shower to be ordered according to transverse momentum of the emissions. Other orderings are possible but need the inclusion of truncated showers in order to restore the soft coherence [111]. From now on, we focus on the k_t ordered showers.

[4] `http://powhegbox.mib.infn.it/`

Let us consider a process with n particles in the final state. POWHEG will produce events that already contain the hardest emission and subsequent radiation induced by a parton shower should respect that bound.

The underlying Born phase space point is selected with a probability proportional to

$$\bar{B}(\Phi_n)d\Phi_n = \left[\sum_{f_b} \bar{B}^{f_b}(\Phi_n)\right] d\Phi_n, \tag{2.23}$$

where f_b is a label that indicates a sum over all Born flavour structures entering the process of interest, and[5]

$$\bar{B}^{f_b}(\Phi_n) = \Big[\mathrm{B}(\Phi_n) + \mathrm{V}(\Phi_n)\Big]_{f_b} + \sum_{\alpha_r \in \{\alpha_r | f_b\}} \int \Big[d\Phi_{\mathrm{rad}} \hat{\mathrm{R}}(\Phi_{n+1})\Big]_{\alpha_r}^{\bar{\Phi}_n^{\alpha_r}=\Phi_n}, \tag{2.24}$$

where B and V denote the Born and the soft-virtual, i.e. containing the integrated counterterms, contributions that have the flavour structure f_b, the index α_r denotes set of real flavour structures and the condition $\{\alpha_r|f_b\}$ stands for real structures whose underlying Born is f_b. The symbol $\hat{\mathrm{R}}$ denotes the real contribution which has been properly regularised, as explained in Section 2.4 of [118] (especially Eqs.(2.83)-(2.89) of the reference). The notation $\bar{\Phi}_n^{\alpha_r} = \Phi_n$ indicates that the $d\Phi_{\mathrm{rad}}$ integral is performed keeping the underlying Born configuration $\bar{\Phi}_n^{\alpha_r}$ fixed and equal to the Born phase space point Φ_n.

Having randomly drawn an underlying Born configuration we generate the radiation using the POWHEG Sudakov form factor,[6]

$$\Delta^{f_b}(\Phi_n, p_t) = \prod_{\alpha_r \in \{\alpha_r | f_b\}} \Delta^{f_b}_{\alpha_r}(\Phi_n, p_t), \tag{2.25}$$

with

$$\Delta^{f_b}_{\alpha_r}(\Phi_n, p_t) = \exp\left\{ - \left[\int d\Phi_{\mathrm{rad}} \frac{\mathrm{R}(\Phi_{n+1})}{\mathrm{B}^{f_b}(\Phi_n)} \Theta\Big(k_t(\Phi_{n+1}) - p_t\Big)\right]_{\alpha_r}^{\bar{\Phi}_n^{\alpha_r}=\Phi_n} \right\}. \tag{2.26}$$

Subsequently, POWHEG generates a p_t value for each region α_r according to a probability distribution

$$P^{f_b}_{\alpha_r}(p_t) = \frac{\partial}{\partial p_t} \Delta^{f_b}_{\alpha_r}(\Phi_n, p_t). \tag{2.27}$$

[5]Note that in order to preserve consistency of our notation and keep the discussion simple, we have not included terms corresponding to the initial-state singularities. The details might be easily filled in using the Refs. [118, 119].

[6]Note that, in contrast to previous section, we have used Φ_n and p_t as arguments of the Sudakov form factor. These are enough to evaluate the initial (upper) and final (lower) scales of the evolution, t_I and t_F.

The individual p_t values are generated with a veto method, and finally the program fixes the radiation region by selecting the highest p_t value. Having picked the radiation region we then generate the radiation variables and obtain a full event that includes a real emission.

We can summarise the full `POWHEG` cross section formula as follows

$$d\sigma_{\texttt{POWHEG}} = \sum_{f_b} \bar{B}^{f_b}(\Phi_n) d\Phi_n \times \left\{ \Delta^{f_b}(\Phi_n, p_t^{\min}) + \sum_{\alpha_r \in \{\alpha_r | f_b\}} \frac{\left[d\Phi_{\rm rad}\, \Theta(k_t - p_t^{\min})\, \Delta^{f_b}(\Phi_n, k_t) \mathrm{R}(\Phi_{\rm n+1}) \right]_{\alpha_r}^{\bar{\Phi}_n^{\alpha_r} = \Phi_n}}{\mathrm{B}^{f_b}(\Phi_n)} \right\}, \tag{2.28}$$

where the $p_t^{\min}$ ia a lower cut-off on the transverse momentum that conceals the unphysical values of the strong coupling or parton distribution functions.

Furthermore, an expectation value for a generic IRC safe observable $\mathcal{O}$ may be evaluated simply as

$$\langle \mathcal{O} \rangle = \sum_{f_b} \int d\Phi_n \bar{B}^{f_b}(\Phi_n) \Big\{ \Delta^{f_b}(\Phi_n, p_t^{\min}) \mathcal{O}_n(\Phi_n) + \sum_{\alpha_r \in \{\alpha_r | f_b\}} \frac{\left[d\Phi_{\rm rad}\, \Theta(k_t - p_t^{\min})\, \Delta^{f_b}(\Phi_n, k_t) \mathrm{R}(\Phi_{\rm n+1}) \mathcal{O}_{n+1}(\Phi_{n+1}) \right]_{\alpha_r}^{\bar{\Phi}_n^{\alpha_r} = \Phi_n}}{\mathrm{B}^{f_b}(\Phi_n)} \right\}. \tag{2.29}$$

In order to check that the Eq. (2.29) yields NLO accuracy we add and subtract a term proportional to $\mathrm{R}(\Phi_{\rm n+1})\mathcal{O}_n(\Phi_n)$, and after reshuffling some of the terms we obtain

$$\begin{aligned} \langle \mathcal{O} \rangle = & \sum_{f_b} \int d\Phi_n \bar{B}^{f_b}(\Phi_n) \\ & \times \left\{ \left[\Delta^{f_b}(\Phi_n, p_t^{\min}) + \sum_{\alpha_r \in \{\alpha_r | f_b\}} \frac{\left[d\Phi_{\rm rad}\, \Theta(k_t - p_t^{\min})\, \Delta^{f_b}(\Phi_n, k_t) \mathrm{R}(\Phi_{\rm n+1}) \right]_{\alpha_r}^{\bar{\Phi}_n^{\alpha_r} = \Phi_n}}{\mathrm{B}^{f_b}(\Phi_n)} \right] \mathcal{O}_n(\Phi_n) \right. \\ & \left. + \sum_{\alpha_r \in \{\alpha_r | f_b\}} \frac{\left[d\Phi_{\rm rad}\, \Theta(k_t - p_t^{\min})\, \Delta^{f_b}(\Phi_n, k_t) \mathrm{R}(\Phi_{\rm n+1}) \Big(\mathcal{O}_{n+1}(\Phi_{n+1}) - \mathcal{O}_n(\Phi_n) \Big) \right]_{\alpha_r}^{\bar{\Phi}_n^{\alpha_r} = \Phi_n}}{\mathrm{B}^{f_b}(\Phi_n)} \right\}. \end{aligned} \tag{2.30}$$

The large square bracket in second line is equal to one by the conservation of probability. Moreover, the last item of the outermost bracket is suppressed for emissions with small k_t by the factor $(\mathcal{O}_{n+1}(\Phi_{n+1}) - \mathcal{O}_n(\Phi_n))$. Hence, we can substitute $\Delta^{f_b}(\Phi_n, k_t) \to 1$

and $\bar{B} \to$ B in this last term, up to higher-order terms in α_s that are at most of the NNLO. This finally leads to

$$\langle \mathcal{O} \rangle = \sum_{f_b} \int d\Phi_n \Bigg\{ \bar{B}^{f_b}(\Phi_n) \mathcal{O}_n(\Phi_n) + \sum_{\alpha_r \in \{\alpha_r | f_b\}} \Big[d\Phi_{\mathrm{rad}} \, \mathrm{R}(\Phi_{\mathrm{n+1}}) \Big(\mathcal{O}_{n+1}(\Phi_{n+1}) - \mathcal{O}_n(\Phi_n) \Big) \Big]_{\alpha_r}^{\bar{\Phi}_n^{\alpha_r} = \Phi_n} \Bigg\}, \tag{2.31}$$

which reflects the fixed-order NLO formula. An interface to a transverse momentum ordered PS simulation will generate subsequent emissions but the first (hardest) one is already properly described according to NLO real matrix element.

In Chapter 4 we will discuss the merging of simulations for different jet multiplicities within `POWHEG` [121], and further provide an NNLO+PS matched results based on the prescription provided in [115].

3
Numerical Resummation

The pioneering approach to numerical resummation in direct space that we adopt in this chapter has been formulated in Refs. [93, 95] and further developed in many contexts, such as jet-vetoed cross sections [122, 123, 124], event shapes [96] or jet rates [97]. Some observables, like for instance the transverse momentum of a colour singlet in hadronic collisions, may vanish in kinematical configurations that feature emissions away from the strict soft and collinear limits. We will refer to such observables as having *zeroes way from the Sudakov region.* These observables require a slightly different resummation procedure that has been formulated [99].

As an example, in this chapter we will consider a production of the colour singlet state in hadronic collision with its decay into two particles,

$$pp \longrightarrow \mathrm{X} \longrightarrow (\ell_1 \ell_2)\,. \tag{3.1}$$

In particular we will keep two examples in mind: the Higgs boson production followed by the decay into pair of photons that has been studied in [16, 17] and the neutral Drell-Yan process with the decay of the Z boson into a pair of charged leptons discussed in [17].

3.1 Background for resummation

Let us now sketch the scene for resummation. We will consider some IRC safe observable $\mathrm{V}(\Phi_{\mathrm{B}}, k_1, \ldots, k_n)$ which is a function of the underlying Born configuration Φ_{B} of the examined process as well as of the momenta of all real emissions, k_1 up to k_n. We will describe the parametrisation of the Born phase space and subsequent real emissions. After the introduction of the concept of *recursive IRC safety* (rIRC) we will discuss a hierarchical decomposition of the real matrix elements and demonstrate a cancellation of the IRC singularities between real and virtual corrections. Finally, we will present an NLL accurate resummation formula.

3.1.1 The observable and parametrisation of the phase space

To parametrise the process illustrated in Eq. (3.1) we consider two reference light-like momenta that will allow us to describe the real emissions

$$\tilde{p}_1 = \frac{M}{2}\,(1,\,0,\,0,\,+1)\,, \qquad \tilde{p}_2 = \frac{M}{2}\,(1,\,0,\,0,\,-1)\,, \tag{3.2}$$

where by M we denote the invariant mass of the considered colour singlet with momentum $p_X = \tilde{p}_1 + \tilde{p}_2$. At Born level the momenta in Eq. (3.2) coincide with the partonic momenta in the rest frame of the colour singlet. Beyond the Born level real QCD radiation is present and the colour singlet may acquire non-zero transverse momentum. In general, the final state will consist of the colour singlet X accompanied by a set of n real partons with momenta $k_1, \ldots, k_n$.

It is useful to describe the momenta k_i by means of the Sudakov parametrisation

$$k_i = \left(1 - y_i^{(1)}\right)\tilde{p}_1 + \left(1 - y_i^{(2)}\right)\tilde{p}_2 + \tilde{\kappa}_{ti}, \tag{3.3}$$

where $\tilde{\kappa}_{ti}$ are space-like four-vectors orthogonal to both $\tilde{p}_1$ and $\tilde{p}_2$. In the reference frame of momenta in Eq. (3.2) each of the vectors $\tilde{\kappa}_{ti}$ has zero time component and lies in the plane perpendicular to $\tilde{p}_1$ and $\tilde{p}_2$. We can write

$$\tilde{\kappa}_{ti} = \left(0,\, \tilde{k}_t\cos\phi_i,\, \tilde{k}_t\sin\phi_i,\, 0\right), \tag{3.4}$$

where ϕ_i is the azimuthal angle between the vector $\vec{\tilde{k}}_{ti}$ and a fixed reference vector $\vec{n}$ orthogonal to the reference momenta $\tilde{p}_1$ and $\tilde{p}_2$. A convenient choice that we will adopt later is to choose $\vec{n}$ in a plane spanned by the $\hat{z}$ axis of (3.2) and momenta of X's decay products.

Given the masslessness of real emissions we can express the length of $\vec{\tilde{k}}_{ti}$ as

$$\tilde{k}_{ti}^2 = \frac{2(\tilde{p}_1 \cdot k_i)\, 2(\tilde{p}_2 \cdot k_i)}{2(\tilde{p}_1 \cdot \tilde{p}_2)}. \tag{3.5}$$

Moreover, using the parametrisation of (3.2) the transverse momentum and rapidity of the real emission i are given by

$$\tilde{k}_{ti}^2 = \left(1 - y_i^{(1)}\right)\left(1 - y_i^{(2)}\right) M^2, \qquad \text{and} \qquad \eta_i = \frac{1}{2} \ln \frac{1 - y_i^{(1)}}{1 - y_i^{(2)}}. \tag{3.6}$$

We now discuss the observable V that is a generic function of the momenta involved in the process. We denote a value of the observable in a particular configuration by v,

$$v = \mathrm{V}(\Phi_{\mathrm{B}}, k_1, \ldots, k_n)\,. \tag{3.7}$$

We also assume that it vanishes in Born-like kinematic configurations. Moreover, we require that for a single soft and collinear emission k the observable V scales as

$$\mathrm{V}_{\mathrm{sc}}(\Phi_{\mathrm{B}}, k) \equiv \mathrm{V}(k) = d_\ell\, g_\ell(\phi) \left(\frac{k_t}{M}\right)^a e^{-b_\ell \eta^{(\ell)}}, \tag{3.8}$$

where k_t is the transverse momentum with respect to the beam axis, $\eta^{(1)} = \eta$ and $\eta^{(2)} = -\eta$, $g_\ell(\phi)$ is a generic function of the angle ϕ and d_ℓ serves as a normalisation factor. We also note that $a > 0$, and $b_\ell > -a$ due to the IRC safety. We will further constrain ourselves to a class of *transverse* observables which do not depend on the rapidity of the emission, i.e. $b_\ell = 0$. In particular, we will consider the case of transverse momentum of colourless system ($d_\ell = g_\ell(\phi) = a = 1$), and the ϕ_η^* ($d_\ell = a = 1$, $g_\ell(\phi) = |\sin\phi|$) [125].

We also indicate that our analysis will be additionally restricted to the class of *inclusive* observables that obey the condition

$$\mathrm{V}(\Phi_{\mathrm{B}}, k_1, \ldots, k_n) = \mathrm{V}(\Phi_{\mathrm{B}}, k_1 + \ldots + k_n). \tag{3.9}$$

Such a requisite is trivially fulfilled for both studied observables – the transverse momentum of the colour singlet as well as the ϕ_η^*.

So far we have presented formulae containing transverse momentum defined in (3.2) parametrisation ($\tilde{k}_t$) and the one measured with respect to the beam axis (k_t). The two are related to each other by recoil effects due to hard-collinear emissions off the leg ℓ. One can derive a relation

$$\vec{k}_{ti} = \vec{\tilde{k}}_{ti} - \frac{\left(1 - y_i^{(1)}\right)}{1 + \sum_{j\in\ell_i}\left(1 - y_j^{(\ell_i)}\right)} \times \left(\sum_{j\in\ell_i} \vec{\tilde{k}}_{tj}\right), \tag{3.10}$$

where $j \in \ell_i$ means that we sum all emissions that originate from the same leg as emission k_i; more details about the derivation can be found in App. A.1. We point out that if one considers the ensemble of soft emissions ($y_i^{(\ell_i)}\simeq 1$) then the two quantities coincide. We will work under such assumption in order to derive the NLL result and we will discuss the treatment of hard-collinear emissions later.

After setting up the stage, we want to define the *logarithmic* accuracy that has been already mentioned in Eq. (2.10). In order to do so we introduce a *cumulative* cross section $\Sigma(v)$ that integrates the distribution $(d\sigma/dv)$ up to a given value v,

$$\Sigma(v) = \int_0^v dv' \, \frac{d\sigma(v')}{dv'}, \tag{3.11}$$

for a particular observable V. The logarithmic accuracy is commonly determined by the perturbative series of the logarithm of the cumulative cross section as

$$\ln \Sigma(v) \equiv \sum_n \left[\mathcal{O}\left(\alpha_s^n L^{n+1}\right) + \mathcal{O}\left(\alpha_s^n L^n\right) + \mathcal{O}\left(\alpha_s^n L^{n-1}\right) + \dots\right], \tag{3.12}$$

where $L = \ln(1/v)$. We refer to the dominant terms $\alpha_s^n L^{n+1}$ as leading logarithmic (LL), to terms $\alpha_s^n L^n$ as next-to-leading logarithmic (NLL) and so on. The underlying formula for evaluation of the cumulative cross section can be depicted as

$$\Sigma(v) = \int d\Phi_{\rm B}\, \mathcal{V}(\Phi_{\rm B}) \sum_{n=0}^{\infty} \int \prod_{i=1}^{n} [dk_i]\, |M(\Phi_{\rm B}, k_1, \dots, k_n)|^2 \; \Theta\big[v - {\rm V}(\Phi_{\rm B}, k_1, \dots, k_n)\big], \tag{3.13}$$

where $\Phi_{\rm B}$ stands for underlying Born phase space, whereas $[dk_i]$ is the phase space for the emission k_i; M is the squared matrix element for n real emissions ($n = 0$ reduces to the Born kinematics case). The symbol $\mathcal{V}(\Phi_{\rm B})$ stands for the virtual corrections to the form factor. Finally, Θ denotes a measurement function that constrains the region of integration.

3.1.2 Recursive IRC safety

One of the crucial concepts underlying all types of calculations presented in Chapter 2 is the IRC safety of the observable. It ensures that cancellations between soft and/or collinear singularities occur when combining real and virtual corrections.

In order to carry out a resummation, a calculation that involves expansion in the strong coupling up to all orders, it is crucial that the observable fulfills certain scaling properties that go under the name of *recursive infrared and collinear* (rIRC) safety. We will briefly explain the main concept following the presentation of Section 2.2.4 of [95]. Let us consider a momentum function $k_i = K_i(\omega)$ such that $\mathrm{V}(\Phi_\mathrm{B}, K_i(\omega)) = v\omega$. A real emission is fully specified by three variables, η_i^0, ξ_i and ϕ_i, which alongside Eq. (3.8) read now

$$\eta_i(\omega) = \eta_i^0 - \frac{\xi_i \ln(v\omega)}{a}, \qquad k_{ti} = \left(\frac{v\omega}{d_{\ell_i}\, g_{\ell_i}(\phi_i)}\right)^{1/a}, \qquad \phi_i(\omega) = \phi_i, \tag{3.14}$$

where ℓ_i denotes the leg that is the emission's origin. Varying ω corresponds to a line in the η-$\ln(k_t)$ (Lund) plane. Note that we have explicitly used the fact that we do not consider rapidity-dependent observables, i.e. $b_\ell = 0$. The IRC safety for an event with $(m+1)$ real partons can be then summarised as a requirement that

$$\lim_{\omega_{m+1}\to 0} \mathrm{V}(\Phi_\mathrm{B}, K_1(v\omega_1), \dots, K_m(v\omega_m), K_{m+1}(v\omega_{m+1})) = \mathrm{V}(\Phi_\mathrm{B}, K_1(v\omega_1), \dots, K_m(v\omega_m)), \tag{3.15}$$

where without loss of generality we have assumed that the last parton becomes soft and/or collinear. In case of an rIRC safe observable we would like that a contribution to the observable from a pair of two soft and/or collinear partons, that are of similar hardness and close in rapidity, is of the same order of magnitude as only one of those partons was present. Such a requirement may be expressed in terms of scaling properties. We therefore require that the limit as the overall hardness scale is decreased,

$$\lim_{v\to 0} \frac{1}{v} \mathrm{V}(\Phi_\mathrm{B}, K_1(v\omega_1), \dots, K_m(v\omega_m)), \tag{3.16}$$

is well-defined and non-zero, and moreover that the two aforementioned limits commute with each other

$$\left[\lim_{\omega_{m+1}\to 0}, \lim_{v\to 0}\right] \mathrm{V}(\Phi_\mathrm{B}, K_1(v\omega_1), \dots, K_m(v\omega_m), K_{m+1}(v\omega_{m+1})) = 0. \tag{3.17}$$

A similar condition should hold for collinear splittings. In practice, the above equation allows us to introduce a small resolution parameter[1] ϵ, independent of the observable v, such that if $\mathrm{V}(\Phi_\mathrm{B}, K_i(\omega)) < \epsilon v$ then the emission i can be ignored in the computation of the observable up to corrections of order $\epsilon^{\mathfrak{p}} v$ with $\mathfrak{p}$ being a positive power. This will allow for an explicit cancellation of the IRC poles between real and virtual corrections, up to all orders.

The recursive IRC safety also provides a decomposition of the real matrix element in such a way that terms contributing at a given logarithmic accuracy are retained.

3.1.3 The decomposition of the real emissions' squared amplitudes

Before discussing the cancellation of the IRC singularities between real and virtual corrections and further deriving the NLL accurate formula we want to look at the n-emissions squared amplitude ($pp \to \mathrm{X} + n$ gluons) in a slightly more detailed manner.

It is particularly convenient to decompose such an amplitude in terms of the n-particle correlated squared amplitudes, $\left|\widetilde{M}_n(k_a, k_b, \ldots)\right|$. Such expansion allows us to discriminate the contributions of the independent and correlated emissions. We can write[2]

$$
\begin{aligned}
\frac{|M(\Phi_\mathrm{B}, k_1, \ldots, k_n)|^2}{|M_B(\Phi_\mathrm{B})|^2} = &\left[\frac{1}{n!}\prod_{i=1}^{n}|M(k_i)|^2\right] + \left\{\sum_{a>b}\frac{1}{(n-2)!}\left[\prod_{\substack{i=1\\ i\neq a,b}}^{n}|M(k_i)|^2\right]\left|\widetilde{M}_2(k_a,k_b)\right|^2\right. \\
&\left. + \sum_{a>b}\sum_{\substack{c>d\\ c,d\neq a,b}}\frac{1}{(n-4)!2!}\left[\prod_{\substack{i=1\\ i\neq a,b,c,d}}^{n}|M(k_i)|^2\right]\left|\widetilde{M}_2(k_a,k_b)\right|^2\left|\widetilde{M}_2(k_c,k_d)\right|^2 + \ldots\right\} \\
&+ \left\{\sum_{a>b>c}\frac{1}{(n-3)!}\left[\prod_{\substack{i=1\\ i\neq a,b,c}}^{n}|M(k_i)|^2\right]\left|\widetilde{M}_3(k_a,k_b,k_c)\right|^2 + \ldots\right\} + \ldots, \qquad (3.18)
\end{aligned}
$$

where the correlated squared amplitudes may be recursively defined as

$$
\begin{aligned}
|\widetilde{M}_1(k_a)|^2 =& \frac{|M(\Phi_\mathrm{B}, k_a)|^2}{|M_B(\Phi_\mathrm{B})|^2} = |M(k_a)|^2, \\
|\widetilde{M}_2(k_a,k_b)|^2 =& \frac{|M(\Phi_\mathrm{B}, k_a, k_b)|^2}{|M_B(\Phi_\mathrm{B})|^2} - \frac{1}{2!}|M(k_a)|^2|M(k_b)|^2,
\end{aligned}
$$

[1]We stress that this should not be mistaken with an ϵ parameter usually invoked for the dimensional regularisation.

[2]If some of the n emissions are quarks, the decomposition formula should be adjusted by changing the multiplicity factors in front of each block.

$$|\widetilde{M}_3(k_a,k_b,k_c)|^2 = \frac{|M(\Phi_\mathrm{B},k_a,k_b,k_c)|^2}{|M_B(\Phi_\mathrm{B})|^2} - |\widetilde{M}(k_a,k_b)|^2|M(k_c)|^2 - |\widetilde{M}(k_a,k_c)|^2|M(k_a)|^2$$
$$- |\widetilde{M}(k_b,k_c)|^2|M(k_b)|^2 - \frac{1}{3!}|M(k_a)|^2|M(k_b)|^2|M(k_c)|^2, \tag{3.19}$$

and so on. The $|\widetilde{M}_n|^2$ contributions encode the part of the amplitude that cannot be factorised into combination of lower-multiplicity blocks. Moreover, they vanish in the strongly-ordered kinematic configurations. Each correlated amplitude respects a perturbative expansion in powers of the strong coupling that account for the virtual corrections to each correlated squared amplitude. Following this thought, we define nPC (n-particle correlated) blocks as

$$|\widetilde{M}_n|^2 \equiv \sum_{j=0}^{\infty} \left(\frac{\alpha_s(\mu)}{2\pi}\right)^{n+j} n\mathrm{PC}^{(j)}(k_a,k_b,\ldots), \tag{3.20}$$

where $\alpha_s(\mu)$ is the strong coupling in the $\overline{\mathrm{MS}}$ scheme evaluated at a common renormalisation scale μ.

Furthermore, using the inclusivity of the observable, Eq. (3.9), we can integrate the nPC blocks for $n > 1$ prior to evaluating observable, namely we exchange

$$\sum_{n=0}^{\infty} \frac{|M(\Phi_\mathrm{B},k_1,\ldots,k_n)|^2}{|M_B(\Phi_\mathrm{B})|^2} \longrightarrow$$
$$\longrightarrow \sum_{n=0}^{\infty} \frac{1}{n!} \left\{ \prod_{i=1}^{n} \left(|M(k_i)|^2 + \int [dk_a][dk_b] |\widetilde{M}_2(k_a,k_b)|^2 \delta^{(2)}\!\left(\vec{k}_{ta}+\vec{k}_{tb}-\vec{k}_{ti}\right) \delta(Y_{ab}-Y_i) \right.\right.$$
$$\left.\left. + \int [dk_a][dk_b][dk_c] |\widetilde{M}_3(k_a,k_b,k_c)|^2 \delta^{(2)}\!\left(\vec{k}_{ta}+\vec{k}_{tb}+\vec{k}_{tc}-\vec{k}_{ti}\right) \delta(Y_{abc}-Y_i) + \ldots \right) \right\}$$
$$\equiv \sum_{n=0}^{\infty} \frac{1}{n!} \prod_{i=1}^{n} |M(k_i)|^2_{\mathrm{inc}}, \tag{3.21}$$

where $Y_{abc\ldots}$ is the rapidity of the $k_a + k_b + k_c + \ldots$ system in the collision's centre-of-mass frame. We refer to such treatment of the n-particle squared amplitude as to the *inclusive approximation*.

3.1.4 The cancellation of IRC singularities and the NLL accurate formula

Having defined the inclusive approximation and the inclusive squared amplitudes $|M(k_i)|_{\mathrm{inc}}$, we can rewrite the Eq. (3.13) as

$$\Sigma(v) = \int d\Phi_\mathrm{B}\, |M_B(\Phi_\mathrm{B})|^2\, \mathcal{V}(\Phi_\mathrm{B}) \sum_{n=0}^{\infty} \int \prod_{i=1}^{n} \frac{1}{n!} [dk_i]\, |M(k_i)|^2_{\mathrm{inc}}\, \Theta\big[v - \mathrm{V}(\Phi_\mathrm{B},k_1,\ldots,k_n)\big], \tag{3.22}$$

where we have left the integral over the Born phase space separated from the ensemble of real emissions. We now want to demonstrate the cancellation of the infra-red and collinear singularities between real and virtual corrections, and further to find a form of the formula in Eq. (3.22) suited for a Monte Carlo implementation.

In order to do so we order the inclusive blocks $|M(k_i)|_{\rm inc}$ according to their contribution to observable V, i.e.

$$\mathrm{V}(k_1) > \mathrm{V}(k_2) > \ldots > \mathrm{V}(k_n). \tag{3.23}$$

Moreover, using the fact that the term with no emissions ($n = 0$) is infinitely suppressed by pure virtual corrections $\mathcal{V}(\Phi_{\rm B})$, we consider only the configurations where the radiation related to the first (hardest) block has already occurred ($n \geqslant 1$). Such ordering, together with rIRC safety, allows us to define a resolution parameter ϵ such that $\epsilon \ll 1$. From now on, we distinguish two types of the real emissions according to their contribution to the observable. We say that an emission k is *resolved* if $\mathrm{V}(k) > \epsilon\mathrm{V}(k_1)$, otherwise we call it *unresolved* and subsequently neglect it in the computation of the observable. We stress again that thanks to rIRC safety such an omission is valid and it differs from the exact treatment (with all emissions entering the computation of the observable) only by power-suppressed terms $\mathcal{O}(\epsilon^p \mathrm{V}(k_1))$. We again recast the Eq. (3.22) as

$$\begin{aligned}
\Sigma(v) = &\int d\Phi_{\rm B}\, |M_B(\Phi_{\rm B})|^2\, \mathcal{V}(\Phi_{\rm B}) \\
&\times \int [dk_1]\, |M(k_1)|^2_{\rm inc} \left[\sum_{l=0}^{\infty} \int \prod_{j=2}^{l+1} \frac{1}{l!} [dk_j]\, |M(k_j)|^2_{\rm inc}\; \Theta\big[\epsilon\mathrm{V}(k_1) - \mathrm{V}(k_j)\big]\right] \\
&\times \left[\sum_{m=0}^{\infty} \int \prod_{i=2}^{m+1} \frac{1}{m!} [dk_i]\, |M(k_i)|^2_{\rm inc}\; \Theta\big[\mathrm{V}(k_j) - \epsilon\mathrm{V}(k_1)\big]\Theta\big[v - \mathrm{V}(\Phi_{\rm B}, k_1, \ldots, k_{m+1})\big]\right],
\end{aligned} \tag{3.24}$$

where in the last squared bracket we collected the ensemble of resolved real emissions leaving the unresolved ones in the squared bracket in the middle line.

The set of unresolved emissions can be conveniently written in terms of exponential function,

$$\exp\left\{\int [dk]\, |M(k)|^2_{\rm inc}\; \Theta\big[\epsilon\mathrm{V}(k_1) - \mathrm{V}(k)\big]\right\}. \tag{3.25}$$

Furthermore, the IRC divergences of the virtual corrections to the form factor exponentiate at all orders [126, 127] and hence we can also write them as

$$\mathcal{V}(\Phi_{\mathrm{B}}) \simeq \mathcal{V}(M^2) = \exp\left\{-\int [dk]\, |M(k)|^2_{\mathrm{inc}}\right\}, \tag{3.26}$$

where we have neglected the constant terms of the virtual corrections which are irrelevant at NLL and used the fact that the remaining singular structure of the virtual corrections depends only on the mass M of the colour singlet. Combining the two yields a finite result, as we keep the ϵ finite for now, which gives rise to the Sudakov suppression factor

$$\begin{aligned}\mathcal{V}(M^2)\times \exp&\left\{\int [dk]\, |M(k)|^2_{\mathrm{inc}}\ \Theta\big[\epsilon \mathrm{V}(k_1) - \mathrm{V}(k)\big]\right\}\\ &\simeq \exp\left\{-\int [dk]\, |M(k)|^2_{\mathrm{inc}}\ \Theta\big[\mathrm{V}(k) - \epsilon \mathrm{V}(k_1)\big]\right\} \equiv e^{-R(\epsilon \mathrm{V}(k_1))},\end{aligned} \tag{3.27}$$

where by $R(\epsilon\mathrm{V}(k_1))$ we denote the Sudakov radiator evaluated at the resolution scale $\epsilon\mathrm{V}(k_1)$. We will now briefly discuss the ingredients that enter the NLL accurate formula, and we will leave the discussion of the $\epsilon \to 0$ limit for the next section.

We can easily write the real emission matrix element in the soft and collinear approximation for a single emission as

$$[dk]|M(k)|^2_{\mathrm{inc}} \simeq [dk]|M(k)|^2_{\mathrm{sc}} = \sum_{\ell=1,2} 2C_\ell \frac{\alpha_s(\mu)}{\pi}\frac{dk_t}{k_t}\frac{dz^{(\ell)}}{1-z^{(\ell)}}\,\Theta\left[(1-z^{(\ell)}) - k_t/M\right]\Theta\left[z^{(\ell)}\right]\frac{d\phi}{2\pi}, \tag{3.28}$$

where C_ℓ is the Casimir of the emitting leg, μ is the renormalisation scale, k_t is the transverse momentum of the emission, Eq. (3.10), and $(1-z^{(\ell)})$ is the fraction of incoming momentum (entering the emission vertex) that is carried by the emitted parton. In general $(1-z^{(\ell)})$ is not the same as $(1-y^{(\ell)})$ and for a single emission the two are related by

$$(1-y^{(\ell)}) = \frac{(1-z^{(\ell)})}{z^{(\ell)}}. \tag{3.29}$$

We can see that in the soft limit $z^{(\ell)} \simeq 1$, hence we get $y^{(\ell)} \simeq z^{(\ell)}$.

Such treatment allows us to control the double-logarithmic terms $\alpha_s^n L^{2n}$, as such terms entirely arise from the $1\mathrm{PC}^{(0)}$ blocks. If we want to control all the leading-logarithmic terms, i.e. $\alpha_s^n L^{n+1}$, we need to include the most singular part of the $1\mathrm{PC}^{(1)}$

and 2PC$^{(0)}$ blocks in the soft-collinear approximation as well. Within the inclusive approximation we find

$$
\begin{aligned}
|M(k)|^2_{\text{inc}} &\simeq |M(k)|^2 + \int [dk_a][dk_b] |\tilde{M}(k_a, k_b)|^2 \delta^{(2)}(\vec{k}_{ta} + \vec{k}_{tb} - \vec{k}_t)\delta(Y_{ab} - Y) \\
&= \frac{\alpha_s(\mu)}{2\pi} 1\text{PC}^{(0)}(k) \left(1 + \alpha_s(\mu)\left(\beta_0 \ln \frac{k_t^2}{\mu^2} + \frac{K}{2\pi}\right) + \dots\right), \qquad (3.30)
\end{aligned}
$$

where β_0 is the leading term of the QCD beta function, the strong coupling is renormalised in the $\overline{\text{MS}}$ scheme, and K denotes the contribution of one-loop anomalous dimension

$$
K = \left(\frac{67}{18} - \frac{\pi^2}{6}\right) C_A - \frac{5}{9} n_f\,, \qquad (3.31)
$$

that enters at NLL. This result has been known for a long time [128] and we see that the leading soft-collinear terms, proportional to β_0, can be entirely taken into account by a proper choice of the scale μ at which the strong coupling is evaluated in the single-emission squared amplitude. Setting μ to k_t brings us to the desired result.

If we are interested in additionally managing all $\alpha_s^n L^n$ terms, which means an NLL accuracy, we need to use not only a proper renormalisation scale, $\mu = k_t$ in Eq. (3.28), but also include K term of Eq. (3.31) and consider a hard-collinear configuration in 1PC$^{(0)}$ blocks. This leads us to

$$
\begin{aligned}
[dk]|M(k)|^2_{\text{inc}} &= [dk] M^2_{\text{CMW}}(k) \\
&+ \sum_{\ell=1,2} \frac{dk_t^2}{k_t^2} \frac{dz^{(\ell)}}{1 - z^{(\ell)}} \frac{d\phi}{2\pi} \frac{\alpha_s(k_t)}{2\pi} \left((1 - z^{(\ell)}) P^{(0)}(z^{(\ell)}) - \lim_{z^{(\ell)} \to 1} \left[(1 - z^{(\ell)}) P^{(0)}(z^{(\ell)})\right]\right), \qquad (3.32)
\end{aligned}
$$

where the subscript CMW refers to well known Catani-Marchesini-Webber scheme for the running of the strong coupling [91] and the whole expression reads

$$
\begin{aligned}
[dk] M^2_{\text{CMW}}(k) = \sum_{\ell=1,2} 2C_\ell \frac{\alpha_s(k_t)}{\pi} &\left(1 + \frac{\alpha_s(k_t)}{2\pi} K\right) \frac{dk_t}{k_t} \frac{d\phi}{2\pi} \\
&\frac{dz^{(\ell)}}{1 - z^{(\ell)}} \Theta\Big((1 - z^{(\ell)}) - k_t/M\Big) \Theta(z^{(\ell)}). \qquad (3.33)
\end{aligned}
$$

The second line of Eq. (3.32) contains the contribution of the hard-collinear part of a 1PC$^{(0)}$ block that had been ignored thus far, the $P^{(0)}(z)$ denotes the leading-order unregularised splitting function. At NLL order we can neglect the effect of the recoil both in the observable as well as in the kinematic boundaries of the phase space. These effects enter at higher logarithmic orders.

As we have already mentioned, the unresolved emissions do not influence the evaluation of the observable and we have exponentiated them in order to cancel the IRC singularities of the virtual corrections. This operation in turn led to the appearance of the Sudakov radiator which acts as a suppression factor for real emissions. Having established the form of the squared matrix element at NLL order we can explicitly construct the corresponding Sudakov form factor as

$$\begin{aligned} R(v) \simeq R_{\mathrm{NLL}}(v) \equiv & \int [dk] M^2_{\mathrm{CMW}}(k) \Theta\left(\ln\left(\frac{k_t}{M}\right)^a - \ln v\right) \\ & + \int [dk] M^2_{\mathrm{CMW}}(k) \ln \bar{d}_\ell \, \delta\left(\ln\left(\frac{k_t}{M}\right)^a - \ln v\right) \\ & + \sum_{\ell=1,2} C_\ell B_\ell \int \frac{dk_t^2}{k_t^2} \frac{\alpha_s(k_t)}{2\pi} \Theta\left(\ln\left(\frac{k_t}{M}\right)^a - \ln v\right) , \end{aligned}$$

where

$$\ln \bar{d}_\ell = \int_0^{2\pi} \frac{d\phi}{2\pi} \ln d_\ell g_\ell(\phi) \,, \tag{3.34}$$

and

$$C_\ell B_\ell = \int_0^1 \frac{dz^{(\ell)}}{1 - z^{(\ell)}} \left((1 - z^{(\ell)}) P^{(0)}(z^{(\ell)}) - \lim_{z^{(\ell)} \to 1} \left[(1 - z^{(\ell)}) P^{(0)}(z^{(\ell)}) \right] \right) . \tag{3.35}$$

Once we have the squared matrix element for a single-emission block in Eq. (3.32) and the Sudakov radiator in Eq. (3.34) we can parametrise the squared amplitude for an emission together with its phase space volume element by

$$\begin{aligned} R_1'\left(\frac{v}{d_1 g_1(\bar{\phi})}\right) &= \int [dk] |M(k)|^2_{\mathrm{inc}} \, (2\pi) \delta(\phi - \bar{\phi}) \, v \delta\left(v - \mathrm{V}(k)\right) \Theta(y^{(2)} - y^{(1)}) \,, \\ R_2'\left(\frac{v}{d_2 g_2(\bar{\phi})}\right) &= \int [dk] |M(k)|^2_{\mathrm{inc}} \, (2\pi) \delta(\phi - \bar{\phi}) \, v \delta\left(v - \mathrm{V}(k)\right) \Theta(y^{(1)} - y^{(2)}) \,, \end{aligned} \tag{3.36}$$

where indexes $\ell = 1$ and $\ell = 2$ refer to the leg that is the origin of the real emission. Using the generic form for the scaling of the rIRC safe observable $\mathrm{V}(k)$ of Eq. (3.8) we can verify that, up to regular terms which are beyond the scope of Eq. (3.8), functions R_ℓ' depend only on the ratio $v/(d_\ell g_\ell(\phi))$. Upon the inclusive integration over the rapidity of momentum k, using the above parametrisation, the Eq. (3.32) reads

$$[dk_i] |M(k_i)|^2_{\mathrm{inc}} = \frac{dv_i}{v_i} \frac{d\phi_i}{2\pi} \sum_{\ell_i = 1,2} R'_{\ell_i}\left(\frac{v_i}{d_{\ell_i} g_{\ell_i}(\phi_i)}\right) = \frac{d\zeta_i}{\zeta_i} \frac{d\phi_i}{2\pi} \sum_{\ell_i = 1,2} R'_{\ell_i}\left(\frac{\zeta_i v_1}{d_{\ell_i} g_{\ell_i}(\phi_i)}\right) , \tag{3.37}$$

where we defined $v_i = \mathrm{V}(k_i)$ and $\zeta_i = \mathrm{V}(k_i)/\mathrm{V}(k_1)$.

At this stage we are in possession of all components required for obtaining the NLL accurate resummed formula. We can write the Eq. (3.24), valid at an NLL order, as follows

$$\Sigma(v) = \int d\Phi_{\mathrm{B}}\,|M_B(\Phi_{\mathrm{B}})|^2 \times \int \frac{dv_1}{v_1}\int_0^{2\pi}\frac{d\phi_1}{2\pi}\,e^{-R(\epsilon v_1)}\sum_{\ell_1=1,2} R'_{\ell_1}\left(\frac{v_1}{d_{\ell_1} g_{\ell_1}(\phi_1)}\right)$$
$$\times \sum_{n=0}^{\infty}\frac{1}{n!}\prod_{i=2}^{n+1}\int\frac{d\zeta_i}{\zeta_i}\int_0^{2\pi}\frac{d\phi_i}{2\pi}\sum_{\ell_i=1,2} R'_{\ell_i}\left(\frac{v_i}{d_{\ell_i} g_{\ell_i}(\phi_i)}\right)\Theta\left[v - \mathrm{V}(\Phi_{\mathrm{B}}, k_1, \ldots, k_{n+1})\right]. \tag{3.38}$$

Let us point out that in the above equation we have exploited the fact that all real-emissions can be treated in the soft kinematics approximation at NLL order and hence phase space is identical for all secondary emissions, $i > 1$. Moreover, we have not yet discussed the proper way of treating parton luminosities. Both of these issues, kinematical effects beyond the NLL order and including parton distribution functions, will be discussed in the following sections.

The Eq. (3.38) is finite in four dimensions and can be implemented in a Monte Carlo generator which can simulate cascades of real emissions and calculate the cumulant $\Sigma_{\mathrm{NLL}}(v)$. This formulation resembles the general NLL formula of the `CAESAR` method for all continuously global and rIRC safe observables in processes with two hard legs [95]. Despite its simplicity the formula in Eq. (3.38) contains effects that are beyond the nominal accuracy and might be disposed of. As an example of an approximation that can be invoked we perform the Taylor expansion of radiator and real emission amplitudes around v_1, namely we set

$$R(\epsilon v_1) = R(v_1) + \frac{dR(v_1)}{dL}\ln\frac{1}{\epsilon} + \mathcal{O}\left(\ln^2\frac{1}{\epsilon}\right),$$
$$R'_{\ell_i}\left(\frac{v_i}{d_{\ell_i} g_{\ell_i}(\phi_i)}\right) = R'_{\ell_i}(v_1) + \mathcal{O}\left(\frac{v_1}{v_i}\,d_{\ell_i} g_{\ell_i}(\phi_i)\right), \tag{3.39}$$

where we abbreviated $L = \ln(1/v_1)$. Such expansion is valid thanks to the rIRC safety of the observable which guarantees that $v_i \sim v_1$ (and consequently $\zeta_i \sim 1$) and the terms neglected in Eq. (3.39) are at most NNLL as a result.

We note that a crucial difference between `CAESAR` implementation and the formulae in Eq. (3.39) is the expansion around the hardest block contribution v_1 instead of the full

Logarithmic order	**Blocks required**	
	$n\mathrm{PC}_{\mathrm{sc}}^{(j)}$	$n\mathrm{PC}^{(j)}$
LL	$1\mathrm{PC}^{(0)}$	—
NLL	$1\mathrm{PC}^{(1)}$, $2\mathrm{PC}^{(0)}$	$1\mathrm{PC}^{(0)}$
NNLL	$1\mathrm{PC}^{(2)}$, $2\mathrm{PC}^{(1)}$, $3\mathrm{PC}^{(0)}$	$1\mathrm{PC}^{(m\leqslant 1)}$, $2\mathrm{PC}^{(0)}$
$\mathrm{N}^3\mathrm{LL}$	$1\mathrm{PC}^{(3)}$, $2\mathrm{PC}^{(2)}$, $3\mathrm{PC}^{(1)}$, $4\mathrm{PC}^{(0)}$	$1\mathrm{PC}^{(m\leqslant 2)}$, $2\mathrm{PC}^{(m\leqslant 1)}$, $3\mathrm{PC}^{(0)}$
...	...	...
$\mathrm{N}^k\mathrm{LL}$	$n+j\leqslant k+1$	$n+j\leqslant k$

Table 3.1: List of nPC blocks necessary at a given logarithmic order. We distinguish between $n\mathrm{PC}_{\mathrm{sc}}^{(j)}$ ones which contain only the leading singularities of the correlated amplitude (soft-collinear limit) and $n\mathrm{PC}^{(j)}$ that include also less singular terms (soft and hard-collinear limits).

observable v. Such a difference is dictated by the nature of the resummed observables considered in this work which feature non-trivial zeroes away from the Sudakov limit. A simple example is posed by the transverse momentum of the colour singlet which can vanish even in the presence of several emissions with finite transverse momentum whose vectorial sum cancels leading to $v \ll v_1$.

In order to extend this treatment to higher orders, we exploit the rIRC safety of the resummed observable to establish a hierarchy between different parts of the amplitude in Eq. (3.18). In general, the n-particle correlated blocks begin to contribute at least one logarithmic order higher than the ones with $(n-1)$-particles, provided that the renormalisation scales in each block are set to the transverse momentum of the particles contained in the block. As a consequence, we can identify a set of blocks which has to be considered at a given logarithmic order and the others can be safely neglected. For example, in order to evaluate NLL accurate resummed prediction for inclusive observables, Eq. (3.9), we have considered $1\mathrm{PC}^{(0)}$ block in both soft and/or collinear limits, and $1\mathrm{PC}^{(1)}$, $2\mathrm{PC}^{(0)}$ blocks in their most singular configuration, i.e. the soft-collinear limit. To obtain an NNLL accurate result, we need to extend the treatment of the two latter blocks into the soft and/or collinear regions as well as add the soft-collinear parts of $1\mathrm{PC}^{(2)}$, $2\mathrm{PC}^{(1)}$ and $3\mathrm{PC}^{(0)}$ amplitudes. A short summary is presented in Table 3.1.

In the last paragraph of this section we would like to review the idea of ordering the resolved blocks and a choice of the ordering variable. We have already used the inclusivity of the observable and evaluated the contribution of each particular block i according to its total momentum k_i, as defined in Eq. (3.30). The contribution v_i allows us to classify a block as resolved/unresolved if $v_i > \epsilon v_1$ / $v_i < \epsilon v_1$, with v_1 being the contribution of the first (hardest) correlated block.

Nevertheless, the choice of an ordering variable is not unique and a particular option can be selected by a convenience in formulating the calculation. In fact, the only necessary property is that we must guarantee cancellation of the IRC divergences of the exponentiated virtual corrections at all orders.

For the whole class of transverse observables, a suitable alternative is to order the inclusive blocks according to $\mathrm{V}(k) = (k_t/M)^a$, k being the momentum of the correlated block. Such a choice coincides with the resummed observable for $d_\ell g_\ell(\phi) = 1$ (*e.g.* p_t of the colour singlet) but is also a well founded choice for $d_\ell g_\ell(\phi) \neq 1$ (*e.g.* the ϕ^*_η in the Drell-Yan production). A particular advantage of using a single ordering variable for a wider class of observables is the simplification of the Monte Carlo implementation. Using the same ordering variable leads to the same Sudakov suppression factor while the observable dependence is completely encoded in the measurement function evaluated on the ensemble of resolved real radiation, $\Theta\left[v - \mathrm{V}(\Phi_\mathrm{B}, k_1, \ldots, k_{n+1})\right]$.

3.1.5 Treatment of the hard and collinear emissions

In deriving the master Eq. (3.38) we have exploited the fact that to obtain an NLL accurate expression it is enough to consider all resolved real emissions as soft and collinear and as a consequence it was possible to disentangle the phase space of all emissions, as they do not affect each other.

However, as soon as we want to go beyond the NLL approximation we need to consider one or more of the real emissions to be hard and collinear to the emitting leg. Such an emission will change the available phase space for all subsequent real emissions. To discuss it in more detail we divide emissions into two sets, the ones that occur before the hard-collinear radiation and the ones that occur afterwards. Namely, the upper bound of the z integration for the i^{th} emission which occurs before the hard-collinear one is

$$z_i^{(\ell)} < 1 - k_{ti}/M, \tag{3.40}$$

as explicitly denoted in Eq. (3.33). However, the hard and collinear emission alters the available phase space for all subsequent radiation on the leg ℓ such that their z upper bound becomes

$$z_i^{(\ell)} < 1 - z_{hc}^{(\ell)} k_{ti}/M, \tag{3.41}$$

where $z_{hc}^{(\ell)}$ corresponds to hard-collinear emission.

In order to deal with hard-collinear emissions we consider the squared matrix element for a single initial-state emission. For convenience, we divide it into several pieces – we note that this is not a physical separation but a technical step to easily tackle various parts. We have:

- A part which modifies the flavour and the momentum fraction of the emitting leg. This term corresponds to en exclusive DGLAP evolution step and the related z integration limit can be extended up to the soft limit ($z = 1$) as the limit is regularised by the plus prescription in the relevant splitting function.

- A part which does not modify the flavour or momentum fraction of the emitting leg. This contribution is similar in nature to the R'-like emissions in Eq. (3.38). This term can be further divided into a hard-collinear part and a soft term. The upper bound on the z integration can be lifted up to $z = 1$ in case of the hard-collinear part while the exact bound is only relevant for the soft term. Nevertheless, we can notice that the phase space measure can be parametrised in terms of y variable instead of z using the fact in the soft limit we have $k_{ti} \simeq \tilde{k}_{ti}$ and

$$\frac{dz_i^{(\ell)}}{1 - z_i^{(\ell)}} = \frac{dy_i^{(\ell)}}{1 - y_i^{(\ell)}} \tag{3.42}$$

  and the y upper bound for all emissions is

$$y_i^{(\ell)} < 1 - k_{ti}/M, \tag{3.43}$$

  where we have used the fact that for the radiation occurring after the hard and collinear emission we have $1 - y_i^{(\ell)} = \left(1 - z_i^{(\ell)}\right)/z_{hc}^{(\ell)}$.

As a consequence, we can again disentangle the phase space of all real emissions in kinematical configurations encapsulating up to one hard-collinear emission, and iterate the procedure at all orders. We emphasise that the lifting of the z integration upper bound, described above, gives rise to regular terms. These non-logarithmic terms will be properly accounted for when considering finite part of the virtual corrections as well as the collinear coefficient functions.

Furthermore, such construction can be repeated for the case including up to two hard and collinear emissions which has to be considered at the N^{3}LL accuracy. For the relevant formulae we refer the reader to Section 2.3.2 of Ref. [16].

3.1.6 Resummation formula at higher logarithmic orders

We have already pointed out that in order to extend the logarithmic accuracy of the resummed formula in Eq. (3.38) we have to allow for a number of hard and collinear emissions in an ensemble of real radiation, and to include the relevant correlated blocks enumerated in Table 3.1. Thanks to arguments discussed in Section 3.1.5, the all-order picture can be obtained by iterating a single-emission probability even at higher logarithmic orders. The treatment of higher-order correlated blocks amounts to considering corrections to the radiator R and its derivative R', as well as additional terms in the anomalous dimensions which describe the evolution of parton distribution functions and coefficient functions.

In order to illustrate the physical picture that has to be considered we show the η-$\ln(k_t)$ plane in Fig. 3.1. The rIRC safety of the observable allows us to consider resolved real emissions that occur only in the strip $\epsilon k_{t1} < k_{ti} < k_{t1}$ labelled as *real emissions*. The softer emissions, with $k_{ti} < \epsilon k_{t1}$, do not modify the observable significantly and hence are treated as unresolved. Their combination with the virtual corrections gives rise to the Sudakov form factor which is associated with the first emission and which vetoes secondary emissions with $k_{ti} > k_{t1}$, in the region labelled as *Sudakov suppression*. The parton distribution functions should be evaluated at a factorization scale μ_0 that is smaller than all of the transverse momenta occurring in an event. However, it is equivalent to evaluate the parton distribution functions at the scale of the first (hardest) emission k_{t1}

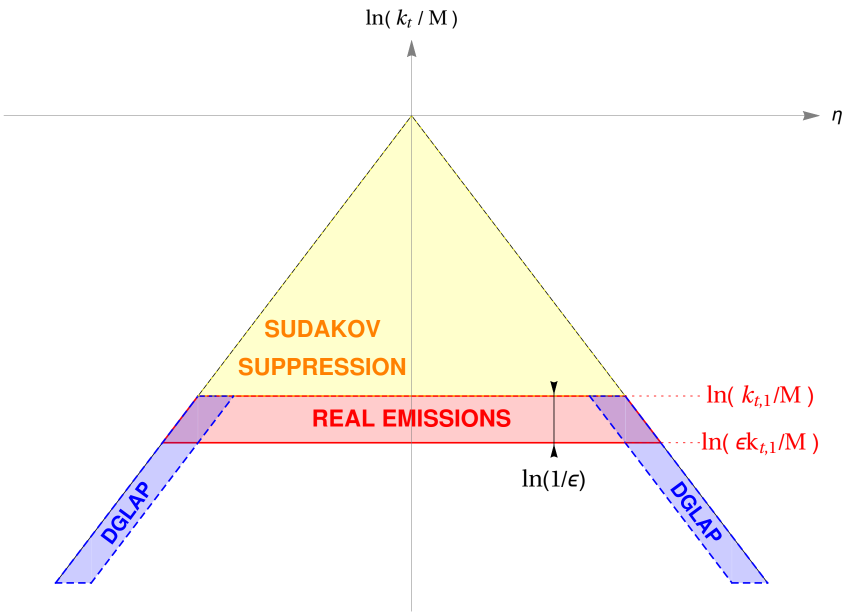

Figure 3.1: Phase space for secondary real emissions. The real emissions that significantly affect the observable and have to be treated as resolved occur in the red strip.

and consider an evolution down to the low scale μ_0. Such evolution is marked as *DGLAP* region in Fig. 3.1 and it has to be performed exclusively in the sector that overlaps with the real emission strip while the inclusive treatment is sufficient in the unresolved region.

In order to derive the necessary formulae regarding the evolution of the parton densities and the collinear coefficient functions we need to establish a few necessary ingredients. It is useful to introduce a matrix notation for a flavour space expressions. We define $\mathbf{f}$ to be an array containing the $2n_f + 1$ parton densities, with n_f denoting the number of active flavours. The coefficient-function matrix can be then expressed as a $(2n_f + 1) \times (2n_f + 1)$ diagonal matrix in flavour space,

$$[\mathbf{C}^{c_\ell}]_{ab} = C_{c_\ell f(a)} \delta_{ab} \,, \tag{3.44}$$

where C_{ij} are the collinear coefficient functions, c_ℓ denotes the flavour of leg ℓ entering the Born process, and $f(a)$ is the flavour corresponding to the a^{th} entry of the parton-density array $\mathbf{f}$. The RG evolution for the matrix $\mathbf{C}^{c_\ell}$ can be expressed in terms of the corresponding anomalous-dimension matrix $\mathbf{\Gamma}^{(C)}$ as

$$\mathbf{\Gamma}^{(C)}(\alpha_s(k_t)) = 2\beta(\alpha_s(k_t)) \frac{d \ln \mathbf{C}^{c_\ell}(\alpha_s(k_t))}{d\alpha_s(k_t)}, \tag{3.45}$$

and the solution can be obtained by a simple exponentiation

$$\mathbf{C}^{c_\ell}(\alpha_s(\mu)) = \exp\left\{-\int_{\mu}^{\mu_0} \frac{dk_t}{k_t}\mathbf{\Gamma}^{(C)}(\alpha_s(k_t))\right\}\mathbf{C}^{c_\ell}(\alpha_s(\mu_0)). \tag{3.46}$$

Note that for simplicity we have dropped a flavour index c_ℓ in the anomalous-dimension matrix as the notation is unambiguous and the flavour of the coefficient function is not modified by the RG evolution.

Furthermore, we need to describe a notation for the DGLAP evolution. It is customary to introduce the Mellin transform of a function $g(x)$:

$$g_{N_\ell} \equiv \int_0^1 dx\, x^{N_\ell - 1} g(x), \tag{3.47}$$

as the DGLAP evolution features convolutions of the parton densities and splitting functions. The evolution of the parton-density vector $\mathbf{f}$ is then

$$\mathbf{f}_{N_\ell}(\mu) = \mathcal{P}\exp\left\{-\int_{\mu}^{\mu_0} \frac{dk_t}{k_t}\frac{\alpha_s(k_t)}{\pi}\mathbf{\Gamma}_{N_\ell}(\alpha_s(k_t))\right\}\mathbf{f}_{N_\ell}(\mu_0), \tag{3.48}$$

where $\mathcal{P}$ denotes the path-ordering and the the matrix $\mathbf{\Gamma}$ is

$$[\mathbf{\Gamma}_{N_\ell}(\alpha_s(\mu))]_{ab} = \int_0^1 dz\, z^{N_\ell - 1}\hat{P}_{f(a)f(b)}(z, \alpha_s(\mu)) \equiv \gamma_{N_\ell; f(a)f(b)}, \tag{3.49}$$

where $\hat{P}_{f(a)f(b)}$ are the regularised splitting functions and the anomalous-dimensions $\gamma_{N_\ell; f(a)f(b)}$ can be expressed in terms of a perturbative series in the strong coupling,

$$\gamma_{N_\ell; f(a)f(b)} = \sum_{n=0}^{\infty}\left(\frac{\alpha_s(\mu)}{2\pi}\right)^n \gamma^{(n)}_{N_\ell; f(a)f(b)}. \tag{3.50}$$

A similar notation can be introduced for the radiator and its derivative. We write

$$[\mathbf{R}'_\ell]_{ab} = R'_\ell \delta_{ab}, \tag{3.51}$$

where R'_ℓ has been already defined in Eq. (3.36). The definition of Sudakov operator $\mathbf{R}$ follows

$$\mathbf{R}(\epsilon k_{t1}) = \sum_{\ell=1}^{2}\int_{\epsilon k_{t1}}^{M} \frac{dk_t}{k_t}\mathbf{R}'_\ell(k_t). \tag{3.52}$$

Finally, the hadronic cumulative cross section, differential in the Born phase space, can be written as

$$\frac{d\Sigma(v)}{d\Phi_B} = \int_{\mathcal{C}_1} \frac{dN_1}{2\pi i} \int_{\mathcal{C}_2} \frac{dN_2}{2\pi i} x_1^{-N_1} x_2^{-N_2} \sum_{c_1,c_2} |M_B(\Phi_{\rm B})|^2_{c_1c_2}\, \mathbf{f}^T_{N_1}(\mu_0)\hat{\mathbf{\Sigma}}^{c_1,c_2}_{N_1,N_2}(v)\mathbf{f}_{N_2}(\mu_0), \quad (3.53)$$

where the sum runs over all possible Born flavour configurations and we explicitly denoted the double inverse Mellin transform, with the contours $\mathcal{C}_1$ and $\mathcal{C}_2$ being parallel to the imaginary axis to the right of all singularities of the integrand. The matrix $\hat{\mathbf{\Sigma}}^{c_1,c_2}_{N_1,N_2}(v)$ encodes the all-order treatment of the radiation which is a result of iterating a single-emission probability. The master equation for the partonic matrix $\hat{\mathbf{\Sigma}}$ is then

$$\begin{aligned}
\hat{\mathbf{\Sigma}}^{c_1,c_2}_{N_1,N_2}(v) = &\left[\mathbf{C}^{c_1;T}_{N_1}(\alpha_s(\mu_0))H(\mu_R)\mathbf{C}^{c_2}_{N_2}(\alpha_s(\mu_0))\right] \int_0^M \frac{dk_{t1}}{k_{t1}} \int_0^{2\pi} \frac{d\phi_1}{2\pi} \\
&\times e^{-\mathbf{R}(\epsilon k_{t1})} \exp\left\{-\sum_{\ell=1}^{2}\left(\int_{\epsilon k_{t1}}^{\mu_0} \frac{dk_t}{k_t}\frac{\alpha_s(k_t)}{\pi}\mathbf{\Gamma}_{N_\ell}(\alpha_s(k_t)) + \int_{\epsilon k_{t1}}^{\mu_0} \frac{dk_t}{k_t}\mathbf{\Gamma}^{(C)}_{N_\ell}(\alpha_s(k_t))\right)\right\} \\
&\sum_{\ell_1=1}^{2}\left(\mathbf{R}'_{\ell_1}(k_{t1}) + \frac{\alpha_s(k_{t1})}{\pi}\mathbf{\Gamma}_{N_{\ell_1}}(\alpha_s(k_{t1})) + \mathbf{\Gamma}^{(C)}_{N_{\ell_1}}(\alpha_s(k_{t1}))\right) \\
&\times \sum_{n=0}^{\infty}\frac{1}{n!}\prod_{i=2}^{n+1}\int_\epsilon^1 \frac{d\zeta_i}{\zeta_i}\int_0^{2\pi}\frac{d\phi_i}{2\pi} \\
&\times \sum_{\ell_i=1}^{2}\left(\mathbf{R}'_{\ell_i}(k_{ti}) + \frac{\alpha_s(k_{ti})}{\pi}\mathbf{\Gamma}_{N_{\ell_i}}(\alpha_s(k_{ti})) + \mathbf{\Gamma}^{(C)}_{N_{\ell_i}}(\alpha_s(k_{ti}))\right) \\
&\times \Theta\left(v - \mathrm{V}(\{\tilde{p}\}, k_1, \dots, k_{n+1})\right), \qquad (3.54)
\end{aligned}$$

where we have used a notation $\zeta_i = k_{ti}/k_{t1}$. The terms proportional to $\mathbf{R}'$ encode the contribution of the radiation which is flavour-diagonal and does not modify the momentum fraction of the incoming partons while the exclusive DGLAP evolution steps are completely disentangled in case of the resolved emissions, the evolution of the coefficient functions and parton densities is related to the terms involving $\mathbf{\Gamma}_{N_\ell}$ and $\mathbf{\Gamma}^{(C)}_{N_\ell}$ operators. Note that at a given order in perturbation theory we need to include effects of the azimuthal correlations related to initial-state gluons. This amounts to adding a contribution with the collinear coefficients functions $\mathbf{G}$, defined as in Ref. [129], to the Eq. (3.54) by adding an analogous terms involving $\mathbf{G}$ functions

$$\left[\mathbf{C}^{c_1;T}_{N_1}(\alpha_s(\mu_0))H(\mu_R)\mathbf{C}^{c_2}_{N_2}(\alpha_s(\mu_0))\right] \to \left[\mathbf{G}^{c_1;T}_{N_1}(\alpha_s(\mu_0))H(\mu_R)\mathbf{G}^{c_2}_{N_2}(\alpha_s(\mu_0))\right], \quad (3.55)$$

and

$$\mathbf{\Gamma}^{(C)}_{N_\ell}(\alpha_s(k_t)) \to \mathbf{\Gamma}^{(G)}_{N_\ell}(\alpha_s(k_t)). \tag{3.56}$$

Such contributions should be considered at $\mathcal{O}(\alpha_s^2)$, and hence at N^{3}LL, for gluon-gluon initiated processes; while entering at even higher order for the quark-initiated ones.

3.1.7 Equivalence with the resummation in b-space formulation

At last, we would like to show an equivalence between the approach outlined in this section to a resummation performed in the impact parameter space in Refs. [130, 86]. We focus on the differential partonic cross section of Eq. (3.54) and the case of the transverse momentum p_t. A similar proof can be carried out for other observables that fall into the transverse and inclusive category.

We start by considering a differential partonic cross section in Mellin space,

$$\frac{d}{d^2\vec{p}_t}\hat{\mathbf{\Sigma}}^{c_1,c_2}_{N_1,N_2}(p_t), \tag{3.57}$$

which can be evaluated using Eq. (3.54) by substituting

$$\Theta\Big(p_t - \mathrm{V}(\{\tilde{p}\},k_1,\dots,k_{n+1})\Big) \longrightarrow \delta^{(2)}\left(\vec{p}_t - \left(\vec{k}_{t1} + \cdots + \vec{k}_{t(n+1)}\right)\right), \tag{3.58}$$

where $\mathrm{V}(\{\tilde{p}\},k_1,\dots)$ is understood to be the transverse momentum of the colour singlet. Without loss of generality we also set $\mu_0 = \mu_R = M$.

We then transform the δ-function into b-space,

$$\delta^{(2)}\left(\vec{p}_t - \left(\vec{k}_{t1} + \cdots + \vec{k}_{t(n+1)}\right)\right) = \int \frac{d^2\vec{b}}{4\pi^2} e^{-i\vec{b}\cdot\vec{p}_t} \prod_{i=1}^{n+1} e^{i\vec{b}\cdot\vec{k}_{ti}}, \tag{3.59}$$

and evaluate the azimuthal integrals in Eq. (3.57) which simply amounts to replacing the factors $e^{\pm i\vec{b}\cdot\vec{k}_t}$ with an appriopriate Bessel function $J_0(bk_t)$. After setting $\epsilon \to 0$, given the cancellation of IRC divergences is manifest, and using the fact that the k_{t1} integrand is a total derivative, we obtain

$$\begin{aligned}\frac{d}{dp_t}\hat{\mathbf{\Sigma}}^{c_1c_2}_{N_1,N_2}(p_t) &= \mathbf{C}^{c_1;T}_{N_1}(\alpha_s(M))H(M)\mathbf{C}^{c_2}_{N_2}(\alpha_s(M))\, p_t \int b\, db J_0(p_t b) \\ &\times \exp\left\{-\sum_{\ell=1}^{2}\int_0^M \frac{dk_t}{k_t}\left(\mathbf{R}'_\ell(k_t) + \frac{\alpha_s(k_t)}{\pi}\mathbf{\Gamma}_{N_\ell}(\alpha_s(k_t)) + \mathbf{\Gamma}^{(C)}_{N_\ell}(\alpha_s(k_t))\right)\Big(1 - J_0(bk_t)\Big)\right\}.\end{aligned} \tag{3.60}$$

Furthermore, we insert the resulting partonic cross section back into the definition of the hadronic cross section in Eq. (3.53) and use the terms proportional to $\mathbf{\Gamma}_{N_\ell}$ and $\mathbf{\Gamma}^{(C)}_{N_\ell}$ to evolve the parton distribution functions and the collinear coefficient functions down to b_0/b, with $b_0 = 2e^{-\gamma_E}$.

After performing an inverse Mellin transform and neglecting subleading (i.e. N^{4}LL) terms we obtain the formula

$$\begin{aligned}\frac{d^2\Sigma(v)}{d\Phi_B dp_t} =& \sum_{c_1,c_2} |M_B(\Phi_\mathrm{B})|^2_{c_1c_2} \\ &\times \int b\, db\, p_t J_0(p_t b)\, \mathbf{f}^T(b_0/b)\mathbf{C}^{c_1;T}_{N_1}(\alpha_s(b_0/b))H(M)\mathbf{C}^{c_2}_{N_2}(\alpha_s(b_0/b))\mathbf{f}(b_0/b) \\ &\times \exp\left\{-\sum_{\ell=1}^{2}\int_0^M \frac{dk_t}{k_t}\mathbf{R}'_\ell(k_t)\Big(1-J_0(bk_t)\Big)\right\}, \end{aligned} \tag{3.61}$$

where we have omitted x_1 and x_2 arguments of the PDFs, which are uniquely determined by the chosen point in the Born phase-space Φ_B. The expression in Eq. (3.61) indeed resembles the one obtained in b-space formulation of the transverse momentum resummation, which reads [86]

$$\begin{aligned}\frac{d^2\Sigma(v)}{d\Phi_B dp_t} =& \sum_{c_1,c_2} |M_B(\Phi_\mathrm{B})|^2_{c_1c_2} \\ &\times \int b\, db\, p_t J_0(p_t b)\, \mathbf{f}^T(b_0/b)\mathbf{C}^{c_1;T}_{N_1}(\alpha_s(b_0/b))H_\mathrm{CSS}(M)\mathbf{C}^{c_2}_{N_2}(\alpha_s(b_0/b))\mathbf{f}(b_0/b) \\ &\times \exp\left\{-\sum_{\ell=1}^{2}\int_0^M \frac{dk_t}{k_t}\mathbf{R}'_{\mathrm{CSS},\ell}(k_t)\,\Theta\left(k_t-\frac{b_0}{b}\right)\right\}, \end{aligned} \tag{3.62}$$

where $\mathbf{R}'_{\mathrm{CSS},\ell}$ and $H_\mathrm{CSS}(M)$ are the Sudakov and hard function used in the impact-parameter space formulation of the resummation [86]. Note that for the sake of simplicity we have omitted the azimuthal correlation terms parametrised by the $\mathbf{G}$ coefficient functions, which nevertheless can be treated in a similar fashion.

We can obtain the ingredients for the N^{3}LL resummation in direct space by comparing the Eqs. (3.61) and (3.62). The corresponding Sudakov radiators are

$$\begin{aligned} R(b) &= \sum_{\ell=1}^{2}\int_0^M \frac{dk_t}{k_t}R'_\ell(k_t)\,\Big(1-J_0(bk_t)\Big), \\ R_\mathrm{CSS}(b) &= \sum_{\ell=1}^{2}\int_0^M \frac{dk_t}{k_t}R'_{\mathrm{CSS},\ell}(k_t)\,\Theta\left(k_t-\frac{b_0}{b}\right), \end{aligned} \tag{3.63}$$

and they can be equivalently represented in terms of the anomalous dimensions A and B, as is usually done,

$$R(b) \equiv \sum_{\ell=1}^{2} \int_{b_0/b}^{M} \frac{dk_t}{k_t} \left(A_\ell(\alpha_s(k_t)) \ln\left(\frac{M^2}{k_t^2}\right) + B_\ell(\alpha_s(k_t)) \right),$$
$$R_{\rm CSS}(b) \equiv \sum_{\ell=1}^{2} \int_{b_0/b}^{M} \frac{dk_t}{k_t} \left(A_{{\rm CSS},\ell}(\alpha_s(k_t)) \ln\left(\frac{M^2}{k_t^2}\right) + B_{{\rm CSS},\ell}(\alpha_s(k_t)) \right). \tag{3.64}$$

The anomalous dimensions A_ℓ and B_ℓ relative to leg ℓ and the hard function H admit an expansion in the strong coupling as

$$A_\ell(\alpha_s) = \sum_{n=1}^{4} \left(\frac{\alpha_s}{2\pi}\right)^n A_\ell^{(n)}, \qquad B_\ell(\alpha_s) = \sum_{n=1}^{3} \left(\frac{\alpha_s}{2\pi}\right)^n B_\ell^{(n)},$$
$$H(M) = 1 + \sum_{n=1}^{2} \left(\frac{\alpha_s(M)}{2\pi}\right)^n H^{(n)}(M), \tag{3.65}$$

and by using the relation[3]

$$\left(1 - J_0(bk_t)\right) \simeq \Theta\left(k_t - \frac{b_0}{b}\right) + \frac{\zeta_3}{12} \frac{\partial^3}{\partial \ln{(Mb/b_0)}^3} \Theta\left(k_t - \frac{b_0}{b}\right) + \dots, \tag{3.66}$$

we obtain

$$A_\ell^{(4)} = A_{{\rm CSS},\ell}^{(4)} - 32 A_\ell^{(1)} \pi^3 \beta_0^3 \zeta_3,$$
$$B_\ell^{(3)} = B_{{\rm CSS},\ell}^{(3)} - 16 A_\ell^{(1)} \pi^2 \beta_0^2 \zeta_3,$$
$$H^{(2)}(M) = H_{\rm CSS}^{(2)}(M) + \frac{8}{3}\pi\beta_0\zeta_3 \sum_{\ell=1}^{2} A_\ell^{(1)}. \tag{3.67}$$

The above equations provide a recipe for obtaining the ingredients for our N^{3}LL resummation from the formulae derived for an impact-parameter space resummation. Physically, the extra terms proportional to ζ_3 arise from the fact that the $\mathcal{O}(\alpha_s^2)$ terms proportional to $\delta(1-z)$ in the coefficient functions in momentum space differ from their b-space counterpart. This difference precisely amounts to the new contributions in Eq. (3.67). We stress that only the full combination of $A_\ell^{(4)}$, $B_\ell^{(3)}$, $H^{(2)}$ and $C^{(2)}$ is resummation-scheme invariant, hence our choice of absorbing the new terms into $A_\ell^{(4)}$, $B_\ell^{(3)}$, $H^{(2)}$ is arbitrary.

[3]See Appendix 3a of Ref. [123] for details.

3.2 N^{3}LL resummation formulae and matching to a fixed-order prediction

The formalism presented in previous sections helped us to prepare all necessary ingredients for an N^{3}LL resummation in direct space. We start this section by stating the final master formula which is a consequence of Eq. (3.53) with ingredients of Eq. (3.54) expanded in a way that all relevant terms are present. We have[4]

$$
\begin{aligned}
&\frac{d\Sigma(v)}{d\Phi_B} = \\
&= \int_0^\infty \frac{dk_{t1}}{k_{t1}} \mathcal{J}(k_{t1}) \frac{d\phi_1}{2\pi} \partial_{\tilde{L}} \left(-e^{-\tilde{R}(k_{t1})} \tilde{\mathcal{L}}_{\mathrm{N^3LL}}(k_{t1}) \right) \int d\mathcal{Z}[\{\tilde{R}', k_i\}] \Theta\left(v - \mathrm{V}(\Phi_B, k_1, \ldots, k_{n+1})\right) \\
&+ \int_0^\infty \frac{dk_{t1}}{k_{t1}} \mathcal{J}(k_{t1}) \frac{d\phi_1}{2\pi} e^{-\tilde{R}(k_{t1})} \int d\mathcal{Z}[\{\tilde{R}', k_i\}] \int_0^1 \frac{d\zeta_s}{\zeta_s} \frac{d\phi_s}{2\pi} \left\{ \frac{\alpha_s^2(k_{t1})}{\pi^2} \hat{P}^{(0)} \otimes \hat{P}^{(0)} \otimes \tilde{\mathcal{L}}_{\mathrm{NLL}}(k_{t1}) \right. \\
&\qquad + \left(\tilde{R}'(k_{t1}) \tilde{\mathcal{L}}_{\mathrm{NNLL}}(k_{t1}) - \partial_{\tilde{L}} \tilde{\mathcal{L}}_{\mathrm{NNLL}}(k_{t1}) \right) \times \left(\tilde{R}''(k_{t1}) \ln \frac{1}{\zeta_s} + \frac{1}{2} \tilde{R}'''(k_{t1}) \ln^2 \frac{1}{\zeta_s} \right) \\
&\qquad \left. - \tilde{R}'(k_{t1}) \left(\partial_{\tilde{L}} \tilde{\mathcal{L}}_{\mathrm{NNLL}}(k_{t1}) - 2 \frac{\beta_0}{\pi} \alpha_s^2(k_{t1}) \hat{P}^{(0)} \otimes \tilde{\mathcal{L}}_{\mathrm{NLL}}(k_{t1}) \ln \frac{1}{\zeta_s} \right) \right\} \\
&\times \left\{ \Theta\left(v - \mathrm{V}(\Phi_B, k_1, \ldots, k_{n+1}, k_s)\right) - \Theta\left(v - \mathrm{V}(\Phi_B, k_1, \ldots, k_{n+1})\right) \right\} \\
&+ \frac{1}{2} \int_0^\infty \frac{dk_{t1}}{k_{t1}} \mathcal{J}(k_{t1}) \frac{d\phi_1}{2\pi} e^{-\tilde{R}(k_{t1})} \int d\mathcal{Z}[\{\tilde{R}', k_i\}] \int_0^1 \frac{d\zeta_{s1}}{\zeta_{s1}} \frac{d\phi_{s1}}{2\pi} \int_0^1 \frac{d\zeta_{s2}}{\zeta_{s2}} \frac{d\phi_{s2}}{2\pi} \tilde{R}'(k_{t1}) \\
&\times \left\{ \tilde{\mathcal{L}}_{\mathrm{NLL}}(k_{t1}) \left(\tilde{R}''(k_{t1}) \right)^2 \ln \frac{1}{\zeta_{s1}} \ln \frac{1}{\zeta_{s2}} - \partial_{\tilde{L}} \tilde{\mathcal{L}}_{\mathrm{NLL}}(k_{t1}) \tilde{R}''(k_{t1}) \left(\ln \frac{1}{\zeta_{s1}} + \ln \frac{1}{\zeta_{s2}} \right) \right. \\
&\qquad \left. + \frac{\alpha_s^2(k_{t1})}{\pi^2} \hat{P}^{(0)} \otimes \hat{P}^{(0)} \otimes \tilde{\mathcal{L}}_{\mathrm{NLL}}(k_{t1}) \right\} \\
&\times \left\{ \Theta\left(v - \mathrm{V}(\Phi_B, k_1, \ldots, k_{n+1}, k_{s1}, k_{s2})\right) - \Theta\left(v - \mathrm{V}(\Phi_B, k_1, \ldots, k_{n+1}, k_{s1})\right) + \right. \\
&\qquad \left. - \Theta\left(v - \mathrm{V}(\Phi_B, k_1, \ldots, k_{n+1}, k_{s2})\right) + \Theta\left(v - \mathrm{V}(\Phi_B, k_1, \ldots, k_{n+1})\right) \right\} \\
&+ \mathcal{O}\left(\alpha_s^n L^{2n-6}\right),
\end{aligned}
\tag{3.68}
$$

[4]Note an additional tilde over some of the symbols and Jacobian factors $\mathcal{J}(k_{t1})$. These are a consequence of using a modified logarithms prescription which is explained later in this section.

where $d\mathcal{Z}$ we denotes an ensemble of soft and collinear emissions with an average of a generic function $G(\Phi_{\rm B}, \{k_i\})$ over the measure $d\mathcal{Z}$ defined as $(\zeta_i \equiv k_{ti}/k_{t1})$

$$\int d\mathcal{Z}[\{\tilde{R}', k_i\}]G(\Phi_{\rm B}, \{k_i\}) = \\ e^{-\tilde{R}'(k_{t1})\ln\frac{1}{\epsilon}} \sum_{n=0}^{\infty} \frac{1}{n!} \prod_{i=2}^{n+1} \int_{\epsilon}^{1} \frac{d\zeta_i}{\zeta_i} \int_0^{2\pi} \frac{d\phi_i}{2\pi} \tilde{R}'(k_{t1}) G(\{\tilde{p}\}, k_1, \ldots, k_{n+1}) \,, \tag{3.69}$$

where the term $\ln(1/\epsilon)$ is regulating the IRC divergences, i.e. the $\ln(1/\epsilon)$ divergence in the exponent resulting from combination of virtual corrections and unresolved real emissions cancels exactly against the divergences contained in the resolved real emissions. The final result is ϵ-independent, and formally a limit $\epsilon \to 0$ can be performed. Subscript s in Eq.(3.68) is used to denote special emissions that are not soft-and-collinear $(\zeta_s \equiv k_{ts}/k_{t1})$ and therefore are not part of the $d\mathcal{Z}$ shower.

We have expanded all ingredients in Eq. (3.68) about the hardest emission k_{t1}. As explained in previous sections such an operation is permitted thanks to rIRC safety of the observable, namely the fact that for all resolved real emissions ζ_i is an $\mathcal{O}(1)$ quantity. This Taylor expansion gives rise to terms involving derivatives of the Sudakov radiator

$$\tilde{R}' = d\tilde{R}/d\tilde{L}, \qquad \tilde{R}'' = d\tilde{R}'/d\tilde{L}, \qquad \tilde{R}''' = d\tilde{R}''/d\tilde{L}, \tag{3.70}$$

where the radiator itself can be represented as

$$\tilde{R}(k_{t1}) = -\tilde{L}\, g_1(\alpha_s\beta_0\tilde{L}) - g_2(\alpha_s\beta_0\tilde{L}) - \left(\frac{\alpha_s}{\pi}\right) g_3(\alpha_s\beta_0\tilde{L}) - \left(\frac{\alpha_s}{\pi}\right)^2 g_4(\alpha_s\beta_0\tilde{L}), \tag{3.71}$$

with $\alpha_s \equiv \alpha_s(\mu_R)$, and the full form of functions g_i is reported in the Appendix A.2.

Before explaining the *modified* logarithms that have appeared in the resummed formulae in this section and were indicated by an overhead tilde, *e.g.* $\tilde{L}$, we briefly describe a method for estimating the size of subleading logarithmic terms that are beyond the nominal accuracy of Eq. (3.68). They may serve as an indicator of the uncertainty of the prediction due to missing higher-order terms. For this purpose we introduce a resummation scale Q as

$$\ln\left(\frac{M}{k_{t1}}\right) = \ln\left(\frac{Q}{k_{t1}}\right) + \ln\left(\frac{M}{Q}\right). \tag{3.72}$$

The ratio (M/Q) is an $\mathcal{O}(1)$ number which we can vary around some central value to obtain an uncertainty band.

Finally, the modified logarithms $\tilde{L}$ have been introduced to ensure that resummation does not affect the hard region of the spectrum when matching to fixed-order (the details of the matching procedure will be described in Section 3.2.3). This is achieved by mapping the limit $k_{t1} \to Q$ onto $k_{t1} \to \infty$ in all terms of the master formula in Eq. (3.68) except for the measurement function. In our implementation we use

$$\ln\left(\frac{Q}{k_{t1}}\right) \longrightarrow \tilde{L} = \frac{1}{p}\ln\left(\left(\frac{Q}{k_{t1}}\right)^p + 1\right), \tag{3.73}$$

where p is a positive real parameter. The criterion that should be respected is that the vanishing of the resummed differential distribution at large values of the observable v should be faster than the one of the corresponding fixed-order prediction. Prescription of Eq. (3.73) is accompanied by the Jacobian related to this transformation

$$\mathcal{J}(k_{t1}) = \left(\frac{Q}{k_{t1}}\right)^p \left(\left(\frac{Q}{k_{t1}}\right)^p + 1\right)^{-1}. \tag{3.74}$$

We stress that the transformation is not performed in the observable and therefore cannot be viewed as a simple change of variables. As a consequence this procedure introduces power-suppressed terms into the result which however vanish at small v.

3.2.1 Treatment of parton luminosity at N^{3}LL

The master formula in Eq. (3.68) features the parton luminosities $\tilde{\mathcal{L}}$ that are evaluated with different logarithmic accuracy, i.e. at given logarithmic order only a finite number of hard-collinear emissions is necessary and we can include the exclusive DGLAP evolution steps directly at the level of parton luminosities.

Knowing that at NLL we do not need to consider hard-collinear kinematics the corresponding parton luminosity reads

$$\tilde{\mathcal{L}}_{\rm NLL}(k_{t1}) = \sum_{c,c'} |\mathcal{M}_B(\Phi_{\rm B})|^2_{cc'} f_c\Big(\mu_F e^{-\tilde{L}}, x_1\Big)\, f_{c'}\Big(\mu_F e^{-\tilde{L}}, x_2\Big), \tag{3.75}$$

where c and c' are the flavour indices of the coloured legs entering the Born matrix element $|\mathcal{M}_B(\Phi_{\rm B})|^2_{cc'}$ which is kept differential in the Born phase space. The momentum fractions x_1 and x_2 can be expressed as

$$x_1 = \frac{M}{\sqrt{s}}\, e^{+Y}, \qquad x_2 = \frac{M}{\sqrt{s}}\, e^{-Y}, \tag{3.76}$$

with M and Y being the mass and the rapidity (in the centre-of-mass frame) of the colour singlet. The scale at which we evaluate the parton distribution functions should be equal to transverse momentum of the first (hardest) emission $\mu = k_{t1}$, which after the change of variables of Eq. (3.73) can be written as $\mu = \mu_F e^{-\tilde{L}}$.

At the NNLL order, we need to consider at most one hard-collinear emission which, together with the changes in the real radiation discussed in previous section, leads to the following luminosity factor

$$\begin{aligned}
\tilde{\mathcal{L}}_{\mathrm{NNLL}}(k_{t1}) &= \sum_{c,c'} |\mathcal{M}_B(\Phi_\mathrm{B})|^2_{cc'} \sum_{i,j} \int_{x_1}^1 \frac{dz_1}{z_1} \int_{x_2}^1 \frac{dz_2}{z_2} f_i\left(\mu_F e^{-\tilde{L}}, \frac{x_1}{z_1}\right) f_j\left(\mu_F e^{-\tilde{L}}, \frac{x_2}{z_2}\right) \\
&\times \Bigg\{\delta_{ci}\delta_{c'j}\delta(1-z_1)\delta(1-z_2)\left(1+\frac{\alpha_s(\mu_R)}{2\pi}\tilde{H}^{(1)}(\mu_R, x_\mathrm{Q})\right) \\
&+ \frac{\alpha_s(\mu_R)}{2\pi}\frac{1}{1-2\alpha_s(\mu_R)\beta_0\tilde{L}}\left(\tilde{C}^{(1)}_{ci}(z_1,\mu_F,x_\mathrm{Q})\delta(1-z_2)\delta_{c'j} + \{z_1 \leftrightarrow z_2; ci \leftrightarrow c'j\}\right)\Bigg\},
\end{aligned} \tag{3.77}$$

where we have used the renormalisation scale μ_R, and $x_\mathrm{Q} = (Q/M)$. We have also included the NLO coefficient functions $\tilde{C}^{(1)}_{ci}$ and the NLO hard virtual corrections $\tilde{H}^{(1)}$ that for the Higgs and Drell-Yan production processes have been obtained in [131, 132, 133], for completeness we report relevant formulae in Appendix A.2.

Finally, at the N^{3}LL order we combine effects of up to two hard-collinear emissions and we obtain

$$\begin{aligned}
\tilde{\mathcal{L}}_{\mathrm{N^3LL}}(k_{t1}) &= \sum_{c,c'} |\mathcal{M}_B(\Phi_\mathrm{B})|^2_{cc'} \sum_{i,j} \int_{x_1}^1 \frac{dz_1}{z_1} \int_{x_2}^1 \frac{dz_2}{z_2} f_i\left(\mu_F e^{-\tilde{L}}, \frac{x_1}{z_1}\right) f_j\left(\mu_F e^{-\tilde{L}}, \frac{x_2}{z_2}\right) \\
&\times \Bigg\{\delta_{ci}\delta_{c'j}\delta(1-z_1)\delta(1-z_2)\left(1+\frac{\alpha_s(\mu_R)}{2\pi}\tilde{H}^{(1)}(\mu_R, x_\mathrm{Q}) + \frac{\alpha_s^2(\mu_R)}{(2\pi)^2}\tilde{H}^{(2)}(\mu_R, x_\mathrm{Q})\right) \\
&+ \frac{\alpha_s(\mu_R)}{2\pi}\frac{1}{1-2\alpha_s(\mu_R)\beta_0\tilde{L}}\left(1-\alpha_s(\mu_R)\frac{\beta_1}{\beta_0}\frac{\ln\left(1-2\alpha_s(\mu_R)\beta_0\tilde{L}\right)}{1-2\alpha_s(\mu_R)\beta_0\tilde{L}}\right) \\
&\times \left(\tilde{C}^{(1)}_{ci}(z_1,\mu_F,x_\mathrm{Q})\delta(1-z_2)\delta_{c'j} + \{z_1 \leftrightarrow z_2; c,i \leftrightarrow c',j\}\right) \\
&+ \frac{\alpha_s^2(\mu_R)}{(2\pi)^2}\frac{1}{(1-2\alpha_s(\mu_R)\beta_0\tilde{L})^2}\left(\tilde{C}^{(2)}_{ci}(z_1,\mu_F,x_\mathrm{Q})\delta(1-z_2)\delta_{c'j} + \{z_1 \leftrightarrow z_2; c,i \leftrightarrow c',j\}\right) \\
&+ \frac{\alpha_s^2(\mu_R)}{(2\pi)^2}\frac{1}{(1-2\alpha_s(\mu_R)\beta_0\tilde{L})^2}\left(\tilde{C}^{(1)}_{ci}(z_1,\mu_F,x_\mathrm{Q})\tilde{C}^{(1)}_{c'j}(z_2,\mu_F,x_\mathrm{Q}) + G^{(1)}_{ci}(z_1)G^{(1)}_{c'j}(z_2)\right) \\
&+ \frac{\alpha_s^2(\mu_R)}{(2\pi)^2}\tilde{H}^{(1)}(\mu_R, x_\mathrm{Q})\frac{1}{1-2\alpha_s(\mu_R)\beta_0\tilde{L}}\left(\tilde{C}^{(1)}_{ci}(z_1,\mu_F,x_\mathrm{Q})\delta(1-z_2)\delta_{c'j} + \{z_1 \leftrightarrow z_2; c,i \leftrightarrow c',j\}\right)\Bigg\},
\end{aligned} \tag{3.78}$$

where we have also included the NNLO coefficient functions $\tilde{C}_{ci}^{(2)}$ and the two-loop hard virtual correction $\tilde{H}^{(2)}$, for details consult Appendix A.2.

The terms that contain convolution operator combining a regularised splitting function, for example $\hat{P}$ with the $\tilde{\mathcal{L}}_{\rm NLL}$, should be interpreted as

$$\hat{P}^{(0)} \otimes \tilde{\mathcal{L}}_{\rm NLL}(k_{t1}) \equiv \sum_{c,c'} |\mathcal{M}_B(\Phi_{\rm B})|^2_{cc'} \Big\{ \left(\hat{P}^{(0)} \otimes f\right)_c \left(\mu_F e^{-\tilde{L}}, x_1\right) f_{c'}\left(\mu_F e^{-\tilde{L}}, x_2\right) \\ + f_c\left(\mu_F e^{-\tilde{L}}, x_1\right) \left(\hat{P}^{(0)} \otimes f\right)_{c'} \left(\mu_F e^{-\tilde{L}}, x_2\right) \Big\}, \quad (3.79)$$

and similar formulae may be written for the other terms of this type. Moreover, the explicit strong coupling factors in Eq. (3.68) should be evaluated using the RG evolution at one-loop, i.e.

$$\alpha_s(k_{t1}) \equiv \frac{\alpha_s(\mu_R)}{1 - 2\alpha_s(\mu_R)\beta_0 \tilde{L}}. \quad (3.80)$$

3.2.2 Validation of the expanded N^{3}LL formula

One of the means of verifying the correctness of a resummed prediction is a comparison with the fixed-order calculation. We can identify and extract terms that are present in both types of calculation and check the agreement between the two.

We can use the fixed-order predictions for the transverse momentum of Higgs boson computed at the NNLO [134] as well as the NNLO accurate ϕ^*_η distribution in the Drell-Yan production process obtained in [135]. We want to point out that at the level of the differential distribution, the NNLO accuracy denotes the derivative of a corresponding N^{3}LO cumulant, namely we control all terms entering the prediction of the distribution up to and including $\mathcal{O}(\alpha_s^3)$ terms with respect to the Born cross section. Throughout this section, we use similar notation for lower orders of the differential distribution. In this fasion we can denote a fixed-order distribution by

$$\left[\frac{d\Sigma}{dv}\right]_{\rm NNLO} = \sum_{i=1}^{3} \frac{d\Sigma^{(i)}_{\rm FIX}}{dv}, \quad (3.81)$$

where we explicitly indicate that the prediction has been obtained using a fixed-order perturbation theory by a subscript FIX.

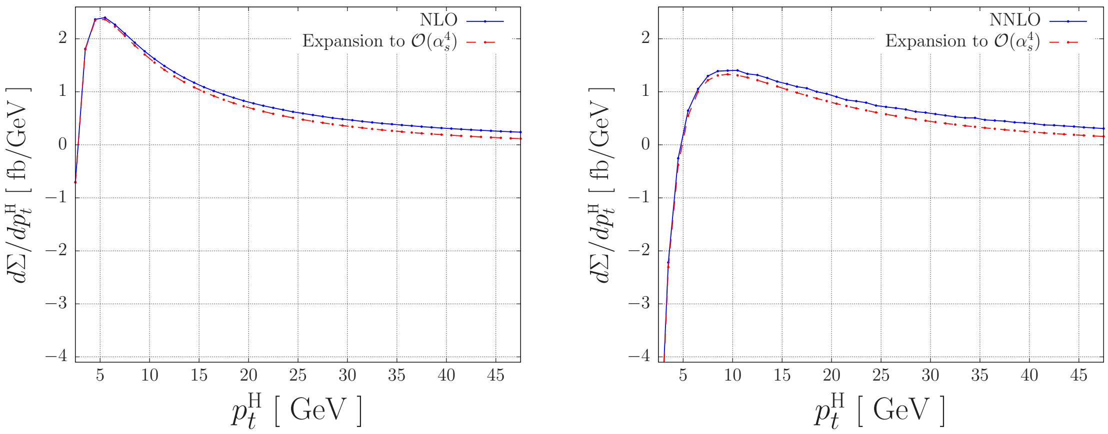

Figure 3.2: Comparison between the fixed-order transverse momentum distribution for Higgs boson production at $\sqrt{s} = 13$ TeV at NLO (left) and NNLO (right) and the expansion of the N^{3}LL resummation formula given in Eq. (3.68) to the corresponding order, i.e. $\mathcal{O}(\alpha_s^4)$ and $\mathcal{O}(\alpha_s^5)$ (namely $\mathcal{O}(\alpha_s^2)$ and $\mathcal{O}(\alpha_s^3)$ relative to Born), respectively.

In order to perform such a comparison with the resummed prediction we can consider a differential distribution of the cumulant computed in Eq. (3.68) and expand it at the third order in the strong coupling

$$\left[\frac{d\Sigma}{dv}\right]_{\rm EXP} = \sum_{i=1}^{3} \frac{d\Sigma^{(i)}_{\rm RES}}{dv}, \tag{3.82}$$

the subscript RES indicates that these terms have been obtained by expanding the resummed prediction. Each of the $(d\Sigma/dv)^{(i)}_{\rm FIX}$ terms contains the same logarithmic structures as the corresponding $(d\Sigma/dv)^{(i)}_{\rm RES}$ ones, however the latter does not carry the information about the non-logarithmic contributions. An optimal region to compare the two predictions is the deep infrared regime of the radiation phase space, where we expect

$$\left(\left[\frac{d\Sigma}{dv}\right]_{\rm NNLO} - \left[\frac{d\Sigma}{dv}\right]_{\rm EXP} \right) \xrightarrow[v\longrightarrow 0]{} 0. \tag{3.83}$$

A detailed discussion of the validation procedure will be presented in the following sections, the validation for transverse momentum distribution of the Higgs boson produced in the gluon-gluon fusion process in Section 3.2.2.1 and the validation of the ϕ^*_η distribution in the Drell-Yan process followed by the Z boson decay into charged leptons in Section 3.2.2.2.

3.2.2.1 The Higgs transverse momentum - validation

In Fig. 3.2 we present the transverse momentum distribution of the Higgs boson $p_t^{\rm H}$ obtained by means of the fixed-order perturbation theory [134] as well as the expanded prediction of the resummed formula (3.68) truncated at a given order of strong coupling. The left panel shows the NLO fixed-order distribution and corresponding resummed formula expanded up to and including $\mathcal{O}(\alpha_s^4)$ terms (i.e. $\mathcal{O}(\alpha_s^2)$ terms relative to Born), the right panels shows the NNLO fixed order distribution and expansion up to $\mathcal{O}(\alpha_s^5)$ terms (i.e. $\mathcal{O}(\alpha_s^3)$ terms relative to Born). We can see that both predictions agree very well below $p_t^{\mathrm{H}} \sim 10$ GeV, where logarithmic terms dominate. Moreover, the size of the non-logarithmic terms remains moderate up to $p_t^{\mathrm{H}} \sim 50$ GeV. We have used the `PDF4LHC15_nnlo_mc` set of parton distribution functions [136].

To put our prediction under even greater scrutiny we can look directly at the difference between $(d\Sigma/d\ln(v))_{\mathrm{FIX}}$ and $(d\Sigma/d\ln(v))_{\mathrm{EXP}}$. In Fig. 3.3, we present such a comparison at various levels of the fixed-order perturbation theory and different orders of the expansion. We first focus on the left panel of the figure. The blue curve quantifies the difference between NLO accurate fixed-order prediction and the corresponding $\mathcal{O}(\alpha_s^4)$ (or $\mathcal{O}(\alpha_s^2)$ relative to Born) expansion of the NNLL accurate resummed formula, which has been extracted from Eq. (3.68). We see that the difference tends to zero as expected. Comparing the NNLO accurate distribution with the NNLL expansion (green curve), we see that the difference does not vanish in the limit $p_t^{\mathrm{H}} \to 0$ but rather diverges. This effect can be attributed to a lack of the NNLO coefficient functions and the two-loop virtual corrections in the NNLL accurate result. Such an omission induces differences at the level of double-logarithmic terms that results in a linear-slope discrepancy at the level of the differential distribution. A situation changes, when instead of the NNLL result we present expansion of the full N^{3}LL formula that includes aforementioned higher-order terms. In this case (red curve) the difference converges to zero featuring however large statistical fluctuations down to instability of the fixed-order prediction in the deep IR region.

Lastly, we take a closer look at the NNLO-N^{3}LL difference in the right panel of Fig. 3.3 that contains only the NNLO part, i.e. $\mathcal{O}(\alpha_s^5)$ terms ($\mathcal{O}(\alpha_s^3)$ terms relative to the Born cross section) extracted from the red curve of the left figure. We focus on the lower inset of the right panel that shows the difference relative to the NNLO coefficient of the fixed-order distribution. We see that the two formulae in question balance each other at the level of

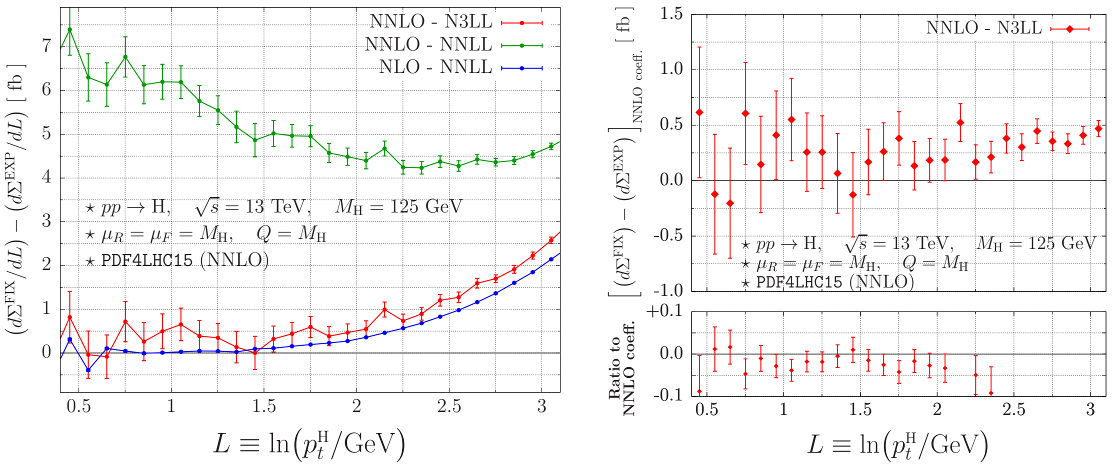

Figure 3.3: Left: difference between the NLO and NNLO fixed-order transverse momentum distribution for Higgs boson production at $\sqrt{s} = 13$ TeV and the expansion of the resummation formula given in Eq. (3.68) to NNLL and N^{3}LL accuracy. Right: difference between the NNLO coefficient of the fixed-order distribution and the corresponding coefficient of the expansion of the N^{3}LL resummation.

$\mathcal{O}(\alpha_s^5)$ terms ($\mathcal{O}(\alpha_s^3)$ terms relative to the Born cross section) proving at the same time the correctness of formula (3.68), at least up terms considered in this subsection.

3.2.2.2 The ϕ^*_η distribution in Drell-Yan process - validation

We can carry out a similar analysis in the case of Drell-Yan production. The two instances are very similar to each other, as both the Higgs production in gluon-gluon fusion as well as the Drell-Yan process are initiated by an annihilation of two coloured partons. Nevertheless, it is instructive to perform a check also for quark-initiated process. Unlike in the Higgs production case the distribution of the electroweak Z boson's virtuality is much broader than the narrow peak present in the $gg \to$ H process. Moreover, an additional complication is posed by the treatment of fiducial cuts that we impose in this case. Inspired by the setup used by ATLAS collaboration [137] for 8 TeV pp collisions, we require

$$p_t^{\ell^\pm} > 20 \text{ GeV}, \qquad |\eta^{\ell^\pm}| < 2.4, \qquad |Y_{\ell\ell}| < 2.4, \qquad 116 \text{ GeV} < M_{\ell\ell} < 150 \text{ GeV}, \tag{3.84}$$

where we have intentionally focused on the high invariant mass ($M_{\ell\ell}$) window in order to magnify the impact of the logarithmic terms. We also use dynamical renormalisation and factorisation scales as well as resummation scale

$$\mu_R = \mu_F = \sqrt{M_{\ell\ell}^2 + p_t^2}\,, \qquad \text{and} \qquad Q = M_{\ell\ell}. \tag{3.85}$$

Note that an additional difference between the fixed-order calculation and the resummed one is caused by the treatment of fiducial cuts. In our implementation the fiducial cuts and dynamical scales are always defined at the level of Born phase space (i.e. Z+0jet kinematics) contrary to the fixed-order calculation where fiducial cuts and dynamical scales are evaluated with full kinematics (i.e. Z+1/2/3jets depending on the type of the correction considered). The two definitions differ from each other unless the extra QCD radiation is extremely soft and collinear to the beam. We have used `NNPDF-3.0` parton densities [138].

In the left panel of Fig. 3.4 we show the difference between the NNLO and the expanded N^{3}LL distributions for the ϕ^*_η as well as the difference between the NLO and the expanded NNLL ones, red and blue curves respectively. On this occasion we have selected the ϕ^*_η instead of the p_t^Z to perform the validation. This is an equivalent choice as both observables carry the same structure of singularities. Similarly to the previous case we see that both curves approach zero when the large logarithms dominate.

In the right panel of Fig. 3.4 we focus on the NNLO coefficient, i.e. the $\mathcal{O}(\alpha_s^3)$ terms that we extract from the NNLO fixed-order and the expanded N^{3}LL distributions. Again, we see that the two balance each other providing a good cancellation in the region dominated by large logarithms. The lower inset shows the ratio of the difference to the fixed-order NNLO coefficient itself. We see that the fluctuations are slightly bigger than in the case of the Higgs boson production, shown in Fig. 3.3, which could have been anticipated as the Z-boson virtuality has a much broader spectrum than the Higgs boson and we have also imposed fiducial cuts in our simulation which in consequence might delay the convergence to even deeper infra-red region. Nevertheless, plots in Fig. 3.4 provide evidence for the similar structure of the logarithmic terms in the fixed-order and resummed predictions.

3.2.3 NNLO + N^{3}LL matching

A fixed-order perturbation theory and a resummation provide two separate but compatible approaches for generating predictions of the QCD theory for particle collisions. The two usually cover different parts of the considered spectra. It is then natural to ask about their matching.

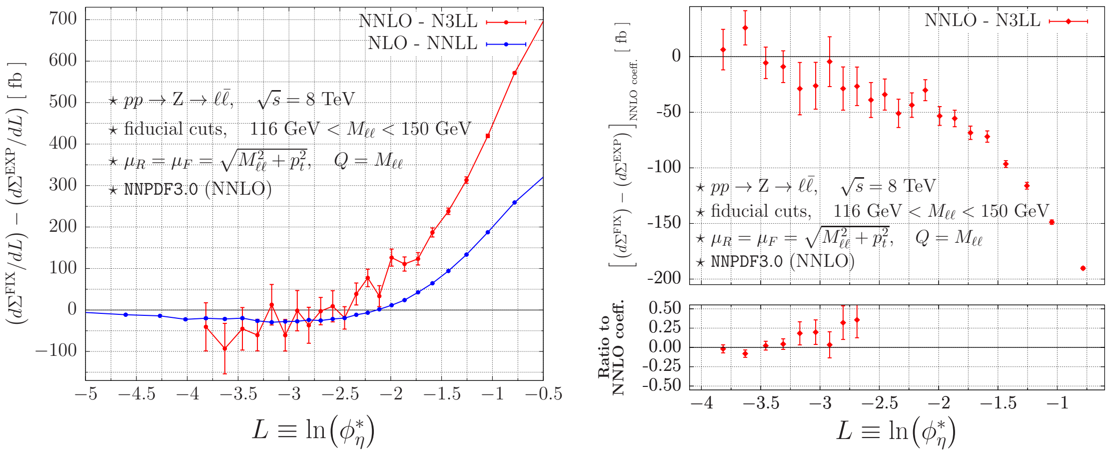

Figure 3.4: Left: difference between the NLO and NNLO ϕ_η^* distributions and the expansion of the NNLL and N^{3}LL resummation formulae to the same perturbative order. Right: difference between the NNLO coefficient of the fixed-order distribution and the corresponding coefficient of the expansion of the N^{3}LL resummation.

We would like to find a procedure that will allow for a consistent combination that will preserve the logarithmic accuracy of the resummed calculation in the $v \to 0$ limit while maintaining the features of the fixed-order perturbation theory in the high-v tail of the distribution.

In order to perform such a matching procedure we will work at the level of the cumulant of the cross section $\Sigma(v)$ that we have already defined in Eq. (3.11). For clarity, we will supply the cumulants corresponding to the resummed cross section and its expansion in the strong coupling, and the fixed-order prediction. We define relevant labels

$$\Sigma^{\mathrm{N^3LL}}(v) = \Sigma_{\mathrm{RES}}(v),$$
$$\Sigma^{\mathrm{EXP}}(v) = \sum_{i=1}^{3} \Sigma^{(i)}_{\mathrm{RES}}(v),$$
$$\Sigma^{\mathrm{N^3LO}}(v) = \sum_{i=1}^{3} \Sigma^{(i)}_{\mathrm{FIX}}(v), \tag{3.86}$$

where $\Sigma_{\mathrm{RES}}(v)$ is the resummed cumulant but for the remainder of this chapter we will explicitly refer to it as the N^{3}LL accurate cumulant, the superscript (i) on the right-hand side denotes the $\mathcal{O}(\alpha_s^i)$ term of the Taylor expansion in powers of the strong coupling of the considered cumulant. We remind the reader of a slight abuse of the notation, i.e. we have

$$\Sigma^{\mathrm{N^3LO}}(v) = \sigma^{\mathrm{N^3LO}} - \int_v^\infty dv' \frac{d\Sigma^{\mathrm{NNLO}}}{dv'}, \tag{3.87}$$

which means that the NNLO distribution $(d\Sigma/dv)^{\rm NNLO}$ is a derivative of the N^{3}LO cumulant. This is a widely used practice as at the leading order we have $v = 0$.

In the case of Higgs production in gluon-gluon fusion, the NNLO accurate distribution has been obtained in Refs. [139, 140, 141, 142], while the N^{3}LO accurate calculation of the total cross section has been reported in Refs. [143, 144]. For the Drell-Yan production, the differential distribution was calculated in Refs. [135, 145]. However, we note that the total cross section is currently known only at the NNLO level. In our implementation we will set the unknown contribution $\sigma^{(3)}_{\rm DY}$ to zero. Such an approximation amounts to an N^{4}LL effect at the level of differential distribution and as such lies beyond the accuracy of the formulae presented in this work.

Having defined the necessary ingredients we can attempt a matching procedure that will consistently combine the resummed prediction with the one from the fixed-order perturbative expansion. One of the most common matching schemes is the additive R scheme, that has been introduced in Ref. [146]. We simply have

$$\Sigma^{\rm MAT}_{add}(v) = \Sigma^{\rm N^3LL}(v) + \Sigma^{\rm N^3LO}(v) - \Sigma^{\rm EXP}(v), \tag{3.88}$$

where at the large-v limit only the fixed-order prediction prevails while the other two tend to zero, and the N^{3}LO and EXP cumulants cancel each other in the limit $v \to 0$, as checked in Section 3.2.2.

Another simple yet powerful class of matching schemes is known as the multiplicative scheme, defined in Refs. [122, 123, 124]. Illustratively, we have

$$\Sigma^{\rm MAT}_{mult}(v) = \Sigma^{\rm N^3LL}(v) \, \left[\frac{\Sigma^{\rm N^3LO}(v)}{\Sigma^{\rm EXP}(v)}\right]_{\{\text{expanded to } \mathcal{O}(\alpha_s^3)\}}, \tag{3.89}$$

where the ratio in the square bracket is expanded in powers of strong coupling up to $\mathcal{O}(\alpha_s^3)$ terms. Similarly to the previous case, the ratio in the square bracket tends to one as $v \to 0$. On the other hand, we reproduce the fixed-order behaviour in the large-v tail of the distribution.

The two matching schemes differ from each other by terms which are subleading, i.e. they amount to N^{4}LL and N^{4}LO effects, and both can serve as good strategies for combining fixed- and all-order perturbative calculations. In our work, we focus on the multiplicative matching scheme and we use one of its variants that will be detailed in the remaining part of this section. One advantage of using the multiplicative scheme with respect to the additive one is the treatment of the low-v region which is naturally dominated by the all-order calculation, nevertheless, the fixed-order simulation may be affected by relatively large numerical instabilities in this region thus spoiling the benefits of resummation. In the multiplicative matching scheme such statistical fluctuations are damped by the resummation factor $\Sigma^{\mathrm{N^3LL}}$. A second convenient fact of the multiplicative solution is the treatment of the N^{3}LO constant terms, which are formally an N^{4}LL effect. Whenever known they are extracted from the fixed-order result in the matching procedure. We recall that our N^{3}LL resummed formula controls all $\mathcal{O}(\alpha_s^n L^{n-3})$ terms at the level of logarithm of Σ_{RES}, which implies that we correctly predict $\mathcal{O}(\alpha_s^n L^{2n-5})$ terms at the level of expanded formula for Σ_{RES}. Using the multiplicative matching procedure of Eq. (3.89) we automatically include constant terms of order $\mathcal{O}(\alpha_s^3)$ relative to Born level in the resummed formula as soon as they are present in the fixed-order results. Such terms reflect the N^{3}LO part of the collinear coefficient functions as well as three-loop virtual corrections. In this way, the matched prediction correctly encodes an additional tower of terms extending the validity of the formula up to and including $\mathcal{O}(\alpha_s^n L^{2n-6})$ terms. We want to stress that this requires a complete knowledge of an N^{3}LO accurate cross section. Unfortunately, this is the case only for the total cross section for the Higgs boson production in the gluon-gluon fusion. In the case of Drell-Yan production, but also for Higgs production with fiducial cuts imposed, the terms $\mathcal{O}(\alpha_s^n L^{2n-6})$ will not be fully included. Nevertheless, as already mentioned above, they are beyond the N^{3}LL accuracy which was the aim of this work. A short comparison of the two matching schemes has been presented in Ref. [17].

The multiplicative matching scheme of Eq. (3.89) has also a drawback that enters in the large-v tail. Indeed, in the limit $\tilde{L} \to 0$ the resummed cumulant $\Sigma^{\mathrm{N^3LL}}$ tends to the integral of $\tilde{\mathcal{L}}_{\mathrm{N^3LL}}(\mu_F)$ over Φ_{B}, evaluated at $\tilde{L} = 0$. Therefore at large-v we obtain

$$\Sigma^{\mathrm{MAT}}_{mult}(v) \sim \Sigma^{\mathrm{N^3LO}}(v)\, \left[1 + \mathcal{O}(\alpha_s^4)\right]. \tag{3.90}$$

Formally, the $\mathcal{O}(\alpha_s^4)$ terms are of higher order but they can be moderate in size for processes with large K-factors, such as the Higgs production in gluon-gluon fusion.

One can imagine various remedies to resolve this possible issue. One possible solution, as presented in Ref. [16], is to modify the resummed component as

$$\Sigma^{\mathrm{N^3LL}} \quad \longrightarrow \quad \left(\Sigma^{\mathrm{N^3LL}}\right)^{Z(v)}, \tag{3.91}$$

where $Z(v)$ is a damping factor defined by the formula

$$Z(v) = \left(1 - \left(\frac{v}{v_0}\right)^u\right)^h \Theta\left(v_0 - v\right), \tag{3.92}$$

with u and h being positive real parameters and v_0 being the point at which the fixed-order result is recovered. Although such a modification helps to minimise the impact of the spurious terms discussed in Eq. (3.90) it introduces additional parameters that enter the final matched result. One has to carefully check that variation of u and h does not lead to sizeable differences which, if present, might have increased the size of the theoretical uncertainty related to the calculation.

In this work we will suggest a slightly different solution that can be implemented without necessity of creating new parameters. For this reason we will normalise the resummed prefactor to its asymptotic value which we denote by

$$\Sigma^{\mathrm{N^3LL}}_{\text{asym.}} = \int_{\text{with cuts}} d\Phi_{\mathrm{B}} \left(\lim_{\tilde{L}\to 0} \tilde{\mathcal{L}}_{\mathrm{N^3LL}}\right), \tag{3.93}$$

where the integration over the Born phase-space is performed with the phase-space cuts taken into account. We then modify our starting point, Eq. (3.89), into

$$\Sigma^{\mathrm{MAT}}_{mult}(v) = \frac{\Sigma^{\mathrm{N^3LL}}(v)}{\Sigma^{\mathrm{N^3LL}}_{\text{asym.}}} \left[\Sigma^{\mathrm{N^3LL}}_{\text{asym.}} \times \frac{\Sigma^{\mathrm{N^3LO}}(v)}{\Sigma^{\mathrm{EXP}}(v)}\right]_{\{\text{expanded to } \mathcal{O}(\alpha_s^3)\}}, \tag{3.94}$$

where the whole square bracket is expanded in powers of the strong coupling up to $\mathcal{O}(\alpha_s^3)$ terms. Given that in the large-v limit,

$$\Sigma^{\mathrm{N^3LL}}(v) \xrightarrow[v \gg Q/M]{} \Sigma^{\mathrm{N^3LL}}_{\text{asym.}}, \tag{3.95}$$

the Eq. (3.94) reproduces the fixed-order result by constriction, and no large spurious corrections arise in this region. The formulae for the case of normalised multiplicative matching, presented in Eq. (3.94), are reported in Appendix A.3.

3.3 Phenomenological studies

In this section we present a short summary of some phenomenological applications of the techniques discussed in this chapter. In Section 3.3.1 we focus on the distribution of the transverse momentum of the Higgs boson. Such a measurement is one of the highlights of the LHC programme. The first results have been already reported [147], and even more data is expected to arrive in the years to come. Then in Section 3.3.2 we discuss the transverse momentum distribution of the Z boson in the Drell-Yan production process along with the distribution of the ϕ^*_η observable. These observables are particularly suited for precision studies at the LHC thanks to clear signatures associated with their measurement, i.e. a pair of charged leptons that can be easily identified in the detectors. We compare our predictions to the results reported by the ATLAS collaboration in Ref. [137].

3.3.1 p_t^{H} distribution in the Higgs boson production

In this section we present results for the transverse momentum distribution of the Higgs boson (p_t^{H}) in case of the inclusive production as well as after imposing fiducial cuts on the decay products of the Higgs boson.

For both calculations we use the same technical setup. We consider 13 TeV *pp* collisions and we work in the heavy-top-quark limit. We use `PDF4LHC15_nnlo_mc` set of parton distribution functions [136]. We use $p = 4$ for the modified logarithms prescription defined in Eq. (3.73). This parameter has been selected considering the scaling of the distribution in large-p_t^{H} limit. We have also verified that a variation of p by a unit shift in both directions does not affect the final result in a significant way.

Finally, we should discuss the scale choice in our simulation. We set renormalisation and factorisation scales to $\mu_R = \mu_F = M_{\mathrm{H}}/2$, while setting $M_{\mathrm{H}} = 125$ GeV. Similarly we set the resummation scale $Q = M_{\mathrm{H}}/2$, i.e. $x_{\mathrm{Q}} = 1/2$. The uncertainty of the prediction is evaluated by performing a seven-scale variation of renormalisation and factorisation scales - we use the standard method of rescaling μ_R and μ_F by a factor of two in either direction, but keeping $1/2 \leqslant \mu_R/\mu_F \leqslant 2$. Additionally, for the central-choice of μ_R and μ_F we evaluate variation of the resummation scale x_{Q} also by a factor of two in both directions around. The resulting uncertainty band is an envelope of all described variations.

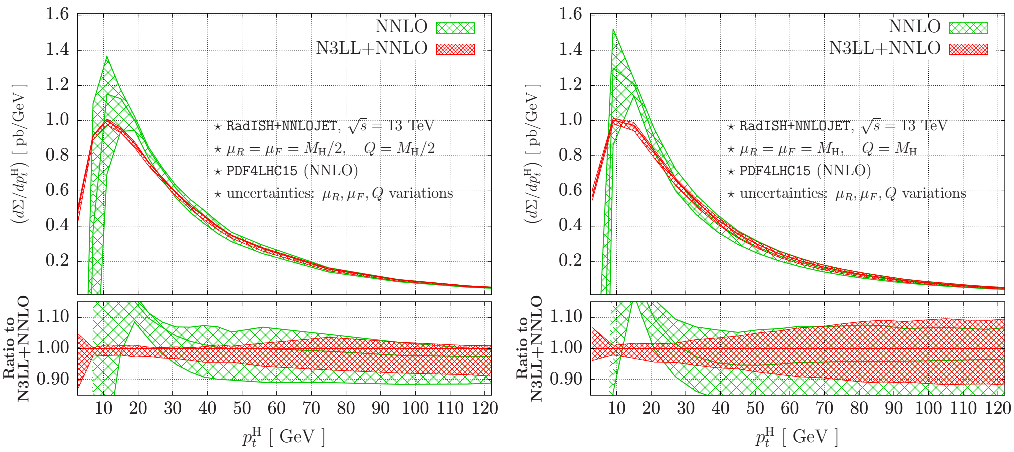

Figure 3.5: Comparison of the transverse momentum distribution for Higgs boson production at NNLO and N^{3}LL+NNLO for a central scale choice of $\mu_R = \mu_F = M_\text{H}/2$ (left) and $\mu_R = \mu_F = M_\text{H}$ (right). In both cases, $Q = M_\text{H}/2$. The lower panel shows the ratio to the N^{3}LL+NNLO prediction.

We start our analysis by comparing the matched distribution and the purely fixed-order one. In Fig. 3.5 we present the NNLO accurate fixed-order prediction (green) and the matched one that combines the N^{3}LL prediction with NNLO accurate one (red). We consider two setups - one where the central renormalisation and factorization scales are set to $\mu_R = \mu_F = M_\text{H}/2$ (left panel) and the one with $\mu_R = \mu_F = M_\text{H}$ (right panel). We keep other settings as described at the beginning of the section. We observe that the prediction with central scales set to M_H gives more cautious estimate of the theoretical uncertainty as the band is significantly larger than in case with $M_\text{H}/2$ as the central-scale choice. Such an effect can be attributed to cancellations in the scale variation [143, 148]. This is particularly visible in the hard region of the spectrum, i.e. $p_t^\text{H} > 50$ GeV, where the fixed-order calculation takes over the resummed one. In the rest of this section we will adopt the latter choice, $\mu = M_\text{H}/2$ as our study focuses purely on the theoretical setup. However, we recognise that the actual comparison of the theoretical prediction with experimental data would require more extensive studies of the optimal scale choices for the calculation.

Before proceeding to predictions in the fiducial region we briefly discuss the comparison between fixed-order and matched predictions at various orders of perturbation theory. We include relevant distributions in Fig. 3.6. We show the NNLL+NLO matched distribution (blue) as a starting point of our considerations, we present also a pure NNLO result (green) and finally we include the N^{3}LL+NNLO matched result as the state-of-the-art calculation.

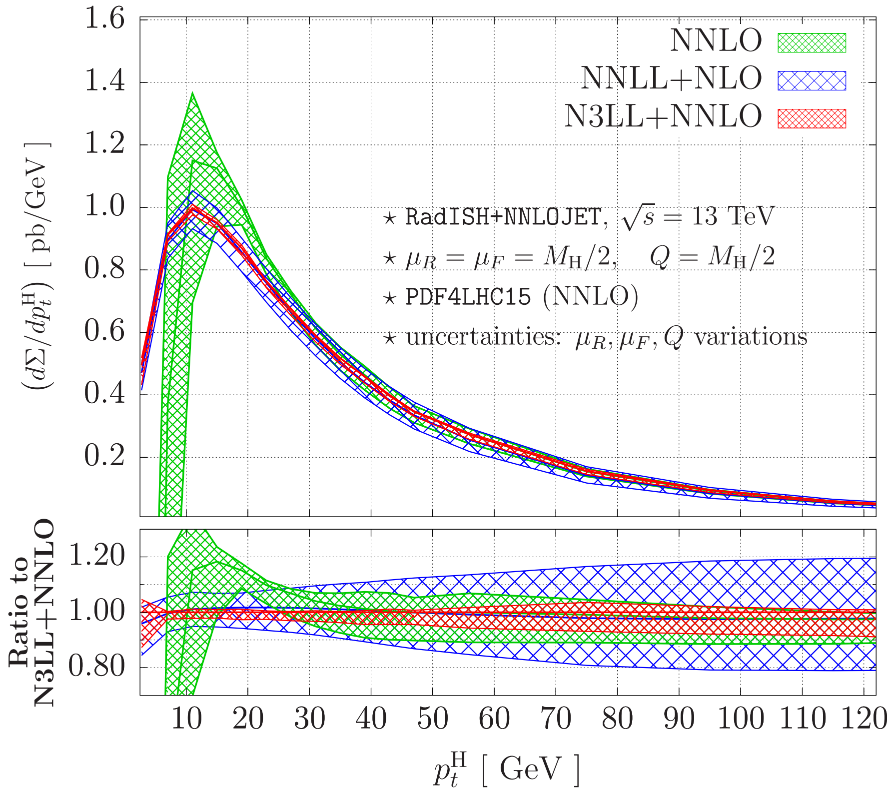

Figure 3.6: Comparison of the transverse momentum distribution for Higgs boson production between N^{3}LL+NNLO, NNLL+NLO, and NNLO at central scale choice of $\mu_R = \mu_F = M_{\mathrm{H}}/2$. The lower panel shows the ratio to the N^{3}LL+NNLO prediction.

We can immediately identify failure of the fixed-order perturbation theory in the $p_t^{\mathrm{H}} \to 0$ limit, as the green distribution diverges to negative infinity. Thanks to resummation matched distributions develop a Sudakov peak around $p_t^{\mathrm{H}} \approx 12$ GeV. We see a considerable reduction of the perturbative uncertainty when moving from the NNLL+NLO prediction to the N^{3}LL+NNLO one. Lastly, as expected in the high-p_t^{H} end of the distribution the matched N^{3}LL+NNLO uncertainty is similar to the one of the NNLO curve.

The experimental measurements are performed within a fiducial phase-space volume which is designed to follow the geometry of the detector as well as optimise the signal-to-background ratio by minimising the impact of events mimicking the signal but originating from other background processes. It is therefore desirable to provide predictions that match the experimental setup and can be directly compared to the data without relying on the modelling of the acceptances. We now focus on the Higgs boson production with its subsequent decay into pair of photons,

$$pp \longrightarrow \mathrm{H} \longrightarrow \gamma\gamma, \tag{3.96}$$

and in particular we consider a distribution of the transverse momentum of the $\gamma\gamma$ system. We work in the narrow-width approximation, i.e. the intermediate Higgs boson is considered to be an on-shell particle. We note that the $\mathrm{H} \to \gamma\gamma$ channel is not the dominant decay mode of the Higgs boson, with a branching ratio of only 2.35×10^{-3}, but the resulting photons can be accurately measured and used for the Higgs boson reconstruction.

The fiducial volume is defined by the set of cuts inspired by the setup used by the ATLAS collaboration [149]

$$\begin{gathered}\min(p_t^{\gamma_1}, p_t^{\gamma_2}) > 31.25 \text{ GeV}, \qquad \max(p_t^{\gamma_1}, p_t^{\gamma_2}) > 43.75 \text{ GeV}, \\ 0 < |\eta^{\gamma_{1,2}}| < 1.37 \ \text{ or } \ 1.52 < |\eta^{\gamma_{1,2}}| < 2.37, \qquad |Y_{\gamma\gamma}| < 2.37\,, \end{gathered} \tag{3.97}$$

where the $p_t^{\gamma_i}$ are the transverse momenta of the two photons, $i = 1, 2$, and η^{γ_i} are their pseudo-rapidities in the centre-of-mass frame. $Y_{\gamma\gamma}$ being the photon-pair rapidity. We note that in our implementation we do not consider the photon-isolation cuts, as these would introduce additional logarithmic structures and consequently spoil the formal N^{3}LL+NNLO accuracy of the final prediction. Such structures are known as non-global logarithms (NGL) and are a result of the observable being sensitive to emissions in only a part of the phase space, i.e. no emissions close to the photon in our case. NGL are a well-known problem which has been studied in many contexts [150, 151] but in our case photon-isolation criteria are not very stringent and their impact can be safely studied in the fixed-order approach.

In Fig. 3.7 we show the transverse momentum distribution of the $\gamma\gamma$ system, we perform a comparison of the matched distribution and the fixed-order one at various perturbative orders, i.e. N^{3}LL+NLO vs. NLO in the left panel and N^{3}LL+NNLO vs. NNLO in the right one. We observe a substantial reduction of the scale uncertainty in the large-$p_t^{\gamma\gamma}$ part of the spectrum when moving from the NLO accurate prediction to the NNLO one for both the purely fixed-order distribution as well as the matched one. We reiterate that a reduction of the uncertainty of the matched prediction for the moderate values

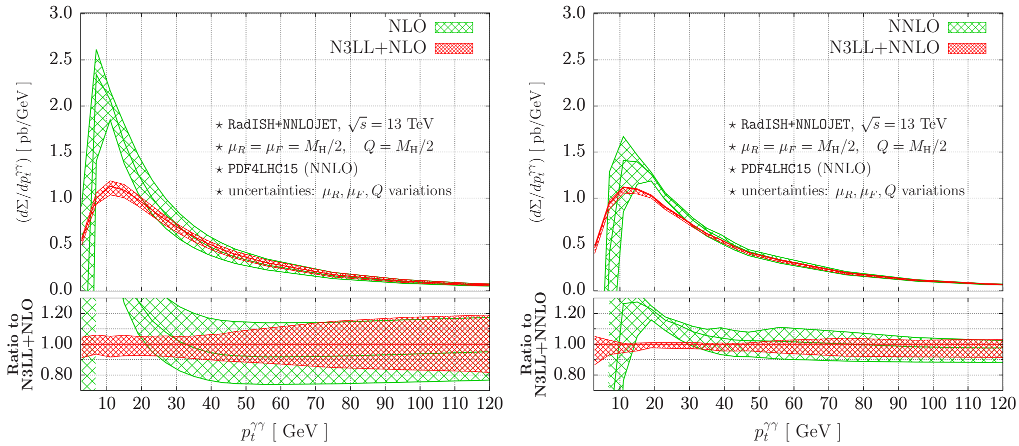

Figure 3.7: Comparison of the transverse momentum distribution for Higgs boson production at $\sqrt{s} = 13$ TeV in the fiducial volume defined by Eq. (3.97) at N^{3}LL+NLO and NLO (left) and N^{3}LL+NNLO and NNLO (right). The lower panel shows the ratio to the matched prediction.

of the transverse momenta can be, at least partially, attributed to the aforementioned cancellations in the scale variation for the adopted central-scale choice, $\mu_R = \mu_F = M_H/2$.

In order to improve on the predictions for the Higgs transverse momentum distribution one should consider other effects which might be comparable in size with the uncertainty of the N^{3}LL+NNLO prediction. One of such effects can be attributed to the impact of other heavy quarks, particularly to the effects induced by massive bottom quarks. Recent studies of the top-bottom interference reported in Refs. [152, 153] suggest that it can lead to distortions of the transverse-momentum spectrum that are as large as $\sim 5\%$ with respect to the HEFT approximation, and the theory uncertainty associated with this contribution being of $\mathcal{O}(20\%)$.

We have demonstrated that currently available predictions, resulting from combination of the fixed-order calculations and the resummation techniques, are under a good control and provide prediction with a few percent scale uncertainty. It is now possible to include fiducial cuts also in the resummed predictions and the final matched result can be directly compared with the experimental data following its release. Such comparisons will not only put the current theoretical predictions under the pressure [153] but might also provide a window into the physics beyond the Standard Model [154, 155].

3.3.2 The p_t^{Z} and ϕ_η^* distributions in Drell-Yan production

One of the most important processes studied at hadron colliders is the Drell-Yan pair production where an colourless vector boson is produced and then decays into a pair of particles. In our analysis we study the case of neutral Drell-Yan process followed by a decay of the Z/γ^* vector boson into a pair of charged leptons, i.e.

$$pp \longrightarrow Z/\gamma^* \longrightarrow \ell^+\ell^-. \tag{3.98}$$

A relatively large cross section combined with a clear detection of charged leptons in the particle detectors provide an excellent setup for studying precision observables [156, 125].

In our analysis we consider 8 TeV proton-proton collisions and study the differential distributions of the transverse momentum of the Drell-Yan pair (p_t^{Z}), as well as the angular observable ϕ_η^* which is defined as

$$\phi_\eta^* \equiv \tan\left(\frac{\phi_{\mathrm{acop}}}{2}\right)\cdot\sin\left(\theta_\eta^*\right), \tag{3.99}$$

where ϕ_{acop} is the acoplanarity angle, $\phi_{\mathrm{acop}} = \pi - \Delta\phi$, with $\Delta\phi$ being the azimuthal angle between the two leptons in the lab frame, with beam direction aligned with the z axis of the reference frame, and the θ_η^* is given by

$$\cos\left(\theta_\eta^*\right) \equiv \tanh\left(\frac{\eta^{\ell^-}-\eta^{\ell^+}}{2}\right), \tag{3.100}$$

where $\eta^{\ell^\pm}$ are the rapidities of the positively and negatively charged leptons respectively.

In the simulation we use `NNPDF3.0` parton densities and similarly to the Higgs boson production case we set $p = 4$ in the modified logarithms prescription of Eq. (3.73).

Given that the invariant masses of produced colour singlets populate a relatively large window around the Z boson mass it may be desirable to dynamically assign renormalisation and factorisation scales on an event-by-event basis. We set the central-scales to $\mu_R = \mu_F = M_T = \sqrt{M_{\ell\ell}{}^2 + p_t^2}$, where $M_{\ell\ell}$ is the invariant mass of the lepton pair and p_t is their transverse momentum. Analogously, we use a dynamical resummation scale and pick $Q = M_{\ell\ell}/2$, i.e. $x_{\mathrm{Q}} = 1/2$, for the central choice. The uncertainty band is estimated in the same way as in case of the Higgs boson production in Section 3.3.1.

The definition of the fiducial phase-space volume follows the one of the measurement performed by ATLAS collaboration reported in Ref. [137]. We require

$$p_t^{\ell^\pm} > 20 \text{ GeV}, \quad |\eta^{\ell^\pm}| < 2.4, \quad |Y_{\ell\ell}| < 2.4, \quad 46 \text{ GeV} < M_{\ell\ell} < 150 \text{ GeV}, \tag{3.101}$$

where $p_t^{\ell^\pm}$ are the transverse momenta of the two leptons, $\eta^{\ell^\pm}$ are their pseudo-rapidities, while $Y_{\ell\ell}$ and $M_{\ell\ell}$ are the rapidity and invariant mass of the dilepton system, respectively. All rapidities and pseudo-rapidities are measured in the hadronic centre-of-mass frame. Furthermore, thanks to a wealth of available data, we consider three different lepton-pair invariant-mass windows:

$$\begin{aligned}
&\star \text{ low invariant mass}: && 46 \text{ GeV} < M_{\ell\ell} < 66 \text{ GeV}, \\
&\star \text{ medium invariant mass}: && 66 \text{ GeV} < M_{\ell\ell} < 116 \text{ GeV}, \\
&\star \text{ high invariant mass}: && 116 \text{ GeV} < M_{\ell\ell} < 150 \text{ GeV}.
\end{aligned} \tag{3.102}$$

The results for the p_t^Z and ϕ_η^* distributions are shown in the remaining part of this section. All plots have the same pattern: the main panels display the comparison of normalised differential distributions at NNLO (green), NNLL+NNLO (blue), and N^{3}LL+NNLO (red), overlaid on the ATLAS data points (black). Correspondingly, the lower insets of each panel show the ratio of the theoretical curves to data, with the same colour code as in the main panels.

We start by showing the normalised p_t^Z distributions in Fig. 3.8. The three panels correspond to the low, medium, and high invariant-mass windows described in Eq. (3.102). First of all we note that the matched N^{3}LL+NNLO prediction and the fixed-order NNLO one are comparable with each other down to intermediate values of the transverse momentum, $p_t^Z <$ 10-15 GeV, while for the region $p_t^Z > 20$ GeV the NNLO prediction alone is sufficient for a detailed comparison with the experimental data. Following that, we discuss a comparison of matched predictions at different orders of perturbation theory. We remark that the best N^{3}LL+NNLO prediction shows a sizeable reduction of the theoretical uncertainty for the low and medium values of p_t^Z in all considered invariant-mass windows. The leftover uncertainty at very low transverse momenta region, where the prediction is dominated by resummation effects, is reduced to a level of 3-5% and is almost comparable

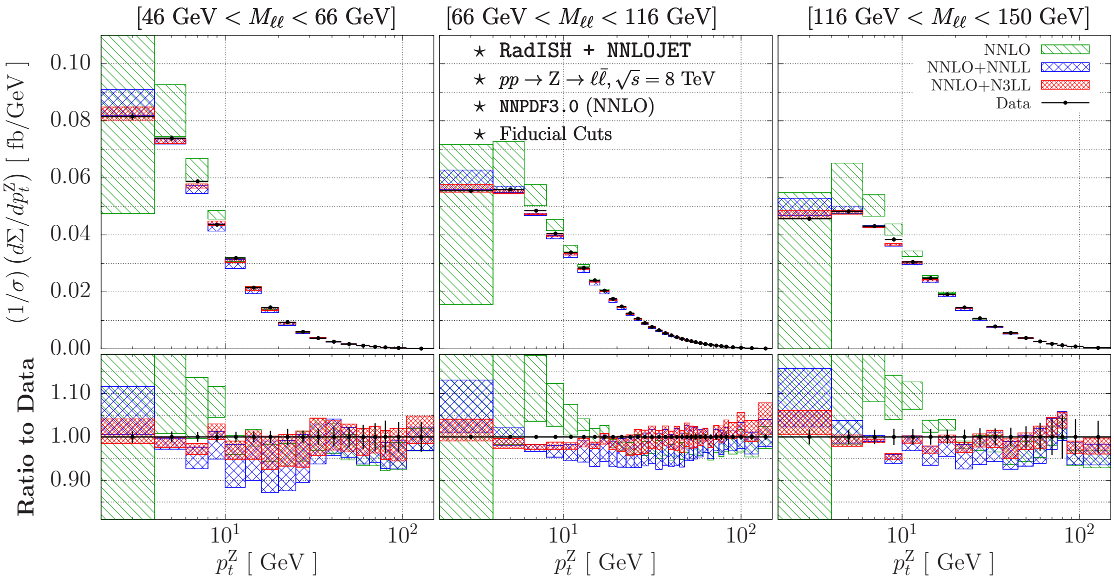

Figure 3.8: Comparison of the normalised transverse momentum distribution for Drell-Yan pair production at NNLO (green), NNLL+NNLO (blue) and N^{3}LL+NNLO (red) at $\sqrt{s} = 8$ TeV integrated over the full lepton-pair rapidity range ($0 < |Y_{\ell\ell}| < 2.4$), in three different lepton-pair invariant-mass windows. For reference, the ATLAS data is also shown, and the lower panel shows the ratio of each prediction to data.

with outstanding experimental precision. The N^{3}LL+NNLO matched prediction is in much better agreement with the data than the NNLL+NNLO one.

In Fig. 3.9, we display the normalised ϕ^*_η distributions obtained for three different lepton-pair invariant-mass windows described in Eq. (3.102). The conclusions that can be drawn from presented results are qualitatively similar to the ones discussed in connection to the p_t^Z distribution cases. Resummation effects are increasingly more important in the region $\phi^*_\eta < 0.2$; the shape of the N^{3}LL+NNLO predictions is distorted with respect to the NNLL+NLO one in the similar way as in case of the p_t^Z calculation. However, at variance with the p_t^Z case the N^{3}LL+NNLO prediction for ϕ^*_η describes data appropriately only in the central and high invariant-mass windows, while in the low invariant-mass window it undershoots the data in the medium-hard region by up to 10%. This tension was already observed in the fixed-order NNLO comparison [135]. With the exception of this, given the large statistical uncertainty of the experimental measurement in this region as well as statistical fluctuations of the theoretical prediction, we can say that the two are in reasonable agreement. Finally we note that, likewise the p_t^Z case, the N^{3}LL+NNLO prediction is favoured over the NNLL+NNLO one by the experimental

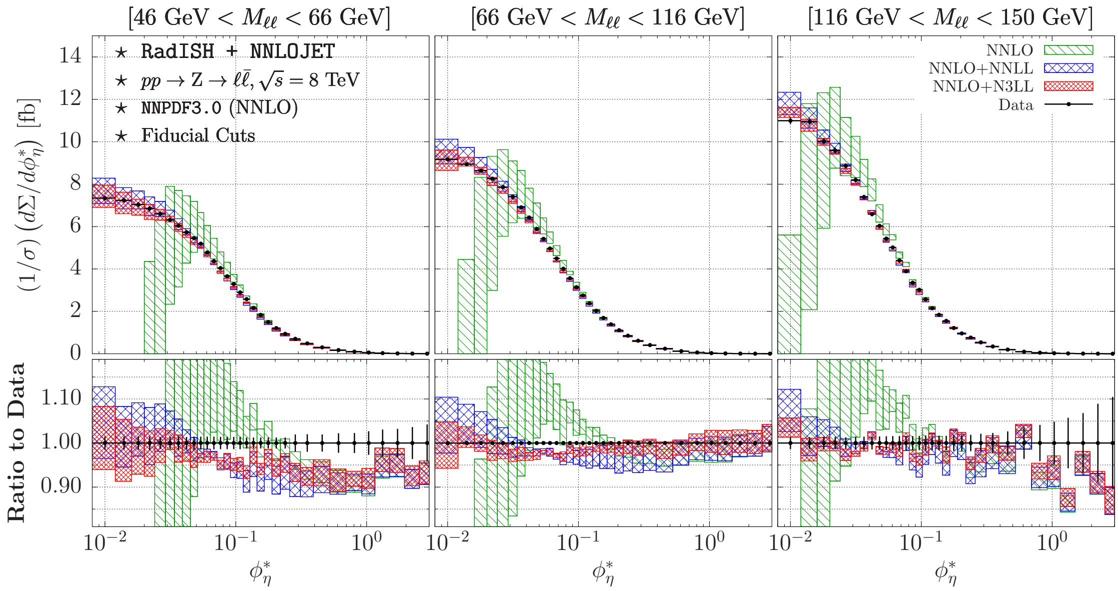

Figure 3.9: Comparison of the normalised ϕ^*_η distribution for Drell-Yan pair production at NNLO (green), NNLL+NNLO (blue) and N^{3}LL+NNLO (red) at $\sqrt{s} = 8$ TeV integrated over the full lepton-pair rapidity range ($0 < |Y_{\ell\ell}| < 2.4$), in three different lepton-pair invariant-mass windows. For reference, the ATLAS data is also shown, and the lower panel shows the ratio of each prediction to data.

data across the whole ϕ^*_η spectrum, especially in the low ϕ^*_η region.

Improving over the N^{3}LL+NNLO matched prediction will be of phenomenological interest, but given the level of perturbative uncertainty it might pose a more involved task. At this level of precision it will be necessary to incorporate QED corrections in the vicinity of the small p_t^Z and ϕ^*_η values as well as to provide an estimate of the impact of non-perturbative effects that could be as large as a few percent in this region. Moreover, a comparable few-percent effect may be generated by the inclusion of quark masses [157, 158], and more precise studies are needed in order to precisely quantify their influence. A non-negligible impact of such effects on observables of current phenomenological interest, such as the determination of the W-boson mass [159], has been recently reported in some analyses [158].

The study of the Drell-Yan pair production is a vital part of the research program at hadron colliders. The experimental precision of the measurements of transverse observables reaches unprecedented levels and has to be accompanied by theoretical predictions of similar quality in order to facilitate efficient comparison. Studies, like the one presented in this section, will be essential for improving models of vector boson production and the extraction of parton distribution functions; but might also become a valuable tool in searching for deviations from the Standard model predictions.

4
Matching NNLO + PS

In this section we will present a method of matching the NNLO accurate predictions to a parton shower (PS) using `POWHEG-BOX` generator equipped with `MiNLO`. We briefly summarise the `MiNLO` method of merging various jet multiplicities without a merging scale. We then explain the requirements that should be satisfied in order to retain NLO accuracy for 0-jet and 1-jet inclusive observables and further we elucidate the extra ingredients to achieve an NNLO+PS matching. We apply this technique in the context of the associated Higgs production (VH), validate our results and provide a short phenomenological study.

4.1 The associated Higgs production

The associated Higgs production, also known as the Higgsstrahlung process, is one of the Higgs boson production modes, in which the Higgs particle is created alongside a massive electroweak gauge boson, W or Z. Although being only the third largest production channel the presence of an electroweak vector boson makes it a promising channel to explore, as the vector boson may decay into leptons and these can serve as ideal triggers for an event to be classified as VH production.

It provides a unique opportunity of getting an insight into VVH couplings which are entirely fixed by the gauge symmetry of the SM but may be modified by some New Physics contributions. Moreover, as it has been suggested in Ref. [160], the LHC might be able to capture the decay of the Higgs boson into a pair of b-quarks and eventually measuring the bottom quark Yukawa coupling. Some first results regarding this channel have been already reported [161, 162, 163, 164].

We have three different subprocesses that fall into this class HZ, HW^+ and HW^-. All of them have been thoroughly studied in the past. Currently, the NNLO QCD corrections are known at the level of inclusive cross section [165] as well as in a fully differential manner [166, 167, 168]. The NLO electroweak (EW) corrections were obtained in Refs. [169, 170]. The NLO QCD calculations have been matched to partons shower in Refs. [171, 172, 173] and more recently an interplay between NLO QCD and NLO EW corrections has been studied [173]. As indicated before, the VH process is often considered in the context of studying properties of the $H \to b\bar{b}$ decay channel. The NNLO QCD corrections to the $VH(H \to b\bar{b})$ process, in the massless b-quarks approximation, have been reported in [174, 175].

4.2 Merging X and X+1jet generators using `MiNLO`

As we have already mentioned in Section 2.4.1, one of the methods of improving the predictive power of parton showers is by merging samples with different jet multiplicity. It is often achieved by introducing an additional and unphysical *merging scale* which separates regions of different jet multiplicities. In this section, we want to describe a procedure that allows for a consistent merging of different jet multiplicities without the need of a merging scale.

The *multi-scale improved NLO* (`MiNLO`) technique has been introduced in Ref. [121] as a way of assigning the renormalisation and factorization scales using the kinematics and dynamics of the process in question. Moreover, in order to account for all large double logarithmic terms that appear in a hard process with widely separated scales, the Sudakov form factors are also attached rendering a calculation finite even in the case of unresolved jet. A slight modification of the original `MiNLO` procedure, as described in Ref. [115], allows for a construction of an X+1jet generator, where X denotes a generic colour singlet, that provides an NLO accurate description of the process with an unresolved jet while maintaining the NLO accuracy also in the region with a resolved jet.

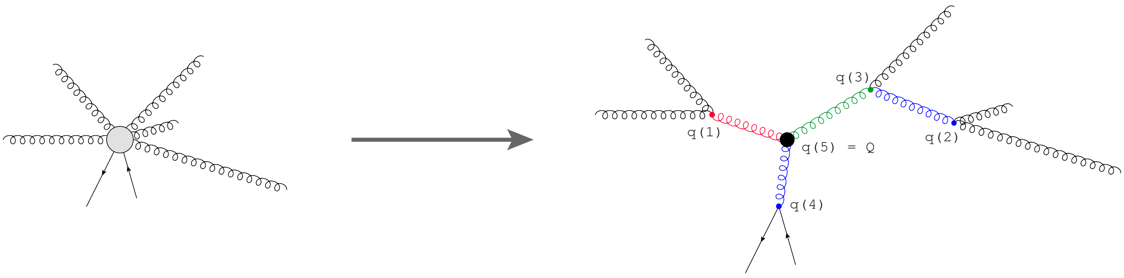

Figure 4.1: A diagram showing an example of clustering sequence described in the text. The most likely branching history is obtained using k_T-clustering algorithm. Note that all splittings require flavour-compatible branchings, i.e. $q \to (qg)$, $g \to (gg)$ or $g \to (q\bar{q})$.

4.2.1 The `MiNLO` method

In order to illustrate the way the `MiNLO` method works, let us consider a process with n coloured partons in the final state. The `POWHEG` $\bar{B}$ function of Eq. (2.24) can be schematically written as

$$\bar{B}_{\texttt{POWHEG}}(\Phi_{\rm B}) = \alpha_s^n(\mu) \times \left[{\rm B}(\Phi_{\rm B}) + \alpha_s(\mu) \left({\rm V}(\mu, \Phi_{\rm B}) + \int d\Phi_{\rm rad} {\rm R}(\Phi_{\rm R}) \right) \right], \tag{4.1}$$

where for the ease of notation we have omitted all other indices such as sum over the contributing Born and real flavour structures. We also note, that in principle the Born (B), virtual (V) and real (R) terms might involve additional m powers of the strong coupling if we are dealing with a loop-induced process, *e.g.* in case of the $gg \to {\rm H}j$ production, we have one coloured parton in final state ($n = 1$) but the Higgs effective vertex features additional two powers of the strong coupling ($m = 2$).

In order to assign a scale for each power of the strong coupling and attach Sudakov form factors to Eq. (4.1) we follow a list of steps:

1. We perform a k_T-clustering of an event in order to construct the most likely branching history (the event skeleton, see Fig. 4.1) and assign scales

$$(q_0) < q_1 < \ldots < q_n \tag{4.2}$$

to each node, as well as a scale Q to the *primary system*, i.e. after clustering the coloured partons.[1] The scale q_0 refers only to the real term in Eq. (4.1). Note

[1]Note that for the purpose of this illustration we have assumed that there are no coloured partons in the primary system, a similar procedure can be described for processes where this is not the case, *e.g.* jet production processes, etc.

that we allow for clustering of partons that are flavour compatible, i.e. $(gg) \to g$, $(qg) \to q$ and $(q\bar{q}) \to g$. For the consistency of the formulae presented below, we also denote $Q_0 = q_1$, as the lower scale entering a Sudakov form factor and $q_{n+1} = Q$ as the scale associated with the primary system.

2. We evaluate the first n powers of the strong coupling in Eq. (4.1) at the clustering scales $\mu_1, \ldots, \mu_n$, with $\mu_i = K_R q_i$, where K_R denotes the factor used for the renormalisation scale variation. The remaining m powers of the strong coupling appearing in the primary system are evaluated at the scale $\mu_Q = K_R Q$. Finally, the extra power of the strong coupling in real and virtual terms should be set to

$$\bar{\alpha}_s \equiv \frac{1}{m+n}\left(\sum_{i=1}^{n} \alpha_s(\mu_i) + m\,\alpha_s(\mu_Q)\right), \tag{4.3}$$

where we have used the bar to emphasise the distinction.

3. The renormalisation scale explicitly appearing in the virtual corrections should be assigned to

$$\mu_R = \left((\mu_Q)^m \times \prod_{i=1}^{n} \mu_i\right)^{1/(m+n)}, \tag{4.4}$$

while the factorization scale appearing in the parton density functions and the collinear subtraction terms should be taken to be equal to $\mu_F = K_F\,\mu_1$, where K_F is the factorization scale variation factor.

4. We attach a Sudakov form factor to each line of the skeleton. To each external line, ℓ, we assign a Sudakov form factor[2] $\Delta_{f(\ell)}(Q_0, q_{i(\ell)})$, where $f(\ell)$ is the flavour of the external line and $i(\ell)$ is the node to which the line is attached. To each internal line joining two nodes i and j, we attach a factor of the form $\Delta_{f(\overline{ij})}(Q_0, q_i)/\Delta_{f(\overline{ij})}(Q_0, q_j)$, where $f(\overline{ij})$ is again the flavour of the line joining nodes i and j, and we assume that $q_i > q_j$. In order to simplify the notation, an overall Sudakov form factor can be defined as

$$\mathcal{S}(q_1, \ldots, q_{n+1}) \equiv \prod_{\ell} \Delta_{f(\ell)}(Q_0, q_{i(\ell)}) \times \prod_{\overline{ij}} \frac{\Delta_{f(\overline{ij})}(Q_0, q_i)}{\Delta_{f(\overline{ij})}(Q_0, q_j)}, \tag{4.5}$$

[2]Note that, in contrast to the notation used in Section 2.4.2, we only mark the lower and upper scales as the arguments of the Sudakov form factor as well as the flavour of the corresponding line, $\Delta_{\text{flav.}}(Q_{\text{low}}, Q_{\text{high}})$.

where the index ℓ runs over all external lines of the skeleton while index $\overline{ij}$ denotes all internal connections, minding that $q_i > q_j$.

5. Finally, the MiNLO-version of the Eq. (4.1) becomes

$$\bar{B}_{\texttt{MiNLO}} = \prod_{i=1}^{n} \alpha_s(\mu_i)\, \mathcal{S}(q_1, \ldots, q_{n+1}) \times \\ \left[\mathrm{B}\cdot\Big(1 - \bar{\alpha}_s\, \mathcal{S}^{(1)}(q_1, \ldots, q_{n+1})\Big) + \bar{\alpha}_s \left[\mathrm{V}(Q) + \mathrm{B}\cdot\beta_0 \log\left(\frac{\mu_R}{Q}\right)\right] + \int d\Phi_{\mathrm{rad}} \mathrm{R} \right], \tag{4.6}$$

where, for simplicity of the notation, we have omitted the phase space arguments Φ_{B}, the $\mathcal{S}^{(1)}$ term denotes the $\mathcal{O}(\alpha_s)$ term of the overall Sudakov form factor expansion,

$$\mathcal{S}^{(1)}(q_1, \ldots, q_{n+1}) = \prod_{\ell} \Delta^{(1)}_{f(\ell)}(Q_0, q_{i(\ell)}) + \prod_{\overline{ij}} \Big(\Delta^{(1)}_{f(\overline{ij})}(Q_0, q_i) - \Delta^{(1)}_{f(\overline{ij})}(Q_0, q_j)\Big)\,, \tag{4.7}$$

that should be removed in order to maintain the the correctness of the $\mathcal{O}(\alpha_s)$ NLO terms. The renormalisation scale of the virtual corrections has been fixed to the one defined in Eq. (4.4) by adding a term $\mathrm{B}\cdot\beta_0 \log(\mu_R/Q)$ to the virtual correction term.

The MiNLO method, yielding the formula in Eq. (4.6), allows to obtain finite results even if the radiation beyond the primary system is integrated inclusively. This provides a merging prescription without specifying a merging scale. A natural question that arises is about the accuracy of the merged MiNLO generator, which we will address in the next section.

4.2.2 The MiNLO accuracy

In this section we will consider an event generator producing a sample of X+1jet events (XJ-MiNLO), with X being a generic colour singlet. We can apply the MiNLO method, detailed in Section 4.2.1, considering X as the primary system. To clarify our notation we will refer to the accuracy of the inclusive X results, with the extra jet integrated out, as (0)-accuracy, while the accuracy of the results for the cross section of the X+1jet process will be cited as (1)-accuracy.

In the case of XJ-MiNLO generator we have one coloured parton in the final state, hence the MiNLO procedure will result in one merging scale which is equal to the transverse momentum of the colour singlet, $q_1 = q_T$, and the primary scale is taken to be the invariant mass of the colour singlet, $Q = M_{\mathrm{X}}$. Hence, according to Eqs. (4.5) and (4.7) we obtain

$$\mathcal{S}(q_T, Q) = \Delta_f^2(q_T, M_{\mathrm{X}}), \qquad \text{and} \qquad \mathcal{S}^{(1)}(q_T, Q) = 2\Delta_f^{(1)}(q_T, M_{\mathrm{X}}), \tag{4.8}$$

where f denotes the flavour of the coloured line, namely $f = g$ for gluon initiated processes and $f = q$ for quark-initiated ones. For simplicity we will drop the flavour index whenever it is unambiguous. The $\bar{B}_{\mathtt{MiNLO}}$ function for the X+1jet production reads

$$\begin{aligned}\bar{B}_{\mathtt{XJ\text{-}MiNLO}} = \alpha_s(q_T)\Delta^2\left(q_T, M_{\mathrm{X}}\right)\Bigg[&\mathrm{B}_{\mathtt{XJ}}\left(1 - 2\bar{\alpha}_s\Delta^{(1)}\left(q_T, M_{\mathrm{X}}\right)\right)\\ &+ \bar{\alpha}_s\left[\mathrm{V}_{\mathtt{XJ}}(M_{\mathrm{X}}) + \mathrm{B}_{\mathtt{XJ}}\cdot\beta_0\log\left(\frac{\mu_R}{M_{\mathrm{X}}}\right)\right] + \int d\Phi_{\mathrm{rad}}\mathrm{R}_{\mathtt{XJ}}\Bigg],\end{aligned} \tag{4.9}$$

which yields the NLO$^{(1)}$ accuracy as we have subtracted the spurious terms proportional to $\bar{\alpha}_s\Delta^{(1)}\left(q_T, M_{\mathrm{X}}\right)$, introduced by the Sudakov form factor. In order to asses the (0)-accuracy of the XJ-MiNLO generator, we need to consider two types of contributions. First of all, the terms which are regular in the limit $q_T \to 0$ will be controlled by the $\mathrm{B}_{\mathtt{XJ}}$ matrix element, as the XJ-MiNLO generator is LO$^{(1)}$ accurate. The second type of contributions consists of terms which are singular in the $q_T \to 0$ limit. These are encoded in the all-order Sudakov form factor; we simply need to make sure that the expressions which are implemented are of high-enough logarithmic accuracy which we will explore in the following part.

So far we have not discussed the accuracy of the Sudakov radiator $\Delta(q_T, M_{\mathrm{X}})$ in detail, using the Eq. (2.21) as a silent assumption. However, if we want to improve the accuracy of the XJ-MiNLO generator we may need to use more accurate expressions for the Sudakov radiator which contains higher-order logarithmic terms. In Chapter 3, we have already introduced radiator including effects up to N^{3}LL order valid for the transverse momentum resummation of the colour singlet. Therefore, similarly to the discussion in Section 3.1.7 (around the Eq. (3.64) in particular), we can write

$$\Delta_f^2(q_T, M_{\mathrm{X}}) \equiv \exp\left\{-\int_{q_T^2}^{M_{\mathrm{X}}^2}\frac{dq^2}{q^2}\left[\mathcal{A}_f(\alpha_s(q^2))\log\left(\frac{M_{\mathrm{X}}^2}{q^2}\right) + \mathcal{B}_f(\alpha_s(q^2))\right]\right\}, \tag{4.10}$$

with $\mathcal{A}_f$ and $\mathcal{B}_f$ admitting the perturbative series expansion in powers of the strong coupling

$$\mathcal{A}_f(\alpha_s) = \sum_{i=1}^{2} \left(\frac{\alpha_s}{2\pi}\right)^n \mathcal{A}_f^{(n)}, \qquad \text{and} \qquad \mathcal{B}_f(\alpha_s) = \sum_{i=1}^{2} \left(\frac{\alpha_s}{2\pi}\right)^n \mathcal{B}_f^{(n)}, \tag{4.11}$$

where we have truncated the series at $\mathcal{O}(\alpha_s^2)$ terms.

We consider the integration of the Eq. (4.9) over the whole q_T spectrum. For this purpose we consider the following integral

$$\int_{\Lambda_{\mathrm{QCD}}^2}^{M_{\mathrm{X}}^2} \frac{dq_T^2}{q_T^2} \log^M \left(\frac{M_{\mathrm{X}}^2}{q_T^2}\right) \alpha_s^{N+1}(q_T)\, \Delta^2(q_T, Q) \approx \left[\alpha_s\left(M_{\mathrm{X}}^2\right)\right]^{N+1-\frac{M+1}{2}}, \tag{4.12}$$

where M and N are integers and we have used the fact that the dominant term in the Sudakov scales as $\alpha_s \log^2\left(M_{\mathrm{X}}^2/q_T^2\right)$. Therefore, in order to achieve the $\mathrm{NLO}^{(0)}$ accuracy, i.e. the right hand side of Eq. (4.12) should scale as $\mathcal{O}(\alpha_s^2)$, we need to have control over terms with $2N-3 < M < 2N$. This means that we need to include correct anomalous dimensions up to and including $\mathcal{B}_f^{(2)}$ term. Moreover, the renormalisation scale that explicitly enters the virtual corrections should be set to q_T and the similar choice is necessary when evaluating the strong coupling value that enters with the virtual and real corrections, i.e. $\bar{\alpha}_s = \alpha_s(q_T)$ in Eq. (4.9).

The anomalous-dimension coefficients $\mathcal{A}_f^{(1)}$, $\mathcal{A}_f^{(2)}$ and $\mathcal{B}_f^{(1)}$ can be read from the formulae in Appendix A.2:

$$\begin{aligned}
&\mathcal{A}_q^{(1)} = A_{\mathrm{DY}}^{(1)}, \qquad \mathcal{A}_q^{(2)} = A_{\mathrm{DY}}^{(2)}, \qquad \mathcal{B}_q^{(1)} = B_{\mathrm{DY}}^{(1)}, \\
&\mathcal{A}_g^{(1)} = A_{\mathrm{ggH}}^{(1)}, \qquad \mathcal{A}_g^{(2)} = A_{\mathrm{ggH}}^{(2)}, \qquad \mathcal{B}_g^{(1)} = B_{\mathrm{ggH}}^{(1)},
\end{aligned} \tag{4.13}$$

using Eqs. (A.19) and (A.20), for the Higgs and the Drell-yan production respectively. The coefficient $\mathcal{B}_f^{(2)}$ will be process dependent, as it has to carry information about the non-singular virtual corrections to the underlying X-production process that originate from the $\mathcal{O}(\alpha_s)$ part of the hard function entering the resummed formula. For that reason we need to slightly modify the formulae in Appendix A.2 in order to be used in the `XJ-MiNLO` implementation, i.e.

$$\begin{aligned}
\mathcal{B}_g^{(2)} &= B_{\mathrm{ggH}}^{(2)} + 2\left(A_{\mathrm{ggH}}^{(1)}\right)^2 \zeta_3 + 2\pi\beta_0\, H_{\mathrm{ggH}}^{(1)}\left(M_{\mathrm{X}}\right), \\
\mathcal{B}_q^{(2)} &= B_{\mathrm{DY}}^{(2)} + 2\left(A_{\mathrm{DY}}^{(1)}\right)^2 \zeta_3 + 2\pi\beta_0\, H_{\mathrm{DY}}^{(1)}\left(M_{\mathrm{X}}\right),
\end{aligned} \tag{4.14}$$

where β_0 has been defined in Eq. (A.8) while the hard functions can be read from Eqs. (A.22) and (A.23).

As a result, the `XJ-MiNLO` generator provides an NLO accurate description of the observables referring to X+1jet process, with an unresolved jet in the final state, as well as an NLO accurate description of the observables which are inclusive over the extra radiation. Such a procedure has been successfully implemented for many processes, starting with the `ZJ`, `WJ` and `HJ` in Ref. [115] and followed by the `HWJ/HZJ` associated Higgs production in Ref. [173]. The technique proved to be functional also in case of processes that require slightly more involved treatment, like the `WWJ` production in Ref. [176] where the one-loop virtual correction to the $pp \to \mathrm{WW}$ depends on the phase space point. Moreover, a reliable treatment of the processes with a coloured parton in the primary system has been presented for the `HJJ` in Ref. [177] or more recently for the single-top plus jet production in Ref. [178].

4.3 Outline of the NNLO+PS reweighting

At this stage we have a `MiNLO` event sample for colour singlet production X at our disposal. As explained in the previous section the `XJ-MiNLO` computation is accurate at NLO for both X inclusive observables as well as X+1jet observables. It seems natural to ask a question how can we upgrade the `XJ-MiNLO` generator up to the NNLO accuracy for 0-jet observables while maintaining current accuracy for 1-jet and 2-jet observables. Such method has been first proposed in Ref. [115] and subsequently implemented for Higgs boson production in gluon-gluon fusion in Ref. [179] as well as for Drell-Yan production in Ref. [180]. In this section we will outline a general framework for achieving NNLO+PS accurate predictions using `MiNLO` approach, while in the following sections we will focus of its application to the associated Higgs production process, i.e. HZ and HW production.

The procedure of achieving the NNLO+PS accuracy we use is based on reweighting Les Houches event sample obtained with `XJ-MiNLO` generator. Such a sample consists of entries which are records containing information about all initial-state and final-state particles involved in a hadronic collision. In our case this list spans over the initial-state partons, a colourless state X (possibly alongside its decay products) and one or two additional final-state partons. The first of the two final-state partons is present simply because we are considering a generator for X+1jet state while the second one, if present, is a result of an emissions corresponding to real correction that is a part of an NLO accurate calculation. In an event sample, the phase space points are selected according to a distribution which reflects the quantum-mechanical squared amplitude. The real emission is generated with a probability given by the Sudakov form factor. As such, records in an event sample are probed with a similar frequency as they would arise in nature, i.e. real experiment.

We can analyse the `XJ-MiNLO` event sample to obtain a distribution of any desired observable, in particular we can construct a multi-differential distribution

$$\frac{d\sigma^{\texttt{MiNLO}}}{d\Phi_{\mathrm{B}}} = C_0(\Phi_{\mathrm{B}}) + \alpha_s C_1(\Phi_{\mathrm{B}}) + \alpha_s^2 \widetilde{C}_2(\Phi_{\mathrm{B}}) + \mathcal{O}(\alpha_s^3), \tag{4.15}$$

where Φ_{B} spans the whole Born phase space for the production (and decay) of colourless system X, and C_i are coefficients which are functions of the underlying phase space Φ_{B}. We explicitly denote higher order terms which are present in the `MiNLO` generator due to all-order resummation which is constraining real emissions.

We will also need a similar multi-differential distribution obtained by using a pure NNLO calculation, which we will denote by

$$\frac{d\sigma^{\texttt{NNLO}}}{d\Phi_{\mathrm{B}}} = C_0(\Phi_{\mathrm{B}}) + \alpha_s C_1(\Phi_{\mathrm{B}}) + \alpha_s^2 C_2(\Phi_{\mathrm{B}}). \tag{4.16}$$

Note that in this case coefficients $C_{1,2}$ are exactly the same as in Eq. (4.15), thanks to the arguments laid out in Section 4.2. There is however a discrepancy at the level of $\mathcal{O}(\alpha_s^2)$ coefficient, which we intend to eliminate in our final result.

We can now rescale weights of all events in our sample by a factor $\mathcal{W}$ which is simply a ratio of Eqs. (4.16) and (4.15), and reads

$$\mathcal{W}(\Phi_{\mathrm{B}}) \equiv \frac{\left(\frac{d\sigma^{\texttt{NNLO}}}{d\Phi_{\mathrm{B}}}\right)}{\left(\frac{d\sigma^{\texttt{MiNLO}}}{d\Phi_{\mathrm{B}}}\right)} = \frac{C_0 + \alpha_s C_1 + \alpha_s^2 \widetilde{C}_2 + \mathcal{O}(\alpha_s^3)}{C_0 + \alpha_s C_1 + \alpha_s^2 C_2} = 1 + \left(\frac{C_2 - \widetilde{C}_2}{C_0}\right)\alpha_s^2 + \ldots. \tag{4.17}$$

We can immediately see that $\mathcal{W}$ is equal to one up to the $\mathcal{O}(\alpha_s^2)$ terms, which implies that such a rescaling does not break the NLO$^{(1)}$ accuracy of the `XJ-MiNLO` generator. We also notice that the reweighted multi-differential distribution

$$\frac{d\sigma^{\texttt{MiNNLO}}}{d\Phi_{\mathrm{B}}} \equiv \frac{d\sigma^{\texttt{MiNLO}}}{d\Phi_{\mathrm{B}}} \times \mathcal{W}(\Phi_{\mathrm{B}}) \tag{4.18}$$

is now, by construction, equal to $d\sigma^{\texttt{NNLO}}/d\Phi_{\mathrm{B}}$ and hence our XJ-MiNLO generator gains NNLO$^{(0)}$ accuracy.

The question that remains is about the (0)-accuracy of observables which are not used in the parametrisation of the underlying phase space and hence not used for reweighting. For resolving this issue, we can use a generic observable F which is a function of the Born kinematics and may even include some fiducial cuts, we only require that it is IRC safe. The expectation value of such an observable can naturally be computed as

$$\langle F\rangle = \frac{1}{\mathrm{Vol}(\Phi)}\int d\Phi\, F(\Phi)\,\frac{d\sigma}{d\Phi}, \tag{4.19}$$

where by Φ we denote a full phase space of XJ-MiNLO events, i.e. volume spanned by Born momenta and real emission. We can now investigate a behaviour of function F in the soft and/or collinear limit for real emissions. We know that for each point in real-kinematics phase space there exist an underlying configuration in Born phase space. If we probe soft and/or collinear limit of real emissions we will find that there exist a limit of such procedure, i.e. a point in Born phase space

$$\Phi \ni x^{(1)} \xrightarrow[\text{soft and/or collinear}]{} x^{(0)} \in \Phi_{\mathrm{B}}. \tag{4.20}$$

Using the IRC safety we can deduce that also F has a smooth limit

$$F(\Phi) \xrightarrow[\Phi\longrightarrow\Phi_{\mathrm{B}}]{} F_B(\Phi_{\mathrm{B}}), \tag{4.21}$$

where we again use a similar limiting procedure and F_B is a value of the observable F computed using underlying Born kinematics. Furthermore, we split observable F into two parts

$$\begin{aligned} F(\Phi) &= F_B(\Phi_{\mathrm{B}}) + [F(\Phi) - F_B(\Phi_{\mathrm{B}})] \\ &= F_B(\Phi_{\mathrm{B}}) + \delta F(\Phi), \end{aligned} \tag{4.22}$$

where F_B is the Born part computed using underlying Born kinematics, and δF is the non-Born component obtained by analysing a full real kinematics. We can compute the two parts of the observable separately. For a Born-like part we have

$$\langle F_B\rangle = \frac{1}{\mathrm{Vol}(\Phi)}\int d\Phi \left(\frac{d\sigma^{\texttt{MiNNLO}}}{d\Phi}\cdot \mathcal{W}(\Phi_{\mathrm{B}})\right) F_B(\Phi_{\mathrm{B}})$$

$$
\begin{aligned}
&= \frac{1}{\mathrm{Vol}(\Phi_{\mathrm{B}})} \int d\Phi_{\mathrm{B}} \left(\frac{d\sigma^{\texttt{MiNNLO}}}{d\Phi_{\mathrm{B}}} \cdot \mathcal{W}(\Phi_{\mathrm{B}}) \right) F_B(\Phi_{\mathrm{B}}) \\
&= \frac{1}{\mathrm{Vol}(\Phi_{\mathrm{B}})} \int d\Phi_{\mathrm{B}} \left(\frac{d\sigma^{\texttt{NNLO}}}{d\Phi_{\mathrm{B}}} \right) F_B(\Phi_{\mathrm{B}}) \\
&= f_0^{(0)} + \alpha_s f_1^{(0)} + \alpha_s^2 f_2^{(0)} + \mathcal{O}(\alpha_s^3),
\end{aligned}
\tag{4.23}
$$

which reconstructs a pure NNLO result up to $\mathcal{O}(\alpha_s^3)$ terms that are beyond the scope of our analysis. To complete our proof we just check that as F is IRC safe observable then its limit, when probing a soft and/or collinear configurations, may depend only upon the point in the underlying Φ_{B} phase space, and hence $\delta F = \mathcal{O}(\alpha_s^2)$ due to the IRC safety of the observable and its inclusive nature. In summary, we can organise these properties into a theorem:

Theorem. An `XJ-MiNLO` parton level generator that is accurate at $\mathcal{O}(\alpha_s^2)$ level for all IRC safe observables that vanish with the transverse momenta of all light partons, and that also reaches $\mathcal{O}(\alpha_s^2)$ accuracy for the variables spanning the full underlying Born phase space Φ_{B} achieves the same level of precision for all IRC safe observables, i.e. it is NNLO$^{(0)}$ accurate.

Such a construction has been already applied in the past in case of the Higgs production in gluon-gluon fusion as well as for Drell-Yan production in Refs. [179, 180] providing a very good agreement between the NNLO calculations and their `MiNNLO` counterpart, proving the method not only to be a consistent framework for achieving NNLO+PS but also one that is feasible to implement.

One of the obstacles that we face when using reweighting method related to the dimensionality of the underlying Born phase space. The more particles are present in the final state, the bigger the phase space is. Obtaining multi-differential distributions that span the full Born phase space and are of sufficient quality, even though straightforward, may be a long and tedious task. In the following section we will present some techniques that allow for practical realisation of NNLO+PS accurate generator in case of associated Higgs production. They have been successfully applied and explored in Refs. [18, 19].

Similar techniques have been utilised in a recent implementation of the WW process at the NNLO+PS accuracy in Ref. [181].

4.3.1 Variant schemes of the NNLO+PS reweighting

It may be asserted that the missing corrections which we include during reweighting originate from the missing double-virtual correction of the underlying process. Indeed, the region associated with the real correction or even double-real correction is described with a similar perturbative accuracy that the one of the fixed-order NNLO calculation, thanks to the NLO$^{(1)}$ accuracy of the `XJ-MiNLO` generator.

Therefore, it seems natural that the reweighting procedure should affect mostly the regions which are close to the underlying Born configurations and go smoothly to one when hard radiation is present. We can propose a variant of the Eq. (4.17) that satisfies this condition. For this reason, for each event we evaluate p_T of the hardest jet clustered with the k_T-algorithm and then define a function $h(p_T)$,

$$h(p_T) = \frac{(\kappa M_{\mathrm{X}})^{\sigma}}{(\kappa M_{\mathrm{X}})^{\sigma} + (p_T)^{\sigma}}, \tag{4.24}$$

where κ and σ are constant parameters. Typically used values include $\kappa = 1$ and $\sigma = 2$. Other choices are also possible and therefore we will always state the type of the smoothing function that we employ.

As a consequence, the reweighting factor $\mathcal{W}(\Phi_{\mathrm{B}})$ becomes p_T dependent and reads

$$\begin{aligned}\mathcal{W}(\Phi_{\mathrm{B}}, p_T) =& h(p_T) \cdot \frac{\int d\sigma^{\texttt{NNLO}} \delta\left(\Phi_{\mathrm{B}} - \Phi_{\mathrm{B}}(\Phi)\right) - \int d\sigma_B^{\texttt{MiNLO}} \delta\left(\Phi_{\mathrm{B}} - \Phi_{\mathrm{B}}(\Phi)\right)}{\int d\sigma_A^{\texttt{MiNLO}} \delta\left(\Phi_{\mathrm{B}} - \Phi_{\mathrm{B}}(\Phi)\right)} \\ &+ \left(1 - h(p_T)\right), \end{aligned}\tag{4.25}$$

where we have used

$$d\sigma_A = d\sigma \cdot h(p_T) \qquad \text{and} \qquad d\sigma_B = d\sigma \cdot \left(1 - h(p_T)\right), \tag{4.26}$$

and the differential refers to a fully differential cross section. This manipulation maintains all the properties that were previously outlined while concentrating the effects of the reweighting in the region close to the underlying Born phase space, as $h(p_T)$ goes to one with $p_T \to 0$, and simultaneously $h(p_T) \to 0$ when hard radiation is present.

4.3.2 Estimating uncertainties of the NNLO+PS sample

The procedure of estimating the theoretical uncertainties associated with a reweighted event sample is very similar to the standard scale variation procedure, where we independently change the renormalisation and factorization scales by a factor K_R and K_F, respectively. Usually, the variation is by a factor of two up and down while keeping $1/2 \leqslant K_R/K_F \leqslant 2$. This leads to 7 different scale choices

$$(K_R, K_F) = (0.5, 0.5),\ (0.5, 1.0),\ (1.0, 0.5),\ (1.0, 1.0),\ (2.0, 1.0),\ (1.0, 2.0),\ (2.0, 2.0).$$

Furthermore, we can now independently vary the fully differential NNLO cross section (by factors K_R and K_F) and the MiNLO cross section (using K'_R and K'_F). This leads to 49 scale variations in the final NNLO+PS accurate event sample, with the central scale set by

$$(K_R, K_F) = (K'_R, K'_F) = (1.0, 1.0). \tag{4.27}$$

We adopt such a choice in the next section concering the NNLO+PS description of the HW production. In the case of HZ production at NNLO+PS accuracy we will use a correlated scale variation, i.e. $(K_R, K_F) = (K'_R, K'_F)$.

4.4 NNLO+PS reweighting for HW process

We consider a process of the HW^+ production with a subsequent decay of the electroweak boson into lepton-neutrino pair

$$pp \longrightarrow \mathrm{HW}^+ \longrightarrow \mathrm{H}\left(\ell^+\nu_\ell\right), \tag{4.28}$$

where $\ell = \{e, \mu\}$ and all spin-correlations are taken into account; we leave the Higgs boson in the final state rather than decaying it. Throughout this section we will consider 13 TeV hadronic collisions and use the `MMHT2014nnlo68cl` parton distribution functions [182], corresponding to a value of $\alpha_s(M_\mathrm{Z}) = 0.118$. We also set $M_\mathrm{W} = 80.399$ GeV, $\Gamma_\mathrm{W} = 2.085$ GeV and $M_\mathrm{H} = 125.0$ GeV. For generating a `MiNLO` event sample we will use a publicly available code `HWJ-MiNLO` that has been prepared and studied in Ref. [173]. The fixed-order NNLO calculation, that is fully-differential, can be performed using the `HVNNLO` code presented in Ref. [166]. For `HWJ-MiNLO` computation the scale choice is dictated by the `MiNLO` procedure; for the NNLO we have used $\mu_0 = M_{\rm W} + M_{\rm H}$ for the central renormalisation and factorisation scale choice.

4.4.1 General setup: parametrisation of the HW phase space

In this case we have three final-state particles produced in a hadronic collision which implies that the Born phase space $\Phi_{\rm B}$ is fully specified by six independent variables, after neglecting an overall azimuthal angle around the beam axis. The six variables that determine a system of coordinates may be freely chosen, however a prudent choice that takes into account physical situation is advisable.

In the case at hand, we are dealing with a decay of an electroweak boson hence a convenient standard choice for three of the six variables is to select invariant mass of the dilepton system ($m_{\ell\nu}$) and two Collins-Soper angles [156] for angular distribution of leptons. To define them we consider a boost from the laboratory frame to the rest frame of the W boson (the $\mathcal{O}'$ frame). Using the positive and negative rapidity beam momenta, p'_A and p'_B respectively, we arrange a $\hat{z}$-axis in this frame such that it bisects the angle between p'_A and $-p'_B$. We then also introduce a transverse unit vector $\hat{q}_\perp$, orthogonal to the $\hat{z}$-axis and lying in the (p'_A, p'_B)-plane, pointing away from $p'_A + p'_B$. The Collins-Soper angles are the polar angle θ^* of the lepton momentum p'_ℓ in $\mathcal{O}'$-frame with respect to $\hat{z}$-axis ($\vec{p}'_\ell \cdot \hat{z} = |\vec{p}'_\ell| \cos\theta^*$) and the azimuthal angle ϕ^* of p'_ℓ measured from $\hat{q}_\perp$ axis ($\vec{p}'_\ell \cdot \hat{q}_\perp = |\vec{p}'_\ell| \sin\theta^* \cos\phi^*$). As the remaining three variables we choose the rapidity of the HW-system ($y_{\rm HW}$), the difference between the rapidity of Higgs boson and W boson ($\Delta y_{\rm HW} = y_{\rm H} - y_{\rm H}$), and finally the transverse momentum of the Higgs boson ($p_{t,\rm H}$). To summarise we have

$$\Phi_{\rm HW} = \{y_{\rm HW}, \Delta y_{\rm HW}, p_{t,\rm H}, m_{\ell\nu}, \cos\theta^*, \phi^*\}\,, \tag{4.29}$$

which given the linear independence of all six variables provides a system of coordinates defined on the underlying Born phase space $\Phi_{\rm HW}$.

Since the decay of a massive spin-one particle is at most quadratic in the lepton momentum $\vec{p}'_\ell$ in the frame $\mathcal{O}'$, we can use spherical harmonic functions $Y_{lm}(\theta^*, \phi^*)$ with $l \leqslant 2$ and $|m| \leqslant l$. This can be understood by observing that the decay of a massive spin-one article is associated with 9 degrees of freedom (the spin-density matrix describing all quantum-interference terms is a 3×3 matrix). We can choose one of the coefficients to be responsible for an overall normalisation of the cross section and leave the remaining eight independent coefficients for parametrisation of the angular dependence. We make a choice that is typical for the Drell-Yan production and write the fully-differential cross section as

$$\begin{aligned}\frac{d\sigma}{d\Phi_{\mathrm{HW}}} &= \frac{d^6\sigma}{dy_{\mathrm{HW}} d\Delta y_{\mathrm{HW}} dp_{t,\mathrm{H}} dm_{\ell\nu} d\cos\theta^* d\phi^*} \\ &= \frac{3}{16\pi}\left(\frac{d\sigma}{d\Phi_{\mathrm{HW}^\star}}\left(1+\cos^2\theta^*\right) + \sum_{i=0}^{7} A_i(\Phi_{\mathrm{HW}^\star}) f_i(\theta^*,\phi^*)\right), \end{aligned} \tag{4.30}$$

where we have introduced the four dimensional phase space $\Phi_{\mathrm{HW}^\star} = \{y_{\mathrm{HW}}, \Delta y_{\mathrm{HW}}, p_{t,\mathrm{H}}, m_{\ell\nu}\}$ that leaves out the Collins-Soper angles, since the angular dependence is now fully encoded in $f_i(\theta^*,\phi^*)$ functions. The functions themselves are suitably adapted basis of spherical harmonics

$$\begin{aligned} f_0(\theta^*,\phi^*) &= \left(1-3\cos^2\theta^*\right)/2\,, & f_1(\theta^*,\phi^*) &= \sin 2\theta^* \cos\phi^*\,, \\ f_2(\theta^*,\phi^*) &= (\sin^2\theta^* \cos 2\phi^*)/2\,, & f_3(\theta^*,\phi^*) &= \sin\theta^* \cos\phi^*\,, \\ f_4(\theta^*,\phi^*) &= \cos\theta^*\,, & f_5(\theta^*,\phi^*) &= \sin\theta^* \sin\phi^*\,, \\ f_6(\theta^*,\phi^*) &= \sin 2\theta^* \sin\phi^*\,, & f_7(\theta^*,\phi^*) &= \sin^2\theta^* \sin 2\phi^*\,. \end{aligned} \tag{4.31}$$

Their integrals vanish when an integral over the whole solid angle $d\Omega^* = d\cos\theta^* d\phi^*$ is performed, moreover thanks to the orthonormality of spherical harmonics we can calculate coefficients $A_i(\Phi_{\mathrm{HW}^\star})$ using the following projections

$$\begin{aligned} A_0(\Phi_{\mathrm{HW}^\star}) &= 4\,(d\sigma/d\Phi_{\mathrm{HW}^\star}) - \langle 10\cos^2\theta^*\rangle\,, & A_1(\Phi_{\mathrm{HW}^\star}) &= \langle 5\sin 2\theta^*\cos\phi^*\rangle\,, \\ A_2(\Phi_{\mathrm{HW}^\star}) &= \langle 10\sin^2\theta^*\cos 2\phi^*\rangle\,, & A_3(\Phi_{\mathrm{HW}^\star}) &= \langle 4\sin\theta^*\cos\phi^*\rangle\,, \\ A_4(\Phi_{\mathrm{HW}^\star}) &= \langle 4\cos\theta^*\rangle\,, & A_5(\Phi_{\mathrm{HW}^\star}) &= \langle 4\sin\theta^*\sin\phi^*\rangle\,, \\ A_6(\Phi_{\mathrm{HW}^\star}) &= \langle 5\sin 2\theta^*\sin\phi^*\rangle\,, & A_7(\Phi_{\mathrm{HW}^\star}) &= \langle 5\sin^2\theta^*\sin 2\phi^*\rangle\,, \end{aligned} \tag{4.32}$$

where the expectation values $\langle f(\theta^*,\phi^*)\rangle$ are functions of $\Phi_{\mathrm{HW}^\star}$ and are computed as

$$\langle f(\theta^*,\phi^*)\rangle = \int \frac{d\Omega^*}{4\pi}\left(\frac{d\sigma}{d\Phi_{\mathrm{HW}}}\right) f(\theta^*,\phi^*)\,. \tag{4.33}$$

Such a setup provides significant advantages over the crude numerical treatment of the angular dependence. To provide smooth and accurate reweighting it is usually sufficient to tabulate multi-differential cross sections in histograms with about 25 bins per direction of phase space. In case of Collins-Soper angles we trade 25^2 bins of the two-dimensional (θ^*, ϕ^*)-histogram for a fully analytical parametrisation that requires only 9 parameters.

The Eq. (4.30) is well-suited for implementation in a numerical code and evaluation using the Monte Carlo technique. Our goal is to obtain the two distributions

$$\frac{d\sigma^{\mathtt{NNLO}}}{d\Phi_{\mathrm{HW}}}, \qquad \text{and} \qquad \frac{d\sigma^{\mathtt{MiNLO}}}{d\Phi_{\mathrm{HW}}}, \tag{4.34}$$

that will allow us to calculate the reweighting factor $\mathcal{W}(\Phi_{\mathrm{HW}})$ for NNLO reweighting of `HWJ-MiNLO` event sample.

4.4.2 Treatment of the Breit-Wigner shape

Since the reweighting procedure relies on the quality of required differential distributions in Eq. (4.34) we would like to use our knowledge of the physical process. In the presented case we are dealing with a decay of massive electroweak vector boson, as a consequence distribution of the invariant mass of its decay products $(d\sigma/dm_{\ell\nu})$ will be described by a Breit-Wigner shape. Assuming that QCD corrections to the process in Eq. (4.28) are independent of the dilepton-system invariant mass, we can neglect this direction of the phase space in the reweighting procedure by integrating it out

$$\begin{aligned} \frac{d^3\sigma}{d(y_{\mathrm{HW}})d(\Delta y_{\mathrm{HW}})d(p_{t,\mathrm{H}})} &= \int dm_{\ell\nu}\, \frac{d\sigma}{d\Phi_{\mathrm{HW}^\star}}, \\ A_i(y_{\mathrm{HW}}, \Delta y_{\mathrm{HW}}, p_{t,\mathrm{H}}) &= \int dm_{\ell\nu}\, A_i(\Phi_{\mathrm{HW}^\star}), \end{aligned} \tag{4.35}$$

where from now on we will explicitly denote three phase-space directions $(y_{\mathrm{HW}}, \Delta y_{\mathrm{HW}}, p_{t,\mathrm{H}})$ for which differential distributions will be tabulated in 3D histograms.

Before attempting the NNLO reweighting and related phenomenological studies, we should validate the last assumption. For this purpose we consider a variable $a_{\ell\nu}$, that is defined as

$$a_{\ell\nu} = \arctan\left(\frac{m_{\ell\nu}^2 - M_{\mathrm{W}}^2}{M_{\mathrm{W}}\Gamma_{\mathrm{W}}}\right), \tag{4.36}$$

and is widely used when numerical integrals of the Breit-Wigner shapes are involved.

The distributions of both $m_{\ell\nu}$ and $a_{\ell\nu}$ are presented in Fig. 4.2, in the left and right panels respectively. We notice that the distribution $(d\sigma/da_{\ell\nu})$ is almost flat and does not

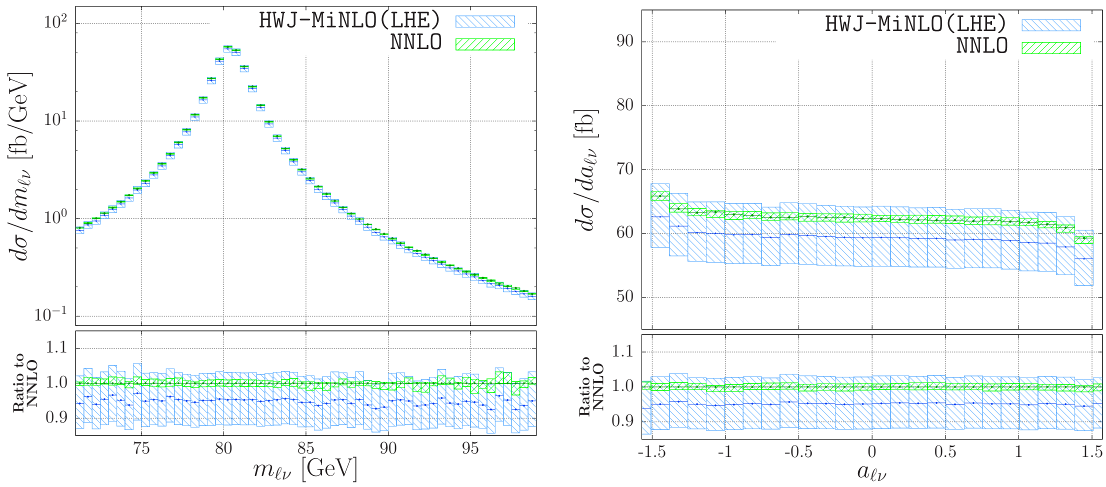

Figure 4.2: Comparison of `HWJ-MiNLO` (blue) and NNLO (green) for $m_{\ell\nu}$ (left) and $a_{\ell\nu}$ (right) defined in Eq. (4.36).

have significant peaks, contrary to $(d\sigma/dm_{\ell\nu})$. This is useful for importance sampling in Monte Carlo integration. The message that is important for validation of our assumption is the flatness of the K-factor between NNLO result and `HWJ-MiNLO` one along $m_{\ell\nu}$ (and similarly $a_{\ell\nu}$) direction. The distributions presented in Fig. 4.2 are integrated over all other directions of the phase space. In order to complete the validation we should look at the NNLO/`MiNLO` K-factor in more differential manner, i.e. to check if the value of the K-factor is the same regardless of the $(y_{\mathrm{HW}}, \Delta y_{\mathrm{HW}}, p_{t,\mathrm{H}})$-bin we are considering. This statement is equivalent to saying that the NNLO/`MiNLO` K-factors for each of remaining Born variables should be the same in every bin in $m_{\ell\nu}$ (or equivalently $a_{\ell\nu}$), for example K-factor for $(d\sigma/dy_{\mathrm{HW}})|_{[m_{\ell\nu}=75\mathrm{GeV}]}$ should be equal to the K-factor for $(d\sigma/dy_{\mathrm{HW}})|_{[m_{\ell\nu}=105\mathrm{GeV}]}$.

For that reason we put under scrutiny K-factors, for all other Born variables used for reweighting, constrained to different bins in $a_{\ell\nu}$. We choose to divide the $a_{\ell\nu}$ spectrum into 25 equally spaced bins. The distributions and K-factors for $(y_{\mathrm{HW}}, \Delta y_{\mathrm{HW}}, p_{t,\mathrm{H}})$ are presented in Fig. 4.3. Boxes show the results integrated over the whole $a_{\ell\nu}$-spectrum, whereas lines correspond to results in singled out bins. In the left-panels boxes represent the theoretical uncertainty of the evaluated distribution obtained according to scale variation method described in Section 4.3.2. The right-panels show the K-factors along the relevant Born variable, specified on the horizontal axis. Boxes represent the statistical uncertainty for the integrated result that has been multiplied by a factor of 5 and as

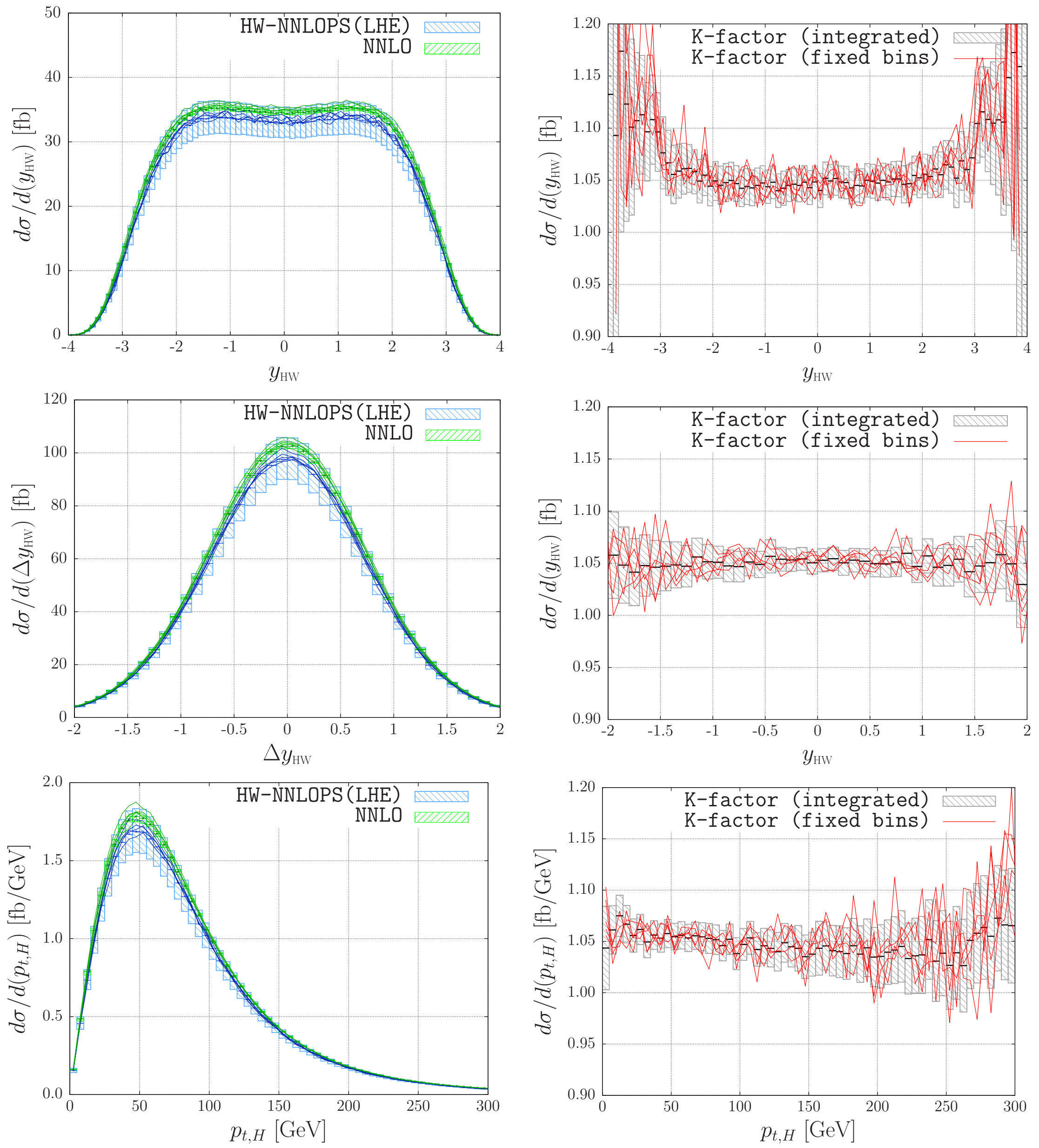

Figure 4.3: Comparison of `HWJ-MiNLO` (blue) and NNLO (green) for Born variables $y_{\mathrm{HW}}, \Delta y_{\mathrm{HW}}, p_{t,\mathrm{H}}$ chosen to perform reweighting. Left-panel: boxes represent results integrated over whole phase space (with theoretical uncertainty), whereas lines come from various $a_{\ell\nu}$ bins (as described in the text). Right-panel: boxes represent the overall K-factor (integrated over $a_{\ell\nu}$) with statistical uncertainty, while lines represent K-factors corresponding to various $a_{\ell\nu}$ bins (bin 3, 8, 13, 18, 23).

such it provides an estimate for the statistical uncertainty for the K-factors computed in single bins (as the expected statistical uncertainty for single bins scales with $\sqrt{N_{\text{bins}}}$ with respect to the integrated result). The red lines correspond to K-factor obtained in a single $a_{\ell\nu}$ bin. We can see that, within statistical fluctuations, K-factors for all of the checked bins are compatible with each other as well as with the integrated K-factor. This shows that the NNLO/`MiNLO` K-factor is indeed independent of $a_{\ell\nu}$ (and subsequently of $m_{\ell\nu}$) and it can be safely neglected in the reweighting procedure.

4.4.3 HW reweighting and validation

We use the modified reweighting procedure described in Section 4.3.1 setting

$$h(p_T) = \frac{(M_{\text{W}} + M_{\text{H}})^2}{(M_{\text{W}} + M_{\text{H}})^2 + (p_T)^2}, \tag{4.37}$$

where p_T has been computed with k_T-algorithm [183, 184] with $R = 0.4$. Moreover, the distributions of Born variables used for reweighting, $(y_{\text{HW}}, \Delta y_{\text{HW}}, p_{t,\text{H}})$, are not flat and hence the use of equally spaced bins is not an optimal choice. We decide to set bin edges in a way that each of the bins across the spectrum contains the same cross section.

In Fig. 4.4 we present both rebinned distributions (left panels) which were used for reweighting as well as unrebinned ones (right panels). There is almost a perfect agreement between NNLO results and reweighted `HW-NNLOPS(LHE)` ones in central-values as well as an envelope of the theoretical uncertainty. Specifically, we can appreciate a notable reduction of the theoretical uncertainty from about $\pm 10\%$ for `HWJ-MiNLO` down to $\pm 2\%$ in case of the reweighted `HW-NNLOPS(LHE)` prediction.

The unrebinned histograms show an extremely good agreement in most part of the spectrum, however we can notice small deviations in corners of the phase space, i.e. $|y_{\text{HW}}| \geqslant 2.8$ or $p_{t,\text{H}} \geqslant 250$ GeV. We point out that both of these regions correspond to the outermost bins of their respective distributions (see the first/last bin in the rebinned distributions for the comparison) and hence they are reweighted with a similar rescaling factor $\mathcal{W}(\Phi_{\text{HW}}, p_T)$. Such discrepancies should vanish when using higher statistics for preparing the results as well as finer binning of the 3D distributions used for reweighting.

A last step of our validation will be devoted to checking the correctness of the reweighting approach based on the Collins-Soper parametrisation of the angular dependence. In

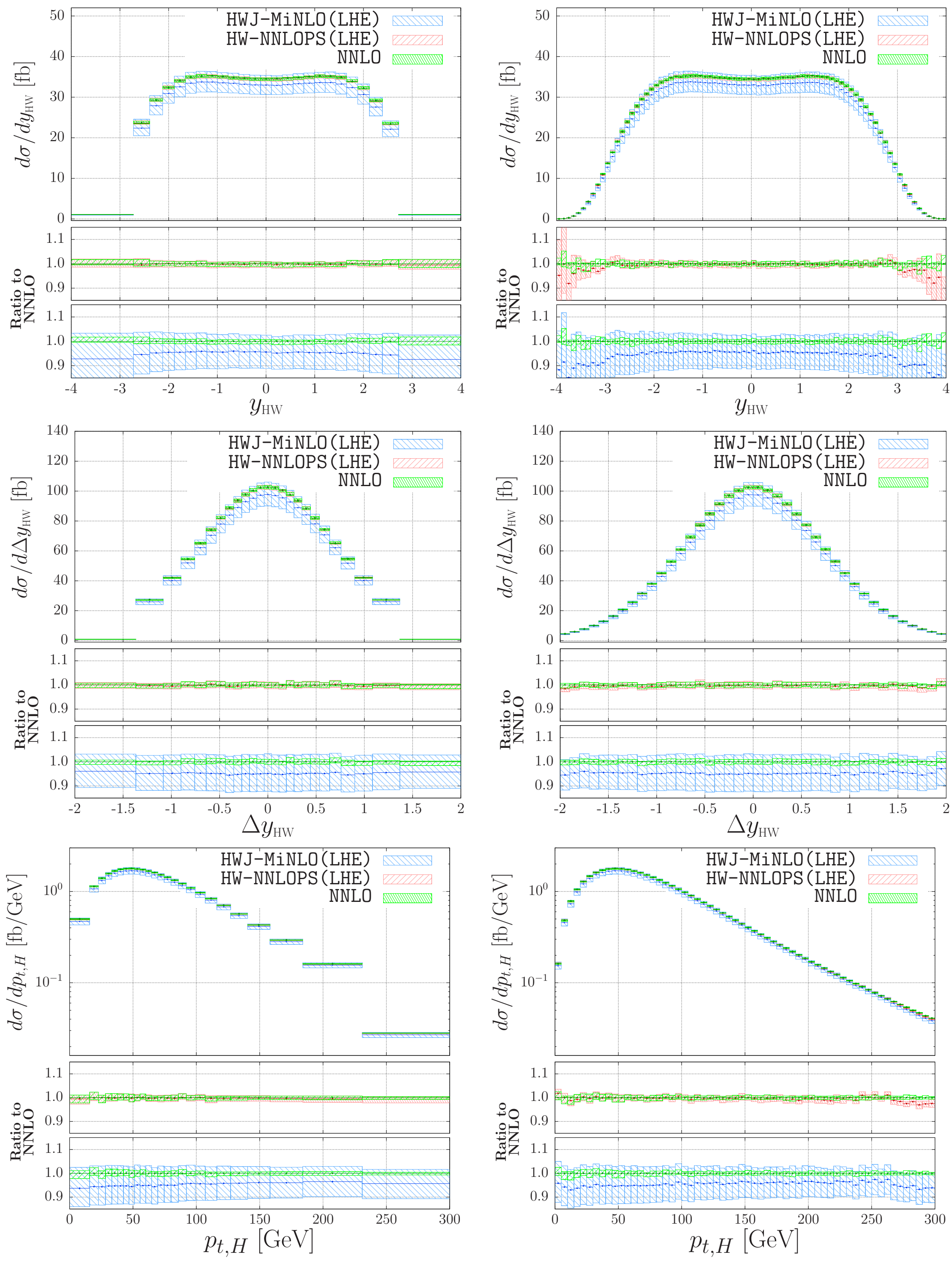

Figure 4.4: Comparison of `HWJ-MiNLO` (blue), `HW-NNLOPS(LHE)` (red) and NNLO (green) predictions for the Born variables, $(y_{\mathrm{HW}}, \Delta y_{\mathrm{HW}}, p_{t,\mathrm{H}})$, chosen to perform reweighting. Left panels show rebinned distributions (used for reweighting), right panels show differential distributions with equispaced bins.

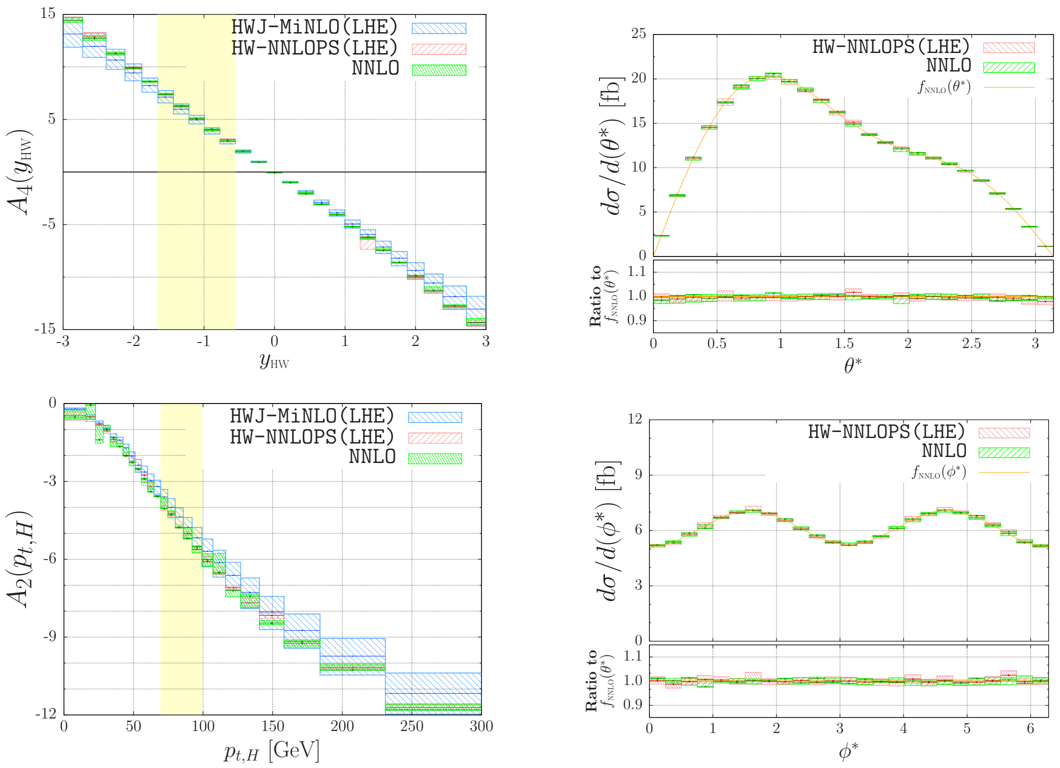

Figure 4.5: Upper panel: The left plot shows the A_4 coefficient as a function of $y_{\rm HW}$. The right plot shows the distribution of θ^* integrated over all variables with $y_{\rm HW}$ restricted to the region marked as yellow band in the left panel. Lower panel: The left plot shows the A_2 coefficient as a function of $p_{t,{\rm H}}$. The right plot shows the distribution of ϕ^* integrated over all variables with $p_{t,{\rm H}}$ restricted to the region marked as yellow band in the left panel.

Fig. 4.5 we analyse a few observables connected to the (θ^*, ϕ^*) angles.

First we discuss the upper panels of the figure which will help us checking the θ^* dependence. In both of these two panels we integrate over all directions of $\Phi_{\rm HW^\star}$, except for $y_{\rm HW}$. In the left panel we additionally perform an integral over $d\Omega^*$, whereas for the right one we restrict this integral only to $d\phi^*$. We can clearly see a dependence of A_4 on the rapidity of the HW resonance. We also notice that after reweighting the `HW-NNLOPS(LHE)` result (red boxes) resembles the result of a pure NNLO calculation (green boxes). In the right panel we present a distribution of the cross section with respect to polar angle θ^*, $(d\sigma/d\theta^*)$. In order to overcome a problem of limited statistics we partially integrate over the remaining variable $y_{\rm HW}$, however we choose a slice, corresponding to yellow band in the left plot, that ensures a non-zero value of A_4 coefficient. We present a direct computation of the NNLO distribution (green boxes), `HW-NNLOPS(LHE)` distribution (red boxes) as well as the NNLO prediction reconstructed from expectation values (restricted

	HWJ-MiNLO	HVNNLO	HW-NNLOPS(LHE)
σ_{fid}	152.49(5) fb $\pm$ 7.0%	158.75(8) fb $\pm$ 1.0%	159.21(30) fb $\pm$ 1.0%

Table 4.1: Fiducial cross-section of $pp \to \mathrm{HW}^+ \to \mathrm{H}\ell^+\nu_\ell$ at $\sqrt{s} = 13$ TeV with leptonic cuts. The uncertainty band is obtained with the scale variation procedure described in Section 4.3.1. Numerical errors for each prediction are quoted in brackets.

to a considered region) of all A_i coefficients (orange line). We can see a good agreement of all three predictions. Finally we come to a discussion about the azimuthal angle, ϕ^*. In the two bottom panels of Fig. 4.5 we present an analysis, similar to the one of θ^*. However, in this case we choose to present coefficient A_2 as a function of $p_{t,\mathrm{H}}$ (left panel) and similarly, for the $(d\sigma/d\phi^*)$, leave this direction only partially integrated (right panel).

In summary, the reweighted event sample HW-NNLOPS(LHE) provides an NNLO accurate description of Born HW observables that were used for reweighting. The method seems to be applicable even though the dimensionality of the underlying phase space is much bigger than in the cases treated previously.

In the next section we will present a short phenomenological study of newly obtained results. In there we will further verify the method for observables that have not been used for reweighting and present differences between pure fixed-order study and results with parton shower evolution.

4.4.4 Phenomenological results for the HW process

For the results presented in this section we use the fiducial cuts that have been proposed in the context of *LHC Higgs Cross Working Group* (LHCHXSWG) studies outlined in Ref. [185]. We require one charged lepton with $|y_\ell| < 2.5$ and $p_{t,\ell} > 15$ GeV, we do not impose a missing energy cut. When considering jet observables, we will reconstruct jets according to anti-k_T algorithm [186] with $R = 0.4$, as implemented in FastJet [187]. We analyse 13 TeV collisions. The quoted numbers reflect cross sections for two lepton families $\{e, \mu\}$, but we note that we do not distinguish their masses, hence the difference between our results and the results for single family is simply a factor of two.

Cross sections in the fiducial volume are quoted in Tab. 4.1. We see that there is a small K-factor of about 1.04 between HWJ-MiNLO and HVNNLO results. The fiducial cross section obtained using a reweighted event sample is compatible with the NNLO one both

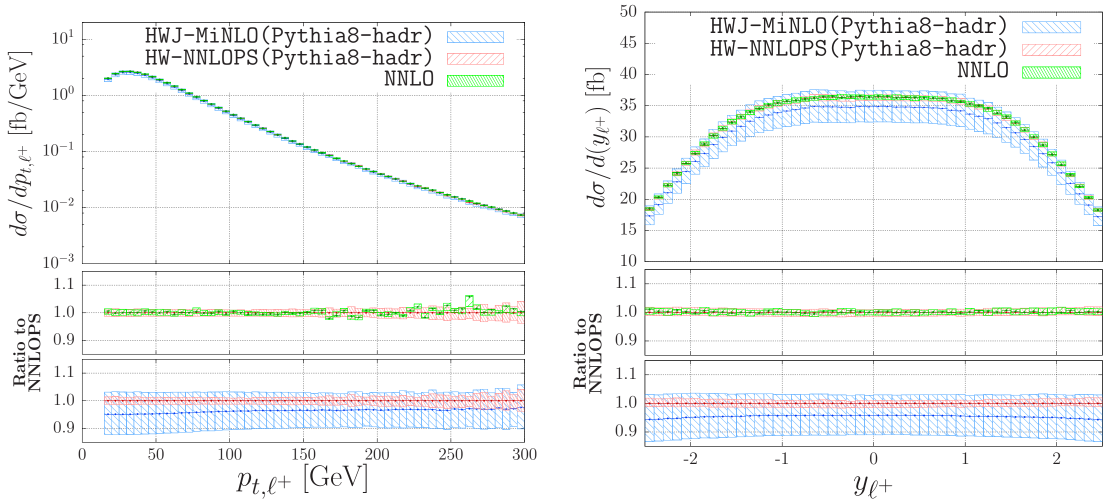

Figure 4.6: Transverse momentum and rapidity of the positively charged lepton ℓ^+ at NNLO (green), `HWJ-MiNLO(Pythia8+hadr)` (blue) and `HW-NNLOPS(Pythia8+hadr)` (red) level.

in central value (up to two standard deviations) as well as the size of the theoretical uncertainty envelope. We notice that the statistical error on the σ_{fid}(`HW-NNLOPS(LHE)`) is larger than the one of `HWJ-MiNLO` and `HVNNLO`. This is because we were trying to estimate a statistical uncertainty related to the reweighting procedure itself. This systematic component has been estimated by varying the number of bins in the 3D histograms used for reweighting as well as performing the procedure without the angular dependence on the (θ^*, ϕ^*) angles, it has been added in quadrature to the statistical one.

We now want to show a few HW observables that were not used for reweighting, nevertheless their distributions should be NNLO accurate according to theorem proved in Section 4.3. We start by analysing transverse momentum and rapidity of the charged lepton, which are presented in Fig. 4.6 (left and right panel respectively). We can see that in both cases `HW-NNLOPS(Pythia8+hadr)` results resemble the `HVNNLO` ones, red and green boxes cover each other up to statistical fluctuations. Furthermore we notice that the difference between `HWJ-MiNLO(Pythia8+hadr)` and `HW-NNLOPS(Pythia8+hadr)` may vary between an almost flat K-factor, like in case of y_ℓ, and a recognisable shape, like in case of $p_{t,\ell}$. Both types of NNLO-vs-(`HWJ-MiNLO`) differences are properly captured and erased by the reweighting procedure.

An interesting pair of observables to compare is the azimuthal angle between the Higgs boson and the charged lepton ($\Delta\phi_{\text{H}\ell}$) and azimuthal angle between the Higgs boson

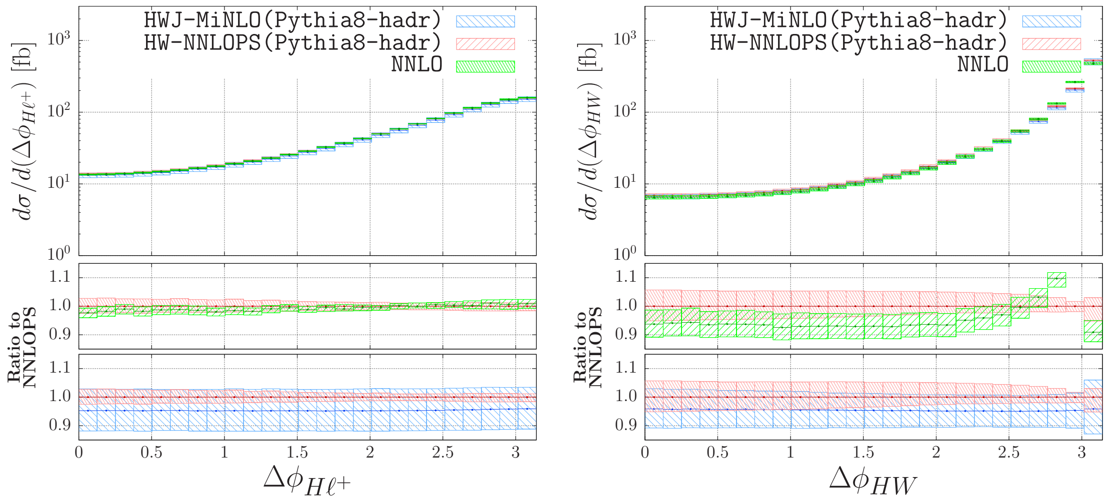

Figure 4.7: Azimuthal angle between the Higgs boson and the charged lepton ($\Delta\phi_{\mathrm{H}\ell}$, left panel) and azimuthal angle between the Higgs boson and the W^+ boson ($\Delta\phi_{\mathrm{HW}}$, right panel).

and the W^+ boson ($\Delta\phi_{\mathrm{HW}}$). We present the relevant distributions in Fig. 4.7. The first distribution, ($d\sigma/d\Delta\phi_{\mathrm{H}\ell}$), presented in thee left panel has a nontrivial shape already at the LO, hence the reweighted event sample `HW-NNLOPS(Pythia8+hadr)` reproduces the pure NNLO result with a very good precision. A small discrepancy may be notices in the limit $\Delta\phi_{\mathrm{H}\ell}\to 0$. In this region where configurations with a hard QCD radiation have bigger impact than in the other limit $\Delta\phi_{\mathrm{H}\ell} \to \pi$. It can be also noticed by a broadening scale uncertainty of the `HW-NNLOPS(Pythia8+hadr)` result, which is a result of enlarged impact of the $\mathcal{O}(\alpha_s, \alpha_s^2)$ corrections with respect to LO prediction. Such an effect is fully exposed in the second distribution of the $\Delta\phi_{\mathrm{HW}}$ angle (right panel). In this instance, the $\Delta\phi_{\mathrm{HW}}$ observable is singular at LO due to a kinematical constraint which forces H and W bosons to be locked in a back-to-back arrangement ($\Delta\phi_{\mathrm{HW}} = \pi$). By noting the departure of the `HVNNLO` result from its all-order `HW-NNLOPS(Pythia8+hadr)` counterpart, one can observe a divergence of the fixed-order NNLO prediction that manifests itself in this limit. This is a common feature of many observables which are constrained at LO and is a characteristic of results obtained in the fixed-order perturbation theory. Finally we note that the scale uncertainty bands of `HWJ-MiNLO(Pythia8+hadr)`, `HW-NNLOPS(Pythia8+hadr)` as well as NNLO prediction are similar in size, as all of these calculations have the same nominal accuracy for 1-jet observables.

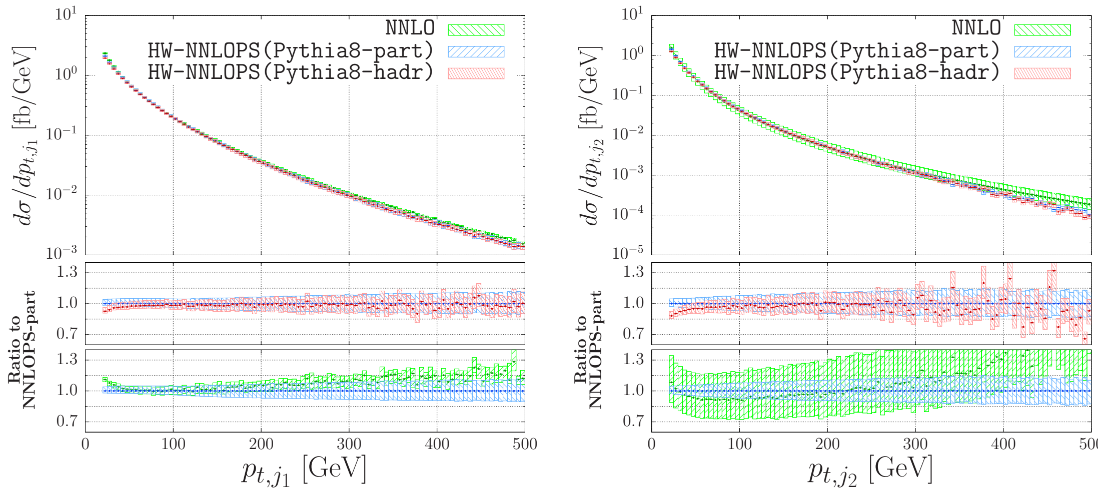

Figure 4.8: The transverse momentum of the two hardest jets in `HVNNLO` (green), `HW-NNLOPS(Pythia8+part)` before hadronization (blue) and `HW-NNLOPS(Pythia8+hadr)` with hadronization (red).

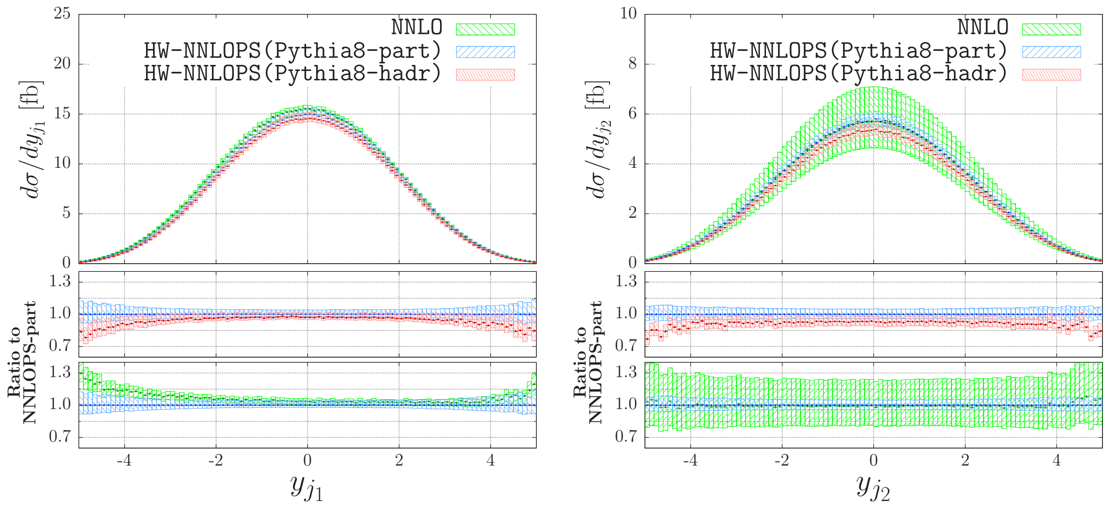

Figure 4.9: The rapidity of the two hardest jets in `HVNNLO` (green), `HW-NNLOPS(Pythia8+part)` before hadronization (blue) and `HW-NNLOPS(Pythia8+hadr)` with hadronization (red).

We now depart from Born-like observables and focus explicitly on predictions for jet-observables. We want to comment on the differences between predictions for the first- and second-jet observables. We impose a cut of 20 GeV for the minimum transverse momentum for a jet. We present the transverse momentum distribution of the two hardest jets in Fig. 4.8 and the distribution of their rapidities in Fig. 4.9. First we inspect the transverse momentum of the hardest jet (left panel of Fig. 4.8). From the ratio plot, we can see that the fixed-order NNLO calculation starts sharply increasing over the `HW-NNLOPS(Pythia8+part)` result as the low-p_t divergence is approached, which is similar behaviour to the one discussed in previous paragraph in terms of the $\Delta\phi_{\mathrm{HW}}$ angle. Because of the minimum jet-p_t cut, we do not observe Sudakov peak in the `HW-NNLOPS` simulations which is located below the transverse momentum cut. We again note that the scale uncertainties of the two types of predictions (the fixed-order NNLO and the all-order `HW-NNLOPS` one) are of similar size, as both capture all terms necessary for NLO$^{(1)}$ accuracy (i.e. NLO accuracy of 1-jet observables). On the other hand, while examining the distribution of the second hardest jet (right panel of Fig. 4.8) we notice that the uncertainty of the NNLO prediction is much larger than the corresponding one for the hardest jet, whereas the uncertainties for the two are similar in the case of the `HW-NNLOPS` prediction. The more reliable estimate of the theoretical uncertainty is the one of the fixed-order NNLO calculation, the calculation of the second-jet observables is formally only leading-order accurate (only $\mathcal{O}(\alpha_s^2)$ terms enter this distributions) and consequently we expect to see a bigger uncertainty. A small size of the `POWHEG` uncertainty band is intrinsically connected to the way the hardest radiation is generated in `POWHEG` simulation and the treatment of its scale variation. It has been previously observed in Ref.[179]. The same discusssion applies to the case of uncertainty bands of the jet rapidity distributions shown in Fig. 4.9.

Next we find it interesting to quantify the size of the non-perturbative effects. These can be inferred by casting an eye on the middle insets in Figs. 4.8-4.9. Hadronization has a sizeable impact on the shapes of jet distributions: differences up to 7-8% can be see in the $p_{t,j1}$ spectrum at small values, and are still visible at a few percent level till relatively hard jets are required ($p_{t,j1} > 100$ GeV). For the secont jet, hadronization effects are similar only slightly more pronounced. Much larger effects can be seen in the rapidity distributions of the two leading jets at very large rapidities, $|y_j| > 3$. This is consistent with the fact that the large rapidity region is correlated with small transverse momenta.

As a last exercise, we scrutinise the HW$^+$ production rates when binned into six different categories:

- without / with jet(s),

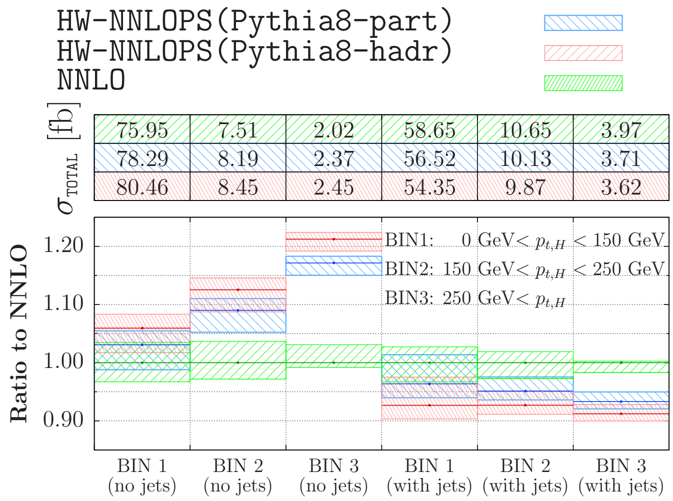

Figure 4.10: Total cross-section binned according to the transverse momentum of the Higgs boson and the presence of jets as described in the text. Jets are defined using the anti-k_t algorithm with $R = 0.4$, $p_{t,j} > 20$ GeV and $|y_j| < 4.5$.

- three bins according to the transverse momentum of the Higgs boson:

$$\begin{aligned} &(1) & 0 &< p_{t,\mathrm{H}} \leqslant 150 \text{ GeV}, \\ &(2) & 150 \text{ GeV} &< p_{t,\mathrm{H}} \leqslant 250 \text{ GeV}, \\ &(3) & 250 \text{ GeV} &< p_{t,\mathrm{H}}. \end{aligned} \tag{4.38}$$

The relevant cross sections are collected in Fig. 4.10. We present results for `HVNNLO` calculation as well as `HW-NNLOPS` predictions at parton and hadron level. We notice considerable differences between fixed-order prediction and the ones with parton shower evolution. We conclude that during PS evolution some QCD radiation may end up outside of the jet hereby softening it. This results in classifying more events as jet-vetoed ones and is evident in the table: the *no-jet* cross sections are larger in case of parton level `HW-NNLOPS` prediction that the fixed-order NNLO computation. The effect is further enlarged once hadronization is applied. Such differences can reach up to +15% for parton level (+20% for hadron level) simulation when we require the Higgs boson to have large transverse momentum. Capturing such effects may be especially important when considering the HW process in the so called *boosted* region [160]. One reason behind such a large enhancement of the *no-jet* cross sections is the relatively low value of the $p_{t,j}$ cut. In Fig. 4.8, we can see that the all-order effects (and further hadronization effects) are growing very quickly below 20 GeV. A remedy in this situation may be using larger value of the $p_{t,j}$ cut or using larger jet radius R. We do not discuss these effects in here, but will briefly return to them in the next section when studying HZ simulation with the Higgs boson decay into b-quarks.

To summarise, we have presented a fully-differential `HW-NNLOPS` generator that may be interfaced with parton shower. We have demonstrated that it achieves an NNLO accuracy for 0-jet (Born) observables. We have analysed and identified some differences between fixed-order and all-order approach. We find that the higher-order effects, captured to some extent by a parton shower, may be very important when realistic fiducial cuts are applied.

4.5 NNLO+PS reweighting for HZ process with $\mathrm{H} \to b\bar{b}$ decay at NLO

In this section we consider the second of the Higgsstrahlung processes, the HZ production. This time we include decays of both the Higgs boson into a pair of b-quarks and an electroweak Z boson into a pair of charged leptons

$$pp \longrightarrow \mathrm{HZ} \longrightarrow \left(b\bar{b}\right)\left(\ell\bar{\ell}\right). \tag{4.39}$$

The decay of the Z boson is treated exactly with all spin correlations between initial- and final-state fermions taken into account. The decay of the Higgs boson is treated at the next-to-leading order in QCD.

Throughout this section we will take only a single lepton family $\ell = \{e\}$ into account. We consider 13 TeV collisions and use the `PDF4LHC15_nnlo_mc` parton distribution functions [138, 182, 188, 189]. We set the mass and the width of the Z boson to $M_\mathrm{Z} = 91.1876$ GeV and $\Gamma_\mathrm{Z} = 2.4952$ GeV. The parameters related to the Higgs boson are $M_\mathrm{H} = 125.0$ GeV, $\Gamma_\mathrm{H} = 4.088$ GeV and a branching ratio for the $\mathrm{H} \to b\bar{b}$ decay is set to $\mathrm{Br}(\mathrm{H} \to \mathrm{b\bar{b}}) = 0.5824$. We now also include contributions that contain the Higgs boson coupled to a heavy-quark loop instead of being radiated off an electroweak boson. These are especially important for the HZ type of associated Higgs production. We include both *top* and *bottom* induced corrections and we set the mass of the heavy quark to a pole mass as it is usually done in publicly available codes [168]: $m_t = 173.2$ GeV and $m_b = 4.92$ GeV. On the contrary, for the bottom Yukawa coupling in $\mathrm{H} \to b\bar{b}$ decay we use

Figure 4.11: Gluon-gluon induced diagrams with a heavy-quark loop.

the $\overline{\mathrm{MS}}$ running mass evaluated at scale $\mu_r = M_{\mathrm{H}}$. The running mass is computed from the pole mass and the conversion is performed using an $\mathcal{O}(\alpha_s^2)$ accurate formula [190]. The numerical value is $m_b(M_{\mathrm{H}}) = 3.16$ GeV.

The Les Houches event sample is generated using the `POWHEG-BOX` generator: `HZJ-MiNLO`, whereas for the fixed-order predictions we use the publicly available `MCFM-8.0` [168] implementation of the HZ process. Similarly to the previous case we set a central renormalisation and factorisation scales to $\mu_0 = M_{\mathrm{Z}} + M_{\mathrm{H}}$ in the fixed-order NNLO computation, whereas the scale choice in `HZJ-MiNLO` is dictated my `MiNLO`.

The HZ production process is very similar to the HW one in many aspects, however there are also significant differences both in the process itself (contributions which were identically zero in HW case) and the reweighting procedure we apply. We will outline these additional modifications throughout this section before moving to phenomenological applications of the reweighted `HZ-NNLOPS` generator.

One of the important differences at $\mathcal{O}(\alpha_s^2)$ order is the appearance of a purely virtual contribution: gluon-gluon induced diagrams with squared heavy-quark loop as depicted in Fig. 4.11. Due to flavour conservation such diagrams do not appear in the HW calculation. It is essential to note that the diagrams are induced by gluon-gluon channel whose luminosity is enhanced in high-energy hadronic collisions and for that reason this contribution amounts to a significant part of the total cross section despite being a term of $\mathcal{O}(\alpha_s^2)$. We will refer to it as the $gg \to$ HZ contribution. We note that it contains terms which scale with heavy-quark Yukawa coupling y_q as well as ones which contain a typical ZZH vertex.

4.5.1 The NLO accurate $\mathrm{H} \to b\bar{b}$ decay in `HZJ-MiNLO` generator

In this section we will consider `MiNLO` prescription only for the production part of the process and perform an NLO QCD calculation of the $\mathrm{H} \to b\bar{b}$ decay in a purely fixed-order approach. For this reason we adapt the `HZJ-MiNLO` code to work within a *resonance improved* `POWHEG-BOX-RES` framework, which is suited for performing QCD calculations with resonances decaying into coloured particles. We treat the Higgs boson decay in the narrow-width approximation (NWA).

At the beginning we need to define a $\bar{B}$ function which is a fundamental object in all `POWHEG` simulations as explained in Section 2.4.2. In case of the `HZJ-MiNLO` code it reads

$$\begin{aligned}\bar{B} = \alpha_s(q_t^2)\Delta_q^2(q_t,Q)\frac{\mathrm{Br}(\mathrm{H}\to b\bar{b})}{\Gamma_{\text{NLO}}}\Big[&B_{\text{HZJ}}(1-2\Delta_q^{(1)}(q_t,Q))d\Gamma_{b\bar{b}}^{(0)}\\ +\left(V_{\text{HZJ}}+\int d\phi_r R_{\text{HZJ}}(\phi_r)\right)d\Gamma_{b\bar{b}}^{(0)}+&B_{\text{HZJ}}\left(d\Gamma_{b\bar{b}}^{(\text{V})}+\int d\phi_r d\Gamma_{b\bar{b}}^{(\text{R})}(\phi_r)\right)\Big]\,,\end{aligned} \tag{4.40}$$

where the Higgs propagator is implicit; $\mathrm{Br}(\mathrm{H}\to b\bar{b})$ is an external parameter and may be set to the best prediction for the Standard Model $\mathrm{H}\to b\bar{b}$ branching ratio; $(B/V/R)_{\text{HZJ}}$ are the Born, virtual and real squared amplitudes for the HZ+1jet production [173] and $d\Gamma_{b\bar{b}}^{(0/\text{V/R})}$ are the Born, virtual and real squared amplitudes for the $\mathrm{H}\to b\bar{b}$ decay, differential in their kinematics. We denote the NLO accurate partial decay width into b-quarks with $\Gamma_{\text{NLO}}=\Gamma_{b\bar{b}}^{(0)}+\Gamma_{b\bar{b}}^{(1)}$. Another ingredient in the `MiNLO` formula of Eq.(4.40) is the Sudakov form factor for quark-induced colour singlet production $\Delta_q(q_t,Q)$ which has been defined in Section 4.2.2, with the hard scale $Q=(p_Z+p_H)^2$ and the transverse momentum of the HZ system q_t entering as its arguments. We note that the HZ system has been reconstructed by adding the momenta of all decay products; that is $(\ell\bar{\ell})$ for the Z boson and $(b\bar{b})$ or $(b\bar{b}g)$ for the Higgs. The formula in Eq. (4.40) incorporates `MiNLO` prescription only for the production part of the process, and match this to a usual `POWHEG` implementation of the $\mathrm{H}\to b\bar{b}$ decay.

In the above equation we implicitly include a factor of α_s inside the NLO corrections; V_{HZJ} and R_{HZJ} as well as $d\Gamma_{b\bar{b}}^{(\text{V})}$ and $d\Gamma_{b\bar{b}}^{(\text{R})}$. In the first two, responsible for corrections to the production stage, the strong coupling is evaluated at $\mu_R=q_t$ similarly to the $\bar{\alpha}_s$ factor in Eq. (4.9), whereas the latter two terms, describing corrections to Higgs boson decay, are evaluated with renormalisation scale equal to Higgs mass, $\mu_r=M_{\mathrm{H}}$, since we do not apply `MiNLO` procedure in the decay of the Higgs boson in this implementation.

In order for the NNLO reweighting to work we need to check if the condition of Eq. (4.17) is satisfied. Upon integration over the phase space of all final-state light partons, the Eq. (4.40) reads

$$d\sigma_{\texttt{MiNLO}}(\Phi_{b\bar{b}\ell\bar{\ell}}) = \mathrm{Br}(\mathrm{H}\to b\bar{b})\cdot \left[\left(d\sigma^{(0)}_{\mathrm{HZ}} + d\sigma^{(1)}_{\mathrm{HZ}}\right)\cdot \frac{d\Gamma^{(0)}_{b\bar{b}} + d\Gamma^{(1)}_{b\bar{b}}}{\Gamma_{\mathrm{NLO}}} + d\tilde{\sigma}^{(2)}_{\mathrm{HZ}}\cdot \frac{d\Gamma^{(0)}_{b\bar{b}}}{\Gamma_{\mathrm{NLO}}}\right] + \mathcal{O}(\alpha_s^3),$$

where $d\Gamma^{(1)}_{b\bar{b}}$ is the NLO correction to Higgs decay, differential in the underlying $\mathrm{H}\to b\bar{b}$ phase space,

$$d\Gamma^{(1)}_{b\bar{b}} = d\Gamma^{(\mathrm{V})}_{b\bar{b}} + \int d\phi_r d\Gamma^{(\mathrm{R})}_{b\bar{b}}(\phi_r)\,.$$

Furthermore, $d\sigma^{(i)}_{\mathrm{HZ}}$ denote the $\mathcal{O}(\alpha_s^i)$ corrections to the HZ production cross section, while $d\tilde{\sigma}^{(2)}_{\mathrm{HZ}}$ stands for the $\mathcal{O}(\alpha_s^2)$ part of the `HZJ-MiNLO` computation, which corresponds to double-real and real-virtual parts of the HZ production at NNLO.

On the other hand the NNLO accurate cross section (*without* the loop-induced $gg\to\mathrm{HZ}$ contribution, which will be discussed later in Section 4.5.3) for the HZ production combined with the NLO accurate description of the decay is computed using `MCFM-8.0` implementation and its output reads

$$d\sigma_{\mathrm{NNLO}}(\Phi_{b\bar{b}\ell\bar{\ell}}) = \mathrm{Br}(\mathrm{H}\to b\bar{b})\cdot \left[d\sigma^{(0)}_{\mathrm{HZ}}\cdot \frac{d\Gamma^{(0)}_{b\bar{b}} + d\Gamma^{(1)}_{b\bar{b}}}{\Gamma_{\mathrm{NLO}}} + \left(d\sigma^{(1)}_{\mathrm{HZ}} + d\sigma^{(2)}_{\mathrm{HZ}}\right)\cdot \frac{d\Gamma^{(0)}_{b\bar{b}}}{\Gamma^{(0)}_{b\bar{b}}}\right]\,.$$

It is easy to check that after integrating out the decay of the Higgs boson we recover the fully-differential NNLO result multiplied by the overall branching ratio. More importantly we can verify that

$$\mathcal{W}(\Phi_{b\bar{b}\ell\bar{\ell}}) = \frac{d\sigma_{\mathrm{NNLO}}(\Phi_{b\bar{b}\ell\bar{\ell}})}{d\sigma_{\texttt{MiNLO}}(\Phi_{b\bar{b}\ell\bar{\ell}})} = 1 + \frac{\left(\sigma^{(2)} - \tilde{\sigma}^{(2)}\right)}{\sigma^{(0)}} + \mathcal{O}\left(\alpha_s^3\right)\,, \tag{4.41}$$

which ensures that also in this case, including the NLO corrections to the decay, the reweighting procedure does not spoil the NLO$^{(1)}$ accuracy of the `HZJ-MiNLO` generator and provides an NLO accurate description of observables in the HZ+1jet region.

At this stage we could have already performed an NNLO reweighting procedure and obtain `HZ-NNLOPS` accurate set of Les Houches events (*without* the loop-induced $gg\to\mathrm{HZ}$ contribution), however we want to discuss one more simplification of the phase-space parametrisation that will allow for more efficient $\mathcal{W}(\Phi_{b\bar{b}\ell\bar{\ell}})$ computation.

4.5.2 Efficient parametrisation of the HZ production phase space

Having four particles in the final state, two leptons ($\ell\bar{\ell}$) and two bottom quarks ($b\bar{b}$), means that the underlying Born phase space has 9 dimensions, after neglecting an irrelevant azimuthal angle and including the initial-state degrees of freedom. We work in the NWA and in this way the reweighting function $\mathcal{W}$ does not depend on the details of the Higgs decay – after all both generators `MCFM-8.0` and `HZJ-MiNLO` are now treating the Higgs boson decay with the same accuracy, up to NLO QCD corrections. Therefore it is suitable to factorise the phase space into

$$d\Phi_{b\bar{b}\ell\bar{\ell}} = d\Phi_{\mathrm{H}\ell\bar{\ell}} \times (2\pi)^3 dq^2 \times d\Phi_{\mathrm{H}\to b\bar{b}}, \tag{4.42}$$

where q^2 is the virtuality of the Higgs boson, $\Phi_{\mathrm{H}\to b\bar{b}}$ is the 2-dimensional phase space of a Higgs boson decay into $b\bar{b}$, and finally $\Phi_{\mathrm{H}\ell\bar{\ell}}$ is the 6-dimensional phase space for the production of an undecayed Higgs boson together with a pair of leptons from the Z boson decay.

Parametrisation of $\Phi_{\mathrm{H}\ell\bar{\ell}}$ can be achieved in a number of ways, one of such realisations has been already presented in Eq. (4.29). We will not change the way the last three dimensions are described. We will use two Collins-Soper angles and related analytical parametrisation, presented earlier in Eqs. (4.30) and (4.31). We will also use invariant mass of the dilepton system $M_{\ell\ell}$ as one of the directions, which nevertheless will be integrated out, relying on the similar assumptions as in the case of HW production in previous section.

In this way we are left with parametrising the remaining three dimensions. The two variables that are intrinsically linked with a colour singlet production in hadronic collisions are the invariant mass and rapidity of the colourless system. Therefore to describe the next two dimensions we use invariant mass and rapidity of the HZ system (M_{HZ} and Y_{HZ} respectively). A natural frame for the description of HZ branching into the electroweak Z boson and the Higgs boson would be the HZ rest-frame. Therefore as a third variable we choose $\cos\alpha$, where α is the polar angle of the Z boson, where the $\hat{z}'$-axis has been determined by boosting the beam axis to the HZ rest-frame. As consequence we have

$$\cos\alpha = \frac{\vec{p}'_Z \cdot \hat{z}'}{|\vec{p}'_Z|\,|\hat{z}'|}, \tag{4.43}$$

where $'$ indicated the frame where HZ system is at rest.

We can now recast the full parametrisation of the $\Phi_{\mathrm{H}\ell\bar{\ell}}$ phase space as

$$\Phi_{\mathrm{H}\ell\bar{\ell}} = \{M_{\mathrm{HZ}}, Y_{\mathrm{HZ}}, \cos\alpha, M_{\ell\ell}, \theta^*, \phi^*\}\,, \tag{4.44}$$

and specify the fully-differential cross section as

$$\begin{aligned}\frac{d\sigma}{d\Phi_{\mathrm{H}\ell\bar{\ell}}} &= \frac{d^6\sigma}{dM_{\mathrm{HZ}}\,dY_{\mathrm{HZ}}\,d\cos\alpha\,dM_{\ell\ell}\,d\cos\theta^* d\phi^*} \\ &= \frac{3}{16\pi}\left(\frac{d\sigma}{d\Phi_{\mathrm{HZ}^\star}}(1+\cos^2\theta^*) + \sum_{i=0}^{7} A_i(\Phi_{\mathrm{HZ}^\star}) f_i(\theta^*,\phi^*)\right)\,, \end{aligned} \tag{4.45}$$

where we have used $\Phi_{\mathrm{HZ}^\star}$ to abbreviate $\{M_{\mathrm{HZ}}, Y_{\mathrm{HZ}}, \cos\alpha, M_{\ell\ell}\}$, and the functions f_i are given in Eq. (4.31) together with method of projecting out A_i coefficients. We note that for practical purposes we will use only the first five A_i coefficients $(A_0, \ldots, A_4)$ and, for simplicity, neglect the remaining three (A_5, A_6, A_7) since their impact on many distributions is numerically negligible and our focus in the phenomenological studies will be concentrated on the observables related to the Higgs boson decay. We remove the dependence upon $M_{\ell\ell}$ along the lines of Eq. (4.35), which reduces $\Phi_{\mathrm{HZ}^\star} \to \{M_{\mathrm{HZ}}, Y_{\mathrm{HZ}}, \cos\alpha\}$. The latter set of variables still has one angular observable in it. It is natural to employ tools of mathematical analysis and parametrise the angular dependence in terms of some spectral functions. It is possible to find a set of orthonormal functions $g_j(\cos\alpha)$ for $\alpha \in \{0, \pi\}$. The details of such construction are characterised in the App. B.1. Such an operation leads us to the following expressions

$$\begin{aligned}\frac{d^3\sigma}{d(M_{\mathrm{HZ}})d(Y_{\mathrm{HZ}})d(\cos\alpha)} &= \sum_{j=0}^{N} c_j(M_{\mathrm{HZ}}, Y_{\mathrm{HZ}})\, g_j\,(\cos\alpha)\,, \\ A_i\,(M_{\mathrm{HZ}}, Y_{\mathrm{HZ}}, \cos\alpha) &= \sum_{j=0}^{N} a_{ij}(M_{\mathrm{HZ}}, Y_{\mathrm{HZ}})\, g_j\,(\cos\alpha)\,, \end{aligned} \tag{4.46}$$

where c_j and a_{ij} are coefficients of only two variables, and N is the upper limit of the sum. In principle $N \to \infty$, however in our case we can infer the number of possible spectral modes entering the calculation by analysing the squared amplitude for the process. In App. B.2 we examine the matrix element for process of our interest, Eq.(4.39), and by exploiting Lorentz symmetries we find that at most polynomials of 5-th degree in $\cos\alpha$ and $\sin\alpha$ can appear in the squared amplitude. Accordingly, we set $N = 10$ in Eq. (4.46).

In summary, our parametrisation of the fully-differential cross section suitable for the NNLO reweighting of `HZJ-MiNLO` Les Houches events reads

$$\frac{d\sigma}{d\Phi_{\mathrm{H}\ell\bar{\ell}}} = \frac{3}{16\pi}\sum_{j=0}^{10}\Big[c_j\left(M_{\mathrm{HZ}},Y_{\mathrm{HZ}}\right)\Big(1+\cos^2\theta^*\Big) \\ +a_{ij}\left(M_{\mathrm{HZ}},Y_{\mathrm{HZ}}\right)f_i(\theta^*,\phi^*)\Big]\;g_j(\cos\alpha), \tag{4.47}$$

where c_j and a_{ij} are 2D histograms, spanning over M_{HZ} and Y_{HZ} directions. The prescription for acquiring functions $g_j(\cos\alpha)$ is comprehensively outlined in App. B.1 alongside method for projecting out the j-th mode.

We clarify that we will use the same $h(p_T)$ function for reweighting as in HW case, Eq. (4.37), exchanging M_{W} to M_{Z}, unless explicitly stated otherwise. We remind the reader, as it was the case so far, we disregard the $gg\to\mathrm{HZ}$ contribution for now and we will include it separately after reweighting of the `HZJ-MiNLO` events. This will be discussed in detail in the next section.

As of now we focus on validating the updated approach to reweighting. In the following plots we will show `HZJ-MiNLO` results in blue, `MCFM-8.0` prediction in green and our new `HZ-NNLOPS(LHE)` results in red. The boxes represent the scale uncertainty. We note that all uncertainties have been estimated using an envelop of 7 scale choices, in case of `HZ-NNLOPS(LHE)` we also use 7 scale combinations to estimate the uncertainty, i.e. the (K_R, K_F) is the same for the NNLO numerator and `MiNLO` denominator in $\mathcal{W}(\Phi_{\mathrm{H}\ell\bar{\ell}})$ rescaling factor.

We start by looking at the distribution of the dilepton system invariant mass $M_{\ell\ell}$, in the left panel of Fig. 4.12. We note that not only the fixed-order NNLO is retrieved by the `HZ-NNLOPS(LHE)` result but also the K-factor between `MCFM-8.0` and `HZJ-MiNLO` is flat up to statistical fluctuations which is along the lines of our assumption allowing for integrating out this phase space direction, as described in Eq. (4.35). The right panel of Fig. 4.12 shows the rapidity of the HZ system and again confirms the practicability of the reweighting method. We can see discrepancies at the edges of the distribution that again can be attributed to the lack of being differential enough, the outermost Y_{HZ} bins start at $|Y_{\mathrm{HZ}}|\approx 2.6$. Subsequently we examine the distribution of the invariant mass of the HZ

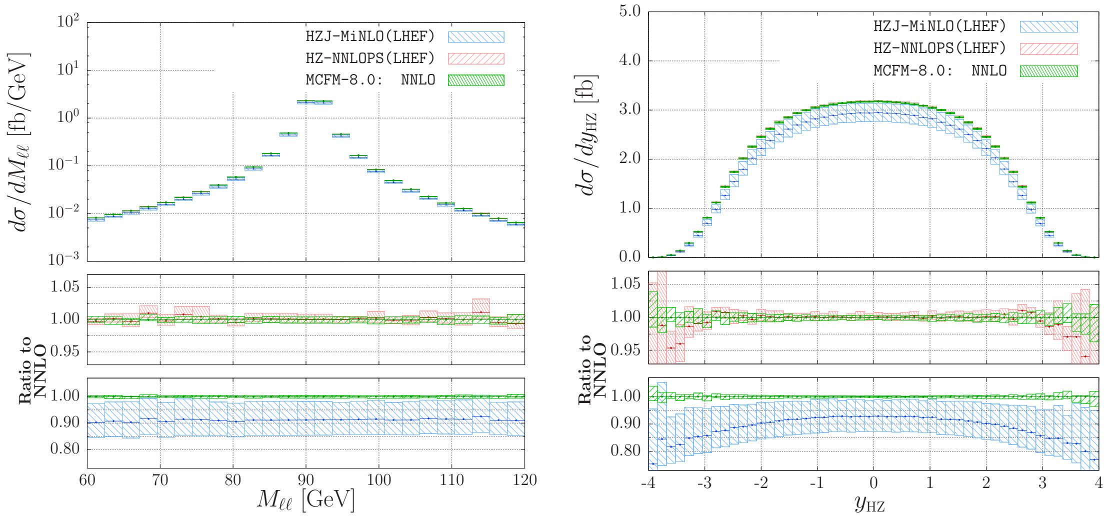

Figure 4.12: The distributions of the invariant mass of the dilepton system $M_{\ell\ell}$ (left panel) and the rapidity of the HZ system (right panel).

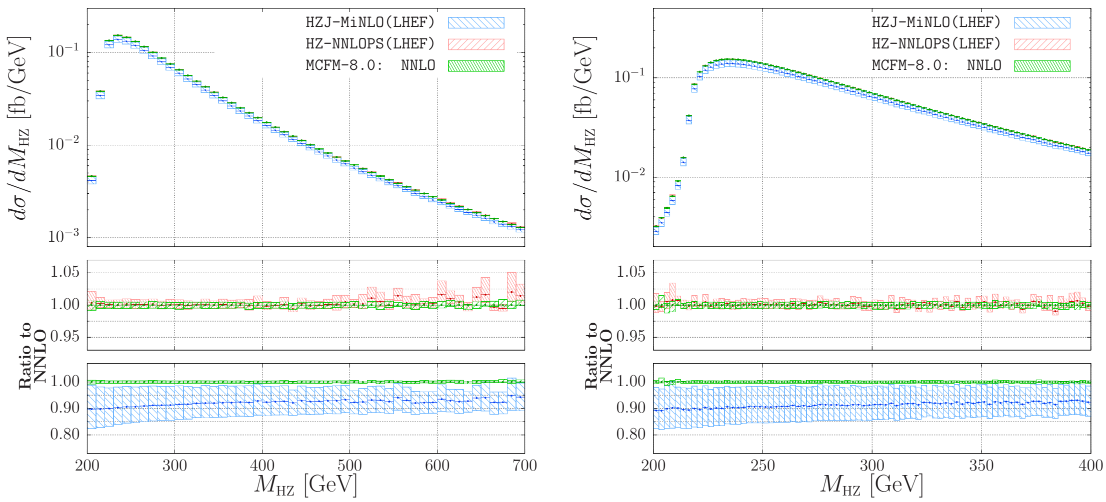

Figure 4.13: The distribution of the invariant mass of the HZ system. We show two different choices of binning to validate the reweighting procedure.

system, which we present in Fig. 4.13. Both panels show the $(d\sigma/dM_{\mathrm{HZ}})$ distribution. We notice that the NNLO accurate result is faithfully reconstructed by the `HZ-NNLOPS(LHE)` computation, even when subjected to a very refined binning like demonstrated in the right panel of Fig. 4.13. For the sake of completeness, we also establish the quality of reconstruction of the other observables used in the reweighting procedure, i.e θ^* and ϕ^* (in Fig. 4.14) as well as cosα. We show a distribution $(d\sigma/d\cos\alpha)$ as well as a Collins-Soper coefficient $A_2(\cos\alpha)$ in the left and right inset of Fig. 4.15.

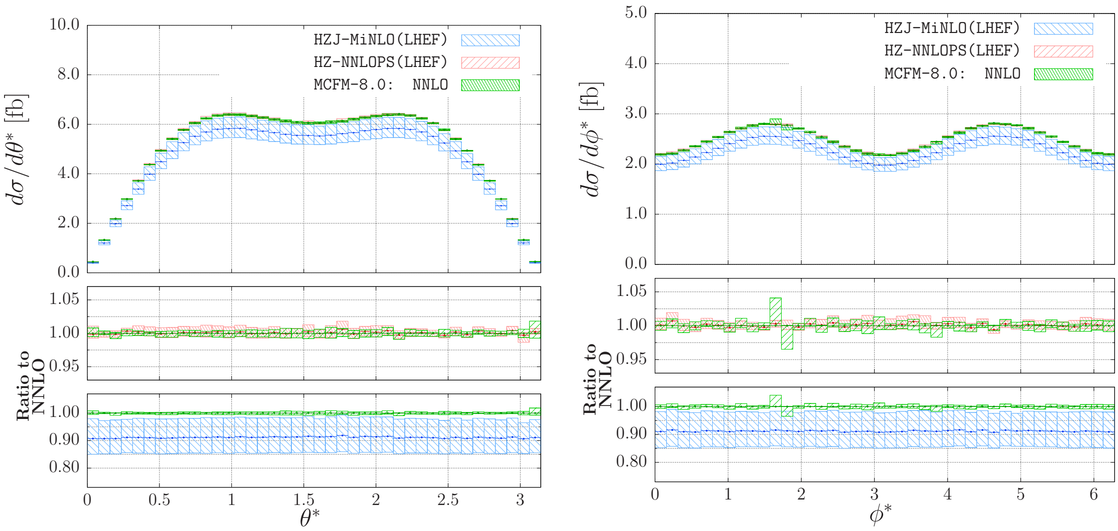

Figure 4.14: The differential distributions of Collins-Soper angles: θ^* (left) and ϕ^* (right). The one-loop squared terms from the $gg \to \mathrm{HZ}$ channel have been omitted.

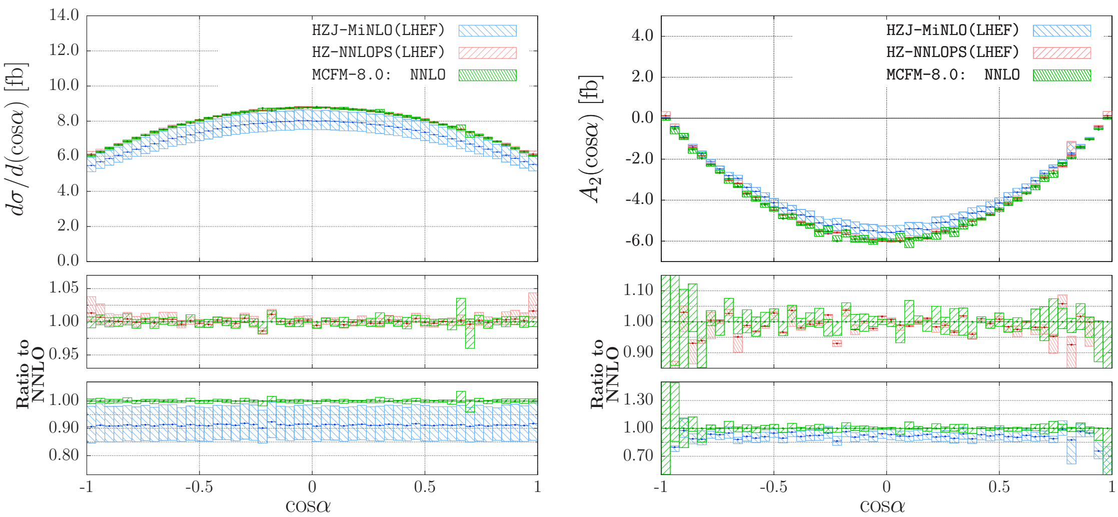

Figure 4.15: The differential distributions of the Z boson polar angle with respect to the beam axis, defined in Eq. (4.43): differential cross section as a function of $\cos\alpha$ (left panel) and the dependence of coefficient $A_2(\cos\alpha)$, see Eq. (4.45). The one-loop squared terms from the $gg \to \mathrm{HZ}$ channel have been omitted.

We now pause for a moment to establish the impact of the $h(p_T)$ function, used in the reweighting prescription, on the distributions of 1-jet observables. We recall that p_T is the transverse momentum of the hardest jet, clustered with k_T-algorithm for $R = 0.4$. We will compare the two choices of the profile function

$$h_1(p_T) = \frac{(M_{\mathrm{Z}} + M_{\mathrm{H}})^2}{(M_{\mathrm{Z}} + M_{\mathrm{H}})^2 + (p_T)^2}\,, \qquad \text{and} \qquad h_2(p_T) = 1\,. \tag{4.48}$$

In the first instance the NNLO corrections have the biggest impact in the region where

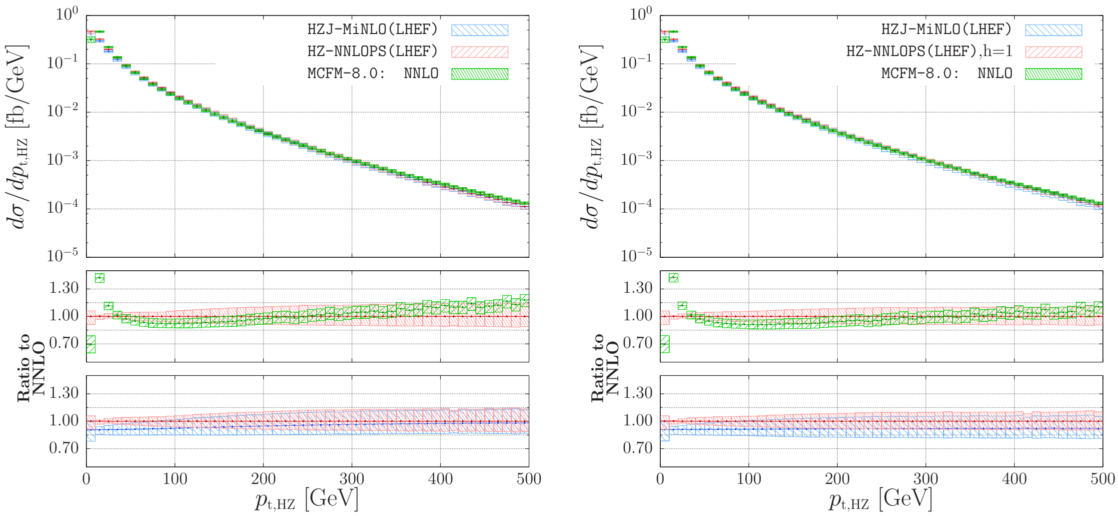

Figure 4.16: The differential distribution of the transverse momentum of the HZ system. We show results for reweighting with damping factor $h = h_1(p_T)$ (left panel) and with uniform reweighting $h = h_2(p_T)$ (right panel). The one-loop squared terms from the $gg \to$HZ channel have been omitted.

$p_T \to 0$ which is the limit where the HZ+1jet kinematics approaches the underlying Born configuration, a natural habitat of virtual corrections. On the other hand, the second choice of $h(p_T)$ function allows for spreading of the NNLO/`MiNLO` K-factor uniformly over the whole HZ+1jet phase space. A specific choice does not affect predictions of the 0-jet observables and the NNLO$^{(0)}$ accuracy is retained regardless of $h(p_T)$. However we can observe some differences for 1-jet observables.

As an example, we focus on the transverse momentum of the HZ system, which vanishes at Born level and acquires non-zero values only in the presence of additional QCD radiation. The relevant distributions, obtained by using the two different prescriptions, is shown in Fig. 4.16. In the lower panels of the figure, we show ratios with respect to our new result, `HZ-NNLOPS(LHE)`. First we consider the relation between `HZJ-MiNLO` and `HZ-NNLOPS(LHE)` that can be seen in the bottom panels (red and blue boxes). As expected, in case of uniform reweighting (r.h.s.) the ratio of the two is approximately constant across the whole $p_{t,\mathrm{HZ}}$ spectrum. In the case with damping (l.h.s.) the `HZJ-MiNLO` and `HZ-NNLOPS(LHE)` predictions approach each other for very large values of $p_{t,\mathrm{HZ}}$. This is an effect of a correlation between the HZ transverse momentum and the amount of hard QCD radiation (p_T entering the $h(p_T)$ function) combined with a behaviour of the rescaling factor $\mathcal{W}$ that acts in accordance with

$$\mathcal{W}(p_T) \xrightarrow[p_T \longrightarrow \infty]{} 1\,. \tag{4.49}$$

Considering the middle panels we can examine the relationship between the pure NNLO result and the reweighted `HZ-NNLOPS(LHE)` one. Both predictions should provide equally good description of the $p_{t,\mathrm{HZ}}$ distribution, at $\mathrm{NLO}^{(1)}$ accuracy. We recollect that the `MCFM-8.0` prediction has been obtained using a static renormalisation scale $\mu_R = M_\mathrm{Z}+M_\mathrm{H}$ for the central value, whereas the scale choice for `HZ-NNLOPS(LHE)` calculation is dictated by `MiNLO` procedure and the central value is equal to $\mu_R = p_{t,\mathrm{HZ}}$ as already mentioned earlier in Section 4.5.1. We can see that the left plot, related to $h = h_1(p_T)$, the green and red central curves cross each other in the region between 200-250 GeV, which contains the part of the spectrum where scales choices for the two simulations are equal to each other. A similar conclusion could be drawn about the relation of `HZJ-MiNLO` and `MCFM-8.0` results, as the damping factor ensures that `HZJ-MiNLO` $\approx$ `HZ-NNLOPS(LHE)` for large enough values of $p_{t,\mathrm{HZ}}$. On the other hand, using the same settings for `HZJ-MiNLO` and `MCFM-8.0` as in the aforementioned case and switching off the damping factor, $h = h_2(p_T)$, leads to an uniform enhancement of the $p_{t,\mathrm{HZ}}$ spectrum in `HZ-NNLOPS(LHE)` prediction and hence the crossing point with `MCFM-8.0` is shifted to much larger values of the transverse momentum, $p_{t,\mathrm{HZ}}$ in the region around 350 GeV. Based on the distribution shown in the right panel we might be tempted to draw a conclusion that uniform rescaling provides a better description of hard-tail of the $p_{t,\mathrm{HZ}}$ distribution. However, the apparent agreement between `MCFM-8.0` and `HZ-NNLOPS(LHE)` results in the region of 350-450 GeV is accidental and if we had looked at even higher transverse momenta, the two results would start to depart from each other, as they were prepared with different scale choice.

4.5.3 Inclusion of the $gg \to$ HZ contribution

We have already mentioned a particular contribution that enters the HZ production and is induced in the gluon-gluon channel, the relevant diagrams were depicted in Fig. 4.11. Such terms have been thoroughly studied in the past, for example in Ref. [165] as well as in Refs. [191, 192] and incorporated into fully differential NNLO calculation in Refs. [167, 168, 174].

It is worth noticing that we need to include only bottom and top quark loops when considering the amplitudes depicted in Fig. 4.11. The box-like diagram (left) not only has quark Yukawa coupling inside but also requires an additional chirality flip due to quark mass along the fermion line, otherwise amplitude vanishes. The triangle-like contribution has a direct coupling of the Z boson to a fermion line, the vector-like part of the coupling gives no contribution due to arguments analogous to the ones of the Furry's theorem (using charge conjugation symmetry) while the remaining axial part is is proportional to the third component of the weak isospin and hence vanishes for mass-degenerate weak isodoublets leaving only the contribution of bottom-top isodoublet.

The $gg \to \mathrm{HZ}$ contribution is known to constitute a significant part of the cross section due to enhancement related to the luminosity of the gluonic channel. They are especially important when the invariant mass of the HZ system is greater than twice the top-quark mass. As a loop-induced process, so far only approximate NLO corrections are known for this channel [193, 194] due to a lack of results of some two-loop amplitudes with multiple scales involved (masses of heavy-quark, Higgs boson, Z boson as well as kinematical invariants).

The finiteness of the $gg \to \mathrm{HZ}$ contribution allows for its independent treatment. Therefore, we have not included it in our reweighting procedure but rather decided to subsequently append it to the NNLO reweighted `HZ-NNLOPS(LHE)` result as a separate subprocess, consisting of only $gg \to \mathrm{HZ}$ events. The additional events will be produced using a `POWHEG` implementation of the loop-induced $gg \to \mathrm{HZ}$ process [173], with both heavy-quarks (bottom and top) included. We indicate that in this case we refrain from including the radiative corrections to the $\mathrm{H} \to b\bar{b}$ decay, as they are formally of $\mathcal{O}(\alpha_s^3)$ order and therefore beyond the scope of this work. The radiation from the decay is fully taken care of by the parton shower evolution. Furthermore, a radiation pattern of the gluon-initiated hard process is typically different from processes involving initial-state quarks. From that point of view, it is important not to include $gg \to \mathrm{HZ}$ contribution through a simple reweighting.

4.5.4 Phenomenological results for the HZ process

Before proceeding to the discussion of phenomenological results, we briefly remark on the interface of the HZ-NNLOPS(LHE) results with parton shower. We use Pythia8 in the *Monash* tune [195] and for the matching we follow an approach similar to the one first introduced for the treatment of the NLO accurate $t\bar{t}$ production [196]. Such approach allows for a generation of radiation also from resonances while maintaining a consistent matching to fixed-order calculation.

In our simulation we set the flag allrad to 0. This means that the POWHEG real emission, feature of the NLO computation, is generated at most from one singular region. Such emission can be associated either to production stage or to the radiation from a resonance. To decide the origin of an emission, POWHEG uses the usual highest bid algorithm. An important requirement for the matching to the parton shower to work properly is that the hardest radiation is generated by POWHEG itself. It is usually achieved by setting a scalup value, for each event in the ensemble, that is responsible for setting an initial scale for parton shower. One subtlety is that the hardness definition used by POWHEG and Pythia8 differ (see App.A of Ref. [196] for the details), therefore after generating a parton shower evolution of an event we recompute the hardness of the first emission and compare it with the value of scalup. If the initial scale is respected we accept the shower, otherwise we repeat the evolution until the condition is fulfilled. We have also checked that the results obtained with our own Pythia8 analysis driver are compatible with those obtained by the procedure encoded in the PowhegHooks-class provided by Pythia8 [197]. We are now well prepared for the phenomenological analysis of the newly obtained HZ-NNLOPS results.

We recall that the detailed list of physical parameters has been specified at the beginning of Section 4.5. We also remind that we consider only a single leptonic family, i.e. e or μ. We include $\mathrm{H} \to b\bar{b}$ radiative corrections as described in the text. The fiducial cuts are partially following the setup of recent ATLAS analysis of Ref. [163]. We require two charged leptons with $|y_\ell| < 2.5$ and $p_{t,\ell} > 7$ GeV, moreover the harder lepton should satisfy $p_{t,\ell} > 27$ GeV. We also introduce the allowed invariant-mass window by imposing

Fiducial cross section	HZJ-MiNLO	MCFM-8.0	HZ-NNLOPS(LHE)	HZ-NNLOPS
no $gg \to$HZ	$6.59^{+7.2\%}_{-6.2\%}$ fb	$7.14^{+0.5\%}_{-0.9\%}$ fb	$7.14^{+0.3\%}_{-0.4\%}$ fb	$6.49^{+0.8\%}_{-0.6\%}$ fb
with $gg \to$HZ	–	$7.92^{+2.0\%}_{-1.5\%}$ fb	$7.90^{+2.8\%}_{-2.0\%}$ fb	$7.16^{+3.1\%}_{-2.1\%}$ fb
no $gg \to$HZ, high-$p_{t,Z}$	$1.13^{+5.9\%}_{-5.3\%}$ fb	$1.21^{+0.1\%}_{-0.2\%}$ fb	$1.21^{+0.2\%}_{-0.3\%}$ fb	$1.13^{+1.5\%}_{-1.2\%}$ fb
with $gg \to$HZ, high-$p_{t,Z}$	–	$1.49^{+5.3\%}_{-4.1\%}$ fb	$1.48^{+5.3\%}_{-4.0\%}$ fb	$1.42^{+6.9\%}_{-5.1\%}$ fb

Table 4.2: Fiducial cross section of $pp \to \mathrm{HZ} \to \left(b\bar{b}\right)(e^+e^-)$ at 13 TeV with leptonic and b-jet cuts. The uncertainty band refers to the scale variation described in the text. Numerical errors for each prediction are beyond the quoted digits.

a condition for the dilepton invariant mass, 81 GeV $< M_{\ell\ell} <$ 101 GeV. To identify an $\mathrm{H} \to b\bar{b}$ decay we look for events that contain at least two b-jets with $|\eta_j| < 2.5$ and $p_{t,j} > 20$ GeV. Unless stated otherwise jets are defined using the flavour-k_T algorithm [198] that provides an infrared safe definition of the flavoured quark jet. In this context we consider only b-quarks to be flavoured, and all other quarks as flavourless, which is compatible with b-tagging techniques implemented in experimental analyses. We set the jet radius parameter to $R = 0.4$. In the situation with more than two b-jets present we will choose a pair with invariant mass that is closest to M_{H}. Moreover, in some of the results we will consider a high-$p_{t,\mathrm{Z}}$ region that corresponds to an additional cut on the Z boson transverse momentum, $p_{t,\mathrm{Z}} > 150$ GeV.

We start our analysis by reporting cross sections in the fiducial volume for various types of simulations. We list our results in Tab. 4.2. The first line of the table show predictions without the additional $p_{t,\mathrm{Z}}$ cut and omitting $gg \to$HZ contributions. We can see that the NNLO/HZJ-MiNLO K-factor is about 1.08 and is properly accounted for in reweighted HZ-NNLOPS(LHE) prediction. We note that reweighting procedure not only reproduces the NNLO central value but also provides a reduction of scale uncertainty from about 7% to below 1%. After inclusion of the $\mathcal{O}(\alpha_s^2)$ $gg \to$HZ contribution, the fiducial cross section increases by about 10%. In this case, however, the scale uncertainty remains at the level of 2-3%, as it is dominated by the new contribution which is described only at the leading order. The last column in the table represents cross sections at the HZ-NNLOPS level. We can see a decrease of the number of events contained in the fiducial volume by about 10%. This effect can be attributed to the impact of parton shower on the jet activity. As the

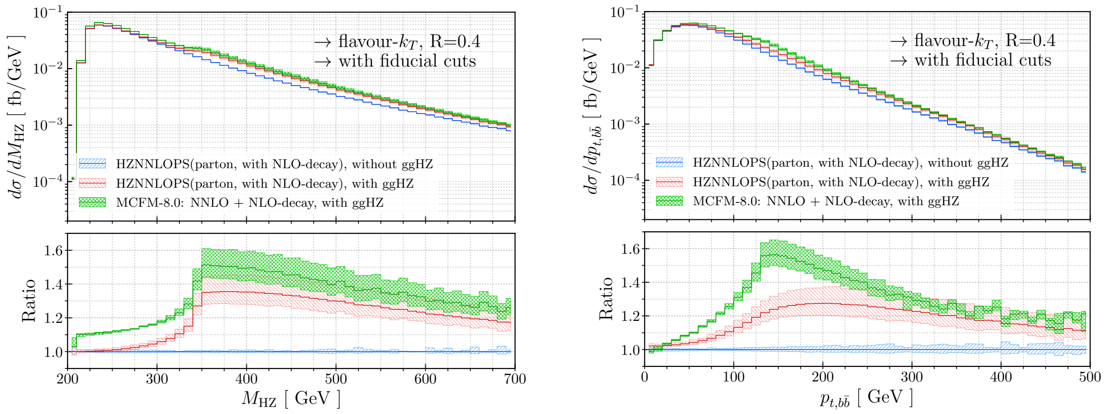

Figure 4.17: The differential distributions of the invariant mass of the HZ system (left panel) and the transverse momentum of the Higgs boson reconstructed from b-jets (right panel). The lower panel illustrate ratio of full results (NNLO as well as NNLO+PS) to the NNLO+PS results without $gg \to$HZ contribution.

additional QCD radiation off the coloured partons tends to soften the jets some b-jets may end up outside the fiducial phase-space volume reducing the recorder cross section.

We now consider the fiducial volume with the additional $p_{t,\rm Z}$ cut reported in the last two rows of Tab. 4.2. We see that the cross sections are reduced by about a factor of 5 with respect to the ones integrated over the whole $p_{t,\rm Z}$ spectrum. We observe a very similar pattern as in the case without $p_{t,\rm Z}$-cut, with a small difference in the impact of the $gg \to$ HZ contribution – in this situation the cross section increases by more than 20% after including this gluonic correction. This is also reflected in larger scale uncertainties than in previous case.

In order to look at the impact of $gg \to$HZ contribution in a slightly bigger capacity, we present in Fig. 4.17 the distributions of the invariant mass of the HZ system ($M_{\rm HZ}$)and the transverse momentum of the Higgs boson as reconstructed from b-quarks ($p_{t,b\bar{b}}$). We note that for the $M_{\rm HZ}$ calculation we use Monte Carlo truth, i.e. momenta of H and Z bosons as passed by the generator instead of ones reconstructed from decay products, while $p_{t,b\bar{b}}$ is obtained from the system of two b-jets used for the Higgs reconstruction, as described earlier. We show the `HZ-NNLOPS` results at parton level with (red) and without (blue) the $gg \to$HZ channel, we also show a result of a fixed-order NNLO accurate calculation obtained with `MCFM-8.0` (blue). The large impact of the new correction is clearly visible. We see that in the case of $M_{\rm HZ}$ distribution the biggest effect (reaching up to +40%) can be observed in the region above 350 GeV, which is a footprint of the top-quark threshold. The difference between `MCFM-8.0` and `HZ-NNLOPS` amounts to a uniform shift. As discussed earlier, parton shower evolution leads to a decrease in the fiducial cross section mainly due to b-jet cuts, however, the HZ invariant mass is not strictly correlated with the Higgs kinematics leading to a moderately constant K-factor between `HZ-NNLOPS` and `MCFM-8.0`.

In the case of $p_{t,b\bar{b}}$, similarly to M_{HZ}, we observe large differences after including $gg \to \mathrm{HZ}$ contribution. For the parton shower prediction a sizeable impact is present for $p_{t,b\bar{b}} \geqslant 100$ GeV, and it reaches up to 30% in region around 200 GeV. The difference between `HZ-NNLOPS` and `MCFM-8.0` is quite different than in case of M_{HZ}: the biggest differences between the fixed-order prediction and the one of a parton shower are located around moderately-high transverse momenta (∼150 GeV), at very high-$p_{t,b\bar{b}}$ the discrepancy becomes much smaller.

4.5.5 Phenomenological analysis of the $\mathrm{H} \to b\bar{b}$ decay

After establishing the accuracy of the `HZ-NNLOPS` generator and describing the interface to parton shower we can now proceed to the analysis of the Higgs boson decay to a pair of b-quarks. We have already outlined the way we define b-jets and how to proceed in case more than two b-flavoured jets are identified. We are then well prepared to study the physical distributions of observables related to $\mathrm{H} \to b\bar{b}$ decay.

As the first exercise we want to examine differences between the properties of the true Higgs boson and the one reconstructed with the help of b-jets. In Fig. 4.18 we show the distribution of the transverse momentum of the true Higgs boson as well as its counterparts related to reconstructed $b\bar{b}$-system. The true distribution is labelled with `MC-truth` (blue) and has been prepared using the momentum of the Higgs boson passed directly from a Monte Carlo generator. The other two curves correspond to the transverse momentum distribution of the $b\bar{b}$-system in `MCFM-8.0` (green) and `HZ-NNLOPS` (red). We choose the true Higgs `HZ-NNLOPS` distribution as a baseline in ratio plots.

We start by discussing the results without the $gg \to \mathrm{HZ}$ contribution, left panels of the figure. In the region of small transverse momenta the difference between red and blue curve is larger for smaller jet radius, this leads to a conclusion that the dominant

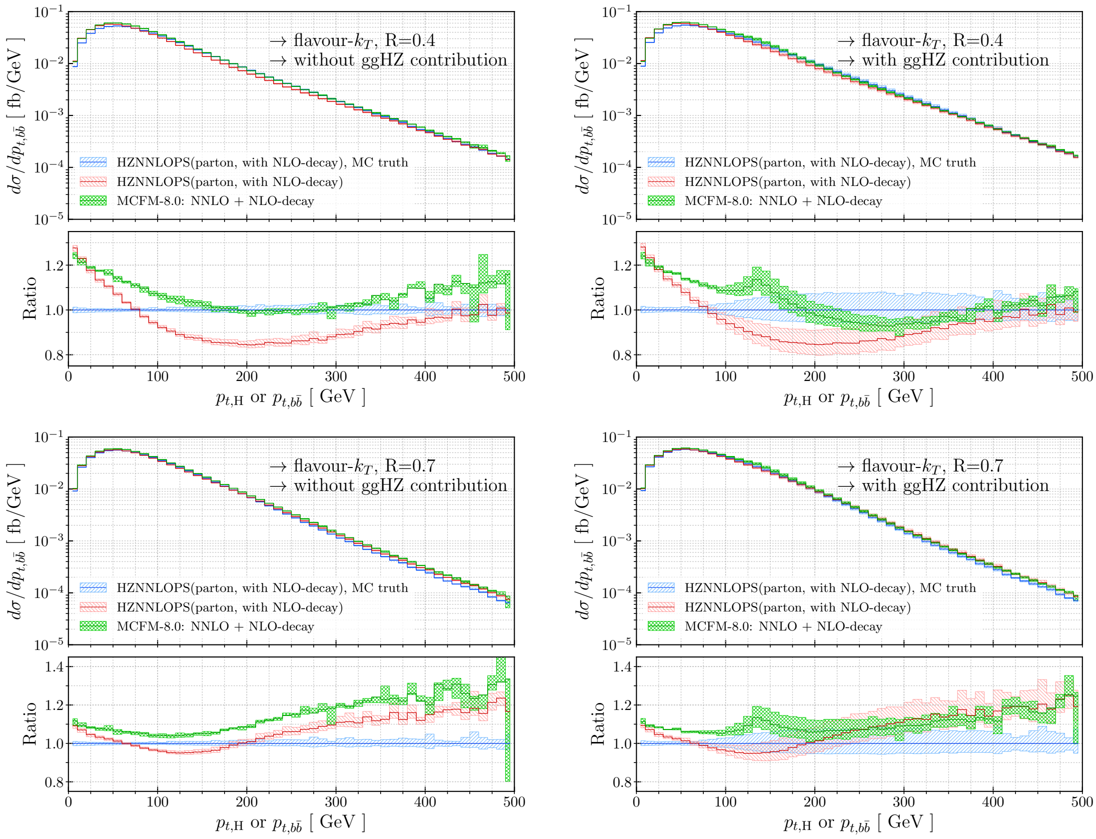

Figure 4.18: The differential distributions of the transverse momentum of the Higgs boson. `MC-truth` label refers to the actual Higgs boson momentum as passed from the event generator, other lines represent the reconstruction of the Higgs boson momentum using the two b-jets with invariant mass closest to M_{H}. The upper two plots show results when jets are clustered with $R = 0.4$, the lower plots refer to $R = 0.7$. Left plots do not include the $gg \to \mathrm{HZ}$ contribution, while the right ones do.

mechanism driving the discrepancy is out-of-jet radiation from the $b\bar{b}$ final state. On the other hand, when considering hard part of the spectrum the `HZ-NNLOPS` $b\bar{b}$ curve is much closer to the `MC-truth` for smaller radius ($R = 0.4$). This means that the effect important in the tail of the distribution is related to the radiation off the initial-state light partons – the smaller R makes it less likely for radiation to be clustered into the $b\bar{b}$-system. Furthermore, we observe sizeable differences between the fixed-order prediction `MCFM-8.0` and the `HZ-NNLOPS` one at intermediate values of $p_{t,b\bar{b}}$ for small R, while they are less pronounced in case of $R = 0.7$. Such outcome can be traced to the inclusivity of the observable which grows with the jet radius R; the more inclusive the observable is, the better the agreement between the fixed-order and parton shower results.

The results including $gg \to \mathrm{HZ}$ contribution are presented in the right panels of Fig. 4.18.

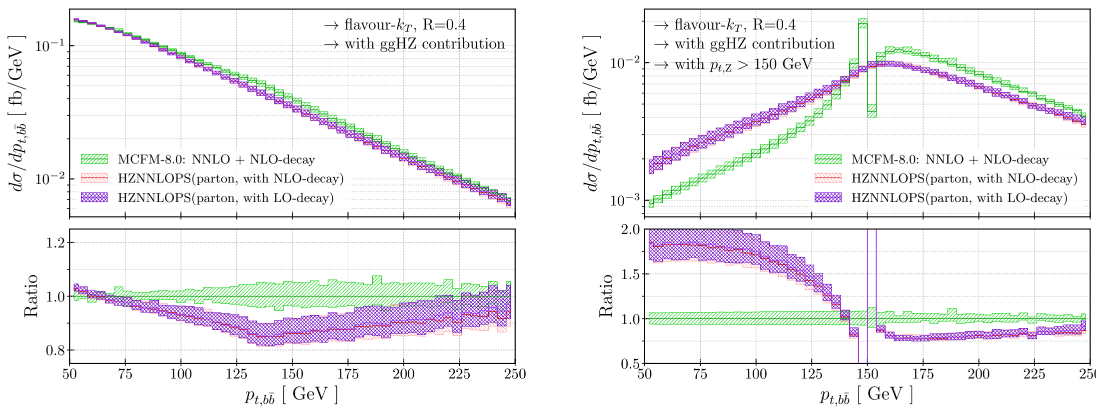

Figure 4.19: The differential distribution of the transverse momentum of the $b\bar{b}$-jet system without (left) and with (right) the $p_{t,\mathrm{Z}} > 150$ GeV cut. Results include the $gg \to$HZ contribution.

One can draw similar conclusions about the shape of the distributions in the small-p_t and large-p_t limits. We also notice a characteristic sharp peak that appears for `MCFM-8.0` result (green) in the ratio plot. It is a feature of the additional $gg \to$HZ contribution, as already observed in right panel of Fig. 4.17: such a peak is smeared by parton shower and hence not observed in the ratio of `HZ-NNLOPS` $p_{t,b\bar{b}}$ prediction (red). We also notice a significant increase in the scale uncertainty of the prediction that includes $gg \to$HZ correction with respect to the one that does not. As already discussed earlier, such effect originates from the fact that loop-induced $gg \to$HZ contribution is described only at the leading-order.

In Fig. 4.19 we again show the transverse momentum of the $b\bar{b}$-system. We show the `HZ-NNLOPS` predictions with LO (purple) and NLO (red) treatment of the $\mathrm{H} \to b\bar{b}$ decay together with `MCFM-8.0` results (green). In case of `HZ-NNLOPS` with LO decay, we leave the radiation from $b\bar{b}$ dipole to parton shower. A first interesting observation is the lack of significant differences between the two `HZ-NNLOPS` simulations, one with NLO $\mathrm{H} \to b\bar{b}$ matrix elements and the other with LO treatment of $\mathrm{H} \to b\bar{b}$. It is remarkable that parton shower equipped with matrix element corrections performs very well and is almost indistinguishable from the full NLO calculation in this case. Moreover, we see that imposing a high-$p_{t,\mathrm{Z}}$ cut leads to a creation of a Sudakov shoulder at $p_{t,b\bar{b}} = 150$ GeV in the fixed-`MCFM-8.0` prediction. Such a behaviour is a well known feature of fixed-order calculations and has been already pointed out in Figs.(6) and (12) of Ref. [175]. It can be associated with soft gluon emissions that occur in kinematical configurations that

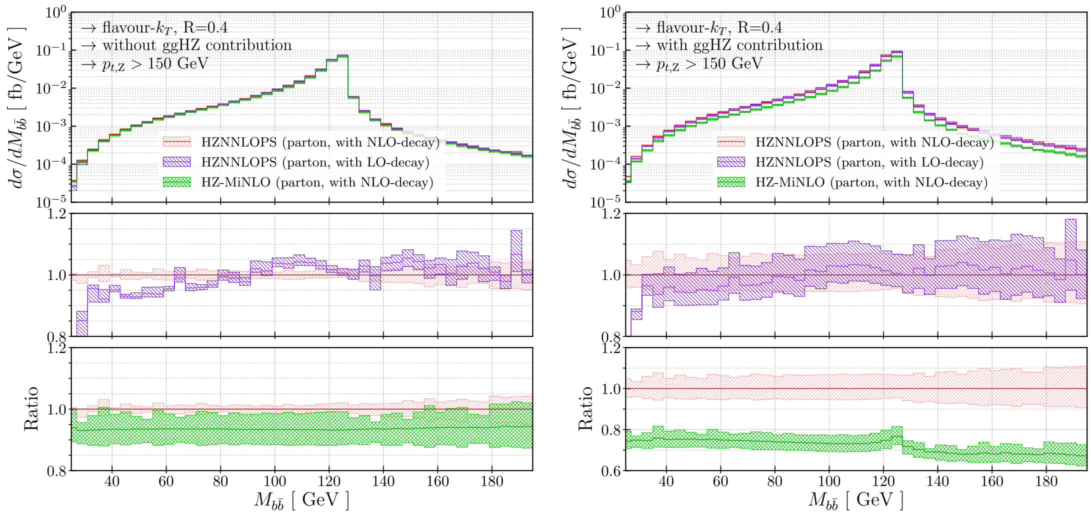

Figure 4.20: The differential distributions of the invariant mass of the $b\bar{b}$-system used for reconstruction of the Higgs boson. Comparison of `HZ-NNLOPS` results with LO and NLO decay matrix elements, excluding $gg \to$HZ channel (left) and with $gg \to$HZ (right).

are close to the $p_{t,\mathrm{Z}} > 150$ GeV cut. On the contrary, the distribution obtained with `HZ-NNLOPS` does not show a similar response to the $p_{t,\mathrm{Z}}$ cut as parton shower captures parts of the resummation effects.

Finally we focus on the spectrum of the invariant mass of the $b\bar{b}$-system, which is one of the most important variables used for identification of a heavy-resonance decay. At leading-order the $M_{b\bar{b}}$ distribution follows an extremely narrow Breit-Wigner function, with a central value and width dictated by the Higgs boson (M_H and Γ_H). At higher-orders it receives sizeable corrections away from the peak. We note that the region below the peak, $M_{b\bar{b}} < M_\mathrm{H}$, is populated only when real emissions from the $b\bar{b}$ dipole occur. On the other hand, to fill the high-$M_{b\bar{b}}$ region above the peak a real radiation from the production stage has to be clustered into b-jets.

In Fig. 4.20 we show the $M_{b\bar{b}}$ distribution obtained by using `HZJ-MiNLO` generator with NLO H $\to b\bar{b}$ decay (green) as well as the ones of `HZ-NNLOPS` generator with LO (purple) and NLO (green) treatment of the decay. We consider case without (left panel) and with (right panel) the $gg \to$HZ contribution. There are a number of features that one can infer from presented histograms. First of all we note that the `HZ-NNLOPS` results with LO/NLO treatment of the decay are again compatible with each other across the whole spectrum with discrepancies reaching the level of at most 5-10% at very low values of $M_{b\bar{b}}$. This again confirms that parton shower captures the corrections to $\mathrm{H} \to b\bar{b}$ decay very well. Moreover such a picture has been also observed when considering NNLO treatment of the decay (compare with right panel of Fig.(11) in Ref. [175]).

Another issue that needs to be discussed is the size of the scale uncertainty band which is very small when no $gg \to \mathrm{HZ}$ contribution is included, reaching only a few percent width. The uncertainty increases when $gg \to \mathrm{HZ}$ events are taken into account as a result of large scale dependence of this contribution, as mentioned in previous section. It is worth pointing out that the Higgs decay is treated only at the LO in $gg \to \mathrm{HZ}$ contribution, hence all these events would contribute only to the peak ($M_{b\bar{b}} = M_{\mathrm{H}}$) and it is only thanks to parton shower that the contribution is smeared over the whole spectrum. The small scale variation is not indicative of the true uncertainty on this distribution and there are two effects that give rise to such a result. One of them is related to the fact that `HZJ-MiNLO` events have been reweighted to NNLO results. In fact, the pure `HZJ-MiNLO` prediction (green band) has larger uncertainty reaching up to ±10%. The second issue enters already at the `HZJ-MiNLO` level as the true fixed-order uncertainty, calculated in `MCFM-8.0`, is of order ±(15-20)%. This is a consequence of a well known fact that, in plain `POWHEG` simulation, the scale is varied only at the level of the $\bar{B}$ function, which is by definition inclusive over radiation, whereas the $M_{b\bar{b}}$ spectrum is sensitive to radiation. A similar outcome has been presented in right panels of Figs. 4.8 and 4.9.

We now want to focus on the comparison between `HZ-NNLOPS` (red) and fixed order calculation (green) presented in Fig. 4.21. We similarly show results without (left) and with (right) $gg \to \mathrm{HZ}$ contribution. Moreover we have studied two cases: jets clustered with $R = 0.4$ (top panels) and $R = 0.7$ (bottom ones). We notice a sizeable enhancement of the spectrum in the region $M_{b\bar{b}} < M_{\mathrm{H}}$. Such an effect has been already observed in Refs. [174, 175] and is even more dramatic in this case. We see an even larger K-factor than the one inferred from Figs.(4) and (11) of Ref. [175], however we must keep in mind that there are number of differences between the two predictions. Barring the differences related to production stage of HZ and HW^- states, the results of [175] are obtained using different fiducial cuts; clustering algorithm with $R = 0.5$ and more stringent cut for b-jets,

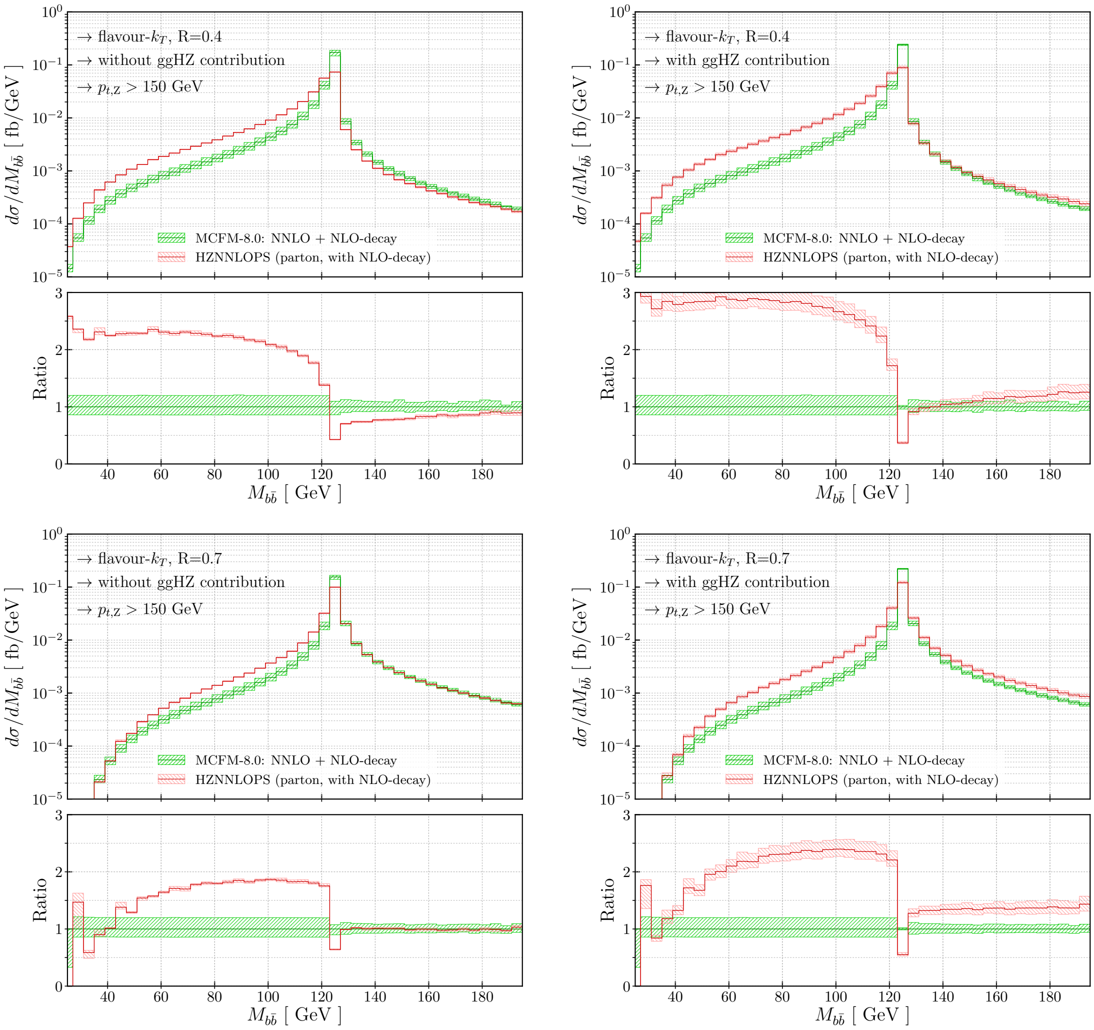

Figure 4.21: The differential distributions of the invariant mass of the $b\bar{b}$-system used for reconstruction of the Higgs boson. We present the results obtained with jet clustering with $R = 0.4$ (top) and $R = 0.7$ (bottom) excluding $gg \to$ HZ channel (left panels) and with $gg \to$ HZ (right panels).

requiring them to be harder than 25 GeV. Secondly, in our case both `MCFM-8.0` as well as `HZ-NNLOPS` use massive b-quarks in calculation, while the approach of Ref. [175] has been obtained using massless quarks. Finally, our plots show the `HZ-NNLOPS` results rather than `HZJ-MiNLO` ones, and as it can be read from Fig. 4.20 this amounts to further increase of the ratio by almost 10% in case without $gg \to$ HZ term. When considering results with $gg \to$ HZ contribution the K-factor between `HZ-NNLOPS` and `MCFM-8.0` is even bigger. As already mentioned earlier, this can be linked to the fact that in case of the fixed-order calculation $M_{b\bar{b}} = M_{\rm H}$ for all $gg \to$ HZ events, whereas the contribution is spread over a whole spectrum by parton shower evolution (i.e. `HZ-NNLOPS`). Comparing the different

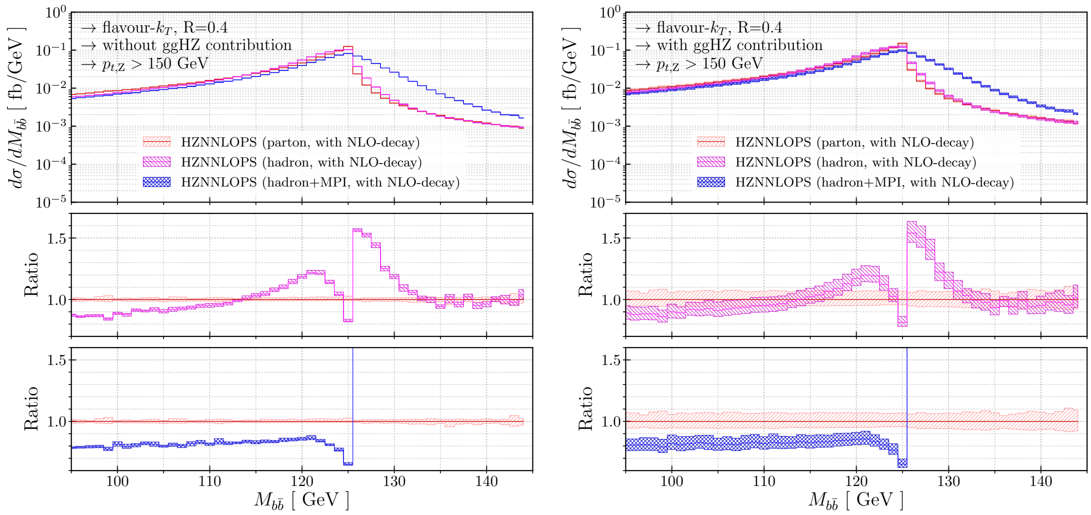

Figure 4.22: The differential distributions of the invariant mass of the $b\bar{b}$-system used for reconstruction of the Higgs boson. Comparison of `HZ-NNLOPS` results with NLO decay matrix elements at parton-, hadron-level and with multi-parton interactions (MPI), excluding $gg \to \mathrm{HZ}$ channel (left panels) and with $gg \to \mathrm{HZ}$ (right panels).

jet radii used for clustering, we see that the fixed-order results and the ones matched to parton shower are closer to each other when jet radius is larger. This comes as a result of inclusivity of the observable which increases along with jet radius.

Lastly, we analyse the $M_{b\bar{b}}$ distribution at various stages of event simulation. In Fig. 4.22 we show `HZ-NNLOPS` results at parton level (red), after hadronization (magenta), and final results after hadronization including MPI effects (blue). We observe that hadronization smears the distribution in the vicinity of the peak, this is the reason for the dip at $M_{b\bar{b}} = M_{\mathrm{H}}$ in the first ratio plots (distribution after hadronization vs. result at purely partonic level). Since colour-connections tend to reduce spatial distances between partons during hadronization, more radiation is clustered within b-jets and hence the region at very low invariant masses is underpopulated with respect to the prediction at parton level. Such effect is further enhanced when we consider MPI, as even more radiation is available for clustering hence moving many events towards larger values of $M_{b\bar{b}}$. In the regime of high invariant masses, $M_{b\bar{b}} > M_{\mathrm{H}}$, hadronization has very little impact. The situation drastically changes when MPI are included due to intensified radiation activity which again provides many additional hadrons to be clustered within b-jets increasing the invariant mass of the $b\bar{b}$-system.

To conclude, we have presented and analysed predictions of a fully-differential `HZ-NNLOPS` generator, that provides description of 0-jet observables at NNLO accuracy while maintaining NLO accuracy of 1-jet observables. We have included a Higgs boson decay into a pair of b-quarks at NLO and examined most important features characteristic for $\mathrm{H} \to b\bar{b}$ decay: the distributions of observables constructed upon the momentum of $b\bar{b}$-system used for reconstructing the Higgs boson. We have also included a $gg \to \mathrm{HZ}$ contribution that appears at $\mathcal{O}(\alpha_s^2)$ order but nevertheless comprises a sizeable part of the total cross section. We have identified large differences between pure NLO decay at fixed-order perturbation theory (`MCFM-8.0`) and when NLO decay is interfaced with parton shower. Such discrepancies were especially large in the case of $M_{b\bar{b}}$ distribution. We know that partially the effect can be attributed to missing higher-order (NNLO) corrections to a decay, as already recognised in Refs. [174, 175]. Due to the size of observed effects, matching a simulation of an NNLO accurate $\mathrm{H} \to b\bar{b}$ decay to a parton shower would be desirable.

5

Exploring the Higgs Sector

In previous chapters of this work we have extensively discussed various methods of tackling problems arising in perturbative QCD and obtaining high-precision predictions for hadronic colliders, such as the LHC. In the last part we would like to illustrate how the precision physics might be used in addressing physical questions appearing in the context of Standard Model extensions. In particular, we will discuss an attempt of constraining the trilinear self-coupling of the Higgs boson using loop-induced effects affecting the associated Higgs production (VH) and vector boson fusion (VBF) Higgs production channels, as well as the Higgs decay widths. Such analysis has been a subject of Ref. [20].

5.1 Preliminaries and the SM Effective Field Theory

The Higgs field is currently the only fundamental scalar field in the Standard Model. It is a doublet under the $SU(2)$ gauge group and is responsible for fermion masses, via Yukawa couplings, as well as masses of the electroweak gauge bosons thanks to the Goldstone bosons resulting from the electroweak symmetry breaking (EWSB) [199, 200, 201].

After the EWSB, the mass and self-interactions of the Higgs field h can be parametrised by the potential

$$\mathcal{L}_{\text{Higgs}} \supset \frac{1}{2}\left(\partial_\mu\right)^2 - \frac{M_{\text{H}}^2}{2}h^2 - \lambda \text{v} h^3 - \frac{\kappa}{4}h^4, \tag{5.1}$$

where $\mathrm{v} = 246.22$ GeV denotes the Higgs vacuum expectation value, $M_{\mathrm{H}} = 125.09$ GeV is the mass of the Higgs boson as measured by the LHC [202], and λ and κ are the dimensionless coupling constants describing the self-interactions of the Higgs field. Withing the SM, the values of the Higgs self-couplings read

$$\lambda = \kappa = \frac{M_{\mathrm{H}}^2}{2\mathrm{v}^2}. \tag{5.2}$$

Measurement and verification of the Higgs boson self-interactions will be a crucial step towards underpinning the mechanism of the EWSB and hence a very important goal of the high-luminosity program at the LHC (HL-LHC), as well as other future high-energy colliders.

A simple way of constraining the coefficients λ and κ is by measuring the cross section for multi-Higgs production channels. Unfortunately, the cross section for $pp \to 3h$ is of $\mathcal{O}(0.1\text{fb})$ at $\sqrt{s} = 14$ TeV and will remain elusive even for the advanced HL-LHC programme. The double-Higgs production, $pp \to 2h$, channel is appreciably better with the cross section of $\mathcal{O}(35\text{fb})$ [203, 204]. Nevertheless, despite availability of the higher-order corrections to the process [205, 206, 207, 208, 209], the measurement itself will be challenging and even with the full data set of the HL-LHC only $\mathcal{O}(1)$ determination of the trilinear coupling seems possible.

A complementary path, that might provide comparable constraints for the λ coupling, resides on studying effects of the anomalous Higgs self-coupling that appear in single-Higgs production channels at the loop-level. Such technique has been first proposed in the context of precision studies in e^+e^- colliders [210, 211] and subsequently applied in the context of the LHC [212, 213, 20].

The Standard Model Lagrangian $\mathcal{L}_{\mathrm{SM}}$ consists of various dimension-four operators that are gauge-invariant under its symmetry group, $SU(3) \otimes SU(2) \otimes U(1)_{\mathrm{Y}}$, providing a renormalisable theory describing the strong interactions as well as the electroweak sector. A comprehensive way of constraining the SM parameters, as well as quantifying possible deviations from the theory, can be formulated by supplying the Lagrangian with higher-dimensional operators constructed with the SM fields and by putting constraints on their Wilson coefficients. Such an approach, in terms of gauge theories, has been described a long time ago [214] and has been used in many different contexts since. A list of dimension-six operators that supply an extension of the SM Lagrangian has been given in Ref. [215] and further scrutinised in Ref. [216]. As a consequence SM Effective Field Theory (SM EFT) was born providing a model-independent framework for constraining the possible effects beyond the SM (BSM). The SM EFT has been actively studied in recent years, some of the results can be found in recent reviews in Refs. [217, 218]. Operators of even higher-dimensions can also be considered. A complete set of dimension-seven operators has been proposed in Ref. [219]; number of higher-order operators can be predicted [220] but no complete basis has been constructed beyond operators of dimension-seven.

For our analysis, we will consider the following extension of the SM Lagrangian

$$\mathcal{L} = \mathcal{L}_{\text{SM}} + \sum_{k\in\{6,H\}} \frac{\bar{c}_k}{\text{v}^2}\mathcal{O}_k, \tag{5.3}$$

where the two additional operators are

$$\mathcal{O}_6 = -\lambda(H^\dagger H)^3, \qquad \text{and} \qquad \mathcal{O}_H = \frac{1}{2}\partial_\mu(H^\dagger H)\partial^\mu(H^\dagger H), \tag{5.4}$$

with λ defined as previously in Eq. (5.1), and H denoting the SM Higgs doublet. Using the canonical normalisation, the trilinear self-coupling term receives a modification

$$\lambda \text{v} h^3 \qquad \longrightarrow \qquad \lambda c_3 \text{v} h^3 \equiv \lambda\left(1 + \bar{c}_6 - \frac{3}{2}\bar{c}_H\right)\text{v}h^3, \tag{5.5}$$

where the Wilson coefficients $\bar{c}_6$ and $\bar{c}_H$ as well as the coupling λ are evaluated at the EWSB scale μ_{W}. Furthermore, we will put an emphasis on the BSM scenarios where the $\bar{c}_6$ coefficient represents the only relevant modification. Corrections originating from $\mathcal{O}_H$ operator are ignored; as they would lead to universal shift in all Higgs boson couplings at tree-level and also induce logarithmically-enhanced contributions to the electroweak oblique parameters at one-loop [221] and hence the $\bar{c}_H$ coefficient can be probed by other means.

In the SM EFT framework we can distinguish two types of corrections affecting the VVh vertex, with V$\in \{\text{W}, \text{Z}\}$. On one hand, we can identify logarithmic terms of

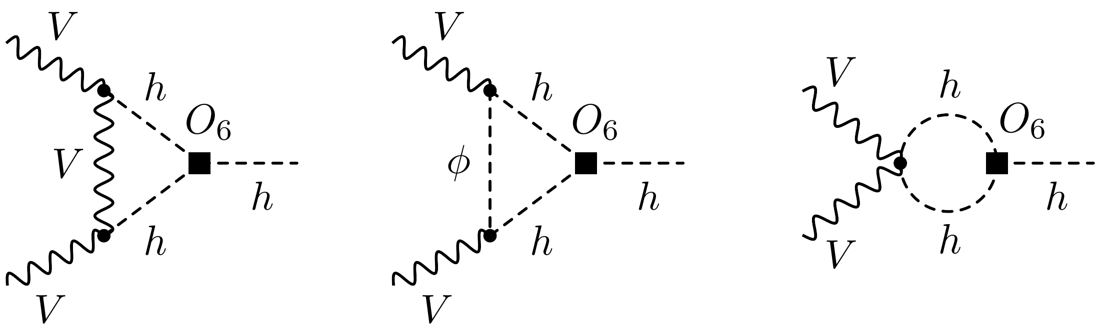

Figure 5.1: The one-loop diagrams with an insertion of the effective operator $\mathcal{O}_6$ which contribute to the VVh vertex at $\mathcal{O}(\lambda)$. The field ϕ corresponds to a Goldstone mode that needs to be included if the calculation is performed in an R_ξ gauge.

the form $\log\left(\Lambda_{\rm NP}/\mu_{\rm W}\right)$ that are induced by the renormalisation group evolution which connects the New Physics scale $\Lambda_{\rm NP}$ to the EWSB scale $\mu_{\rm W}$. Since the $\mathcal{O}_6$ operator does not mix with others at the one-loop level [222, 223, 224], the VVh vertex is free of logarithmically-enhanced corrections proportional to $\bar{c}_6$ at first non-trivial order in perturbation theory. The second type of corrections corresponds to the finite contributions that arise the loop-induced effects in the VVh Green's function with a modified h^3 self-interaction. The renormalised vertex

$$\mathrm{V}^\mu(q_1) + \mathrm{V}^\nu(q_2) \longrightarrow h(q_1+q_2), \qquad \text{with } (q_1+q_2)^2 = M_{\rm H}, \tag{5.6}$$

receives contributions from several one-loop diagrams, illustrated in Fig. 5.1, and a tree-level counterterm graph involving Higgs wave-function renormalisation. The relevant contributions can be determined using `FeynArts` [225] and `FormCalc` [226], and they read

$$\Gamma^{\mu\nu}_{\rm V}(q_1,q_2) = 2\left(\sqrt{2}G_F\right)^{1/2} M_{\rm V}^2\Big[\eta^{\mu\nu}\left(1+\mathcal{F}_1(q_1^2,q_2^2)\right) + q_1^\mu q_2^\nu \mathcal{F}_2(q_1^2,q_2^2)\Big], \tag{5.7}$$

where $G_F = 1/(\sqrt{2}\mathrm{v}^2)$ is the Fermi constant, $\eta^{\mu\nu}$ is the metric tensor, $M_{\rm V}$ is the mass, and q_1^μ and q_2^ν are the four-momenta of external gauge bosons. The vertex function $\Gamma^{\mu\nu}_{\rm V}(q_1,q_2)$ contains only Lorentz structures that give rise to a non-vanishing contributions when contracting with massless fermion lines. The relevant formulae for form factors $\mathcal{F}_1$ and $\mathcal{F}_2$ are reported in Appendix C. Note that the SM tree-level contribution has been included in the definition of $\Gamma^{\mu\nu}_{\rm V}(q_1,q_2)$.

In the next sections we will report modifications to cross sections and decay widths originating from the modified VVh vertex.

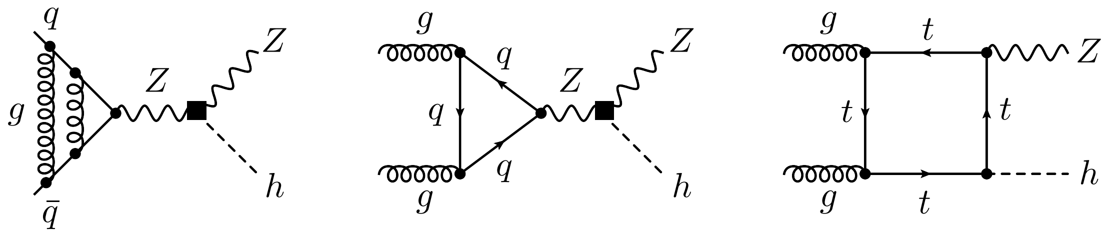

Figure 5.2: Examples of diagrams that contribute to $pp \to$ HZ in NNLO QCD calculation. The black square indicates an insertion of the modified VVh vertex.

5.2 Corrections to the Higgs production and decay modes

In this section we report the modifications that appear in the cross sections and decay widths once the $\mathcal{O}_6$ operator is included. We briefly describe the numerical implementation of VH/VBF production modes, while leaving all the relevant formulae as well as description of the decay widths calculation for the Appendix C.

5.2.1 Implementation of the VH modifications

We use the existing `MCFM-8.0` implementation of the fully differential NNLO QCD calculation of the $pp \to$ VH processes [168].

In the NLO QCD computation the effects due to modified VVh vertex factorise and can be easily included by modification of the relevant `MCFM-8.0` routines. However, at NNLO we encounter different types of corrections which we illustrate in Fig. 5.2. The first family of diagrams, depicted in the left-hand-side diagram of Fig. 5.2, corresponds to the Drell-Yan-like corrections which contain an s-channel Z boson exchange and can also be factorized similarly to the case of $\mathcal{O}(\alpha_s)$ diagrams. The second type of contributions involve diagrams that feature a heavy-quark loop and the Higgs boson radiated directly off the heavy-quark line (see the right-hand-side diagram of Fig. 5.2) or where the Higgs boson is coupled to the electroweak Z boson (see the middle diagram). A careful analysis of the numerical code allows for adjustment of the routines related to the corrections involving a heavy-quark loop and a ZZh modified vertex, hence these $\mathcal{O}(\lambda)$ corrections have been included in our analysis. However, the $\mathcal{O}(\lambda)$ corrections to the diagrams that contain the Higgs boson directly coupled to a heavy-quark loop (see the right diagram of Fig. 5.2) would require knowledge of some two-loop integrals with multiple scales involved; these are currently unknown, therefore we omit this class of diagrams. Effects of the Higgs wave-function renormalisation are universal and we take them into account. All relevant formulae are reported in Appendix C.2.

5.2.2 Implementation of the VBF modifications

To obtain the predictions for the VBF Higgs production we employ the structure-function approach [227] that describes the process as a double deep-inelastic scattering (DIS) process with two virtual electroweak gauge bosons fusing into a Higgs boson. Up to small interference effects between the two fermionic lines, the differential VBF Higgs cross section can be constructed using a modified $\mathrm{VV}h$ vertex and the two DIS hadronic tensors.

Our numerical calculations rely on the MC codes developed in Ref. [67] with suitably modified coefficients of the structure functions. We report all relevant formulae in Appendix C.2 and further details can be found in Section 6 of Ref. [20].

5.2.3 Numerical results

In this section we summarise the impact of the modified $\mathrm{VV}h$ vertex, that contains effects of the anomalous Higgs self-coupling, on the inclusive cross sections σ_I with $I \in \{\mathrm{HW}, \mathrm{HZ}, \mathrm{VBF}\}$, as well as the relevant differential distributions. We also report changes that appear in the partial decay widths, $\Gamma(\mathrm{H} \to \mathrm{F})$, for various final states F and corresponding branching ratios, $\mathrm{Br}(\mathrm{H} \to \mathrm{F})$. For our predictions we have used the `PDF4LHC15_nnlo_mc` PDFs [136]. The central scale choice for factorization and renormalisation scales is $\mu_0 = M_\mathrm{V} + M_\mathrm{H}$ for the VH process and $\mu_0 = M_\mathrm{H}$ for the VBF Higgs production.

For the calculation of partial decay widths we have used $\alpha_s(M_\mathrm{H}) = 0.1127$, the masses and decay widths of the electroweak gauge bosons are $M_\mathrm{Z} = 91.15$ GeV and $M_\mathrm{W} = 80.37$ GeV with $\Gamma_\mathrm{Z} = 2.4958$ GeV and $\Gamma_\mathrm{W} = 2.0886$ GeV. The fermion masses used in our calculations are $m_t = 173.2$ GeV, $m_b(M_\mathrm{H}) = 2.81$ GeV and $m_c(M_\mathrm{H}) = 0.65$ GeV for the top, bottom and charm quarks respectively. Moreover we set $m_\tau = 1.777$ GeV. The quoted masses for bottom and charm quarks correspond to the $\overline{\mathrm{MS}}$ masses and have been obtained using two-loop running. The total decay width of the Higgs boson is

$\sqrt{s}$ / σ_I	HW	HZ	VBF
8 TeV	(0.76 ± 0.02) pb	(0.42 ± 0.01) pb	(1.66 ± 0.04) pb
13 TeV	(1.49 ± 0.03) pb	(0.87 ± 0.03) pb	(3.94 ± 0.08) pb

Table 5.1: The SM inclusive cross section for various Higgs production channels $I \in \{\mathrm{HW}, \mathrm{HZ}, \mathrm{VBF}\}$. We show results for hadronic collisions with the centre-of-mass energy equal to 8 TeV (first row) and 13 TeV (second row). The quoted uncertainties include scale, PDF and α_s errors.

$\Gamma_{\mathrm{H}} = 4.088$ GeV.[1]

We report the total cross sections for various channels I in the Table 5.1. The corresponding modifications originating from the $\mathcal{O}_6$ operator parametrised in terms of the $\bar{c}_6$ Wilson coefficient at $\sqrt{s} = 8$ TeV are

$$\begin{aligned}
\sigma_{\mathrm{HW}}^{8\,\mathrm{TeV}} &= \left(\sigma_{\mathrm{HW}}^{8\,\mathrm{TeV}}\right)_{\mathrm{SM}} \times \left(1 + 7.4 \cdot 10^{-3}\,\bar{c}_6 - 1.5 \cdot 10^{-3}\,\bar{c}_6^2\right), \\
\sigma_{\mathrm{HZ}}^{8\,\mathrm{TeV}} &= \left(\sigma_{\mathrm{HZ}}^{8\,\mathrm{TeV}}\right)_{\mathrm{SM}} \times \left(1 + 7.5 \cdot 10^{-3}\,\bar{c}_6 - 1.5 \cdot 10^{-3}\,\bar{c}_6^2\right), \\
\sigma_{\mathrm{VBF}}^{8\,\mathrm{TeV}} &= \left(\sigma_{\mathrm{VBF}}^{8\,\mathrm{TeV}}\right)_{\mathrm{SM}} \times \left(1 + 3.3 \cdot 10^{-3}\,\bar{c}_6 - 1.5 \cdot 10^{-3}\,\bar{c}_6^2\right),
\end{aligned} \tag{5.8}$$

and similarly at $\sqrt{s} = 13$ TeV we have

$$\begin{aligned}
\sigma_{\mathrm{HW}}^{13\,\mathrm{TeV}} &= \left(\sigma_{\mathrm{HW}}^{13\,\mathrm{TeV}}\right)_{\mathrm{SM}} \times \left(1 + 8.2 \cdot 10^{-3}\,\bar{c}_6 - 1.5 \cdot 10^{-3}\,\bar{c}_6^2\right), \\
\sigma_{\mathrm{HZ}}^{13\,\mathrm{TeV}} &= \left(\sigma_{\mathrm{HZ}}^{13\,\mathrm{TeV}}\right)_{\mathrm{SM}} \times \left(1 + 8.0 \cdot 10^{-3}\,\bar{c}_6 - 1.5 \cdot 10^{-3}\,\bar{c}_6^2\right), \\
\sigma_{\mathrm{VBF}}^{13\,\mathrm{TeV}} &= \left(\sigma_{\mathrm{VBF}}^{13\,\mathrm{TeV}}\right)_{\mathrm{SM}} \times \left(1 + 3.3 \cdot 10^{-3}\,\bar{c}_6 - 1.5 \cdot 10^{-3}\,\bar{c}_6^2\right).
\end{aligned} \tag{5.9}$$

The dependence is illustrated in the left panel of Fig. 5.3. We can see that the linear term in the $\bar{c}_6$ parabola differs between VH and VBF Higgs production. This is because the terms affecting the linear component come both from the counterterm graphs involving the Higgs wave-function renormalisation as well as from the one-loop diagrams presented in Fig. 5.1. On the other hand, the quadratic term is universal for all processes as it stems only from the counterterms which are kinematically independent. In order to better illustrate the impact of the $\mathcal{O}(\lambda)$ corrections of the $\mathcal{O}_6$ operator we plot the ratio of the deviation from the SM to the reference SM cross section, $(\Delta\sigma_I/(\sigma_I)_{\mathrm{SM}})$, as a function of

[1] The total width of the Higgs boson as well as the branching ratios for individual channels have been taken from the *LHC Higgs Cross Section Working Group, CERN report 4*: `https://twiki.cern.ch/twiki/bin/view/LHCPhysics/CERNYellowReportPageBR`

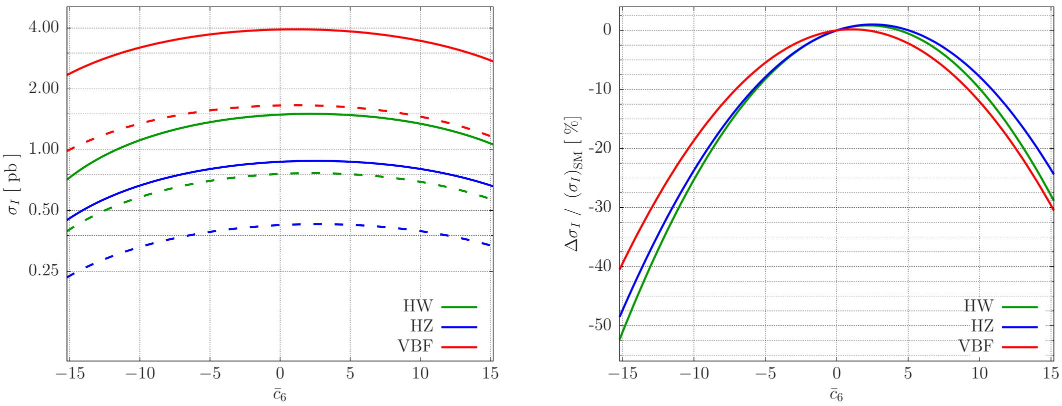

Figure 5.3: Left panel: Predictions for the inclusive HW, HZ and VBF Higgs production cross sections, σ_I, as a function of the $\bar{c}_6$ Wilson coefficient. The dashed lines correspond to $\sqrt{s} = 8$ TeV and solid lines to $\sqrt{s} = 13$ TeV. Right panel: Relative modifications of σ_I as a functions of $\bar{c}_6$, only results for $\sqrt{s} = 13$ TeV are shown.

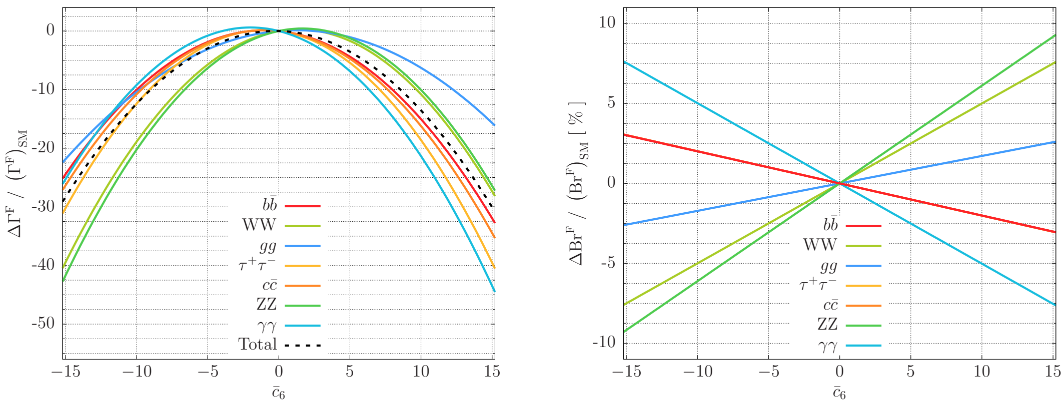

Figure 5.4: Shifts in the partial decay widths (left panel) and the branching ratios (right panel) of the various Higgs boson decay channels as a function of the $\bar{c}_6$ Wilson coefficient. The coloured solid lines correspond to individual decay channels, while the black dashed curve marks the full Higgs decay width.

the Wilson coefficient. The relevant curve is shown in the right panel of Fig. 5.3. The modifications reach about -25% and -30% at $\bar{c}_6 \simeq -15$ and $\bar{c}_6 \simeq +15$, respectively. We have drawn only a curve for $\sqrt{s} = 13$ TeV as the effects for $\sqrt{s} = 8$ TeV are of similar size, given the resemblance of functional forms in Eqs. (5.8) and (5.9).

We show the relative corrections to the various partial decay widths, $\left(\Delta\Gamma^{\mathrm{F}} / \left(\Gamma^{\mathrm{F}}\right)_{\mathrm{SM}}\right)$, as a function of the $\bar{c}_6$ Wilson coefficient in the left panel of Fig. 5.4. We again see that all of them follow very similar paths and are essentially always negative. This is, as in the inclusive cross section case, a result of the universal correction due to the Higgs wave-function renormalisation which dominates at large values values of the Wilson

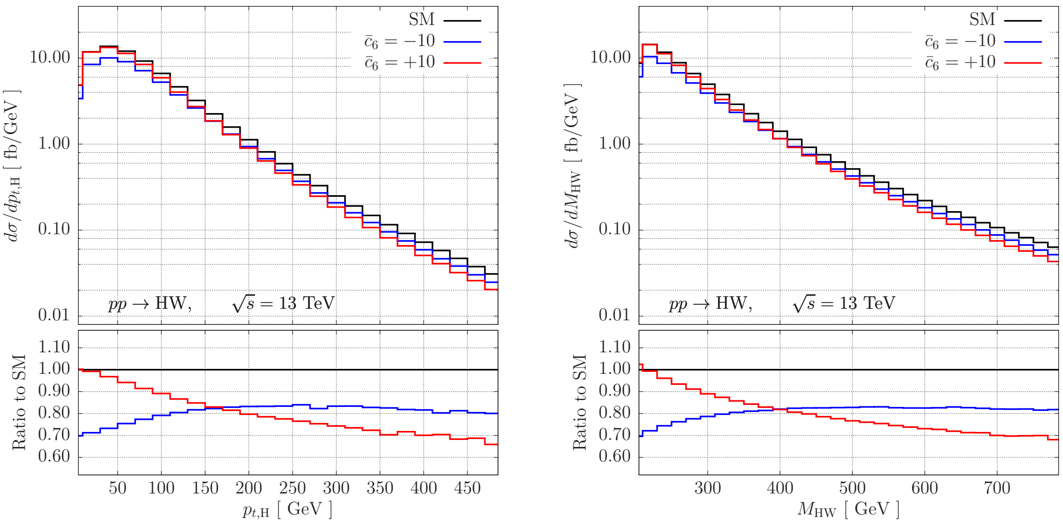

Figure 5.5: Comparison of the distributions of the Higgs boson's transverse momentum $p_{t,\mathrm{H}}$ (left panel) and the invariant mass of the HW system M_{HW} (right panel). The upper panels show the SM prediction (black) as well as the cases $\bar{c}_6 = -10$ (blue) and $\bar{c}_6 = +10$ (red). The lower panels show the ratios to the benchmark SM prediction. The results correspond to $pp \to \mathrm{HW}$ process at $\sqrt{s} = 13$ TeV.

coefficient, $\bar{c}_6 \gg 1$. The effect for the total decay width $\Delta\Gamma_{\mathrm{H}}$ is about -30% for $\bar{c}_6 \simeq \pm 15$. The impact on branching ratios, however, is substantially smaller reaching up to $\pm 10\%$ for comparable modifications of $\bar{c}_6$. This is too a consequence of a homogeneous universal correction that governs the leading behaviour at large values of the $\bar{c}_6$ coefficient since the quadratic dependence is cancelled out in the branching ratio.

Finally, we briefly discuss the modifications that appear in differential distributions of the VH and VBF Higgs production channels. We begin our discussion with the distributions corresponding to $pp \to \mathrm{HW}$ process at $\sqrt{s} = 13$ TeV. In Fig. 5.5, we show the results for the cases of the Higgs boson's transverse momentum $p_{t,\mathrm{H}}$ (left panel) and the invariant mass of the HW system M_{HW} (right panel). All results have been produced with the modified `MCFM-8.0` code, described in Section 5.2.1, at the NNLO QCD accuracy. It is clear that the presented distributions provide sensitivity to the anomalous $\bar{c}_6$ modification of the Higgs self-coupling. For $\bar{c}_6 = -10$, both distributions start at the level of -30% with respect to the SM prediction and they get slightly closer as $p_{t,\mathrm{H}}$ (or M_{HW}) increases, reaching a plateau at about -20% with respect to the SM at large values of $p_{t,\mathrm{H}}$ (or M_{HW}). In case of $\bar{c}_6 = +10$, on the other hand, the distributions start almost at the

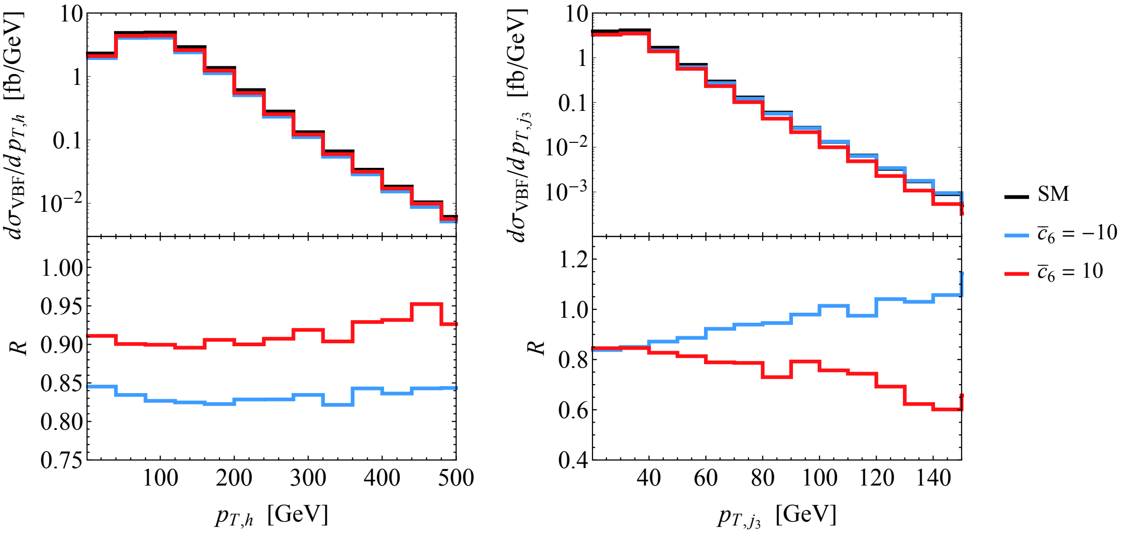

Figure 5.6: Comparison of the distributions of the Higgs boson's transverse momentum $p_{t,\rm H}$ (left panel) and the transverse momentum of the third hardest jet $p_{t,j3}$ (right panel). The upper panels show the SM prediction (black) as well as the cases $\bar{c}_6 = -10$ (blue) and $\bar{c}_6 = +10$ (red). The lower panels show the ratios to the benchmark SM prediction. The results correspond to VBF Higgs production process at $\sqrt{s} = 13$ TeV.

SM dropping down to relative corrections of about -30% with respect to the benchmark distribution. Such a behaviour enables us to distinguish between positive/negative sign of the $\bar{c}_6$ Wilson coefficient. The behaviour of the distribution at large values of $p_{t,\rm H}$ and $M_{\rm HW}$ can be understood from the $\sqrt{s} \to \infty$ limit of the VVh vertex modification. In this limit only the Higgs wave-function renormalisation contributes and this correction is independent of the kinematics leading to an approximately constant modification of the distribution at large transverse momenta or large invariant masses.

Furthermore, we investigate the distributions of the Higgs transverse momentum $p_{t,\rm H}$ and the transverse momentum of the third hardest jet $p_{t,j3}$ in the VBF Higgs production case. We show the relevant distributions in the left and right panels of the Fig. 5.6, respectively. We follow the same colour code as in the case of Fig. 5.5. In order to provide more realistic predictions we have implemented the VBF selection cuts, which require at least two jets with $p_{t,j} > 25$ GeV and $|y_j| < 4.5$. Moreover the two hardest jets should be separated by a $\Delta y_{j1j2} > 5$ gap in rapidity, have an invariant mass $M_{j1j2} > 600$ GeV and be in opposite hemispheres, i.e. $y_{j1} \cdot y_{j2} < 0$. Jets are defined using the anti-k_t algorithm [186] with jet radius $R = 0.4$, as implemented in `FastJet` [187]. We notice that, unlike in the HW case, the shape of the distribution of the Higgs transverse momentum $p_{t,\mathrm{H}}$ is only mildly affected by the presence of the anomalous $\mathcal{O}_6$ interaction term. This feature can be explained by realising that even for large $p_{t,\mathrm{H}}$ one of the squared momenta Q_1^2 or Q_2^2, that enters the form factors $\mathcal{F}_{1,2}(Q_1^2, Q_2^2)$, can be small. As a consequence, a range of $Q_{1,2}^2$ values is probed for a fixed $p_{t,\mathrm{H}}$ bin and the constant ratio to the SM reflects such averaging. Similar behaviour is also reflected for instance for the transverse momentum of the first and second hardest jet, and hence the ratios corresponding to $p_{t,j1}$ and $p_{t,j2}$ turn out to be almost flat as well. A very different observation can be made when considering a distribution of the third hardest jet $p_{t,j3}$. When the transverse momentum of the third jet is hard, both Q_1^2 and Q_2^2 tend to be hard as well. As a result, an increase in the magnitude of both virtualities, Q_1^2 and Q_2^2, provides an approximately linear modification in the form factors $\mathcal{F}_{1,2}(Q_1^2, Q_2^2)$ and consequently a linear shape in the ratio to the SM benchmark distributions can be observed in the right panel of Fig. 5.6. Unfortunately, the effects are only moderate for the $p_{t,j3}$ values that are accessible at the LHC. The important lesson, that might be taken from these results, is that since the VVh vertex corrections do depend in a non-trivial way on the external momenta, the effects of the $\mathcal{O}_6$ operator not only change the overall size of the cross sections but also alter the shapes of some corresponding distributions. As at least some of the discussed distributions might be measured at the HL-LHC, they can be used as an aid in providing bounds on the anomalous $\bar{c}_6$ Wilson coefficient.

5.3 Putting bounds on the Higgs self-coupling

In this section we will estimate the bounds on the $\bar{c}_6$ Wilson coefficient that result from the measurement of the VH/VBF Higgs production cross sections. In order to evaluate the quality of the method we will compare this bound with the one that may be obtained if studying the double-Higgs production channel. As it has been the case so far we will assume that the modifications of the Wilson coefficient of the $\mathcal{O}_6$ operator supply the dominant contribution to the observable under consideration, and subsequently neglect all other dimension-six operators.

5.3.1 Constraints from the double-Higgs production

For testing the Higgs self-coupling in the $pp \to \mathrm{HH}$ process we will use the results of the search

$$pp \longrightarrow \mathrm{HH} \longrightarrow (b\bar{b})(b\bar{b}), \tag{5.10}$$

performed by the ATLAS collaboration using the 13.3 fb^{-1} data set of the $\sqrt{s} = 13$ TeV collisions [228]. The non-resonant double-Higgs production has been constrained to be less than 330 fb, which is approximately 29 times larger than the predicted SM value, $\left(\sigma_{2b2\bar{b}}^{13\ \mathrm{TeV}}\right)_{\mathrm{SM}} = 11.3^{+0.9}_{-1.0}$ fb. Using the `HPAIR` code[2] [229] we obtain the cross section as a function of the $\bar{c}_6$ coefficient

$$\sigma_{2b2\bar{b}}^{13\ \mathrm{TeV}} = \left(\sigma_{2b2\bar{b}}^{13\ \mathrm{TeV}}\right)_{\mathrm{SM}} \times \left(1 - 0.82\,\bar{c}_6 + 0.29\,\bar{c}_6^2\right), \tag{5.11}$$

which further can be translated into a bound

$$\bar{c}_6 \in [-9.5, 12.3]\,, \tag{5.12}$$

at the 95% confidence level (CL), if theoretical uncertainties are taken into account. The small rate together with a mild dependence of the cross section on the Higgs self-coupling λ make the $pp \to \mathrm{HH}$ production channel very challenging. Additional obstacle is posed by the difficulty of selecting the signal from backgrounds. These issues will make it hard to measure the $\bar{c}_6$ coefficient even after the HL-LHC phase. The study of the $b\bar{b}\gamma\gamma$ channel performed by the ATLAS collaboration [230] predicts a limit of

$$\bar{c}_6 \in [-2.3, 7.7]\,, \tag{5.13}$$

at the 95% CL with 3 ab^{-1} of integrated luminosity. Multivariate analyses together with combinations of $b\bar{b}\gamma\gamma$ channel with other decay modes, such as $\tau\bar{\tau}b\bar{b}$ [231] or $b\bar{b}b\bar{b}$ may allow for an improvement of the bounds but it is unclear by how much precisely.

[2] `http://tiger.web.psi.ch/hpair/`

5.3.2 Constraints from the VH/VBF Higgs production

Finally, we will use our predictions introduced earlier in this section to establish bounds on the Higgs self-coupling by using the VH/VBF single-Higgs production modes.

In order to compare the experimental results with theoretical predictions we can define the signal strengths

$$\mu_I^{\mathrm{F}} = \frac{\sigma_I}{(\sigma_I)_{\mathrm{SM}}} \frac{\mathrm{Br}^{\mathrm{F}}}{(\mathrm{Br}^{\mathrm{F}})_{\mathrm{SM}}}\,, \tag{5.14}$$

which combine the production cross section σ_I and the branching ratios Br^{F}, since only their resultant product can be measured experimentally. Such formalism can be utilised to test the compatibility of the LHC measurements with the SM predictions and to interpret the data in the context of New Physics searches. A signal strength equal to one, $\mu_I^{\mathrm{F}} = 1$, corresponds to a measurement compatible with the SM prediction.

The current constraints on the $\bar{c}_6$ Wilson coefficient may be obtained using the LHC Run I data analysed by the ATLAS and CMS collaborations [202]. The relevant signal strengths can be read from the Table 13 of the Ref. [202], and we have

$$\begin{gathered} \mu^{b\bar{b}}_{\mathrm{VH/VBF}} = 0.65^{+0.30}_{-0.29}\,, \qquad \mu^{\mathrm{WW}}_{\mathrm{VH/VBF}} = 1.38^{+0.41}_{-0.37}\,, \\ \mu^{\tau\bar{\tau}}_{\mathrm{VH/VBF}} = 1.12^{+0.37}_{-0.35}\,, \qquad \mu^{\mathrm{ZZ}}_{\mathrm{VH/VBF}} = 0.48^{+1.37}_{-0.91}\,, \qquad \mu^{\gamma\gamma}_{\mathrm{VH/VBF}} = 1.05^{+0.44}_{-0.41}\,, \end{gathered} \tag{5.15}$$

where the quoted uncertainties contain the experimental uncertainty as well as the SM theory error. Using these results in a χ^2 fit yields the following limit on the $\bar{c}_6$ Wilson coefficient

$$\bar{c}_6 \in [-13.6, 16.9]\,, \tag{5.16}$$

where the errors quoted in Eq. (5.15) have been included in the fit but no uncertainty due to missing higher-order λ corrections has been considered. Note that this bound is weaker than the current limit obtained with $pp \to \mathrm{HH}$ but the difference is not striking and the data used for obtaining the Eq. (5.16) corresponds only to the LHC Run I ($\sqrt{s} = 8$ TeV) while bound in Eq. (5.12) refers to the $\sqrt{s} = 13$ TeV data set.

Furthermore, we can estimate the future sensitivity of the HL-LHC programme to the $\bar{c}_6$ coefficient, as the studies of the sensitivity for signal strengths of various channels have been performed by the ATLAS and CMS collaborations [232, 233]. We use the predictions for the HL-LHC data set corresponding to 3 ab^{-1} of integrated luminosity and study two scenarios, based on the results reported in the 4$^{\text{th}}$ and 5$^{\text{th}}$ column of Table 1 of [232]. The first scenario includes the theory uncertainties, estimated using currently available theoretical predictions, and reads

$$\Delta\mu^{b\bar{b}}_{\mathrm{HW}} = \pm 37\%\,, \quad \Delta\mu^{\gamma\gamma}_{\mathrm{HW}} = \pm 19\%\,,$$
$$\Delta\mu^{b\bar{b}}_{\mathrm{HZ}} = \pm 14\%\,, \quad \Delta\mu^{\gamma\gamma}_{\mathrm{HZ}} = \pm 28\%\,, \quad \Delta\mu^{\mathrm{ZZ}}_{\mathrm{HV}} = \pm 13\%\,, \tag{5.17}$$
$$\Delta\mu^{\mathrm{WW}}_{\mathrm{VBF}} = \pm 15\%\,, \quad \Delta\mu^{\tau\bar{\tau}}_{\mathrm{VBF}} = \pm 19\%\,, \quad \Delta\mu^{\mathrm{ZZ}}_{\mathrm{VBF}} = \pm 21\%\,, \quad \Delta\mu^{\gamma\gamma}_{\mathrm{VBF}} = \pm 22\%\,,$$

while the second one operates under the assumption of complete reduction of theoretical uncertainty and predicts

$$\Delta\mu^{b\bar{b}}_{\mathrm{HW}} = \pm 36\%\,, \quad \Delta\mu^{\gamma\gamma}_{\mathrm{HW}} = \pm 17\%\,,$$
$$\Delta\mu^{b\bar{b}}_{\mathrm{HZ}} = \pm 13\%\,, \quad \Delta\mu^{\gamma\gamma}_{\mathrm{HZ}} = \pm 27\%\,, \quad \Delta\mu^{\mathrm{ZZ}}_{\mathrm{HV}} = \pm 12\%\,, \tag{5.18}$$
$$\Delta\mu^{\mathrm{WW}}_{\mathrm{VBF}} = \pm 9\%\,, \quad \Delta\mu^{\tau\bar{\tau}}_{\mathrm{VBF}} = \pm 15\%\,, \quad \Delta\mu^{\mathrm{ZZ}}_{\mathrm{VBF}} = \pm 16\%\,, \quad \Delta\mu^{\gamma\gamma}_{\mathrm{VBF}} = \pm 15\%\,.$$

Assuming that the central values of the future measurements will coincide with the SM predictions in every channel mentioned in Eqs. (5.17) and Eq. (5.18), we can repeat the exercise of performing a χ^2 fit and predicting the constraining power of the HL-LHC programme for the $\mathcal{O}_6$ anomalous coupling. The two relevant bounds are

$$\bar{c}_6 \in [-7.0, 10.9] \qquad \text{for HL-LHC with all uncertainties,}$$
$$\bar{c}_6 \in [-6.2, 9.6] \qquad \text{for HL-LHC with no theory uncertainty.} \tag{5.19}$$

These predictions allow for testing the Higgs self-coupling at a similar level as the ones originating from the direct extraction from the $pp \to$ HH channel, presented in Section 5.3.1. The Eqs. (5.17) and (5.18) show that the theoretical uncertainty is not the limiting factor for the extraction of the $\bar{c}_6$ limits from VH/VBF Higgs production modes.

To conclude this chapter we note that the anomalous Higgs self-coupling may be constrained in the single-Higgs production channels, such as VH/VBF Higgs production, using the loop-induced probes. The quality of the limits is comparable with the ones obtained through a more direct probe, i.e. the measurement of the double-Higgs production cross section. Furthermore, thanks to considerably larger cross sections for single-Higgs production channels it is realistic to assume that the differential measurements, like the ones mentioned in Section 5.2.3, might appear during the HL-LHC operation. They can further strengthen the predictions shown in Eq. (5.19). Making this statement more precise would, however, require a more thorough study.

Finally, similar loop-induced effects might be explored in the context of other single-Higgs production modes, like the Higgs production cross section in the gluon-gluon fusion or even in the Higgs boson transverse momentum distribution (by studying $pp \to \mathrm{H}j$ process).

6
Conclusions

The common theme that has been present throughout this thesis is precision physics at hadron colliders. Theoretical predictions for the LHC experiment are, in many cases, available with an unprecedented theoretical accuracy thanks to a rapid development of methods treating various domains in the perturbative QCD. We have tried to address only a small part of this landscape by engaging into all-order calculations, such as resummation and parton showers, and matching them to the fixed-order results.

After a short introduction to the main concepts in Chapter 2 we have described an implementation of an N^{3}LL accurate resummation performed in the direct space in Chapter 3. Our focus has been put on the colour singlet production in hadronic collisions and we have presented results for the transverse-momentum spectrum of the Higgs boson, produced in gluon-gluon fusion, as well as the transverse-momentum and the ϕ^*_η distributions in the Drell-Yan production process. Our predictions have been matched to an NNLO accurate fixed-order calculation resulting in a precise description of the distribution across the whole spectrum. The distributions for the Drell-Yan process have been compared to the experimental data collected by the ATLAS collaboration yielding a very good agreement within the quoted errors. The technique offers a wide-range of applications with many interesting directions to pursue, including the transverse-momentum spectrum in the charged Drell-Yan process or a joint resummation where the p_t spectrum of the colour singlet is examined in a presence of a jet-veto cut. A further automation might be achieved in a form of a simple interface to the existing publicly-available NNLO accurate Monte Carlo codes.

In Chapter 4 we have considered an alternative approach to treating the QCD corrections up to all orders in powers of the strong coupling, namely the parton shower. We have invoked the `MiNLO` method which provides a recipe for merging event generators with various jet multiplicities in a way that allows to retain the NLO QCD accuracy for 0-jet and 1-jet observables. Furthermore, the technique may be utilised to improve the accuracy of the 0-jet observables up to the NNLO accuracy by employing results of an independent fixed-order calculation, and then such an event sample might be interfaced with a parton shower algorithm. We have exploited this method in the scope of the associated Higgs production process (VH). We have presented a short phenomenological study and analysed some effects that might escape the scrutiny of the fixed-order perturbation theory. In the case of HZ production we have subsequently implemented the NLO QCD corrections to the $\mathrm{H} \to b\bar{b}$ decay mode and studied the impact of the parton shower on the Higgs boson properties, as reconstructed from the two b-jets, which provide a more adequate description for a comparison with experimental data that will be collected at the LHC in the years to come. A natural continuation would be to include also a matched NNLO+PS treatment of the $\mathrm{H} \to b\bar{b}$ decay. Moreover, the `MiNLO` procedure provides an attractive framework to be exploited in more complex processes, *e.g.* involving more coloured partons in the final state.

Finally, in Chapter 5 we have examined some loop-induced effects corresponding to extensions of the Standard Model (SM). We have worked in a model-independent framework of the SM Effective Field Theory (EFT) that allows to parametrise the possible New Physics phenomena in terms of higher-dimensional operators involving the SM degrees of freedom. We have considered a particular operator that affects the Higgs boson self-coupling. We have analysed its influence on the production cross sections, in VH process and the VBF Higgs production, as well as on the Higgs boson decay widths. We have provided constraints on the associated Wilson coefficient using the currently available data as well as predictions for the future High Luminosity LHC sensitivities. This method, due to its generality, may be also engaged for examination of other Standard Model processes. Moreover, an extensive analysis considering an interplay between various SM EFT operators might be of interest in the future. One of the drawbacks lies in the need for calculating the two loop-amplitudes for massive particles which is a cumbersome task.

The LHC program, at the moment of writing this thesis, is still before its high-luminosity phase which will offer a wealth of data appearing continuously over the next years. In some part, a success of this program will depend on the advancement of the precision of theoretical calculations. This will put pressure on the methods currently used as well as require many new ideas in the field of perturbative QCD and beyond.

A
Resummation formulae

A.1 Kinematics of a hard-collinear emission

The transverse momentum of the Sudakov parametrisation in Eq. (3.3) is related to the transverse momentum computed with respect to the beam axis by recoil effects due to hard-collinear emissions. We want to present a short derivation of a precise formula that connects the two, which has already been reported in Eq. (3.10).

To illustrate this link we consider a set of emissions off, without loss of generality, only the first leg. The momentum of the initial-state parton p_1 before any radiation is related to the momentum $\tilde{p}_1$ by

$$p_1 = \tilde{p}_1 + \sum_{j\in\mathbf{1}} k_j, \tag{A.1}$$

where we have explicitly stated that we consider only emissions radiated off leg one ($j\in\mathbf{1}$). Using the Sudakov parametrisation of the real parton momenta we obtain

$$p_1 = \left[1 + \sum_{j\in\mathbf{1}} \left(1 - y_j^{(1)}\right)\right] \tilde{p}_1 + \left[\sum_{j\in\mathbf{1}} \left(1 - y_j^{(2)}\right)\right] \tilde{p}_2 + \sum_{j\in\mathbf{1}} \tilde{\kappa}_{tj}. \tag{A.2}$$

Let us now consider an emission k_i which can be represented in the Sudakov parametrisation as

$$k_i = \left(1 - y_i^{(1)}\right) \tilde{p}_1 + \left(1 - y_i^{(2)}\right) \tilde{p}_2 + \tilde{\kappa}_{ti}. \tag{A.3}$$

On the other hand, we could equivalently use a coordinate system fixed by the direction of the beam axis, i.e. using the momenta of partons p_1 and p_2, before any radiation occurs:

$$\begin{aligned} k_i &= \left(1 - x_i^{(1)}\right) p_1 + \left(1 - x_i^{(2)}\right) p_2 + \kappa_{ti} \\ &= \left(1 - x_i^{(1)}\right) p_1 + \left(1 - x_i^{(2)}\right) \tilde{p}_2 + \kappa_{ti}, \end{aligned} \tag{A.4}$$

where in the second line we have used the fact that in our simplified setup we consider a set of emissions radiated off the leg one, hence $p_2 = \tilde{p}_2$; $\left(1 - x_i^{(1)}\right)$ and $\left(1 - x_i^{(2)}\right)$ are the coordinates representing the p_1 and p_2 components and κ_{ti} is the transverse momentum with respect to the beam axis (similarly to the Sudakov parametrisation of Eq. (3.3) κ_{ti} is perpendicular to both p_1 and p_2).

We can now substitute the p_1 parametrisation of Eq. (A.2) into Eq. (A.4) and obtain:

$$\begin{aligned} k_i = \left(1 - x_i^{(1)}\right) &\left[1 + \sum_{j \in \mathbf{1}} \left(1 - y_j^{(1)}\right)\right] \tilde{p}_1 + \left[\left(1 - x_i^{(2)}\right) + \left(1 - x_i^{(1)}\right) \sum_{j \in \mathbf{1}} \left(1 - y_j^{(2)}\right)\right] \tilde{p}_2 \\ &+ \left(1 - x_i^{(1)}\right) \sum_{j \in \mathbf{1}} \tilde{\kappa}_{tj} + \kappa_{ti}, \end{aligned} \tag{A.5}$$

which should correspond to the Sudakov parametrisation. By comparing the $\tilde{p}_1$ components of Eqs. (A.3) and (A.5), we find

$$\left(1 - x_i^{(1)}\right) = \frac{\left(1 - y_i^{(1)}\right)}{1 + \sum_{j \in \mathbf{1}} \left(1 - y_j^{(1)}\right)}. \tag{A.6}$$

In this example we have considered a set of emissions radiated off one leg, but one can present a similar construction for more general case. The relation of Eq. (A.6) provides a link between k_{ti} and $\tilde{k}_{ti}$ which has been presented in Eq. (3.10).

A.2 Formulae for an N^{3}LL accurate resummation

In this section we report some of the ingredients that have been used for the evaluation of the N^{3}LL accurate expression that has been introduced and discussed in Chapter 3.

We start by reporting our convention for the renormalisation group (RG) running of the strong coupling. A differential equation governing this evolution reads

$$\frac{d\alpha_s(\mu)}{d \ln \mu^2} = \beta(\alpha_s) \equiv -\alpha_s \left(\beta_0 \alpha_s + \beta_1 \alpha_s^2 + \beta_2 \alpha_s^3 + \beta_3 \alpha_s^4 + \dots\right), \tag{A.7}$$

where the coefficients of the β-function are

$$\beta_0 = \frac{11C_A - 2n_f}{12\pi}, \qquad \beta_1 = \frac{17C_A^2 - 5C_A n_f - 3C_F n_f}{24\pi^2}, \tag{A.8}$$

$$\beta_2 = \frac{2857C_A^3 + (54C_F^2 - 615C_F C_A - 1415C_A^2)n_f + (66C_F + 79C_A)n_f^2}{3456\pi^3}, \tag{A.9}$$

$$\begin{aligned}\beta_3 = \frac{1}{(4\pi)^4}\Bigg\{ & C_A C_F n_f^2 \frac{1}{4}\left(\frac{17152}{243} + \frac{448}{9}\zeta_3\right) + C_A C_F^2 n_f \frac{1}{2}\left(-\frac{4204}{27} + \frac{352}{9}\zeta_3\right) \\ & + \frac{53}{243} C_A n_f^3 + C_A^2 C_F n_f \frac{1}{2}\left(\frac{7073}{243} - \frac{656}{9}\zeta_3\right) + C_A^2 n_f^2 \frac{1}{4}\left(\frac{7930}{81} + \frac{224}{9}\zeta_3\right) \\ & + \frac{154}{243} C_F n_f^3 + C_A^3 n_f \frac{1}{2}\left(-\frac{39143}{81} + \frac{136}{3}\zeta_3\right) + C_A^4\left(\frac{150653}{486} - \frac{44}{9}\zeta_3\right) \\ & + C_F^2 n_f^2 \frac{1}{4}\left(\frac{1352}{27} - \frac{704}{9}\zeta_3\right) + 23C_F^3 n_f + n_f \frac{d_F^{abcd} d_A^{abcd}}{N_A}\left(\frac{512}{9}9 - \frac{1664}{3}\zeta_3\right) \\ & + n_f^2 \frac{d_F^{abcd} d_F^{abcd}}{N_A}\left(-\frac{704}{9} + \frac{512}{3}\zeta_3\right) + \frac{d_A^{abcd} d_A^{abcd}}{N_A}\left(-\frac{80}{9} + \frac{704}{3}\zeta_3\right)\Bigg\}, \end{aligned} \tag{A.10}$$

with

$$\frac{d_F^{abcd} d_F^{abcd}}{N_A} = \frac{N_c^4 - 6N_c^2 + 18}{96N_c^2}, \qquad \frac{d_F^{abcd} d_A^{abcd}}{N_A} = \frac{N_c(N_c^2 + 6)}{48},$$
$$\frac{d_A^{abcd} d_A^{abcd}}{N_A} = \frac{N_c^2(N_c^2 + 36)}{24}, \tag{A.11}$$

and $C_A = N_c$, $C_F = \frac{N_c^2 - 1}{2N_c}$, and $N_c = 3$.

The Sudakov radiator $\tilde{R}$ has been represented in Eq. (3.71) in terms of $g_i(\lambda)$ functions, where we have defined

$$\lambda = \alpha_s(\mu_R)\beta_0 \tilde{L}, \tag{A.12}$$

where the modified logarithm $\tilde{L}$ has been defined in Eq. (3.73). For simplicity we use abbreviations

$$x_{\mathrm{Q}} \equiv \frac{Q}{M}, \qquad x_{\mathrm{R}} \equiv \frac{\mu_R}{M}. \qquad \text{and} \qquad x_{\mathrm{F}} \equiv \frac{\mu_F}{M}. \tag{A.13}$$

The functions $g_i(\lambda)$ are read:

$$g_1(\lambda) = \frac{A^{(1)}}{\pi\beta_0} \frac{2\lambda + \ln(1 - 2\lambda)}{2\lambda}, \tag{A.14}$$

$$
\begin{aligned}
g_2(\lambda) =& \frac{1}{2\pi\beta_0}\ln(1-2\lambda)\left(A^{(1)}\ln\frac{1}{x_{\mathrm{Q}}^2}+B^{(1)}\right)-\frac{A^{(2)}}{4\pi^2\beta_0^2}\frac{2\lambda+(1-2\lambda)\ln(1-2\lambda)}{1-2\lambda}\\
&+A^{(1)}\Bigg(-\frac{\beta_1}{4\pi\beta_0^3}\frac{\ln(1-2\lambda)((2\lambda-1)\ln(1-2\lambda)-2)-4\lambda}{1-2\lambda}\\
&\quad-\frac{1}{2\pi\beta_0}\frac{(2\lambda(1-\ln(1-2\lambda))+\ln(1-2\lambda))}{1-2\lambda}\ln\frac{x_{\mathrm{R}}^2}{x_{\mathrm{Q}}^2}\Bigg),
\end{aligned}
\tag{A.15}
$$

$$
\begin{aligned}
g_3(\lambda) =& \left(A^{(1)}\ln\frac{1}{x_{\mathrm{Q}}^2}+B^{(1)}\right)\left(-\frac{\lambda}{1-2\lambda}\ln\frac{x_R^2}{x_{\mathrm{Q}}^2}+\frac{\beta_1}{2\beta_0^2}\frac{2\lambda+\ln(1-2\lambda)}{1-2\lambda}\right)\\
&-\frac{1}{2\pi\beta_0}\frac{\lambda}{1-2\lambda}\left(A^{(2)}\ln\frac{1}{x_{\mathrm{Q}}^2}+B^{(2)}\right)-\frac{A^{(3)}}{4\pi^2\beta_0^2}\frac{\lambda^2}{(1-2\lambda)^2}\\
&+A^{(2)}\left(\frac{\beta_1}{4\pi\beta_0^3}\frac{2\lambda(3\lambda-1)+(4\lambda-1)\ln(1-2\lambda)}{(1-2\lambda)^2}-\frac{1}{\pi\beta_0}\frac{\lambda^2}{(1-2\lambda)^2}\ln\frac{x_{\mathrm{R}}^2}{x_{\mathrm{Q}}^2}\right)\\
&+A^{(1)}\Bigg(\frac{\lambda\left(\beta_0\beta_2(1-3\lambda)+\beta_1^2\lambda\right)}{\beta_0^4(1-2\lambda)^2}+\frac{(1-2\lambda)\ln(1-2\lambda)\left(\beta_0\beta_2(1-2\lambda)+2\beta_1^2\lambda\right)}{2\beta_0^4(1-2\lambda)^2}\\
&\quad+\frac{\beta_1^2}{4\beta_0^4}\frac{(1-4\lambda)\ln^2(1-2\lambda)}{(1-2\lambda)^2}-\frac{\lambda^2}{(1-2\lambda)^2}\ln^2\frac{x_{\mathrm{R}}^2}{x_{\mathrm{Q}}^2}\\
&\quad-\frac{\beta_1}{2\beta_0^2}\frac{(2\lambda(1-2\lambda)+(1-4\lambda)\ln(1-2\lambda))}{(1-2\lambda)^2}\ln\frac{x_{\mathrm{R}}^2}{x_{\mathrm{Q}}^2}\Bigg),
\end{aligned}
\tag{A.16}
$$

$$
\begin{aligned}
g_4(\lambda) =& \frac{A^{(4)}(3-2\lambda)\lambda^2}{24\pi^2\beta_0^2(2\lambda-1)^3}\\
&+\frac{A^{(3)}}{48\pi\beta_0^3(2\lambda-1)^3}\Bigg\{3\beta_1(1-6\lambda)\ln(1-2\lambda)+2\lambda\Bigg(\beta_1(5\lambda(2\lambda-3)+3)\\
&\quad+6\beta_0^2(3-2\lambda)\lambda\ln\frac{x_{\mathrm{R}}^2}{x_{\mathrm{Q}}^2}\Bigg)+12\beta_0^2(\lambda-1)\lambda(2\lambda-1)\ln\frac{1}{x_{\mathrm{Q}}^2}\Bigg\}\\
&+\frac{A^{(2)}}{24\beta_0^4(2\lambda-1)^3}\Bigg\{32\beta_0\beta_2\lambda^3-2\beta_1^2\lambda(\lambda(22\lambda-9)+3)\\
&\quad+12\beta_0^4(3-2\lambda)\lambda^2\ln^2\frac{x_{\mathrm{R}}^2}{x_{\mathrm{Q}}^2}+6\beta_0^2\ln\frac{x_{\mathrm{R}}^2}{x_{\mathrm{Q}}^2}\times\\
&\quad\left(\beta_1(1-6\lambda)\ln(1-2\lambda)+2(\lambda-1)\lambda(2\lambda-1)\left(\beta_1+2\beta_0^2\ln\frac{1}{x_{\mathrm{Q}}^2}\right)\right)
\end{aligned}
$$

$$
\begin{aligned}
&+3\beta_1\Bigg(\beta_1\ln(1-2\lambda)(2\lambda+(6\lambda-1)\ln(1-2\lambda)-1)\\
&-2\beta_0^2(2\lambda-1)(2(\lambda-1)\lambda-\ln(1-2\lambda))\ln\frac{1}{x_{\mathrm{Q}}^2}\Bigg)\Bigg\}\\
+\;&\frac{\pi A^{(1)}}{12\beta_0^5(2\lambda-1)^3}\Bigg\{\beta_1^3(1-6\lambda)\ln^3(1-2\lambda)+3\ln(1-2\lambda)\Bigg(\beta_0^2\beta_3(2\lambda-1)^3\\
&+\beta_0\beta_1\beta_2\left(1-2\lambda\left(8\lambda^2-4\lambda+3\right)\right)+4\beta_1^3\lambda^2(2\lambda+1)\\
&+\beta_0^2\beta_1\ln\frac{x_{\mathrm{R}}^2}{x_{\mathrm{Q}}^2}\left(\beta_0^2(1-6\lambda)\ln\frac{x_{\mathrm{R}}^2}{x_{\mathrm{Q}}^2}-4\beta_1\lambda\right)\Bigg)\\
&+3\beta_1^2\ln^2(1-2\lambda)\left(2\beta_1\lambda+\beta_0^2(6\lambda-1)\ln\frac{x_{\mathrm{R}}^2}{x_{\mathrm{Q}}^2}\right)\\
&+3\beta_0^2(2\lambda-1)\ln\frac{1}{x_{\mathrm{Q}}^2}\Bigg(-\beta_1^2\ln^2(1-2\lambda)+2\beta_0^2\beta_1\ln(1-2\lambda)\ln\frac{x_{\mathrm{R}}^2}{x_{\mathrm{Q}}^2}\\
&+4\lambda\left(\lambda\left(\beta_1^2-\beta_0\beta_2\right)+\beta_0^4(\lambda-1)\ln^2\frac{x_{\mathrm{R}}^2}{x_{\mathrm{Q}}^2}\right)\Bigg)\\
&+2\lambda\Bigg(\beta_0^2\beta_3((15-14\lambda)\lambda-3)+\beta_0\beta_1\beta_2(5\lambda(2\lambda-3)+3)\\
&+4\beta_1^3\lambda^2+2\beta_0^6(3-2\lambda)\lambda\ln^3\frac{x_{\mathrm{R}}^2}{x_{\mathrm{Q}}^2}+3\beta_0^4\beta_1\ln^2\frac{x_{\mathrm{R}}^2}{x_{\mathrm{Q}}^2}\\
&+6\beta_0^2\lambda(2\lambda+1)\left(\beta_0\beta_2-\beta_1^2\right)\ln\frac{x_{\mathrm{R}}^2}{x_{\mathrm{Q}}^2}-8\beta_0^6\left(4\lambda^2-6\lambda+3\right)\zeta_3\Bigg)\Bigg\}\\
+\;&\frac{B^{(3)}(\lambda-1)\lambda}{4\pi\beta_0(1-2\lambda)^2}+\frac{B^{(2)}\left(\beta_1\ln(1-2\lambda)-2(\lambda-1)\lambda\left(\beta_1-2\beta_0^2\ln\frac{x_{\mathrm{R}}^2}{x_{\mathrm{Q}}^2}\right)\right)}{4\beta_0^2(1-2\lambda)^2}\\
+\;&\frac{\pi B^{(1)}}{4\beta_0^3(1-2\lambda)^2}\Bigg\{4\lambda\left(\lambda\left(\beta_1^2-\beta_0\beta_2\right)+\beta_0^4(\lambda-1)\ln^2\frac{x_{\mathrm{R}}^2}{x_{\mathrm{Q}}^2}\right)\\
&-\beta_1^2\ln^2(1-2\lambda)+2\beta_0^2\beta_1\ln(1-2\lambda)\ln\frac{x_{\mathrm{R}}^2}{x_{\mathrm{Q}}^2}\Bigg\}. \qquad\text{(A.17)}
\end{aligned}
$$

The expressions for the anomalous dimensions $A^{(i)}$ and $B^{(i)}$ are extracted from Refs. [234, 235, 236, 237] for Higgs boson production and Refs. [238, 239, 236, 237] for the Drell-Yan production. The N^{3}LL anomalous dimension $A^{(4)}$, both for the Drell-Yan process and Higgs boson production, is at present incomplete since the four-loop cusp anomalous dimension is unknown. In the above expressions this contribution is set to zero.

In the following pages we report various coefficients and anomalous dimensions that enter the resummation formulae listed above. We note that in the following expressions we single out the new terms:

$$\Delta\mathrm{A}^{(4)} = -64\pi^3\beta_0^3\zeta_3, \qquad \Delta\mathrm{B}^{(3)} = -32\pi^2\beta_0^2\zeta_3, \qquad \Delta\mathrm{H}^{(2)} = \frac{16}{3}\pi\beta_0\zeta_3, \tag{A.18}$$

which are a feature of momentum space resummation, and do not appear in the anomalous dimensions in b-space (see Section 3.1.7 for details).

For the Higgs boson production in gluon-gluon fusion the coefficients $A^{(i)}$ and $B^{(i)}$ which have been used in evaluation of the above formulae are

$$\begin{aligned}
A^{(1)}_{\mathrm{ggH}} =& 2C_A, \\
A^{(2)}_{\mathrm{ggH}} =& \left(\frac{67}{9} - \frac{\pi^2}{3}\right) C_A^2 - \frac{10}{9} C_A n_f, \\
A^{(3)}_{\mathrm{ggH}} =& \left(-22\zeta_3 - \frac{67\pi^2}{27} + \frac{11\pi^4}{90} + \frac{15503}{324}\right) C_A^3 + \left(\frac{10\pi^2}{27} - \frac{2051}{162}\right) C_A^2 n_f \\
&+ \left(4\zeta_3 - \frac{55}{12}\right) C_A C_F n_f + \frac{50}{81} C_A n_f^2, \\
A^{(4)}_{\mathrm{ggH}} =& \left(\frac{121}{3}\zeta_3\zeta_2 - \frac{8789\zeta_2}{162} - \frac{19093\zeta_3}{54} - \frac{847\zeta_4}{24} + 132\zeta_5 + \frac{3761815}{11664}\right) C_A^4 + \left(-\frac{4\zeta_3}{9} - \frac{232}{729}\right) C_A n_f^3 \\
&+ \left(-\frac{22}{3}\zeta_3\zeta_2 + \frac{2731\zeta_2}{162} + \frac{4955\zeta_3}{54} + \frac{11\zeta_4}{6} - 24\zeta_5 - \frac{31186}{243}\right) C_A^3 n_f \\
&+ \left(-\frac{38\zeta_3}{9} - 2\zeta_4 + \frac{215}{24}\right) C_A C_F n_f^2 + \left(\frac{272\zeta_3}{9} + 11\zeta_4 - \frac{7351}{144}\right) C_A^2 C_F n_f \\
&+ \left(-\frac{103\zeta_2}{81} - \frac{47\zeta_3}{27} + \frac{5\zeta_4}{6} + \frac{13819}{972}\right) C_A^2 n_f^2 + C_A \Delta\mathrm{A}^{(4)}, \\
B^{(1)}_{\mathrm{ggH}} =& -\frac{11}{3} C_A + \frac{2}{3} n_f, \\
B^{(2)}_{\mathrm{ggH}} =& \left(\frac{11\zeta_2}{6} - 6\zeta_3 - \frac{16}{3}\right) C_A^2 + \left(\frac{4}{3} - \frac{\zeta_2}{3}\right) C_A n_f + C_F n_f, \\
B^{(3)}_{\mathrm{ggH}} =& \left(\frac{22\zeta_3\zeta_2}{3} - \frac{799\zeta_2}{81} - \frac{5\pi^2\zeta_3}{9} - \frac{2533\zeta_3}{54} - \frac{77\zeta_4}{12} + 20\zeta_5 - \frac{319\pi^4}{1080} + \frac{6109\pi^2}{1944} + \frac{34219}{1944}\right) C_A^3 \\
&+ \left(\frac{103\zeta_2}{81} + \frac{202\zeta_3}{27} - \frac{5\zeta_4}{6} + \frac{41\pi^4}{540} - \frac{599\pi^2}{972} - \frac{10637}{1944}\right) C_A^2 n_f \\
&+ \left(-\frac{2\zeta_3}{27} + \frac{5\pi^2}{162} + \frac{529}{1944}\right) C_A n_f^2 + \left(2\zeta_4 - \frac{\pi^4}{45} - \frac{\pi^2}{12} + \frac{241}{72}\right) C_A C_F n_f
\end{aligned}$$

$$- \frac{1}{4} C_F^2 n_f - \frac{11}{36} C_A n_f^2 + C_A \Delta \mathrm{B}^{(3)}. \tag{A.19}$$

The Drell-Yan production, on the other hand, is a $q\bar{q}$ initiated process and the relevant coefficients for the resummation formulae read

$$\begin{aligned}
A_{\mathrm{DY}}^{(1)} =& 2C_F, \\
A_{\mathrm{DY}}^{(2)} =& \left(\frac{67}{9} - \frac{\pi^2}{3}\right) C_A C_F - \frac{10}{9} C_F n_f, \\
A_{\mathrm{DY}}^{(3)} =& \left(\frac{15503}{324} - \frac{67\pi^2}{27} + \frac{11\pi^4}{90} - 22\zeta_3\right) C_A^2 C_F + \left(-\frac{2051}{162} + \frac{10\pi^2}{27}\right) C_A C_F n_f \\
&+ \left(-\frac{55}{12} + 4\zeta_3\right) C_F^2 n_f + \frac{50}{81} C_F n_f^2, \\
A_{\mathrm{DY}}^{(4)} =& \left(\frac{3761815}{11664} - \frac{8789\zeta_2}{162} - \frac{19093\zeta_3}{54} + \frac{121\zeta_2\zeta_3}{3} - \frac{847\zeta_4}{24} + 132\zeta_5\right) C_A^3 C_F \\
&+ \left(-\frac{232}{729} - \frac{4\zeta_3}{9}\right) C_F n_f^3 + \left(\frac{215}{24} - \frac{38\zeta_3}{9} - 2\zeta_4\right) C_F^2 n_f^2 \\
&+ \left(-\frac{31186}{243} + \frac{2731\zeta_2}{162} + \frac{4955\zeta_3}{54} - \frac{22\zeta_2\zeta_3}{3} + \frac{11\zeta_4}{6} - 24\zeta_5\right) C_A^2 C_F n_f \\
&+ \left(-\frac{7351}{144} + \frac{272\zeta_3}{9} + 11\zeta_4\right) C_A C_F^2 n_f + \left(\frac{13819}{972} - \frac{103\zeta_2}{81} - \frac{47\zeta_3}{27} + \frac{5\zeta_4}{4}\right) C_A C_F n_f^2 \\
&+ C_F \Delta \mathrm{A}^{(4)}, \\
B_{\mathrm{DY}}^{(1)} =& -3C_F, \\
B_{\mathrm{DY}}^{(2)} =& \left(-\frac{17}{12} - \frac{11\pi^2}{12} + 6\zeta_3\right) C_A C_F + \left(-\frac{3}{4} + \pi^2 - 12\zeta_3\right) C_F^2 + \left(\frac{1}{6} + \frac{\pi^2}{6}\right) C_F n_f, \\
B_{\mathrm{DY}}^{(3)} =& \left(\frac{22\zeta_3\zeta_2}{3} - \frac{799\zeta_2}{81} - \frac{11\pi^2\zeta_3}{9} + \frac{2207\zeta_3}{54} - \frac{77\zeta_4}{12} - 10\zeta_5 - \frac{83\pi^4}{360} - \frac{7163\pi^2}{1944} + \frac{151571}{3888}\right) C_A^2 C_F \\
&+ \left(\frac{4\pi^2 - 51}{3}\zeta_3 + 60\zeta_5 - \frac{2\pi^4}{5} - \frac{3\pi^2}{4} - \frac{29}{8}\right) C_F^3 + \left(\frac{34\zeta_3}{3} + 2\zeta_4 - \frac{7\pi^4}{54} - \frac{13\pi^2}{36} + \frac{23}{4}\right) C_F^2 n_f \\
&+ \left(-\frac{2}{3}\pi^2\zeta_3 - \frac{211\zeta_3}{3} - 30\zeta_5 + \frac{247\pi^4}{540} + \frac{205\pi^2}{36} - \frac{151}{16}\right) C_A C_F^2 \\
&+ \left(\frac{103\zeta_2}{81} - \frac{128\zeta_3}{27} - \frac{5\zeta_4}{6} + \frac{11\pi^4}{180} + \frac{1297\pi^2}{972} - \frac{3331}{243}\right) C_A C_F n_f \\
&+ \left(\frac{10\zeta_3}{27} - \frac{5\pi^2}{54} + \frac{1115}{972}\right) C_F n_f^2 + C_F \Delta \mathrm{B}^{(3)}.
\end{aligned} \tag{A.20}$$

The hard-virtual coefficient function can be expressed in terms of a Taylor series in powers of the strong coupling,

$$H(M) = 1 + \sum_{n=1}^{2} \left(\frac{\alpha_s(M)}{2\pi} \right)^n H^{(n)}(M), \tag{A.21}$$

where we limit ourselves only to the first two terms of the expansion. We recollect that, as explained in Section 3.2.3, the three-loop correction, if available, is automatically included by the use of multiplicative matching scheme. The exact formulae for the Higgs boson production and the Drell-Yan process are

$$\begin{aligned} H^{(1)}_{\mathrm{ggH}}(M) =& C_A \left(5 + \frac{7}{6}\pi^2 \right) - 3C_F, \\ H^{(2)}_{\mathrm{ggH}}(M) =& \frac{5359}{54} + \frac{137}{6} \ln \frac{m_H^2}{m_t^2} + \frac{1679}{24}\pi^2 + \frac{37}{8}\pi^4 - \frac{499}{6}\zeta_3 + C_A \Delta\mathrm{H}^{(2)}, \qquad n_f = 5, \end{aligned} \tag{A.22}$$

and

$$\begin{aligned} H^{(1)}_{\mathrm{DY}}(M) =& C_F \left(-8 + \frac{7}{6}\pi^2 \right), \\ H^{(2)}_{\mathrm{DY}}(M) =& -\frac{57433}{972} + \frac{281}{162}\pi^2 + \frac{22}{27}\pi^4 + \frac{1178}{27}\zeta_3 + C_F \Delta\mathrm{H}^{(2)}, \qquad n_f = 5. \end{aligned} \tag{A.23}$$

The symbols $\tilde{H}$ that appear in the luminosity prefactors, in Eqs. (3.75), (3.77), (3.78), are defined as

$$\begin{aligned} \tilde{H}^{(1)}(\mu_R, x_{\mathrm{Q}}) &= H^{(1)}(\mu_R) + \left(-\frac{1}{2} A^{(1)} \ln x_{\mathrm{Q}}^2 + B^{(1)} \right) \ln x_{\mathrm{Q}}^2, \\ \tilde{H}^{(2)}(\mu_R, x_{\mathrm{Q}}) &= H^{(2)}(\mu_R) + \frac{(A^{(1)})^2}{8} \ln^4 x_{\mathrm{Q}}^2 - \left(\frac{A^{(1)} B^{(1)}}{2} + \frac{A^{(1)}}{3} \pi \beta_0 \right) \ln^3 x_{\mathrm{Q}}^2 \\ &\quad + \left(\frac{-A^{(2)} + (B^{(1)})^2}{2} + \pi \beta_0 \left(B^{(1)} + A^{(1)} \ln \frac{x_{\mathrm{Q}}^2}{x_{\mathrm{R}}^2} \right) \right) \ln^2 x_{\mathrm{Q}}^2 \\ &\quad - \left(-B^{(2)} + B^{(1)} 2\pi\beta_0 \ln \frac{x_{\mathrm{Q}}^2}{x_{\mathrm{R}}^2} \right) \ln x_{\mathrm{Q}}^2 + H^{(1)}(\mu_R) \ln x_{\mathrm{Q}}^2 \left(-\frac{1}{2} A^{(1)} \ln x_{\mathrm{Q}}^2 + B^{(1)} \right). \end{aligned} \tag{A.24}$$

Finally we report the expansion of the collinear coefficient functions C_{ab}

$$C_{ab}(z) = \delta(1-z)\delta_{ab} + \sum_{n=1}^{2} \left(\frac{\alpha_s(\mu)}{2\pi} \right)^n C^{(n)}_{ab}(z), \tag{A.25}$$

where μ is the same scale that enters parton densities. The first-order expansion has been known for a long time and reads

$$C^{(1)}_{ab}(z) = -\hat{P}^{(0),\epsilon}_{ab}(z) - \delta_{ab}\delta(1-z)\frac{\pi^2}{12}, \tag{A.26}$$

where $\hat{P}_{ab}^{(0),\epsilon}(z)$ is the $\mathcal{O}(\epsilon)$ part of the leading-order regularised splitting functions $\hat{P}_{ab}^{(0)}(z)$

$$\begin{aligned}
&\hat{P}_{qq}^{(0)}(z) = C_F \left[\frac{1+z^2}{(1-z)_+} + \frac{3}{2}\delta(1-z)\right], && \hat{P}_{qq}^{(0),\epsilon}(z) = -C_F(1-z),\\
&\hat{P}_{qg}^{(0)}(z) = \frac{1}{2}\left[z^2 + (1-z)^2\right], && \hat{P}_{qg}^{(0),\epsilon}(z) = -z(1-z),\\
&\hat{P}_{gq}^{(0)}(z) = C_F \frac{1+(1-z)^2}{z}, && \hat{P}_{gq}^{(0),\epsilon}(z) = -C_F z,\\
&\hat{P}_{gg}^{(0)}(z) = 2C_A\left[\frac{z}{(1-z)_+} + \frac{1-z}{z} + z(1-z)\right] + 2\pi\beta_0\delta(1-z), && \hat{P}_{gg}^{(0),\epsilon}(z) = 0.
\end{aligned} \tag{A.27}$$

The second-order collinear coefficient functions $C_{ab}^{(2)}(z)$, as well as the G coefficients (see Eqs. (3.75), (3.77), (3.78)) for gluon-fusion processes are obtained in Refs. [131, 133], while for quark-induced processes they are derived in Ref. [132]. In the present work we extract their expressions using the results of Refs. [131, 132]. For gluon-fusion processes, the $C_{gq}^{(2)}$ and $C_{gg}^{(2)}$ coefficients normalised as in Eq. (A.26) are extracted from Eqs. (30) and (32) of Ref. [131], respectively, where we use the hard coefficients of Eqs. (A.22) *without* the new term $\Delta\mathrm{H}^{(2)}$ in the $H_g^{(2)}(M)$ coefficient.[1] The coefficient $G^{(1)}$ is taken from Eq. (13) of Ref. [131]. Similarly, for quark-initiated processes, we extract $C_{qg}^{(2)}$ and $C_{qq}^{(2)}$ from Eqs. (32) and (34) of Ref. [132], respectively, where we use the hard coefficients from Eqs. (A.23) *without* the new term $\Delta\mathrm{H}^{(2)}$ in the $H_q^{(2)}(M)$ coefficient. The remaining quark coefficient function $C_{q\bar{q}}^{(2)}$, $C_{q\bar{q}'}^{(2)}$ and $C_{qq'}^{(2)}$ are extracted from Eq. (35) of the same article.

The coefficients $\tilde{C}$ in Eqs. (3.75), (3.77), (3.78) are defined as

$$\begin{aligned}
\tilde{C}_{ab}^{(1)}(z,\mu_F,x_\mathrm{Q}) &= C_{ab}^{(1)}(z) + \hat{P}_{ab}^{(0)}(z)\ln\frac{x_\mathrm{Q}^2}{x_\mathrm{F}^2},\\
\tilde{C}_{ab}^{(2)}(z,\mu_F,x_\mathrm{Q}) &= C_{ab}^{(2)}(z) + \pi\beta_0\hat{P}_{ab}^{(0)}(z)\left(\ln^2\frac{x_\mathrm{Q}^2}{x_\mathrm{F}^2} - 2\ln\frac{x_\mathrm{Q}^2}{x_\mathrm{F}^2}\ln\frac{x_\mathrm{Q}^2}{x_\mathrm{R}^2}\right)\\
&\quad + \hat{P}_{ab}^{(1)}(z)\ln\frac{x_\mathrm{Q}^2}{x_\mathrm{F}^2} + \frac{1}{2}(\hat{P}^{(0)}\otimes\hat{P}^{(0)})_{ab}(z)\ln^2\frac{x_\mathrm{Q}^2}{x_\mathrm{F}^2}\\
&\quad + (C^{(1)}\otimes\hat{P}^{(0)})_{ab}(z)\ln\frac{x_\mathrm{Q}^2}{x_\mathrm{F}^2} - 2\pi\beta_0 C_{ab}^{(1)}(z)\ln\frac{x_\mathrm{Q}^2}{x_\mathrm{R}^2}.
\end{aligned} \tag{A.28}$$

[1] These must be replaced by $H^{(1)} \to H^{(1)}/2$ and $H^{(2)} \to H^{(2)}/4$ to match the convention of Refs. [131, 132].

A.3 Multiplicative matching formulae

In this part we report the formulae which are necessary to implement the multiplicative matching scheme that has been described in Section 3.2.3.

It is useful to introduce a convenient notation for the perturbative expansion of the various ingredients. We have

$$\sigma_{\text{tot}}^{\text{N}^3\text{LO}} = \sum_{i=0}^{3} \sigma^{(i)}, \qquad \text{and} \qquad \Sigma^{\text{N}^3\text{LO}}(v) = \sigma^{(0)} + \sum_{i=1}^{3} \Sigma_{\text{FIX}}^{(i)}(v), \tag{A.29}$$

with

$$\Sigma_{\text{FIX}}^{(i)}(v) = \sigma^{(i)} + \bar{\Sigma}_{\text{FIX}}^{(i)}(v), \qquad \text{and} \qquad \bar{\Sigma}_{\text{FIX}}^{(i)}(v) \equiv -\int_v^{\infty} dv' \, \frac{d\Sigma_{\text{FIX}}^{(i)}(v')}{dv'}. \tag{A.30}$$

Furthermore, we have the resummed cumulative cross section and its perturbative expansion

$$\Sigma^{\text{N}^3\text{LL}}(v) = \Sigma_{\text{RES}}(v), \qquad \text{and} \qquad \Sigma^{\text{EXP}}(v) = \sum_{i=1}^{3} \Sigma_{\text{RES}}^{(i)}(v). \tag{A.31}$$

Finally, we present the formulae for the asymptotic, i.e. with $\tilde{L} \to 0$, resummed cumulant used for dealing with the spurious terms affecting the multiplicative matched result. It has been defined in Eq. (3.93), and we repeat the formula for completeness:

$$\Sigma_{\text{asym.}}^{\text{N}^3\text{LL}} = \int d\Phi_{\text{B}}{}_{\text{with cuts}} \left(\lim_{\tilde{L} \to 0} \tilde{\mathcal{L}}_{\text{N}^3\text{LL}} \right), \tag{A.32}$$

where the integration over the Born phase-space is performed with the phase-space cuts taken into account and after taking the limit, the luminosity reads

$$\begin{aligned}
\tilde{\mathcal{L}}_{\text{N}^3\text{LL}}^{\tilde{L}\to 0} = \sum_{c,c'} |\mathcal{M}_B(\Phi_{\text{B}})|_{cc'} \sum_{i,j} \int_{x_1}^{1} \frac{dz_1}{z_1} \int_{x_2}^{1} \frac{dz_2}{z_2} f_i\!\left(\mu_F, \frac{x_1}{z_1}\right) f_j\!\left(\mu_F, \frac{x_2}{z_2}\right) \\
\times \Bigg\{ \delta_{ci}\delta_{c'j}\delta(1-z_1)\delta(1-z_2) \left(1 + \frac{\alpha_s(\mu_R)}{2\pi} \tilde{H}^{(1)}(\mu_R, x_{\text{Q}}) + \frac{\alpha_s^2(\mu_R)}{(2\pi)^2} \tilde{H}^{(2)}(\mu_R, x_{\text{Q}}) \right) \\
+ \frac{\alpha_s(\mu_R)}{2\pi} \left(\tilde{C}_{ci}^{(1)}(z_1, \mu_F, x_{\text{Q}})\delta(1-z_2)\delta_{c'j} + \{z_1 \leftrightarrow z_2; c, i \leftrightarrow c', j\} \right) \\
+ \frac{\alpha_s^2(\mu_R)}{(2\pi)^2} \tilde{H}^{(1)}(\mu_R, x_{\text{Q}}) \left(\tilde{C}_{ci}^{(1)}(z_1, \mu_F, x_{\text{Q}})\delta(1-z_2)\delta_{c'j} + \{z_1 \leftrightarrow z_2; c, i \leftrightarrow c', j\} \right) \\
+ \frac{\alpha_s^2(\mu_R)}{(2\pi)^2} \left(\tilde{C}_{ci}^{(2)}(z_1, \mu_F, x_{\text{Q}})\delta(1-z_2)\delta_{c'j} + \{z_1 \leftrightarrow z_2; c, i \leftrightarrow c', j\} \right)
\end{aligned}$$

$$+\frac{\alpha_s^2(\mu_R)}{(2\pi)^2}\Big(\tilde{C}^{(1)}_{ci}(z_1,\mu_F,x_{\rm Q})\tilde{C}^{(1)}_{c'j}(z_2,\mu_F,x_{\rm Q})+G^{(1)}_{ci}(z_1)G^{(1)}_{c'j}(z_2)\Big)\Bigg\},\tag{A.33}$$

and again we can expand it in the power series in the strong coupling

$$\Sigma^{\rm N^3LL}_{\rm asym.}=\sigma^{(0)}+\sum_{i=1}^{2}\Sigma^{(i)}_{\rm asym.},\tag{A.34}$$

where superscript (i) denotes the $\mathcal{O}(\alpha_s^i)$ term. Similar formulae can be derived for $\tilde{\mathcal{L}}^{\tilde{L}\to 0}_{\rm NLL}$ and $\tilde{\mathcal{L}}^{\tilde{L}\to 0}_{\rm NNLL}$ luminosities.

Finally, the formula for matching to the N^{3}LO cumulant, i.e. expression that is NNLO accurate at the level of distribution ($d\Sigma/dv$), reads

$$\begin{aligned}
\Sigma^{\rm MAT}_{\rm mult}(v)=\frac{\Sigma^{\rm N^3LL}}{\Sigma^{\rm N^3LL}_{\rm asym.}}\Bigg[&\sigma^{(0)}+\Big\{\sigma^{(1)}+\bar{\Sigma}^{(1)}+\Sigma^{(1)}_{\rm asym.}-\Sigma^{(1)}_{\rm N^3LL}\Big\}\\
&+\Bigg\{\sigma^{(2)}+\bar{\Sigma}^{(2)}+\Sigma^{(2)}_{\rm asym.}-\Sigma^{(2)}_{\rm N^3LL}+\frac{\Sigma^{(1)}_{\rm asym.}}{\sigma^{(0)}}\Big(\sigma^{(1)}+\bar{\Sigma}^{(1)}\Big)\\
&\quad+\frac{(\Sigma^{(1)}_{\rm N^3LL})^2}{\sigma^{(0)}}-\frac{\Sigma^{(1)}_{\rm N^3LL}}{\sigma^{(0)}}\Big(\sigma^{(1)}+\bar{\Sigma}^{(1)}+\Sigma^{(1)}_{\rm asym.}\Big)\Bigg\}\\
&+\Bigg\{\sigma^{(3)}+\bar{\Sigma}^{(3)}-\Sigma^{(3)}_{\rm N^3LL}-\frac{(\Sigma^{(1)}_{\rm N^3LL})^3}{(\sigma^{(0)})^2}+\frac{(\Sigma^{(1)}_{\rm N^3LL})^2}{(\sigma^{(0)})^2}\Big(\sigma^{(1)}+\bar{\Sigma}^{(1)}+\Sigma^{(1)}_{\rm asym.}\Big)\\
&\quad+\frac{1}{\sigma_0}\Big((\sigma^{(1)}+\bar{\Sigma}^{(1)})(\Sigma^{(2)}_{\rm asym.}-\Sigma^{(2)}_{\rm N^3LL})+\Sigma^{(1)}_{\rm asym.}(\sigma^{(2)}+\bar{\Sigma}^{(2)}-\Sigma^{(2)}_{\rm N^3LL})\Big)\\
&\quad-\frac{1}{(\sigma^{(0)})^2}\Sigma^{(1)}_{\rm N^3LL}\Big(\Sigma^{(1)}_{\rm asym.}(\sigma^{(1)}+\bar{\Sigma}^{(1)})+\sigma^{(0)}(\sigma^{(2)}+\bar{\Sigma}^{(2)}+\Sigma^{(2)}_{\rm asym.}-2\Sigma^{(2)}_{\rm N^3LL})\Big)\Bigg\}\Bigg],
\end{aligned}\tag{A.35}$$

where we have grouped the terms entering at the NLO, NNLO, and N^{3}LO level within separate curly brackets.

B

Polar angle distributions: decomposition and analysis

B.1 Spectral decomposition of functions of polar angle

It is natural to use spectral analysis when dealing with functions which depend upon angular variables. Periodic functions of one variable, *e.g.* angle ϕ, can be easily mapped into a series of Fourier modes. However, a generic function F of a polar angle α in the three-dimensional spherical coordinate system is defined only on the interval $\alpha \in [0, \pi]$ and not necessarily periodic. The most general parametrisation of such angular dependence can be written in terms of polynomials of cosα and sinα, and it reads

$$F(\alpha) = \sum_{a=0}^{\infty} \Big(C_{1a} (\cos\alpha)^a + C_{2a} (\sin\alpha)(\cos\alpha)^a \Big) \,, \tag{B.1}$$

where we have used the fact that quadratic and higher terms in sinα can always be reduced to at most linear piece. Eq. (B.1) reads equivalently

$$\begin{aligned} F(x) &= \sum_{a=0}^{\infty} \Big(C_{1a}\, x^a + C_{2a}\, x^a \sqrt{1-x^2} \Big) \\ &= \sum_{i=0}^{\infty} \bar{C}_i f_i(x) \end{aligned} \tag{B.2}$$

with

$$f_i(x) = \left(\sqrt{1-x^2}\right)^{\mathrm{mod(i,2)}} x^{\lfloor i/2 \rfloor} \,,$$

$$x = \cos\alpha, \qquad x \in [-1;+1]. \tag{B.3}$$

The above functions f_i, although very simple, are not orthonormal. As a last step, equipped with a scalar product between two functions,

$$\langle F|G\rangle \equiv \int_{-1}^{+1} F(x)\, G(x)\, dx\,, \tag{B.4}$$

we can transform the basis of functions $\{f_i\}$ into an orthonormal set $\{g_j\}$ by means of a Gram-Schmidt recurrence relation

$$\begin{aligned} k=0: &\qquad \begin{cases} \tilde{g}_0 = & f_0, \\ g_0 = & \tilde{g}_0/\langle\tilde{g}_0|\tilde{g}_0\rangle \end{cases} \\ k>0: &\qquad \begin{cases} \tilde{g}_k = & f_k - \sum_{j=0}^{k-1}\langle g_j|f_k\rangle\cdot g_j, \\ g_k = & \tilde{g}_k/\langle\tilde{g}_k|\tilde{g}_k\rangle. \end{cases} \end{aligned} \tag{B.5}$$

We are now able to express a generic function F in terms of the spectral modes g_j as

$$F(x) = \sum_{j=0}^{N} c_j\, g_j(x)\,, \qquad \text{with} \qquad c_n = \langle g_n|F\rangle. \tag{B.6}$$

B.2 Hadronic tensor structures in the $pp \to \mathrm{B}$ matrix element

Hadronic collisions are closely related to the non-perturbative aspects of the strong interactions. Nevertheless, we can use Lorentz symmetries and gauge invariance to predict the tensor structures that appear in matrix elements for proton-proton collisions.

When considering the associated Higgs production in pp collision, we can distinguish two stages of the process, i.e. the production of the off-shell gauge boson, that may be parametrised by the hadronic tensor $H_{\mu\nu}$, and the decay of the gauge boson into Higgs boson and a pair of leptons, described by the decay tensor $D_{\mu\nu}$. Since we are considering only QCD corrections and we do not consider interference effects between production stage and the products of the Higgs boson, the full matrix element can be parametrised as

$$|\mathcal{M}(p_1,p_2,q,\ell_1,\ell_2)|^2 = \frac{H_{\mu\nu}(p_1,p_2,q)\cdot D^{\mu\nu}(q,\ell_1,\ell_2)}{\left(q^2-M_{\mathrm{Z}}^2\right)^2 + M_{\mathrm{Z}}^2\Gamma_{\mathrm{Z}}^2}, \tag{B.7}$$

where p_1 and p_2 are the momenta of the incoming protons, q is the momentum of the off-shell gauge boson before radiating off the Higgs boson, while ℓ_1 and ℓ_2 are the momenta

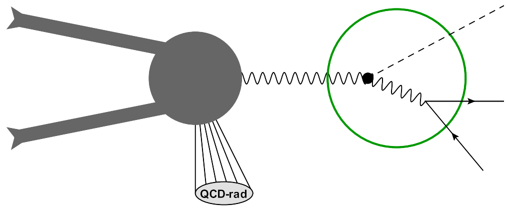

Figure B.1: Amplitude for production of a weak gauge boson in proton-proton collision with subsequent branchings into Higgs boson and pair of leptons.

of the two leptons that are produced. The momentum of the Higgs boson p_{H} can be obtained from q and lepton momenta ℓ_1 and ℓ_2 using the conservation of momentum.

We can parametrise the hadronic tensor as

$$H_{\sigma\sigma'} = (\varepsilon(q))^{\mu}_{\sigma}\; H_{\mu\nu}(p_1, p_2, q)\; (\varepsilon^*(q))^{\nu}_{\sigma'}\,, \tag{B.8}$$

where the ε four-vectors denote polarisation tensors of the gauge boson in the amplitude and its conjugate part, corresponding to polarisations σ and σ' respectively. The most general covariant form for the hadronic tensor [240, 241] reads

$$\begin{aligned} H_{\mu\nu}(p_1,p_2,q) &= H_1\left(g_{\mu\nu} - \frac{q_\mu q_\nu}{q^2}\right) + H_2\,\tilde{p}_{1\mu}\tilde{p}_{1\nu} + H_3\,\tilde{p}_{2\mu}\tilde{p}_{2\nu} \\ &+ H_4\big(\tilde{p}_{1\mu}\tilde{p}_{2\nu} + \tilde{p}_{2\mu}\tilde{p}_{1\nu}\big) + H_5\big(\tilde{p}_{1\mu}\tilde{p}_{2\nu} - \tilde{p}_{2\mu}\tilde{p}_{1\nu}\big) \\ &+ H_6\epsilon^{\mu\nu\rho\sigma}p_{1\rho}q_\sigma + H_7\epsilon^{\mu\nu\rho\sigma}p_{2\rho}q_\sigma \\ &+ H_8\big(\tilde{p}_{1\mu}\,\epsilon^{\nu\rho\sigma\kappa}p_{1\rho}p_{2\sigma}q_\kappa + \{\mu\leftrightarrow\nu\}\big) + H_9\big(\tilde{p}_{2\mu}\,\epsilon^{\nu\rho\sigma\kappa}p_{1\rho}p_{2\sigma}q_\kappa + \{\mu\leftrightarrow\nu\}\big), \end{aligned} \tag{B.9}$$

where $\tilde{p}_{i\mu} = p_{i\mu} - (p_i q)/q^2 q_\mu$.

On the other hand, the decay tensor $D_{\mu\nu}$ responsible for the gauge boson branching into Higgs boson and subsequent decay of the gauge boson into pair of leptons (see green circle in Fig. B.1) can be parametrised as

$$D_{\sigma\sigma'} = (\varepsilon(q))_{\mu,\sigma}\; D^{\mu\nu}(q,\ell_1,\ell_2)\; (\varepsilon^*(q))_{\nu,\sigma'}\,, \tag{B.10}$$

where $D^{\mu\nu}(q,\ell_1,\ell_2)$ tensor can be written as, for simplicity we omit overall coupling constants,

$$D^{\mu\nu} = \frac{g^{\mu\alpha}\Big(-g_{\alpha\tilde{\alpha}} + \frac{k_\alpha k_{\tilde{\alpha}}}{M_{\mathrm{Z}}^2}\Big)L^{\tilde{\alpha}\tilde{\beta}}\Big(-g_{\beta\tilde{\beta}} + \frac{k_\beta k_{\tilde{\beta}}}{M_{\mathrm{Z}}^2}\Big)g^{\beta\nu}}{\big(k^2 - M_{\mathrm{Z}}^2\big)^2 + M_{\mathrm{Z}}^2\Gamma_{\mathrm{Z}}^2}\,, \tag{B.11}$$

with $k = \ell_1 + \ell_2$ is the momentum of the gauge boson after radiating off the Higgs boson. The $L^{\tilde{\alpha}\tilde{\beta}}$ tensor depends on the momenta of leptons as well as their vector (V_ℓ) and axial (A_ℓ) coupling to the gauge boson, it reads

$$L^{\tilde{\alpha}\tilde{\beta}} = \mathrm{Tr}\left[\gamma^{\tilde{\alpha}} \left(V_\ell + A_\ell \gamma_5\right) \not{\ell}_1 \gamma^{\tilde{\beta}} \left(V_\ell + A_\ell \gamma_5\right) \not{\ell}_2\right], \tag{B.12}$$

We can express the lepton momenta as $\ell_1 = \ell$ and $\ell_2 = k - \ell$. Plugging this into Eq. (B.12) and then further into Eq. (B.11), we find out that the momentum k appears in the final amplitude in Eq. (B.7) with at most power 5. This argument is analogous to the one used in Ref. [156] to obtain the general form of the angular dependence of Drell-Yan decays.

C

Loop-induced VVh corrections in the SM EFT

In this appendix, we report the components that enter the modified VVh vertex, introduced in Eq. (5.7), as well as the effects that appear in the VH/VBF cross sections and the Higgs decay widths.

The modifications can be expressed in terms of one-loop Passarino-Veltman (PV) scalar integrals

$$B_0\Big(p_1^2, m_0^2, m_1^2\Big) = \frac{\mu_R^{4-d}}{i\pi^{d/2} r_\Gamma} \int \frac{d^d l}{\prod_{i=0,1} P(l+p_i, m_i)}\,, \tag{C.1}$$

$$B_0'\Big(p_1^2, m_0^2, m_1^2\Big) = \left.\frac{\partial B_0(k^2, m_0^2, m_1^2)}{\partial k^2}\right|_{k^2=p_1^2}\,, \tag{C.2}$$

$$C_0\Big(p_1^2, (p_1-p_2)^2, p_2^2, m_0^2, m_1^2, m_2^2\Big) = \frac{\mu_R^{4-d}}{i\pi^{d/2} r_\Gamma} \int \frac{d^d l}{\prod_{i=0,1,2} P(l+p_i, m_i)}\,, \tag{C.3}$$

and the tensor coefficients of the triangle integrals are

$$C^\mu\Big(p_1^2, (p_1-p_2)^2, p_2^2, m_0^2, m_1^2, m_2^2\Big) = \frac{\mu_R^{4-d}}{i\pi^{d/2} r_\Gamma} \int \frac{d^d l\; l^\mu}{\prod_{i=0,1,2} P(l+p_i, m_i)}\,, \tag{C.4}$$

$$C^{\mu\nu}\Big(p_1^2, (p_1-p_2)^2, p_2^2, m_0^2, m_1^2, m_2^2\Big) = \frac{\mu_R^{4-d}}{i\pi^{d/2} r_\Gamma} \int \frac{d^d l\; l^\mu l^\nu}{\prod_{i=0,1,2} P(l+p_i, m_i)}\,, \tag{C.5}$$

where μ_R is the renormalisation scale. We work in $d = 4 - 2\epsilon$ space-time dimensions and hence

$$r_\Gamma = \frac{\Gamma^2(1-\epsilon)\Gamma(1+\epsilon)}{\Gamma(1-2\epsilon)}, \tag{C.6}$$

with $\Gamma(z)$ being the usual Euler gamma function. Functions

$$P(k,m) = k^2 - m^2 \tag{C.7}$$

denote the propagators appearing in the integrals and $p_0 \equiv 0$. These definitions match the corresponding ones of the `LoopTools` package [226]. The tensor integrals C^μ and $C^{\mu\nu}$ can be reduced to linear combinations of Lorentz-covariant tensors constructed from the metric tensor $g^{\mu\nu}$ and linearly independent set of the four-momenta p_i^μ. Alongside conventions of `LoopTools`, we define

$$C^\mu = \sum_{i=1,2} p_i^\mu C_i\,, \qquad C^{\mu\nu} = \eta^{\mu\nu} C_{00} + \sum_{i,j=1,2} p_i^\mu p_j^\nu C_{ij}\,. \tag{C.8}$$

It is worth mentioning that of all integrals appearing in our one-loop calculations only B_0 and C_{00} are UV divergent. Moreover, these divergent integrals appear in the final results always in terms of the UV-finite combination, $B_0 - 4C_{00}$.

Having defined all ingredients, we report the analytic expressions for the form factors appearing in the modified VVh vertex in Eq. (5.7):

$$\mathcal{F}_1(q_1^2, q_2^2) = \frac{\lambda \bar{c}_6}{(4\pi)^2}\left(-3B_0 - 12\left(m_V^2 C_0 - C_{00}\right) - \frac{9m_h^2}{2}\left(\bar{c}_6 + 2\right) B_0'\right)\,, \tag{C.9}$$

$$\mathcal{F}_2(q_1^2, q_2^2) = \frac{\lambda \bar{c}_6}{(4\pi)^2}\, 12\left(C_1 + C_{11} + C_{12}\right)\,, \tag{C.10}$$

where for the sake of simplicity we have omitted the arguments of the one-loop PV functions, they read

$$B_0 = B_0\left(M_{\rm H}^2, M_{\rm H}^2, M_{\rm H}^2\right)\,, \qquad \text{and} \qquad C_0 = C_0\left(M_{\rm H}^2, q_1^2, q_2^2, M_{\rm H}^2, M_{\rm H}^2, M_{\rm V}^2\right)\,. \tag{C.11}$$

Analogous definitions hold for the derivative B_0' of the scalar bubble integral as well as for the tensor coefficients C_2, C_{11}, C_{12} and C_{00}. Notice that the term proportional to B_0' integral in Eq. (C.9) corresponds to the counterterm of the one-loop renormalised Higgs wave-function, it is the only term that features quadratic dependence on the $\bar{c}_6$ Wilson coefficient. We remark that, in contrast to Ref. [213], we do not include an all-order resummation of the wave-function contribution since already at $\mathcal{O}(\lambda^2)$ the correction in the SM EFT would be incomplete due to missing two-loop Higgs-boson self-energy diagrams.

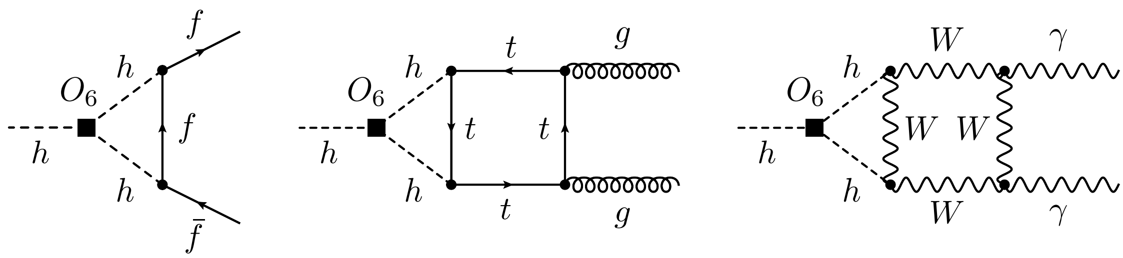

Figure C.1: The one-loop diagrams with an insertion of the effective operator $\mathcal{O}_6$ which contribute to the partial decay widths of the Higgs boson.

C.1 Corrections to Higgs partial decay widths

The determination of signal strengths for various Higgs boson channels requires a knowledge of the impact of the $\mathcal{O}_6$ operator on the partial decay widths of the Higgs boson. Such modifications arise from considering Feynman diagrams with an insertion of the anomalous operator, some of which are depicted in Fig. C.1.

In this section we collect the relevant formulae that encode the $\mathcal{O}(\lambda)$ modifications of the decay widths due to the anomalous Higgs self-coupling, $\bar{c}_6$. We note that the $\mathcal{O}(\lambda^2)$ terms, resulting from the squared matrix elements with an $\mathcal{O}_6$ insertion, are dropped for consistency as the terms with similar scaling but resulting from the interference between tree-level SM diagrams and loop-level SM EFT diagrams are not currently known.

Higgs decay to a pair of light fermions, $\mathrm{H} \to f\bar{f}$

In case of the Higgs boson decay into a pair of light fermions, $f \in \{q, \ell\}$, the modification of the partial decay width can be expressed as

$$\Delta\Gamma(\mathrm{H} \to f\bar{f}) = \frac{N_c^f G_F M_\mathrm{H} m_f^2}{4\sqrt{2}\pi} \left(1 - \frac{4\, m_f^2}{M_\mathrm{H}^2}\right)^{3/2} \Delta_f, \tag{C.12}$$

where $N_c^q = 3$, $N_c^\ell = 1$ and all quark masses m_q are understood as the renormalised $\overline{\mathrm{MS}}$ masses evaluated at the scale M_H, while in the case of leptons m_ℓ denotes the pole mass of the corresponding lepton. The Δ_f term encodes the functional dependence of the $\Delta\Gamma(\mathrm{H} \to f\bar{f})$ on the loop-induced effect of the $\mathcal{O}_6$ operator insertion; it reads

$$\Delta_f = \frac{\lambda \bar{c}_6}{(4\pi)^2} \,\mathrm{Re}\Big(-12 m_f^2 \,(C_0 - C_1 - C_2) - 9 M_\mathrm{H}^2 \,(\bar{c}_6 + 2)\, B_0' \Big)\,, \tag{C.13}$$

with

$$C_0 = C_0(m_f^2, M_\mathrm{H}^2, m_f^2, m_f^2, M_\mathrm{H}^2, M_\mathrm{H}^2)\,, \tag{C.14}$$

and analogue definitions for the tensor coefficients C_1 and C_2. Notice that the flavour dependent part, i.e. proportional to the square of the fermion mass, of the modification is suppressed with respect to the universal correction resulting from the Higgs wave function renormalisation which is multiplied by M_{H}^2. Hence, to a good approximation, the Δ_f corrections are universal.

Higgs decay to a pair of EW gauge bosons, $\mathrm{H} \to \mathrm{VV}$

The partial width of the Higgs decay into pair of massive EW gauge bosons contains two parts; one with one real and one virtual gauge boson, $\mathrm{H} \to \mathrm{VV}^*$ and the second with two virtual gauge bosons, $\mathrm{H} \to \mathrm{V}^*\mathrm{V}^*$. The full modification of the width can be expressed in a form similar to the one presented in Ref. [242] and it reads

$$\Delta\Gamma(\mathrm{H} \to \mathrm{VV}) = \frac{1}{\pi^2} \int_0^{M_{\mathrm{H}}^2} \frac{dq_1^2\, M_{\mathrm{V}}\Gamma_{\mathrm{V}}}{(q_1^2 - M_{\mathrm{V}}^2)^2 + M_{\mathrm{V}}^2\Gamma_{\mathrm{V}}^2} \int_0^{(M_{\mathrm{H}}-q_1)^2} \frac{dq_2^2\, M_{\mathrm{V}}\Gamma_{\mathrm{V}}}{(q_2^2 - M_{\mathrm{V}}^2)^2 + M_{\mathrm{V}}^2\Gamma_{\mathrm{V}}^2}\, I_{\mathrm{V}}\,, \tag{C.15}$$

with

$$I_{\mathrm{V}} = \frac{G_F M_{\mathrm{H}}^3}{8\sqrt{2}\pi}\, N_{\mathrm{V}} \sqrt{\alpha(q_1^2, q_2^2, M_{\mathrm{H}}^2)}\, \beta(q_1^2, q_2^2, M_{\mathrm{H}}^2)\, \Delta_{\mathrm{V}}, \tag{C.16}$$

where the symmetry factors are $N_{\mathrm{W}} = 1$ and $N_{\mathrm{Z}} = 1/2$; the functions α and β read

$$\alpha(x, y, z) = \left(1 - \frac{x}{z} - \frac{y}{z}\right)^2 - \frac{4xy}{z^2}\,, \qquad \beta(x, y, z) = \alpha(x, y, z) + \frac{12xy}{z^2}\,, \tag{C.17}$$

and the modification is

$$\begin{aligned}\Delta_{\mathrm{V}} = \frac{\lambda\bar{c}_6}{(4\pi)^2} \mathrm{Re}\Bigg[& - 6B_0 - 24\left(M_{\mathrm{V}}^2 C_0 - C_{00}\right) \\ & - \frac{12\alpha(q_1^2, q_2^2, M_{\mathrm{H}}^2)\,(q_1^2 + q_2^2 - M_{\mathrm{H}}^2)}{\beta(q_1^2, q_2^2, M_{\mathrm{H}}^2)}\,(C_1 + C_{11} + C_{12}) - 9M_{\mathrm{H}}^2\,(\bar{c}_6 + 2)\, B_0'\Bigg]\,.\end{aligned} \tag{C.18}$$

In this case the arguments of the scalar and tensor PV integrals are the same as defined in Eq. (C.11).

Higgs decay to a pair of massless gauge bosons, $\mathrm{H} \to \gamma\gamma$ and $\mathrm{H} \to gg$

Finally, we report decay widths of the Higgs boson to a pair of massless gauge bosons, i.e. $\mathrm{H} \to \gamma\gamma$ or $\mathrm{H} \to gg$. We note that these channels arise from coupling of the Higgs boson to the massless gauge bosons through a heavy-quark loop or a loop of massive W-bosons. The partial widths can be parametrised as

$$\Delta\Gamma(\mathrm{H} \to gg) = \frac{G_F \alpha_s^2 M_\mathrm{H}^3}{36\sqrt{2}\pi^3} \left| \sum_q A_q \right|^2 \Delta_g \,, \tag{C.19}$$

$$\Delta\Gamma(\mathrm{H} \to \gamma\gamma) = \frac{G_F \alpha_{em}^2 M_\mathrm{H}^3}{128\sqrt{2}\pi^3} \left| \sum_f \frac{4 N_c^f Q_f^2}{3} A_f - A_W \right|^2 \Delta_\gamma \,, \tag{C.20}$$

where $\alpha_s = \alpha_s(M_\mathrm{H})$ and $\alpha_{em} = 1/137.04$. The electric charges of the fermions are $Q_u = 2/3$, $Q_d = -1/3$ and $Q_\ell = -1$. The leading-order form factors A_f and A_W are

$$A_f = \frac{3\tau_f}{2} \left[1 + (1 - \tau_f) \arctan^2 \frac{1}{\sqrt{\tau_f - 1}} \right] , \tag{C.21}$$

$$A_\mathrm{W} = 2 + 3\tau_\mathrm{W} + 3\tau_\mathrm{W}(2 - \tau_\mathrm{W}) \arctan^2 \frac{1}{\sqrt{\tau_\mathrm{W} - 1}} \,, \tag{C.22}$$

with

$$\tau_f = 4m_f^2/M_\mathrm{H}^2 \qquad \text{and} \qquad \tau_\mathrm{W} = 4M_\mathrm{W}^2/M_\mathrm{H}^2. \tag{C.23}$$

The $\mathcal{O}(\lambda)$ corrections arising from the diagrams shown in the Fig. C.1 (middle and right diagrams) are

$$\Delta_g = \frac{\lambda \bar{c}_6}{(4\pi)^2} \left(+ 8.42 - 9 m_h^2 \, (\bar{c}_6 + 2) \, B_0' \right) , \tag{C.24}$$

$$\Delta_\gamma = \frac{\lambda \bar{c}_6}{(4\pi)^2} \left(- 3.70 - 9 m_h^2 \, (\bar{c}_6 + 2) \, B_0' \right) . \tag{C.25}$$

Note that the integral B_0' has no imaginary part for an on-shell Higgs kinematics, hence taking a real part (Re) is not necessary.

C.2 Corrections to the Higgs production

In this section, we summarise the formulae for the $\mathcal{O}(\lambda)$ modifications of the production cross section due to an insertion of the $\mathcal{O}_6$ SM EFT operator. Similarly to calculations of the partial decay widths, in order to maintain the consistency of the calculation, we neglect the $\mathcal{O}(\lambda^2)$ corrections arising from the squared matrix elements.

Treatment of the VH production channel

In order to illustrate the form of the $\bar{c}_6$ modifications in the VH production channel, we present the LO QCD formulae for the change in partonic cross section

$$\Delta\hat{\sigma}_{\mathrm{HV}} = \frac{G_F^2 M_{\mathrm{V}}^4}{72\pi}\,\bar{N}_{\mathrm{V}}\,\sqrt{\alpha(M_{\mathrm{V}}^2, M_{\mathrm{H}}^2, \hat{s})}\;\frac{\alpha(M_{\mathrm{V}}^2, M_{\mathrm{H}}^2, \hat{s})\,\hat{s} + 12 M_{\mathrm{V}}^2}{\left(\hat{s} - M_{\mathrm{V}}^2\right)^2}\,\delta_{\mathrm{V}}\,, \tag{C.26}$$

where $\hat{s}$ denotes the virtuality of the s-channel vector boson, the symmetry factors are

$$\bar{N}_{\mathrm{W}} = 1 \qquad \text{and} \qquad \bar{N}_{\mathrm{Z}} = \left(1 - 8T_3^q Q_q \sin^2\theta_{\mathrm{W}} + 8Q_q^2 \sin^4\theta_{\mathrm{W}}\right)/2, \tag{C.27}$$

with T_3^q denoting the third component of the weak isospin and Q_q the electric charge of the relevant quark q; and $\sin^2\theta_{\mathrm{W}} = \left(1 - (M_{\mathrm{W}}/M_{\mathrm{Z}})^2\right)$ is the weak mixing angle. The function δ_{V} encodes the corrections due to insertions of the modified VVh vertex, and it reads

$$\begin{aligned}\delta_{\mathrm{V}} = \frac{\lambda\bar{c}_6}{(4\pi)^2}\,\mathrm{Re}\Bigg[&- 6B_0 - 24\left(M_{\mathrm{V}}^2 C_0 - C_{00}\right) \\ &- \frac{12\alpha(M_{\mathrm{V}}^2, M_{\mathrm{H}}^2, \hat{s})\,\hat{s}\,(M_{\mathrm{V}}^2 - M_{\mathrm{H}}^2 + \hat{s})}{\alpha(M_{\mathrm{V}}^2, M_{\mathrm{H}}^2, \hat{s})\,\hat{s} + 12M_{\mathrm{V}}^2}\,(C_1 + C_{11} + C_{12}) - 9M_{\mathrm{H}}^2\,(\bar{c}_6 + 2)\,B_0'\Bigg]\,,\end{aligned} \tag{C.28}$$

where the arguments of the scalar and tensor triangle integral are

$$C_0 = C_0(M_{\mathrm{H}}^2, \hat{s}, M_{\mathrm{V}}^2, M_{\mathrm{H}}^2, M_{\mathrm{H}}^2, M_{\mathrm{V}}^2)\,, \tag{C.29}$$

while the arguments of the B_0 integral are denoted in Eq. (C.11). The function $\alpha(x, y, z)$ has been already defined in Eq. (C.17). We point out that the expression for δ_{V} agrees with an analytic expression for the $e^+e^- \to$ HZ process given in Ref. [210].

The $\mathcal{O}_6$ modifications at the NLO QCD do factorise and could also be summarised using formulae that resemble the Eq. (C.28). At the NNLO QCD, we encounter two types of QCD corrections: ones that are similar in fashion to the $\mathcal{O}(\alpha_s^2)$ corrections to the Drell-Yan process and others where the Higgs boson is directly coupled to a heavy-quark loop. In case of the latter, the $\mathcal{O}_6$ modifications do not factorise and we implement them at the matrix element level whenever possible (see Section 5.2.1 for details).

Treatment of the VBF Higgs production channel

The treatment of the $\bar{c}_6$ modifications in the VBF Higgs production requires slightly more intricate formulae. The differential VBF Higgs production cross section is given by a product of the two VVh vertices, $\Gamma^{\mu\nu}_{\rm V}(q_1,q_2)$ and the two DIS hadronic tensors $W^{\rm V}_{\mu\nu}$:[1]

$$\begin{aligned} d\sigma_{\rm VBF} =& \frac{G_F^2 M_{\rm V}^2}{s} \times \frac{1}{Q_1^2+M_{\rm V}^2} \times \frac{1}{Q_2^2+M_{\rm V}^2} \\ & \times W^{\rm V}_{\mu\nu}(x_1,Q_1^2)\,\Gamma^{\mu\rho}_{\rm V}(q_1,q_2)\Big(\Gamma^{\nu\sigma}_{\rm V}(q_1,q_2)\Big)^*\,W^{\rm V}_{\rho\sigma}(x_2,Q_2^2)\;d\Phi_3, \end{aligned} \tag{C.30}$$

where $d\Phi_3$ denotes the 3-particle VBF phase space, $Q_i^2 = -q_i^2$, and we define the usual DIS variables as

$$x_i = \frac{Q_i^2}{2P_i{\cdot}q_i}, \tag{C.31}$$

with P_i^μ being the initial state proton four-momenta, $i = \{1,2\}$.

We can express the hadronic tensor using the standard DIS structure functions $F^{\rm V}_m(x_i,Q_i^2)$ with $m = 1,2,3$:

$$W^{\mu\nu}_{\rm V}(x_i,Q_i^2) = \left(-g^{\mu\nu} - \frac{q_i^\mu q_i^\nu}{Q_i^2}\right) F_1^{\rm V}(x_i,Q_i^2) + \frac{\hat{P}_i^\mu \hat{P}_i^\nu}{P_{ii}}\,F_2^{\rm V}(x_i,Q_i^2) \tag{C.32}$$

$$+\, i\epsilon^{\mu\nu\rho\sigma}\,\frac{P_{i\rho}q_{i\sigma}}{2P_{ii}}\,F_3^{\rm V}(x_i,Q_i^2)\,, \tag{C.33}$$

with $\epsilon^{\mu\nu\rho\sigma}$ being the fully antisymmetric Levi-Civita tensor, and we have introduced the abbreviations

$$P_{ij} = P_i{\cdot}q_j \qquad \text{and} \qquad \hat{P}_i^\mu = P_i^\mu + \frac{P_{ii}}{Q_i^2}\,q_i^\mu. \tag{C.34}$$

Using the decomposition of the hadronic tensor in Eq. (C.32) as well as the form of the modified VVh vertex from Eq. (5.7), we can express

$$\begin{aligned} W^{\rm V}_{\mu\nu}(x_1,Q_1^2)\,\Gamma^{\mu\rho}_{\rm V}(q_1,q_2)\Big(\Gamma^{\nu\sigma}_{\rm V}(q_1,q_2)\Big)^*\,W^{\rm V}_{\rho\sigma}(x_2,Q_2^2) =& \\ = 4\sqrt{2}G_F M_{\rm V}^4 \sum_{m,n=1}^{3} \omega_{mn}\,F^{\rm V}_m(x_1,Q_1^2)\,F^{\rm V}_n(x_2,Q_2^2),& \end{aligned} \tag{C.35}$$

where ω_{mn} is a set of coefficients that can be parametrised using

$$\mathcal{C}_1 = 1 + 2\mathcal{F}_1(Q_1^2,Q_2^2) \qquad \text{and} \qquad \mathcal{C}_1 = 2\mathcal{F}_1(Q_1^2,Q_2^2), \tag{C.36}$$

[1] We use symbol $W_{\rm V}$ for the DIS hadronic tensor to prevent confusion with the one defined in Section B.2.

where the form factors $\mathcal{F}_i(Q_1^2, Q_2^2)$ have been defined in Eqs. (C.9) and (C.10). The coefficients themselves are

$$
\begin{aligned}
\omega_{11} &= (2\mathcal{C}_1 - q_{12}\,\mathcal{C}_2) + (\mathcal{C}_1 + q_{12}\,\mathcal{C}_2)\,\frac{q_{12}^2}{Q_1^2 Q_2^2}\,,\\
\omega_{12} &= -\mathcal{C}_1\,\frac{P_{22}}{Q_2^2} - (\mathcal{C}_1 + q_{12}\,\mathcal{C}_2)\left(\frac{P_{21}^2}{P_{22}Q_1^2} + \frac{2P_{21}\,q_{12}}{Q_1^2Q_2^2} + \frac{P_{22}\,q_{12}^2}{Q_1^2Q_2^4}\right)\,,\\
\omega_{21} &= -\mathcal{C}_1\,\frac{P_{11}}{Q_1^2} - (\mathcal{C}_1 + q_{12}\,\mathcal{C}_2)\left(\frac{P_{12}^2}{P_{11}Q_2^2} + \frac{2P_{12}\,q_{12}}{Q_1^2Q_2^2} + \frac{P_{11}\,q_{12}^2}{Q_1^4Q_2^2}\right)\,,\\
\omega_{22} &= \frac{1}{P_{11}P_{22}\,Q_1^4Q_2^4}\bigg[\mathcal{C}_1\left(p_{12}\,Q_1^2Q_2^2 + P_{11}P_{21}\,Q_2^2 + P_{12}P_{22}\,Q_1^2 + P_{11}P_{22}\,q_{12}\right)^2\\
&\quad + \mathcal{C}_2\left(P_{12}\,Q_1^2 + P_{11}\,q_{12}\right)\left(P_{21}\,Q_2^2 + P_{22}\,q_{12}\right)\\
&\qquad \times\left(p_{12}\,Q_1^2Q_2^2 + P_{11}P_{21}\,Q_2^2 + P_{12}P_{22}\,Q_1^2 + P_{11}P_{22}\,q_{12}\right)\bigg]\,,\\
\omega_{33} &= \frac{1}{4P_{11}P_{22}}\bigg[2\mathcal{C}_1\,(p_{12}\,q_{12} - P_{12}P_{21})\\
&\quad - \mathcal{C}_2\left\{P_{12}P_{22}Q_1^2 + \left(p_{12}\,Q_1^2 + P_{11}P_{21}\right)Q_2^2 + (P_{11}P_{22} + P_{12}P_{21})\,q_{12} - p_{12}\,q_{12}^2\right\}\bigg]\,,
\end{aligned}
\tag{C.37}
$$

where we have used the short-hand notations

$$
q_{12} = q_1\!\cdot\!q_2 \qquad \text{and} \qquad p_{12} = P_1\!\cdot\!P_2. \tag{C.38}
$$

We recollect that, as in all other cases, we have neglected the $\mathcal{O}(\lambda)$ corrections, i.e. the products of form factors $\mathcal{F}_i \cdot \mathcal{F}_j$.

References

[1] T. P. Cheng and L. F. Li, *Gauge Theory of Elementary Particle Physics.* Oxford Univ. Press, Oxford, UK, 1984.

[2] M. E. Peskin and D. V. Schroeder, *An Introduction to quantum field theory.* Addison-Wesley, Reading, USA, 1995.

[3] M. Bohm, A. Denner, and H. Joos, *Gauge Theories of the Strong and Electroweak interaction.* Teubner, Stuttgart, Germany, 2001.

[4] P. Nason *Conf. Proc.* C9705251 (1997) 94–149.

[5] J. M. Campbell, J. W. Huston, and W. J. Stirling *Rept. Prog. Phys.* 70 (2007) 89, [hep-ph/0611148].

[6] G. P. Salam in *ESHEP 2009 Proceedings*, 2010. arXiv:1011.5131.

[7] S. Höche in *TASI 2014 Proceedings*, 2015. arXiv:1411.4085.

[8] R. K. Ellis, W. J. Stirling, and B. R. Webber, *QCD and collider physics.* Cambridge Univ. Press, Cambridge, UK, 1996.

[9] J. Collins, *Foundations of perturbative QCD.* Cambridge Univ. Press, Cambridge, UK, 2011.

[10] T. Plehn, *Lectures on LHC Physics*, vol. 886. Springer, Heidelberg, Germany, 2015.

[11] C. Duhr *Nucl. Part. Phys. Proc.* 273-275 (2016) 2128–2135.

[12] G. Heinrich in *LHC Physics Conference*, 2017. arXiv:1710.04998.

[13] G. Luisoni and S. Marzani *J. Phys.* G42 (2015), no. 10 103101, [arXiv:1505.04084].

[14] T. Sjostrand in *SUSSP65 Proceedings*, 2009. arXiv:0911.5286.

[15] A. Buckley et al. *Phys. Rept.* 504 (2011) 145–233, [arXiv:1101.2599].

[16] W. Bizon, P. F. Monni, E. Re, L. Rottoli, and P. Torrielli arXiv:1705.09127.

[17] W. Bizon, X. Chen, A. G.-D. Ridder, T. Gehrmann, N. Glover, A. Huss, P. F. Monni, E. Re, L. Rottoli, and P. Torrielli arXiv:1805.05916.

[18] W. Astill, W. Bizon, E. Re, and G. Zanderighi *JHEP* 06 (2016) 154, [arXiv:1603.01620].

[19] W. Astill, W. Bizon, E. Re, and G. Zanderighi arXiv:1804.08141.

[20] W. Bizon, M. Gorbahn, U. Haisch, and G. Zanderighi *JHEP* 07 (2017) 083, [`arXiv:1610.05771`].

[21] K. G. Wilson *Phys. Rev.* D10 (1974) 2445–2459.

[22] D. J. Gross and F. Wilczek *Phys. Rev. Lett.* 30 (1973) 1343–1346.

[23] H. D. Politzer *Phys. Rev. Lett.* 30 (1973) 1346–1349.

[24] Particle Data Group Collaboration, C. Patrignani et al. *Chin. Phys.* C40 (2016), no. 10 100001.

[25] M. Gell-Mann *Phys. Lett.* 8 (1964) 214–215.

[26] G. Zweig CERN-TH-401 (1964).

[27] C.-N. Yang and R. L. Mills *Phys. Rev.* 96 (1954) 191–195.

[28] S. Weinberg *Phys. Rev.* D8 (1973) 605–625.

[29] S. Weinberg *Phys. Rev.* D8 (1973) 4482–4498.

[30] H. Lehmann, K. Symanzik, and W. Zimmermann *Nuovo Cim.* 1 (1955) 205–225.

[31] H. Lehmann, K. Symanzik, and W. Zimmermann *Nuovo Cim.* 6 (1957) 319–333.

[32] L. D. Faddeev and V. N. Popov *Phys. Lett.* B25 (1967) 29–30.

[33] G. Leibbrandt *Rev. Mod. Phys.* 59 (1987) 1067.

[34] G. 't Hooft and M. J. G. Veltman *Nucl. Phys.* B44 (1972) 189–213.

[35] C. Becchi, A. Rouet, and R. Stora *Commun. Math. Phys.* 42 (1975) 127–162.

[36] C. Becchi, A. Rouet, and R. Stora *Annals Phys.* 98 (1976) 287–321.

[37] I. V. Tyutin LEBEDEV-75-39 (1975).

[38] K. Symanzik *Commun. Math. Phys.* 23 (1971) 49–86.

[39] C. G. Callan, Jr. *Phys. Rev.* D5 (1972) 3202–3210.

[40] K. G. Wilson and J. B. Kogut *Phys. Rept.* 12 (1974) 75–200.

[41] F. Herzog, B. Ruijl, T. Ueda, J. A. M. Vermaseren, and A. Vogt *JHEP* 02 (2017) 090, [`arXiv:1701.01404`].

[42] T. Luthe, A. Maier, P. Marquard, and Y. Schroder *JHEP* 10 (2017) 166, [`arXiv:1709.07718`].

[43] M. Creutz, *Quarks, gluons and lattices.* Cambridge Monographs on Mathematical Physics. Cambridge Univ. Press, Cambridge, UK, 1985.

[44] S. L. Adler *Phys. Rev.* 177 (1969) 2426–2438.

[45] J. S. Bell and R. Jackiw *Nuovo Cim.* A60 (1969) 47–61.

[46] L. D. Landau *Nucl. Phys.* 13 (1959) 181–192.

[47] V. V. Sudakov *Sov. Phys. JETP* 3 (1956) 65–71. [Zh. Eksp. Teor. Fiz.30,87(1956)].

[48] S. Catani and M. H. Seymour *Nucl. Phys.* B485 (1997) 291–419, [`hep-ph/9605323`]. [Erratum: Nucl. Phys.B510,503(1998)].

[49] S. Catani *Phys. Lett.* B427 (1998) 161–171, [`hep-ph/9802439`].

[50] T. Kinoshita *J. Math. Phys.* 3 (1962) 650–677.

[51] T. D. Lee and M. Nauenberg *Phys. Rev.* 133 (1964) B1549–B1562.

[52] G. F. Sterman and S. Weinberg *Phys. Rev. Lett.* 39 (1977) 1436.

[53] V. N. Gribov and L. N. Lipatov *Sov. J. Nucl. Phys.* 15 (1972) 438–450. [Yad. Fiz.15,781(1972)].

[54] Y. L. Dokshitzer *Sov. Phys. JETP* 46 (1977) 641–653. [Zh. Eksp. Teor. Fiz.73,1216(1977)].

[55] G. Altarelli and G. Parisi *Nucl. Phys.* B126 (1977) 298–318.

[56] H.-W. Lin et al. *Prog. Part. Nucl. Phys.* 100 (2018) 107–160, [`arXiv:1711.07916`].

[57] R. P. Feynman *Phys. Rev. Lett.* 23 (1969) 1415–1417.

[58] J. D. Bjorken and E. A. Paschos *Phys. Rev.* 185 (1969) 1975–1982.

[59] J. C. Collins, D. E. Soper, and G. F. Sterman *Adv. Ser. Direct. High Energy Phys.* 5 (1989) 1–91, [`hep-ph/0409313`].

[60] S. Frixione, Z. Kunszt, and A. Signer *Nucl. Phys.* B467 (1996) 399–442, [`hep-ph/9512328`].

[61] S. Catani and M. Grazzini *Phys. Lett.* B446 (1999) 143–152, [`hep-ph/9810389`].

[62] S. Catani and M. Grazzini *Nucl. Phys.* B570 (2000) 287–325, [`hep-ph/9908523`].

[63] S. Catani and M. Grazzini *Phys. Rev. Lett.* 98 (2007) 222002, [`hep-ph/0703012`].

[64] A. Gehrmann-De Ridder, T. Gehrmann, and E. W. N. Glover *JHEP* 09 (2005) 056, [`hep-ph/0505111`].

[65] G. Somogyi, Z. Trocsanyi, and V. Del Duca *JHEP* 06 (2005) 024, [`hep-ph/0502226`].

[66] M. Czakon *Phys. Lett.* B693 (2010) 259–268, [`arXiv:1005.0274`].

[67] M. Cacciari, F. A. Dreyer, A. Karlberg, G. P. Salam, and G. Zanderighi *Phys. Rev. Lett.* 115 (2015), no. 8 082002, [`arXiv:1506.02660`]. [Erratum: Phys. Rev. Lett.120,no.13,139901(2018)].

[68] J. Gaunt, M. Stahlhofen, F. J. Tackmann, and J. R. Walsh *JHEP* 09 (2015) 058, [`arXiv:1505.04794`].

[69] R. Boughezal, K. Melnikov, and F. Petriello *Phys. Rev.* D85 (2012) 034025, [`arXiv:1111.7041`].

[70] F. Caola, K. Melnikov, and R. Röntsch *Eur. Phys. J.* C77 (2017), no. 4 248, [arXiv:1702.01352].

[71] W. T. Giele and E. W. N. Glover *JHEP* 04 (2004) 029, [hep-ph/0402152].

[72] G. Ossola, C. G. Papadopoulos, and R. Pittau *Nucl. Phys.* B763 (2007) 147–169, [hep-ph/0609007].

[73] A. van Hameren, J. Vollinga, and S. Weinzierl *Eur. Phys. J.* C41 (2005) 361–375, [hep-ph/0502165].

[74] R. K. Ellis and G. Zanderighi *JHEP* 02 (2008) 002, [arXiv:0712.1851].

[75] V. Hirschi, R. Frederix, S. Frixione, M. V. Garzelli, F. Maltoni, and R. Pittau *JHEP* 05 (2011) 044, [arXiv:1103.0621].

[76] G. Bevilacqua, M. Czakon, M. V. Garzelli, A. van Hameren, A. Kardos, C. G. Papadopoulos, R. Pittau, and M. Worek *Comput. Phys. Commun.* 184 (2013) 986–997, [arXiv:1110.1499].

[77] G. Cullen, N. Greiner, G. Heinrich, G. Luisoni, P. Mastrolia, G. Ossola, T. Reiter, and F. Tramontano *Eur. Phys. J.* C72 (2012) 1889, [arXiv:1111.2034].

[78] E. Remiddi and J. A. M. Vermaseren *Int. J. Mod. Phys.* A15 (2000) 725–754, [hep-ph/9905237].

[79] T. Gehrmann and E. Remiddi *Nucl. Phys.* B601 (2001) 248–286, [hep-ph/0008287].

[80] T. Binoth and G. Heinrich *Nucl. Phys.* B585 (2000) 741–759, [hep-ph/0004013].

[81] G. Heinrich *Int. J. Mod. Phys.* A23 (2008) 1457–1486, [arXiv:0803.4177].

[82] S. Borowka, G. Heinrich, S. P. Jones, M. Kerner, J. Schlenk, and T. Zirke *Comput. Phys. Commun.* 196 (2015) 470–491, [arXiv:1502.06595].

[83] C. Anastasiou, C. Duhr, F. Dulat, E. Furlan, T. Gehrmann, F. Herzog, and B. Mistlberger *Phys. Lett.* B737 (2014) 325–328, [arXiv:1403.4616].

[84] C. Anastasiou, C. Duhr, F. Dulat, F. Herzog, and B. Mistlberger *Phys. Rev. Lett.* 114 (2015) 212001, [arXiv:1503.06056].

[85] F. A. Dreyer and A. Karlberg *Phys. Rev. Lett.* 117 (2016), no. 7 072001, [arXiv:1606.00840].

[86] J. C. Collins, D. E. Soper, and G. F. Sterman *Nucl. Phys.* B250 (1985) 199–224.

[87] C. W. Bauer, S. Fleming, and M. E. Luke *Phys. Rev.* D63 (2000) 014006, [hep-ph/0005275].

[88] C. W. Bauer, S. Fleming, D. Pirjol, and I. W. Stewart *Phys. Rev.* D63 (2001) 114020, [hep-ph/0011336].

[89] C. W. Bauer and I. W. Stewart *Phys. Lett.* B516 (2001) 134–142, [hep-ph/0107001].

[90] C. W. Bauer, D. Pirjol, and I. W. Stewart *Phys. Rev.* D65 (2002) 054022, [hep-ph/0109045].

[91] S. Catani, B. R. Webber, and G. Marchesini *Nucl. Phys.* B349 (1991) 635–654.

[92] S. Catani, G. Turnock, B. R. Webber, and L. Trentadue *Phys. Lett.* B263 (1991) 491–497.

[93] A. Banfi, G. P. Salam, and G. Zanderighi *JHEP* 01 (2002) 018, [hep-ph/0112156].

[94] A. Banfi, G. P. Salam, and G. Zanderighi *Phys. Lett.* B584 (2004) 298–305, [hep-ph/0304148].

[95] A. Banfi, G. P. Salam, and G. Zanderighi *JHEP* 03 (2005) 073, [hep-ph/0407286].

[96] A. Banfi, H. McAslan, P. F. Monni, and G. Zanderighi *JHEP* 05 (2015) 102, [arXiv:1412.2126].

[97] A. Banfi, H. McAslan, P. F. Monni, and G. Zanderighi *Phys. Rev. Lett.* 117 (2016), no. 17 172001, [arXiv:1607.03111].

[98] A. Banfi, B. K. El-Menoufi, and P. F. Monni arXiv:1807.11487.

[99] P. F. Monni, E. Re, and P. Torrielli *Phys. Rev. Lett.* 116 (2016), no. 24 242001, [arXiv:1604.02191].

[100] C. W. Bauer and P. F. Monni arXiv:1803.07079.

[101] J. Alwall, P. Demin, S. de Visscher, R. Frederix, M. Herquet, F. Maltoni, T. Plehn, D. L. Rainwater, and T. Stelzer *JHEP* 09 (2007) 028, [arXiv:0706.2334].

[102] J. Alwall, M. Herquet, F. Maltoni, O. Mattelaer, and T. Stelzer *JHEP* 06 (2011) 128, [arXiv:1106.0522].

[103] T. Sjostrand, S. Mrenna, and P. Z. Skands *JHEP* 05 (2006) 026, [hep-ph/0603175].

[104] T. Sjostrand, S. Mrenna, and P. Z. Skands *Comput. Phys. Commun.* 178 (2008) 852–867, [arXiv:0710.3820].

[105] G. Corcella, I. G. Knowles, G. Marchesini, S. Moretti, K. Odagiri, P. Richardson, M. H. Seymour, and B. R. Webber *JHEP* 01 (2001) 010, [hep-ph/0011363].

[106] M. Bahr et al. *Eur. Phys. J.* C58 (2008) 639–707, [arXiv:0803.0883].

[107] T. Gleisberg, S. Hoeche, F. Krauss, M. Schonherr, S. Schumann, F. Siegert, and J. Winter *JHEP* 02 (2009) 007, [arXiv:0811.4622].

[108] M. Bengtsson and T. Sjostrand *Phys. Lett.* B185 (1987) 435.

[109] S. Frixione and B. R. Webber *JHEP* 06 (2002) 029, [hep-ph/0204244].

[110] S. Frixione and B. R. Webber hep-ph/0612272.

[111] P. Nason *JHEP* 11 (2004) 040, [hep-ph/0409146].

[112] S. Catani, F. Krauss, R. Kuhn, and B. R. Webber *JHEP* 11 (2001) 063, [hep-ph/0109231].

[113] K. Hamilton and P. Nason *JHEP* 06 (2010) 039, [arXiv:1004.1764].

[114] W. T. Giele, L. Hartgring, D. A. Kosower, E. Laenen, A. J. Larkoski, J. J. Lopez-Villarejo, M. Ritzmann, and P. Skands *PoS* DIS2013 (2013) 165, [arXiv:1307.1060].

[115] K. Hamilton, P. Nason, C. Oleari, and G. Zanderighi *JHEP* 05 (2013) 082, [arXiv:1212.4504].

[116] S. Alioli, C. W. Bauer, C. Berggren, F. J. Tackmann, J. R. Walsh, and S. Zuberi *JHEP* 06 (2014) 089, [arXiv:1311.0286].

[117] M. Dasgupta, F. A. Dreyer, K. Hamilton, P. F. Monni, and G. P. Salam arXiv:1805.09327.

[118] S. Frixione, P. Nason, and C. Oleari *JHEP* 11 (2007) 070, [arXiv:0709.2092].

[119] S. Alioli, P. Nason, C. Oleari, and E. Re *JHEP* 06 (2010) 043, [arXiv:1002.2581].

[120] J. Alwall et al. *Comput. Phys. Commun.* 176 (2007) 300–304, [hep-ph/0609017].

[121] K. Hamilton, P. Nason, and G. Zanderighi *JHEP* 10 (2012) 155, [arXiv:1206.3572].

[122] A. Banfi, G. P. Salam, and G. Zanderighi *JHEP* 06 (2012) 159, [arXiv:1203.5773].

[123] A. Banfi, P. F. Monni, G. P. Salam, and G. Zanderighi *Phys. Rev. Lett.* 109 (2012) 202001, [arXiv:1206.4998].

[124] A. Banfi, F. Caola, F. A. Dreyer, P. F. Monni, G. P. Salam, G. Zanderighi, and F. Dulat *JHEP* 04 (2016) 049, [arXiv:1511.02886].

[125] A. Banfi, S. Redford, M. Vesterinen, P. Waller, and T. R. Wyatt *Eur. Phys. J.* C71 (2011) 1600, [arXiv:1009.1580].

[126] L. J. Dixon, L. Magnea, and G. F. Sterman *JHEP* 08 (2008) 022, [arXiv:0805.3515].

[127] L. Magnea and G. F. Sterman *Phys. Rev.* D42 (1990) 4222–4227.

[128] D. Amati, A. Bassetto, M. Ciafaloni, G. Marchesini, and G. Veneziano *Nucl. Phys.* B173 (1980) 429–455.

[129] S. Catani and M. Grazzini *Nucl. Phys.* B845 (2011) 297–323, [arXiv:1011.3918].

[130] G. Parisi and R. Petronzio *Nucl. Phys.* B154 (1979) 427–440.

[131] S. Catani and M. Grazzini *Eur. Phys. J.* C72 (2012) 2013, [arXiv:1106.4652]. [Erratum: Eur. Phys. J.C72,2132(2012)].

[132] S. Catani, L. Cieri, D. de Florian, G. Ferrera, and M. Grazzini *Eur. Phys. J.* C72 (2012) 2195, [arXiv:1209.0158].

[133] T. Gehrmann, T. Luebbert, and L. L. Yang *JHEP* 06 (2014) 155, [arXiv:1403.6451].

[134] X. Chen, T. Gehrmann, E. W. N. Glover, A. Huss, Y. Li, D. Neill, M. Schulze, I. W. Stewart, and H. X. Zhu arXiv:1805.00736.

[135] A. Gehrmann-De Ridder, T. Gehrmann, E. W. N. Glover, A. Huss, and T. A. Morgan *JHEP* 11 (2016) 094, [arXiv:1610.01843].

[136] J. Butterworth et al. *J. Phys.* G43 (2016) 023001, [arXiv:1510.03865].

[137] ATLAS Collaboration, G. Aad et al. *Eur. Phys. J.* C76 (2016), no. 5 291, [arXiv:1512.02192].

[138] NNPDF Collaboration, R. D. Ball et al. *JHEP* 04 (2015) 040, [arXiv:1410.8849].

[139] R. Boughezal, C. Focke, W. Giele, X. Liu, and F. Petriello *Phys. Lett.* B748 (2015) 5–8, [arXiv:1505.03893].

[140] R. Boughezal, F. Caola, K. Melnikov, F. Petriello, and M. Schulze *Phys. Rev. Lett.* 115 (2015), no. 8 082003, [arXiv:1504.07922].

[141] F. Caola, K. Melnikov, and M. Schulze *Phys. Rev.* D92 (2015), no. 7 074032, [arXiv:1508.02684].

[142] X. Chen, J. Cruz-Martinez, T. Gehrmann, E. W. N. Glover, and M. Jaquier *JHEP* 10 (2016) 066, [arXiv:1607.08817].

[143] C. Anastasiou, C. Duhr, F. Dulat, E. Furlan, T. Gehrmann, F. Herzog, A. Lazopoulos, and B. Mistlberger *JHEP* 05 (2016) 058, [arXiv:1602.00695].

[144] B. Mistlberger arXiv:1802.00833.

[145] R. Boughezal, J. M. Campbell, R. K. Ellis, C. Focke, W. T. Giele, X. Liu, and F. Petriello *Phys. Rev. Lett.* 116 (2016), no. 15 152001, [arXiv:1512.01291].

[146] S. Catani, L. Trentadue, G. Turnock, and B. R. Webber *Nucl. Phys.* B407 (1993) 3–42.

[147] ATLAS Collaboration, M. Aaboud et al. *JHEP* 10 (2017) 132, [arXiv:1708.02810].

[148] M. Bonvini, S. Marzani, C. Muselli, and L. Rottoli *JHEP* 08 (2016) 105, [arXiv:1603.08000].

[149] ATLAS Collaboration, M. Aaboud et al. arXiv:1802.04146.

[150] M. Dasgupta and G. P. Salam *Phys. Lett.* B512 (2001) 323–330, [hep-ph/0104277].

[151] A. J. Larkoski, I. Moult, and D. Neill *JHEP* 09 (2015) 143, [arXiv:1501.04596].

[152] J. M. Lindert, K. Melnikov, L. Tancredi, and C. Wever *Phys. Rev. Lett.* 118 (2017), no. 25 252002, [arXiv:1703.03886].

[153] F. Caola, J. M. Lindert, K. Melnikov, P. F. Monni, L. Tancredi, and C. Wever *Submitted to: JHEP* (2018) [arXiv:1804.07632].

[154] F. Bishara, U. Haisch, P. F. Monni, and E. Re *Phys. Rev. Lett.* 118 (2017), no. 12 121801, [arXiv:1606.09253].

[155] M. Grazzini, A. Ilnicka, M. Spira, and M. Wiesemann *JHEP* 03 (2017) 115, [arXiv:1612.00283].

[156] J. C. Collins and D. E. Soper *Phys. Rev.* D16 (1977) 2219.

[157] P. Pietrulewicz, D. Samitz, A. Spiering, and F. J. Tackmann *JHEP* 08 (2017) 114, [arXiv:1703.09702].

[158] E. Bagnaschi, F. Maltoni, A. Vicini, and M. Zaro arXiv:1803.04336.

[159] ATLAS Collaboration, M. Aaboud et al. *Eur. Phys. J.* C78 (2018), no. 2 110, [arXiv:1701.07240].

[160] J. M. Butterworth, A. R. Davison, M. Rubin, and G. P. Salam *Phys. Rev. Lett.* 100 (2008) 242001, [arXiv:0802.2470].

[161] CMS Collaboration, S. Chatrchyan et al. *Phys. Rev.* D89 (2014), no. 1 012003, [arXiv:1310.3687].

[162] ATLAS Collaboration, G. Aad et al. *JHEP* 01 (2015) 069, [arXiv:1409.6212].

[163] ATLAS Collaboration, M. Aaboud et al. *JHEP* 12 (2017) 024, [arXiv:1708.03299].

[164] CMS Collaboration, A. M. Sirunyan et al. *Phys. Lett.* B780 (2018) 501–532, [arXiv:1709.07497].

[165] O. Brein, A. Djouadi, and R. Harlander *Phys. Lett.* B579 (2004) 149–156, [hep-ph/0307206].

[166] G. Ferrera, M. Grazzini, and F. Tramontano *Phys. Rev. Lett.* 107 (2011) 152003, [arXiv:1107.1164].

[167] G. Ferrera, M. Grazzini, and F. Tramontano *Phys. Lett.* B740 (2015) 51–55, [arXiv:1407.4747].

[168] J. M. Campbell, R. K. Ellis, and C. Williams *JHEP* 06 (2016) 179, [arXiv:1601.00658].

[169] M. L. Ciccolini, S. Dittmaier, and M. Kramer *Phys. Rev.* D68 (2003) 073003, [hep-ph/0306234].

[170] A. Denner, S. Dittmaier, S. Kallweit, and A. Muck *JHEP* 03 (2012) 075, [arXiv:1112.5142].

[171] S. Frixione and B. R. Webber hep-ph/0506182.

[172] K. Hamilton, P. Richardson, and J. Tully *JHEP* 04 (2009) 116, [arXiv:0903.4345].

[173] G. Luisoni, P. Nason, C. Oleari, and F. Tramontano *JHEP* 10 (2013) 083, [arXiv:1306.2542].

[174] G. Ferrera, G. Somogyi, and F. Tramontano arXiv:1705.10304.

[175] F. Caola, G. Luisoni, K. Melnikov, and R. Röntsch arXiv:1712.06954.

[176] K. Hamilton, T. Melia, P. F. Monni, E. Re, and G. Zanderighi *JHEP* 09 (2016) 057, [arXiv:1606.07062].

[177] R. Frederix and K. Hamilton *JHEP* 05 (2016) 042, [arXiv:1512.02663].

[178] S. Carrazza, R. Frederix, K. Hamilton, and G. Zanderighi arXiv:1805.09855.

[179] K. Hamilton, P. Nason, E. Re, and G. Zanderighi *JHEP* 10 (2013) 222, [arXiv:1309.0017].

[180] A. Karlberg, E. Re, and G. Zanderighi *JHEP* 09 (2014) 134, [arXiv:1407.2940].

[181] E. Re, M. Wiesemann, and G. Zanderighi arXiv:1805.09857.

[182] L. A. Harland-Lang, A. D. Martin, P. Motylinski, and R. S. Thorne *Eur. Phys. J.* C75 (2015), no. 5 204, [arXiv:1412.3989].

[183] S. Catani, Y. L. Dokshitzer, M. H. Seymour, and B. R. Webber *Nucl. Phys.* B406 (1993) 187–224.

[184] S. D. Ellis and D. E. Soper *Phys. Rev.* D48 (1993) 3160–3166, [hep-ph/9305266].

[185] LHC Higgs Cross Section Working Group Collaboration, D. de Florian et al. arXiv:1610.07922.

[186] M. Cacciari, G. P. Salam, and G. Soyez *JHEP* 04 (2008) 063, [arXiv:0802.1189].

[187] M. Cacciari, G. P. Salam, and G. Soyez *Eur. Phys. J.* C72 (2012) 1896, [arXiv:1111.6097].

[188] S. Dulat, T.-J. Hou, J. Gao, M. Guzzi, J. Huston, P. Nadolsky, J. Pumplin, C. Schmidt, D. Stump, and C. P. Yuan *Phys. Rev.* D93 (2016), no. 3 033006, [arXiv:1506.07443].

[189] S. Carrazza, J. I. Latorre, J. Rojo, and G. Watt *Eur. Phys. J.* C75 (2015) 474, [arXiv:1504.06469].

[190] K. G. Chetyrkin, J. H. Kuhn, and M. Steinhauser *Comput. Phys. Commun.* 133 (2000) 43–65, [hep-ph/0004189].

[191] B. Hespel, F. Maltoni, and E. Vryonidou *JHEP* 06 (2015) 065, [arXiv:1503.01656].

[192] D. Goncalves, F. Krauss, S. Kuttimalai, and P. Maierhöfer *Phys. Rev.* D92 (2015), no. 7 073006, [arXiv:1509.01597].

[193] L. Altenkamp, S. Dittmaier, R. V. Harlander, H. Rzehak, and T. J. E. Zirke *JHEP* 02 (2013) 078, [arXiv:1211.5015].

[194] R. V. Harlander, A. Kulesza, V. Theeuwes, and T. Zirke *JHEP* 11 (2014) 082, [arXiv:1410.0217].

[195] P. Skands, S. Carrazza, and J. Rojo *Eur. Phys. J.* C74 (2014), no. 8 3024, [arXiv:1404.5630].

[196] J. M. Campbell, R. K. Ellis, P. Nason, and E. Re *JHEP* 04 (2015) 114, [arXiv:1412.1828].

[197] T. Sjöstrand, S. Ask, J. R. Christiansen, R. Corke, N. Desai, P. Ilten, S. Mrenna, S. Prestel, C. O. Rasmussen, and P. Z. Skands *Comput. Phys. Commun.* 191 (2015) 159–177, [arXiv:1410.3012].

[198] A. Banfi, G. P. Salam, and G. Zanderighi *Eur. Phys. J.* C47 (2006) 113–124, [hep-ph/0601139].

[199] P. W. Higgs *Phys. Rev. Lett.* 13 (1964) 508–509.

[200] G. S. Guralnik, C. R. Hagen, and T. W. B. Kibble *Phys. Rev. Lett.* 13 (1964) 585–587.

[201] F. Englert and R. Brout *Phys. Rev. Lett.* 13 (1964) 321–323.

[202] ATLAS, CMS Collaboration, G. Aad et al. *JHEP* 08 (2016) 045, [arXiv:1606.02266].

[203] A. Djouadi, W. Kilian, M. Muhlleitner, and P. M. Zerwas *Eur. Phys. J.* C10 (1999) 45–49, [hep-ph/9904287].

[204] J. Grigo, J. Hoff, K. Melnikov, and M. Steinhauser *Nucl. Phys.* B875 (2013) 1–17, [arXiv:1305.7340].

[205] E. W. N. Glover and J. J. van der Bij *Nucl. Phys.* B309 (1988) 282–294.

[206] D. de Florian and J. Mazzitelli *Phys. Rev. Lett.* 111 (2013) 201801, [arXiv:1309.6594].

[207] S. Dawson, S. Dittmaier, and M. Spira *Phys. Rev.* D58 (1998) 115012, [hep-ph/9805244].

[208] S. Borowka, N. Greiner, G. Heinrich, S. P. Jones, M. Kerner, J. Schlenk, and T. Zirke *JHEP* 10 (2016) 107, [arXiv:1608.04798].

[209] S. Borowka, N. Greiner, G. Heinrich, S. Jones, M. Kerner, J. Schlenk, U. Schubert, and T. Zirke *Phys. Rev. Lett.* 117 (2016), no. 1 012001, [arXiv:1604.06447]. [Erratum: Phys. Rev. Lett.117,no.7,079901(2016)].

[210] M. McCullough *Phys. Rev.* D90 (2014), no. 1 015001, [arXiv:1312.3322]. [Erratum: Phys. Rev.D92,no.3,039903(2015)].

[211] C. Shen and S.-h. Zhu *Phys. Rev.* D92 (2015), no. 9 094001, [arXiv:1504.05626].

[212] M. Gorbahn and U. Haisch *JHEP* 10 (2016) 094, [arXiv:1607.03773].

[213] G. Degrassi, P. P. Giardino, F. Maltoni, and D. Pagani *JHEP* 12 (2016) 080, [arXiv:1607.04251].

[214] S. Weinberg *Phys. Lett.* 91B (1980) 51–55.

[215] W. Buchmuller and D. Wyler *Nucl. Phys.* B268 (1986) 621–653.

[216] B. Grzadkowski, M. Iskrzynski, M. Misiak, and J. Rosiek *JHEP* 10 (2010) 085, [arXiv:1008.4884].

[217] G. Passarino and M. Trott arXiv:1610.08356.

[218] I. Brivio and M. Trott arXiv:1706.08945.

[219] L. Lehman *Phys. Rev.* D90 (2014), no. 12 125023, [arXiv:1410.4193].

[220] B. Henning, X. Lu, T. Melia, and H. Murayama *JHEP* 08 (2017) 016, [arXiv:1512.03433].

[221] J. Elias-Miró, C. Grojean, R. S. Gupta, and D. Marzocca *JHEP* 05 (2014) 019, [arXiv:1312.2928].

[222] E. E. Jenkins, A. V. Manohar, and M. Trott *JHEP* 10 (2013) 087, [arXiv:1308.2627].

[223] E. E. Jenkins, A. V. Manohar, and M. Trott *JHEP* 01 (2014) 035, [arXiv:1310.4838].

[224] R. Alonso, E. E. Jenkins, A. V. Manohar, and M. Trott *JHEP* 04 (2014) 159, [arXiv:1312.2014].

[225] T. Hahn *Comput. Phys. Commun.* 140 (2001) 418–431, [hep-ph/0012260].

[226] T. Hahn and M. Perez-Victoria *Comput. Phys. Commun.* 118 (1999) 153–165, [hep-ph/9807565].

[227] T. Han, G. Valencia, and S. Willenbrock *Phys. Rev. Lett.* 69 (1992) 3274–3277, [hep-ph/9206246].

[228] ATLAS Collaboration, M. Aaboud et al. arXiv:1804.06174.

[229] R. Grober, M. Muhlleitner, M. Spira, and J. Streicher *JHEP* 09 (2015) 092, [arXiv:1504.06577].

[230] The ATLAS Collaboration, ATL-PHYS-PUB-2014-019.

[231] The ATLAS Collaboration, ATL-PHYS-PUB-2015-046.

[232] The ATLAS Collaboration, ATL-PHYS-PUB-2014-016.

[233] CMS Collaboration, CMS-NOTE-13-002 arXiv:1307.7135.

[234] D. de Florian and M. Grazzini *Nucl. Phys.* B616 (2001) 247–285, [hep-ph/0108273].

[235] T. Becher, M. Neubert, and D. Wilhelm *JHEP* 05 (2013) 110, [arXiv:1212.2621].

[236] Y. Li and H. X. Zhu *Phys. Rev. Lett.* 118 (2017), no. 2 022004, [arXiv:1604.01404].

[237] A. A. Vladimirov *Phys. Rev. Lett.* 118 (2017), no. 6 062001, [arXiv:1610.05791].

[238] C. T. H. Davies and W. J. Stirling *Nucl. Phys.* B244 (1984) 337–348.

[239] T. Becher and M. Neubert *Eur. Phys. J.* C71 (2011) 1665, [arXiv:1007.4005].

[240] J. G. Korner and E. Mirkes *Nucl. Phys. Proc. Suppl.* 23B (1991) 9–13.

[241] C. S. Lam and W.-K. Tung *Phys. Rev.* D18 (1978) 2447.

[242] A. Grau, G. Panchieri, and R. J. N. Phillips *Phys. Lett.* B251 (1990) 293–298.